Towards stimulated cyclotron emission in Dirac systems

Benjamin Benhamou-Bui

THÈSE POUR OBTENIR LE GRADE DE DOCTEUR

DE L'UNIVERSITÉ DE MONTPELLIER

En Physique

École doctorale: Information, Structures et Systèmes

Unité de recherche: Laboratoire Charles Coulomb

Towards stimulated cyclotron emission in Dirac systems

Présentée par Benjamin BENHAMOU-BUI
le 03 / 12 / 2025

Sous la direction de Frédéric TEPPE
et Benoît JOUAULT

Devant le jury composé de

Cristiano CIUTI, Professeur, MPQ UPCité, Paris, France	**Président**
Giacomo SCALARI, Professeur, ETH Zürich, Suisse	**Rapporteur**
Yanko TODOROV, Directeur de recherche, LPEM ESPCI CNRS, Paris, France	**Rapporteur**
Milan ORLITA, Directeur de recherche , LNCMI CNRS, Grenoble, France	**Examinateur**
Juliette MANGENEY, Directrice de recherche, LPENS CNRS, Paris, France	**Examinateur**
Frédéric TEPPE, Directeur de recherche, L2C CNRS, Montpellier, France	**Directeur**
Benoît JOUAULT, Directeur de recherche, L2C CNRS, Montpellier, France	**Co-directeur**
Christophe CONSEJO, Ingénieur de recherche, L2C Université de Montpellier, France	**Co-encadrant**

UNIVERSITÉ DE MONTPELLIER

Acknowledgments

Mes premiers remerciements vont naturellement vers les membres du jury, Cristiano Ciuti, Giacomo Scalari, Yanko Todorov, Milan Orlita et Juliette Mangeney, qui ont accepté et pris le temps de juger mon travail de thèse. Quelques mentions spéciales tout de même. Merci Cristiano pour le support théorique et la disponibilité dans les échanges (jamais vu quelqu'un d'aussi réactif sur WhatsApp). J'ai énormément appris sur les polaritons de Landau grâce à toi et je connais maintenant les meilleurs coins de la Seine pour pêcher... Un énorme merci à toi Milan pour l'accueil au LNCMI à Grenoble. Au cours de ces deux séjours, j'ai été très bien entouré, tant par toi (super barista) que par tes étudiants de l'époques Jan et Florian.

Comment conclure une thèse sans remercier mes encadrants de thèse, Christophe, Benoît et Fred. Merci Christophe pour l'expertise expérimentale, j'ai énormément appris à tes côté, tant du côté de la rigueur expérimentale que de la mesure elle même. J'ai adoré nos campagnes de manip à deux, même les samedis et dimanches que nous avont passé à papoter et à réviser nos vélos. Tu es vraiment quelqu'un de profondément gentil et tu n'hésites pas à dire "bravo" quand tu le penses et ça fait du bien! Tu n'hésites pas non plus à dire quand quelqu'un (moi?) fait une connerie et ça aussi c'est malgré tout appréciable... Merci Benoît pour ta présence dans cet encadrement. Même si on s'est quelque peu éloignés scientifiquement après le stage de master, ton apport dans cette thèse aura été plus que décisif grâce à ta rigueur sans faille et ton insatiable curiosité, sans oublier ta puissance en programmation pythonesque. En parlant de puissance, j'ai pu découvrir à quel point tu étais monstrueux sur un vélo et je te remercie de nous avoir trimballé lors de superbes sorties dans les Cévennes ou au mont Ventoux. Le petit défi qui tient entres nous ne sera définitivement pas facile à relever de mon côté... Last but definitely not least un grand merci à toi Fred. Tu es LA personne qui m'a convaincu de venir faire mon stage de master à Montpellier, dans un labo et une ville que je ne connaissais pas. Je me souviens encore entrer dans ton bureau complètement dépité et perdu et en ressortir (presque) convaincu que je voulais faire ma thèse dans l'équipe,

après t'avoir entendu parler avec ferveur de l'émission Landau et de la vaste et fascinante famille des isolants topologiques. Tu es pour moi un modèle de chercheur, passionné et rigoureux, et un chef d'équipe et encadrant exemplaire car tu sais interagir avec les gens et les toucher, qualité rare en recherche fondamentale... Je pense que si je poursuis ma carrière dans la recherche académique, ce sera en grande partie pour te ressembler, merci encore.

Merci au reste de l'équipe TEST: Sandra, Cédric, Laurent, Jérémie, Camilla, Guillaume, Salah et Elsa pour la super ambiance au quotidien. Mentions spéciales à Guillaume pour le super thé et Salah pour les skills incroyables en salle blanche. *Moustache graciàs* to you Elsa for bringing so much joy in the office and for the emotional support at the end of the thesis, your listening skills were very important to me. I am also grateful for having met Juanan and I thank you both for welcoming me and giving me the best time in Salamanca. Merci aux anciens de l'équipe TEST/TQNS: Sebastian, Colin, Boris et Maria pour les supers moments passés ensembles. Et évidemment merci à toi Titou, le chasseur d'histoire, le buveur d'antésite, le collectionneur de mues de cigales, le dessinateur de zizi masqué et j'en passe... Tu as litéralement sauvé mes deux premières années de thèses grâce à ton indéfectible volonté pour se biturer et notre rivalité ClashRoyalesque, merci infiniment. Pour finir, merci à tous les membres du laboratoire croisés quotidiennement: Edouard pour ton expertise de polissage, Bertrand pour ton combat permanent pour subvenir à nos besoins en Helium liquide, ExtremChris pour toutes les discussions sur l'environnement et les supers moments triathlons (c'est quand même grâce à toi que j'ai découvert ce magnifique sport), la S2QTeam pour la coolitude et enfin Dominique, JC, Carole, Audrey, Béatrice et Christelle pour l'efficacité administrative et la bonne humeur au quotidien.

Merci à ma super famille BLYMP pour le soutien depuis toutes ces années. Merci papa et maman pour m'avoir permis de faire ce que je voulais de mes études et de m'avoir transmis cette curiosité qui vous caractérise tant. Merci Prune pour ton amour et tes rires. Et enfin merci à toi Math, Berni, de partager tous ces merveilleux moments avec moi, merci pour ton enthousiasme, merci pour ton écoute et tes conseils, j'espère que tu es fière de ton jumeau. Je vous aime tous très fort (même toi Kit même si je le montre pas trop).

Merci aux copaines rencontrés pendant la thèse, comme toujours, du bon travail ne se fait jamais sans de bons ami·e·s. Un énorme merci tout d'abord à toi Thomdog (Thomas?) pour ton soutien, surtout en cette fin de thèse difficile émotionnellement. Merci pour tous les bons moments partagés, chez toi à mater le stade Toulousain, dans l'eau à boire toute la piscine, sur le vélo à me cacher derrière ton dos énorme et au bar bien sûr. Merci pour les fous-rires et les cafés, tout ça a été très important pour moi. Grand merci en vrac à tous

les autres: Domi&Loucif pour tous les super moments à Mtp (Monster Block!!) et Gnèvaaaanh, Théo pour l'ouverture d'esprit au quotidien, Romain pour les défis sportifs (et la mise en lien avec des mecs trop beaux et trop forts), Khalil pour la beauté, Valentin pour l'aléatoire, Josh pour la musique et le bateau et enfin Giacomo, Giac'prime, Elsa (thanks again for the wonderful cake), Daniel, Hugo, Shadi et Alice.

Merci aux copaines de toujours. Milles merci Eva, ma ptite patate, d'être à mes côtés depuis toutes ces années, ton soutien et ton écoute ont été très précieux sur cette fin de thèse. Merci à UnJourUnPorno (à quand un ouveau nom??) pour tous les moments et vacances rafraîchissantes. Merci à tout VincennesZoo pour tout, littéralement tout depuis le lycée. Merci à la team Au Bureau depuis les bancs de l'ENS, Jojo, Tomo, Alex (le groupe dont on ne doit pas prononcer le nom..), Didi, Elio, Max, Cass, je vous aime fort. Merci à toi mon Théo pour les aventures et l'écoute, tu me fais énormément de bien. Merci aux Yavbous depuis la prépa, j'espère que vous êtes fiers de votre monstre préféré.

Merci enfin à toi Ju, sans qui je n'aurais pas vécu cette aventure dans le Sud. Déménager à Montpellier a été, je pense, la meilleure décision de ma vie et je suis tellement heureux de partager ta vie et pour longtemps encore j'espère.

Résumé

L'utilisation du rayonnement térahertz (THz) connaît un essor rapide, allant de la recherche fondamentale aux applications variées telles que les communications, la sécurité ou les tests non destructifs. Pourtant, un problème technologique subsiste : aucun dispositif compact à base de semiconducteurs ne permet une émission continuement accordable sur toute la gamme 1–5 THz. Cette thèse s'inscrit dans ce contexte, en explorant les propriétés physiques des matériaux de Dirac et les phénomènes fondamentaux susceptibles de conduire à de nouvelles sources THz.

Les travaux expérimentaux portent sur l'étude magnéto-spectroscopique d'hétérostructures semi-conductrices, avec un accent particulier sur l'émission cyclotron (ou émission Landau). Alors que la magnéto-absorption repose sur la transition entre niveaux de Landau par absorption de photons, l'émission Landau correspond au processus inverse, c'est-à-dire la recombinaison radiative de porteurs excités vers des niveaux d'énergie plus bas. Ce mécanisme a permis la réalisation du seul laser à niveaux de Landau à ce jour, le laser p-Ge, capable de couvrir une large portion du domaine THz grâce à l'accordabilitité par le champ magnétique. Cependant, son fonctionnement nécessite de forts champs magnétiques et électriques ainsi que des températures cryogéniques, limitant son utilisation à la recherche fondamentale.

Les puits quantiques à base de HgTe, identifiés dans les années 2000 comme matériaux de Dirac et topologiques, permettent une émission de Landau intense sur tout le spectre THz, à des champs magnétiques bien plus faibles. Le premier résultat de cette thèse a consisté à démontrer que cette phase de Dirac permet une accordabilité électrique de la fréquence d'émission grâce à la modulation de la densité électronique par effet de grille. Des expériences menées sous champs électriques et magnétiques croisés intenses visant à explorer des régimes de transport extrêmes ont aussi révélé la forte non-parabolicité de la structure de bande à travers la dynamique des porteurs chauds.

Ce comportement met en évidence l'une des principales limites des semiconducteurs II–VI : leur sensibilité à la température et la complexité de fabrication, rendant difficile l'obtention des champs électriques intenses nécessaires

à une inversion de population. Une autre approche pour atteindre l'émission stimulée consiste à exploiter le fort couplage lumière–matière, menant à la formation de quasi-particules hybrides appelées polaritons. Ces entités peuvent condenser dans un état quantique unique et émettre une lumière cohérente lors de leur recombinaison radiative. Une cavité Fabry–Perot THz a ainsi été conçue, dont la résonance est couplée à la transition cyclotron des structures à base de HgTe, favorisant la formation de polaritons de Landau. Leur existence a été confirmée par des mesures de magnéto-réflectivité. Nous avons ensuite démontré l'électroluminescence de ces polaritons et montré que le système opère à proximité du seuil laser. L'amélioration du facteur de qualité de la cavité apparaît comme la voie la plus prometteuse pour atteindre le régime laser polaritonique et réaliser un émetteur THz compact.

Enfin, la thèse s'ouvre sur une autre famille de semi-conducteurs, les composés III–V, moins sensibles à la température, technologiquement matures et pouvant présenter de hautes mobilités électroniques. L'émission de Landau a été étudiée dans des puits à base d'InSb et de GaAs, ainsi que dans une hétérostructure exotique en super-réseau à base d'InAs et de GaInSb. Ce système, qui abrite une phase de Dirac tridimensionnelle, apparaît comme un candidat particulièrement prometteur pour la réalisation d'un laser à niveaux de Landau capable de combler le fossé technologique du domaine térahertz.

Contents

Chapter 1

Introduction

Contents

1.1 Motivation: filling the Terahertz technological gap

The Terahertz (THz) frequency range is a part of the electromagnetic spectrum conventionally located between 0.3 THz and 10 THz. It is at the interface between microwaves and infrared (IR) radiations and thus exhibits a combination of properties from both regions. The energy of THz waves corresponds to that of many fundamental excitations in solids, liquids, and gases, such as phonons, plasmons, electron spin resonances, cyclotron resonances, molecular vibrations, and others. Moreover, THz radiations are non-ionizing and can penetrate a wide variety of non-conducting materials such as plastics, composite materials, concrete, clothes, but also living tissues, among others. It has therefore a very broad

field of applications beyond fundamental physics, ranging from medical imaging or chemical spectroscopy to ultrafast wireless communications and security [1]. For a long time, the THz spectrum remained largely inaccessible due to the lack of efficient sources and detectors. Although the situation has improved in recent years, this technological gap has not yet been fully bridged as we will see later on. On the side of THz radiation sources, and considering the position of this frequency range within the electromagnetic spectrum, THz radiations can be generated through two main approaches. The first approach, based on electronic technologies, covers the lower-frequency end of the THz spectrum, near the microwave region, and is mainly based on of multiplier circuits based on Schottky diodes [2] and oscillating circuits including a component featuring a negative resistance. To achieve this second part, a wide number of solutions have been developed but one can cite Gunn diodes [3], resonant tunneling diodes [4] and impact ionizing avalanche transit time diodes [5]. These solid sources have the advantages to be very compact and can efficiently cover the low frequency part of the THz range up to about 1 THz [6, 7]. On the other hand, the second family of solid sources is mainly composed of quantum cascade laser (QCL) [8]. These are semiconductors-based lasers operating at a fixed output frequency but allowing to cover the upper part of the THz range (above 10 THz) thanks to heterostructure design. Thanks to recent improvements, it was possible to lower the output frequency of such lasers and THz-QCLs can now cover the 1 to 5 THz frequency range, with output powers reaching 1 W and operating at rather high temperatures up to 250 K, relying on Peltier coolers [9]. However, these single-mode sources don't allow a very wide range of tunability. Indeed, despite sophisticated cavity design, people could only reach frequency tuning ranges of few hundreds of GHz [9]. Therefore, there is currently a lack of THz source able to be continuously tuned across the 1 to 5 THz frequency range, that we will call "THz gap" in the following.

Some experimental techniques, not based in solid states sources, can nonetheless allow to perform spectroscopy within the whole THz range. One widely used is the time-domain spectroscopy (TDS) technique where a broad-band radiation (typically ranging from 500 GHz to 4 THz) is emitted thanks to a photoconductive antenna when submitted to an ultrafast optical pulse [10]. Another way to cover this THz gap is the use of gas-based laser, using CO_2 as a pump of a second laser based on different other gases as methanol or formic acid for example, that can produce several intense monochromatic emission lines from below 1 THz up to several THz, depending on the gas mixture and the pressure [11]. However, all these techniques are either very bulky or not tunable, which can be significant drawbacks for applications.

We will therefore investigate how to obtain a compact, solid-state-based source that is powerful enough and easily tunable to fully cover the THz technological gap.

1.2 Overview of the cyclotron-resonance-based emitters

The idea to use cyclotron resonance of electrons to generate THz waves arose in the late 1950s. The cyclotron resonance (CR) is a phenomenon that happens when the frequency of an incident radiation matches the one of the natural carrier's rotation when submitted to a magnetic field. This cyclotron resonance frequency (for non-relativistic carriers) is given by

$$\omega_c = \frac{qB}{m}, \tag{1.1}$$

where q is the carrier's charge, B the magnetic field strength and m the mass of the carrier. For example, the CR frequency of an electron in free space submitted to a magnetic field

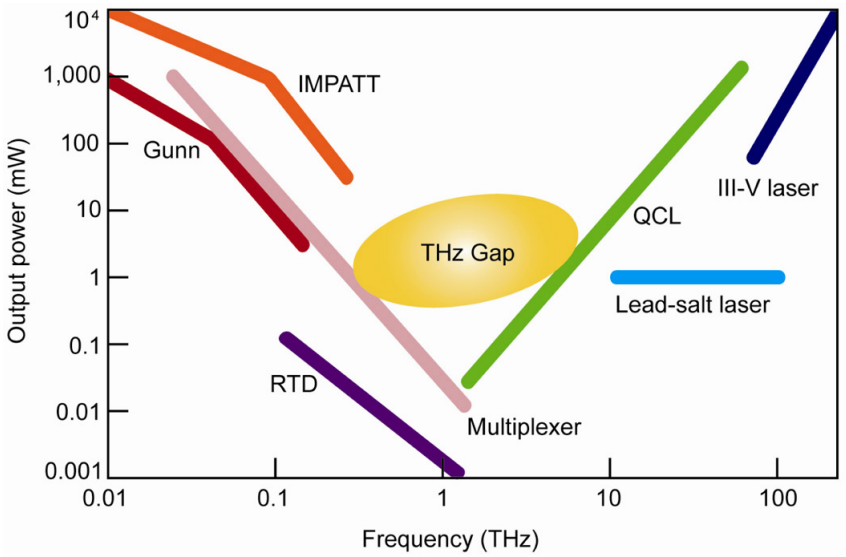

Figure 1.1: Highlighting of the THz technological gap. Adapted from [6].

intensity of 1 T is around 28 GHz, falling in the millimeter wave range. Therefore, the idea to have stimulated emission, tunable with magnetic field, has emerged at this period. In particular, it led to the development of the yet most powerful source of millimeter light that is the gyrotron [12, 13]. When submitted to a transverse magnetic field, relativistic electrons produced by an electron gun can emit intense radiation by a gyration motion. It has been demonstrated that a state-of-the-art gyrotron could produce light at 300 GHz and with an output power of 1.5 kW [13]. However, it is a very bulky set-up and despite the intense emission, the output frequency remains far from the interest zone that is the THz gap. It is clear from Eq. 1.1 that if we want to reach the THz range with this technique while maintaining reasonably low magnetic field strength, it is necessary to reduce the mass of the carriers. That is why CR emission is very interesting in semiconductors systems. Indeed, in addition to being more compact, electrons can have effective masses 10 to 50 times lower than in vacuum, thus shifting the CR frequency towards the THz gap.

Developments of cyclotron-resonance-based emitters in semiconductors have been very productive in the 1970s. Back then, cyclotron resonance was a well established experimental method to characterize the effective mass and band structure of semiconductors. The development of numerical methods for scattering process calculations in crossed electric and magnetic fields enabled physicists to develop potential carrier distribution inversion methods in semiconductors. One of the main challenges that the physicists encountered is the Auger effect or Auger scattering. It is a non-radiative carrier-carrier recombination, first discovered in the 20s in the context of X-rays spectroscopy of ionized gas, that can be dominant in semiconductors. It occurs when two excited carriers are close in energy and interact, one being scattered down in energy and the other being scattered up. The electron that is scattered towards higher energies can then relax by the assistance of phonons and it results in no net emission of photon. For this mechanism to be possible, there must be a state available for the down-scattered carrier and for the up-scattered one. If we now look at the LLs landscape for a parabolic band-structure (we will detail its computation later on), one can see on Fig. 1.2 that, since all the levels are equidistant, as soon as carriers are excited towards high indexes LLs, one can find a lot of sets of empty LLs that could host electron after an Auger scattering event. Therefore, in parabolic systems, non-radiative Auger processes can be very

large, limiting the output optical power available at the end.

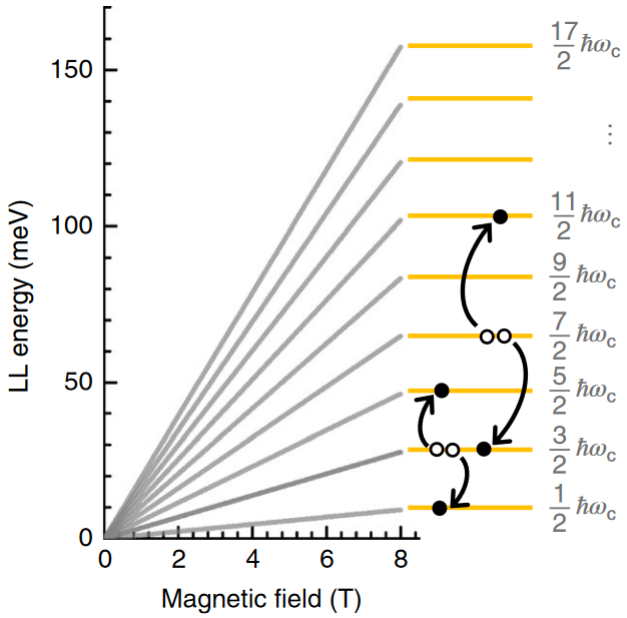

Figure 1.2: Magnetic field dependence of the LLs for electrons in a parabolic band structure (light grey lines). Several non-radiative Auger processes are sketched for a fixed magnetic field. Adapted from [14].

In this framework of minimizing this non-radiative Auger effect, people have started to look for material featuring non-parabolicities in their band-structure. It has led to the realization of two THz sources in bulk p-doped Germanium that are the light-hole Landau level (LL) laser [15–19] and the CR-based Negative Effective Mass Amplifier and Generator (NEMAG) [20, 21]. While the last one was shown to be emitting very efficiently but in a restricted frequency range (between 100 and 300 GHz for magnetic fields ranging from 2 to 6 T), the first one is the only, up to date, solid-state THz source that can emit through the entire THz gap in a continuously tunable manner with the applied magnetic field. Indeed, it is capable of generating radiation of frequency ranging from 500 GHz to 3.5 THz with magnetic field of 1 to 6 T [22]. The only drawback that this technique encountered is the high required magnetic field, implying a high bulkiness (due to the need for superconducting coil) and a low-speed tunability (due to the magnetic field sweeping time).
We will now take time to develop the principle of this p-Ge LL laser in order to understand how to improve it.

1.3 Description of the p-Ge Landau level laser

This section aims at describing the different building blocks of the Landau level laser operation and to see the application on the p-Ge system. We will only focus on the one-band case, where only the light-holes are involved in the emission, because it is more representative of the phenomenon at play in our structures. However, the most efficient version of the p-Ge LL laser was obtained by taking advantages of light-hole to heavy-hole transitions [23].

1.3.1 Landau levels quantization

When submitted to a high enough magnetic field, the band structure of a semiconductors is strongly modified. It leads to the well known Landau levels where the energy bands becomes quantized in sub-bands. To describe electrons in the presence of a magnetic field, we need to replace the momentum **p** by π = **p** + e**A** where **A** is the potential vector and e the electron charge. For a magnetic field aligned with the z direction, we can choose the Landau gauge, giving $\vec{A}$ = (- By, 0, 0). If we now apply this formalism to a two-dimensional parabolic system, the Hamiltonian becomes

$$H = \frac{(\mathbf{p} + e\mathbf{A})^2}{2m^*} + V(z), \tag{1.2}$$

where m^* is the effective mass of the semiconductor and $V(z)$ a confinement potential along the z direction. We can separate the Hamiltonian in two terms:

$$H_z = \frac{p_z^2}{2m^*} + V(z), \tag{1.3}$$

$$H_{xy} = \frac{p_y^2}{2m^*} + \frac{(p_x - eBy)^2}{2m^*}. \tag{1.4}$$

The first term does not depend on the magnetic field and will give bound states due to the confinement. At the quantum limit, only the lower energy one will be populated. The second term can be solved by using the following *Ansatz* function:

$$\psi(x, y) = e^{ik_x x}\eta(y) \tag{1.5}$$

and it leads to the following eigenvalue problem:

$$\left[\frac{p_y^2}{2m^*} + \frac{1}{2}m^*\omega_c^2\left(y - \frac{\hbar k_x}{eB}\right)^2\right]\eta(y) = E\,\eta(y), \tag{1.6}$$

which is nothing else than a one-dimensional quantum mechanical harmonic oscillator, centered around $y_0 = \frac{\hbar k_x}{eB}$. Therefore, the eigenvalues read:

$$E_n = \hbar\omega_c\left(n + \frac{1}{2}\right) + \frac{p_z^2}{2m}, \tag{1.7}$$

where $n \geqslant 0$ is a quantum number labeling the different Landau sub-bands. We retrieve the fact that, as we saw earlier with Fig. 1.2, the LLs of a parabolic band-structure disperse linearly with the magnetic field. This means that all the neighbor levels are spaced by the same amount of energy $\hbar\omega_c$.

However, due to the coupling between its two valence bands and a split-off one, p-Ge does not have a purely parabolic band-structure [22] (see sketch of Fig. 1.3). The two valence bands can be modeled using the effective 4-bands Luttinger Hamiltonian [25]

$$H_{Lutt} = \frac{\hbar^2}{2m_0}\left[\gamma_1 k^2 - 2\gamma_2\sum_i k_i^2 J_i^2 - 4\gamma_3\sum_{i\neq j} k_i k_j J_i J_j\right], \tag{1.8}$$

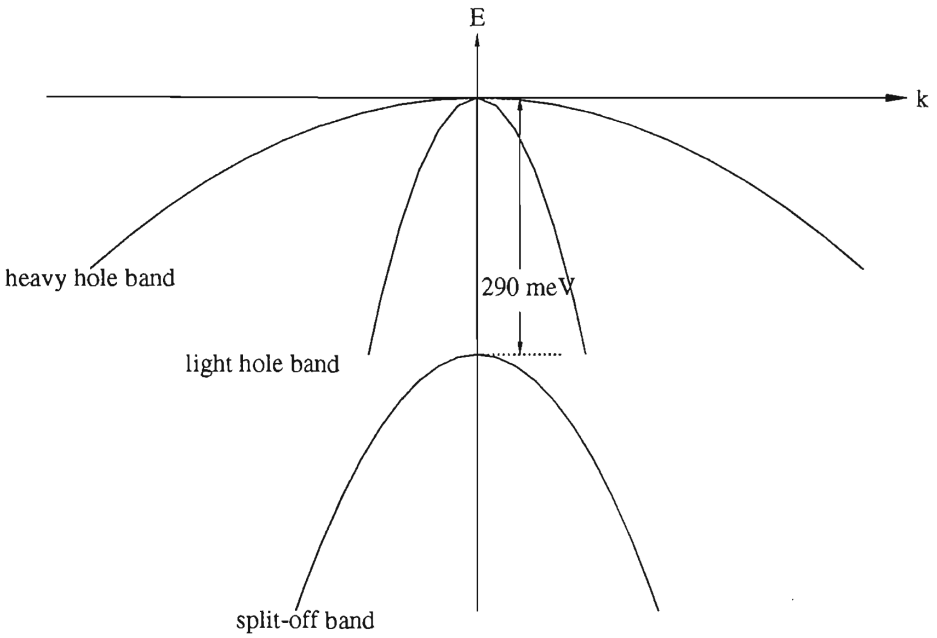

Figure 1.3: **Sketch of the valence bands in p-Ge.** Adapted from [24].

where γ_i are the Luttinger parameters, J_i the spin matrices and $k = (k_x, k_y, k_z)$. In the first order in k^2, Eq. 1.8 reduces to give

$$E_{HH}^{(0)}(k) = \frac{\hbar^2 k^2}{2m_0}(\gamma_1 - 2\gamma) \quad \text{and} \quad E_{LH}^{(0)}(k) = \frac{\hbar^2 k^2}{2m_0}(\gamma_1 + 2\gamma), \tag{1.9}$$

where $\gamma \equiv \gamma_2 = \gamma_3$ in a spherical approximation and HH (resp. LH) stands for heavy-hole (resp. light-hole). These two expressions are parabolic approximations and give the two effective masses for the hole bands $m^*_{LH/HH} = \dfrac{m_0}{\gamma_1 \pm 2\gamma}$. When taking into account the effect of the third split-off band (due to the spin-orbit coupling for example), we can treat the problem perturbatively as follow:

$$E_{LH/HH}(k) = \mathcal{A}k^2 + \mathcal{B}k^2 + \mathcal{O}(k^6), \tag{1.10}$$

where $\mathcal{A} = \dfrac{\hbar}{2m^*_{LH/HH}}$ and $\mathcal{B}$ is a function of the γ_i and the energy distance Δ between the two valence band and the split-off one, so that $\mathcal{B} \simeq \dfrac{\mathcal{A}^2}{\Delta}$. At first order we have $k^2 \simeq \dfrac{E}{\mathcal{A}}$ and Eq. 1.10 can be written as

$$E(k) \simeq \mathcal{A}k^2 + \mathcal{B}\left(\frac{E}{\mathcal{A}}\right)^2, \tag{1.11}$$

and therefore:

$$E(k)\left(1 - \frac{\mathcal{B}}{\mathcal{A}^2}E\right) \simeq \mathcal{A}k^2. \tag{1.12}$$

We finally obtain the compact form

$$E\left(1 - \frac{E}{\Delta}\right) = \frac{\hbar^2 k^2}{2m^*}, \tag{1.13}$$

which takes into account a small non-parabolicity correction. The smaller Δ is, namely the closer from the two valence bands the split-off band is, the more pronounced the non-parabolicities will be.

We can now compute the associated Landau level dispersion by applying the same procedure as detailed at the beginning of this subsection. The LLs can be computed by numerically solving the following equation [26]:

$$(a+b)\sqrt{ab} + (b-a)^2 \log\left(\frac{\sqrt{b}-\sqrt{a}}{\sqrt{b-a}}\right) = 0, \tag{1.14}$$

where

$$a = E_n - \epsilon_\perp, \qquad b = \Delta + E_n + \epsilon_\perp, \tag{1.15}$$

and

$$\epsilon_\perp = -\frac{\Delta}{2} + \sqrt{\left(\frac{\Delta}{2}\right)^2 + \Delta\hbar\omega_c\left(n+\frac{1}{2}\right)}. \tag{1.16}$$

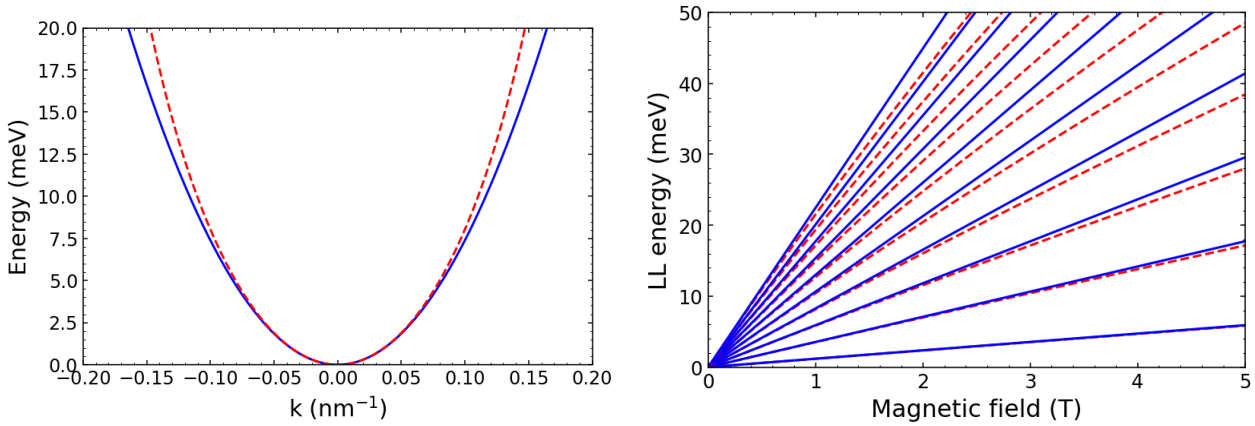

(a) (b)

Figure 1.4: **Comparison between the parabolic and non-parabolic models.**
(a) Band dispersion and (b) LLs dispersion with magnetic field for a purely parabolic system (solid blue lines) and a non-parabolic one (red dashed lines).

Figure 1.4a shows the comparison between a purely parabolic band and a band computed with Eq. 1.13, taking Δ = 100 meV. On Fig. 1.4b is plotted the associated LLs dispersions according to Eq. 1.14. It is clear that the non-parabolicity correction in the band-structure induces the breaking of the equidistance of the LLs. This is a key ingredient in the functioning of the p-Ge Landau level laser as its valence band features non-parabolicities and therefore, Auger scattering processes are highly reduced.

1.3.2 Streaming motion

In the past, several theoretical propositions in the aim of achieving a light amplification in a cyclotron resonance system have been made. The most convincing one was proposed by *T. Kurosawa* [27] and relies on the fact that in most materials, the interaction between carriers and optical phonons is very efficient. Therefore, in specific crossed electric and magnetic fields, it could be possible to accumulate carriers in the phase space and eventually induce

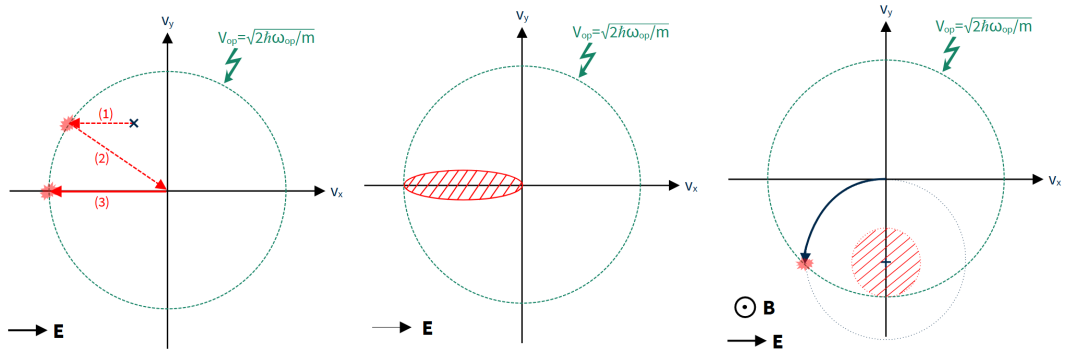

Figure 1.5: **Streaming motion, in velocity space, of a carrier under crossed electric and magnetic fields.**
(a) The carrier is first accelerated from its initial state to the optical phonon velocity (1). It is then scattered back to the center of the velocity space by emitting an optical phonon (2). It is again accelerated toward the optical phonon speed where it will be scattered (3). (b) After a short time, all the carriers are compelled to move in a restricted zone of the velocity space, identified by the red dashed area. (c) When a magnetic field is applied, the situation is similar except that the carriers are now accelerated in circular orbits, where the center is the drift velocity E/B. After a certain time, more and more carriers will be trapped in the dashed area of the velocity space.

a population inversion. When subjected to an electric field, the electrons' speed increases (see step (1) of Fig. 1.5a). The carrier's velocity is however limited by the electron-optical phonon interaction. It is usually very efficient and as soon as the carrier reaches a velocity close to the optical phonon one (represented as the dashed green circle V_{op} on Fig. 1.5), it looses all its kinetic energy by emitting a phonon (see step (2) of Fig. 1.5a). Since the electric field is still on, the electron is again accelerated until it reaches the optical-phonon velocity and so on (see step (3) of Fig. 1.5a). After a certain time, all the carriers are compelled in a restricted area in the velocity space (see Fig. 1.5b) and describe a streaming motion.

The situation is similar when a magnetic field is now applied, perpendicular to the electric field and to the 2DEG plan. The difference is that the carriers now follow circular trajectories in the velocity space, centered around the drift velocity $\frac{E}{B}$. When $\frac{E}{B} < \frac{V_{op}}{2}$, there are no orbits crossing the optical phonon velocity and no streaming effect occurs. Now if $\frac{E}{B} > V_{op}$, all the orbits crosses the optical phonon limit, thus establishing a streaming regime. Finally, for the particular condition where

$$1 \leqslant \frac{V_{op}}{(E/B)} \leqslant 2, \tag{1.17}$$

some orbits cross the optical phonon velocity but some do not. Therefore, a streaming regime takes place but some carriers are still following closed orbits and are never scattered by the optical phonons. This situation is depicted on Fig. 1.5c, where the streaming motion is sketched by the blue arrow and the closed orbits are contained in the red dashed area. Carriers following a streaming motion can be scattered towards the dashed area here it will stay for a long time, leading to an accumulation of electrons in this specific zone of the velocity space.

One should notice that, for this particular motion to establish, carriers should have the

time to reach the optical-phonon velocity and should be able to stay long enough in the accumulation area before being scattered by any other mean. This condition can be expressed as $\tau > T_{op}$, where τ is the momentum relaxation time of the carriers that can be estimated by transport measurements and T_{op} the time-of-flight for on electron to reach the optical phonon velocity. Therefore, a high quality crystal is required for this streaming motion to take place.

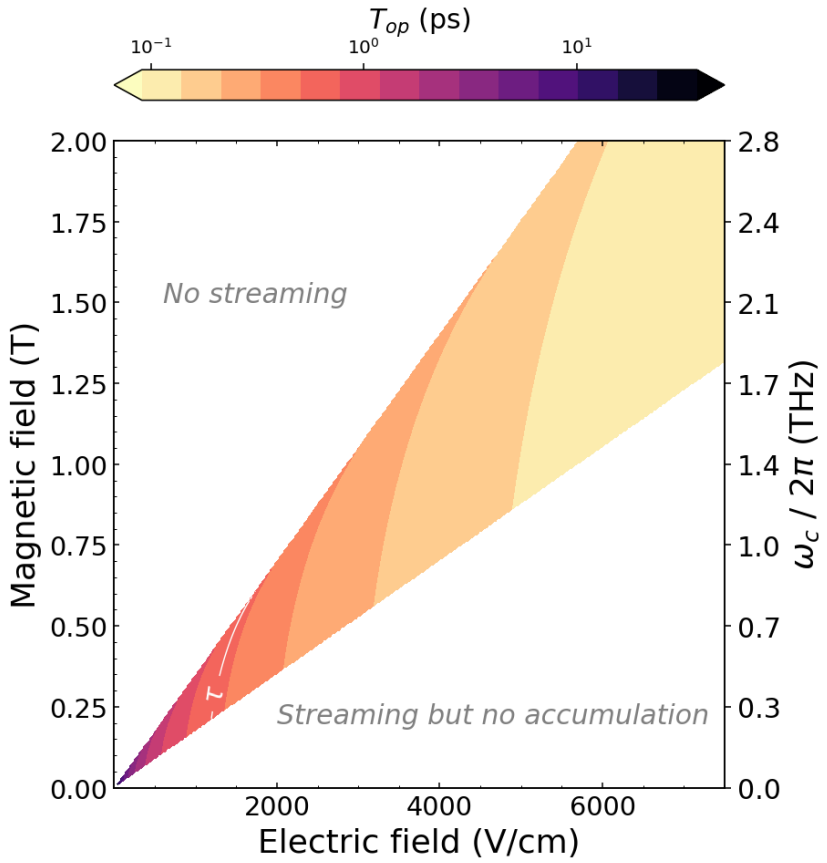

Figure 1.6: **Streaming motion conditions for HgTe-based QW.**
False-color mapping of the time-of-flight T_{op} that takes a carrier to reach the optical phonon speed. The white areas highlight the electric and magnetic field region where the streaming motion is impossible ($\frac{E}{B} < \frac{V_{op}}{2}$) or when it is allowed but no accumulation can occur ($\frac{E}{B} > V_{op}$). The iso-level labeled τ emphasizes the $T_{op} < \tau$ condition. The streaming regime is thus restrained to the right part of this iso-level.

All these conditions are summarized in Fig. 1.6. By solving the equation of motion of a carrier of charge e and mass m_c in crossed electric and magnetic fields, we can show that the time-of-flight T_{op} is given by:

$$T_{op} = \frac{2}{\omega_c} \arcsin\left(\frac{V_{op}B}{2E}\right). \tag{1.18}$$

Figure 1.6 shows the evolution of T_{op} when varying the electric and magnetic field strengths. The following parameters were taken: $m^* = 0.02\ m_0$ and $V_{op} = 5.7\times10^2$ m/s, which are characteristic of HgTe-based QW as we will see later. Two white areas are added to take condition 1.17 into account. A specific iso-level, labeled τ, is added to highlight the fact

that T_{op} should be compared to the typical carrier scattering time. Therefore, the conditions favorable to a streaming motion and leading to a carrier accumulation in the velocity space are located at the right of the iso-level, in the colored area of Fig. 1.6.

1.3.3 Landau level lasing in one band

If we now take into account the Landau levels structuration, carriers accumulated in the specific area in velocity space can only access quantized orbits. It was shown [27] that, if the electron-optical-phonon is strong enough, high index LLs will be more populated than low indexes ones. Indeed, as mentioned previously, if this interaction is efficient, the carriers' velocity after an optical phonon emission will be close to zero. The small remaining energy after the scattering event can be enough for the electron to reach a high index LL, as it orbits are passing close to the v = 0 point (see Fig. 1.7a). Finally, LLs close to the drift velocity center are less likely to be populated and the distribution area will result in a doughnut shape. Figure 1.7b depicts the resulting inversion-population mechanism in k-space, for

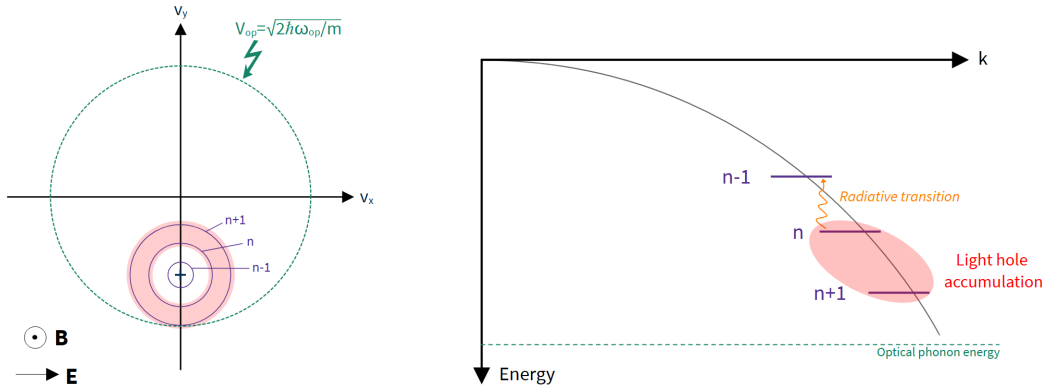

Figure 1.7: **Principle of the inversion population of light-holes in p-Ge.**
(a) Representation of the LLs involved in the accumulation area previously identified. As a result of strong electron-optical-phonon interaction, the area has a doughnut shape. (b) Representation of the inversion population mechanism in the k-space. Due to the streaming motion, there is an accumulation of light-hole in the higher indexes LLs. Radiative transitions can occur between subsequent LLs. The grey curve is the zero-field band-structure of light-holes in p-Ge. Adapted from [23].

the light-hole band of p-Ge. Carriers accumulate in high indexes LLs thanks to the electric field induced streaming motion. The radiative transitions occur between higher and lower LLs indexes and result in a lasing effect when the system is put in an adequate cavity. It was demonstrated [23] that, with gold-coated Mylar mirrors and electrical pulses of 1 μs duration and 2 kV of amplitude, one could obtain an emission ranging from 1 THz to 3 THz when tuning the magnetic field from 2 T to 4.5 T, and with an output power of around 50 mW.

As mentioned earlier, the p-Ge band-structure also features a second valence band that is the heavy-hole one. However, due to its higher effective mass, for a crossed fields configuration setting the light-holes in a bounded motion situation (see Fig. 1.7a), the heavy-holes will be in a pure streaming motion where the carriers are constantly traveling from the center of the velocity space to the optical phonon speed [23]. When scattered back to the k =

0 point, some of the heavy-holes can be tunneled towards the light-holes band. Therefore, this additional band acts as a reservoir that feeds the light-hole band, where the population inversion takes place, making the lasing effect even more efficient compared to a purely one-band mechanism.

A certain number of drawbacks are to be noted. The first one being that the required electric field is very large, almost causing the breakdown of the material. The second is the low-temperature operation. Indeed, in order to reach 4.5 T, liquid Helium temperature is required for the superconducting coil.

1.4 The Dirac materials class for Landau emission

A Dirac material is a condensed matter system in which the band-structure can be described by the Dirac equation. Whether it is 2D or 3D, it usually results in a linear (or almost linear) band-structure in particular points of the reciprocal space and therefore leads to non-equidistant LL ladders. Indeed, as we saw earlier with Eq. 1.21, for a fixed magnetic field strength, the energy scales up with the square-root of the LL's index. In this sense, as the Auger process should be reduced in these systems, they are interesting for achieving a LL laser. We will here only focus on graphene, HgTe-based quantum wells and some heterostructures of the III-V family but a lot of other materials have demonstrated such a Dirac phase and therefore would also be of great interest.

1.4.1 Graphene

Graphene is a well known 2D Van der Waals material, discovered and characterized for the first time by *Novoselov* and *Geim* in 2004 [31]. It is an atomically thin layer of graphite and it has been demonstrated, both theoretically [28] and experimentally [29], that its band-structure is well described by the Dirac equation, giving rise to a 2D Dirac cone in particular points of the reciprocal space (see Fig. 1.8a and b).

We can compute its LLs fan chart by following the same procedure as earlier. The Hamiltonian will be transformed as followed [32]

$$H = \pm\sqrt{2}\frac{\hbar v_F}{l_B}\begin{pmatrix} 0 & \hat{a} \\ \hat{a}^\dagger & 0 \end{pmatrix}, \tag{1.19}$$

where v_F is the Fermi velocity, defining the slope of the linear band-structure, $l_B = \sqrt{\frac{\hbar}{eB}}$ the magnetic length and $\hat{a}^\dagger$ (resp. $\hat{a}$) the creation (resp. destruction) operator, defined as

$$\hat{a} = \frac{l_B}{\sqrt{2}\hbar}(\hat{\pi}_x - i\hat{\pi}_y) \quad \text{and} \quad \hat{a}^\dagger = \frac{l_B}{\sqrt{2}\hbar}(\hat{\pi}_x + i\hat{\pi}_y), \tag{1.20}$$

$\pi_{\hat{x}/y}$ being the impulsion operators. From equation 1.19, it is quite easy to deduce the eigenvalues that define the LLs structure of such a linear band:

$$E_n = \pm\hbar\omega_c\sqrt{n} = \pm v_F\sqrt{2q\hbar Bn}, \tag{1.21}$$

where this time, the CR pulsation is now defined as $\omega_c = \frac{\sqrt{2}v_F}{l_B}$.

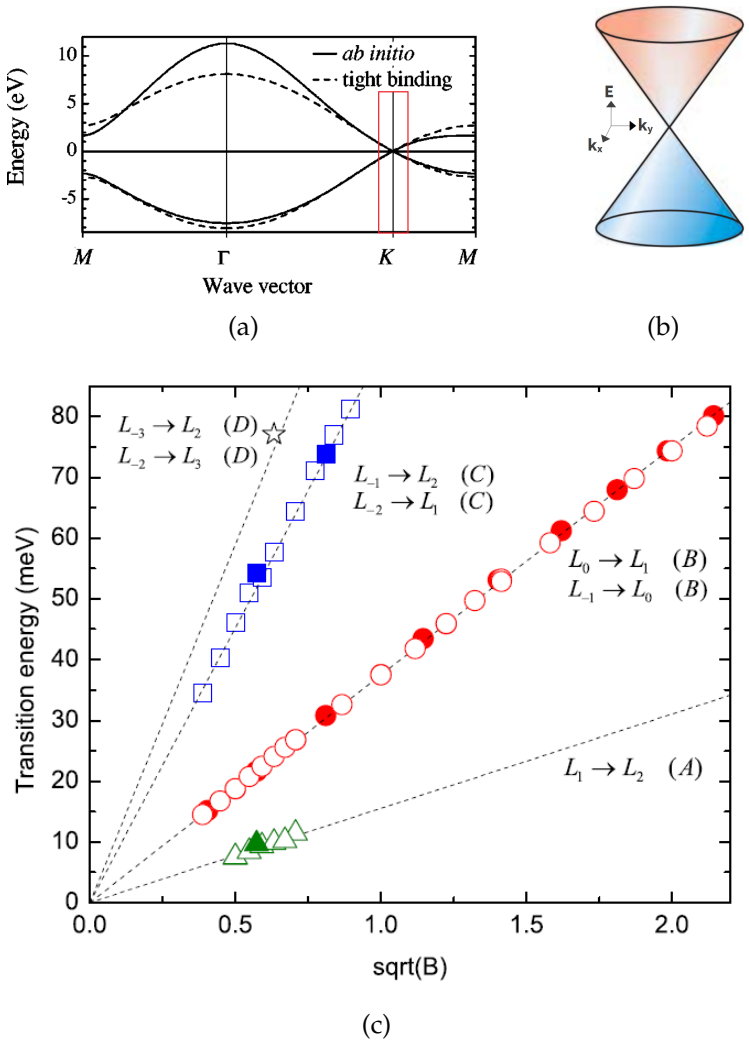

Figure 1.8: **Evidence of the Dirac nature of graphene.**
(a) Theoretical calculation of the band-structure of graphene. It evidences a band touching at K point and a linear dispersion at low energy. Adapted from [28]. (b) Representation of the 2D Dirac cone in the plane of the graphene sheet and at the K point (red square of b)). Adapted from [29]. (c) Transitions observed by magneto-transmission experiments on graphene, along with their labels. The dashed lines are simultaneous fits giving the parameter $v_F = 1.03 \times 10^6$ m/s. Adapted from [30].

Equation 1.21 shows that the graphene LLs follow a square-root evolution with magnetic field. This behavior is very different from the parabolic case and in particular, LL spectroscopy is a very efficient probe of the nature of the materials' band-structure [35, 36]. A plot of the LLs evolution is shown on Fig. 1.9a and its square-root dependence with respect to the magnetic field has been perfectly verified soon after graphene's discovery[30] (see Fig. 1.8c).

The non-equidistancy of graphene's LLs, supposedly reducing the Auger mechanisms, has revived the possibility of achieving a low-field tunable LL laser [37]. Thanks to pump-probe analysis of the carriers' relaxation times, it was indeed successfully demonstrated that Auger scattering was reduced due to the Dirac nature of carriers in graphene [38].

However, it was shown a few years later that a strong Auger effect remains as subsets of Landau levels with matching energies continue to exist[39, 40] (as illustrated on Fig. 1.9a).

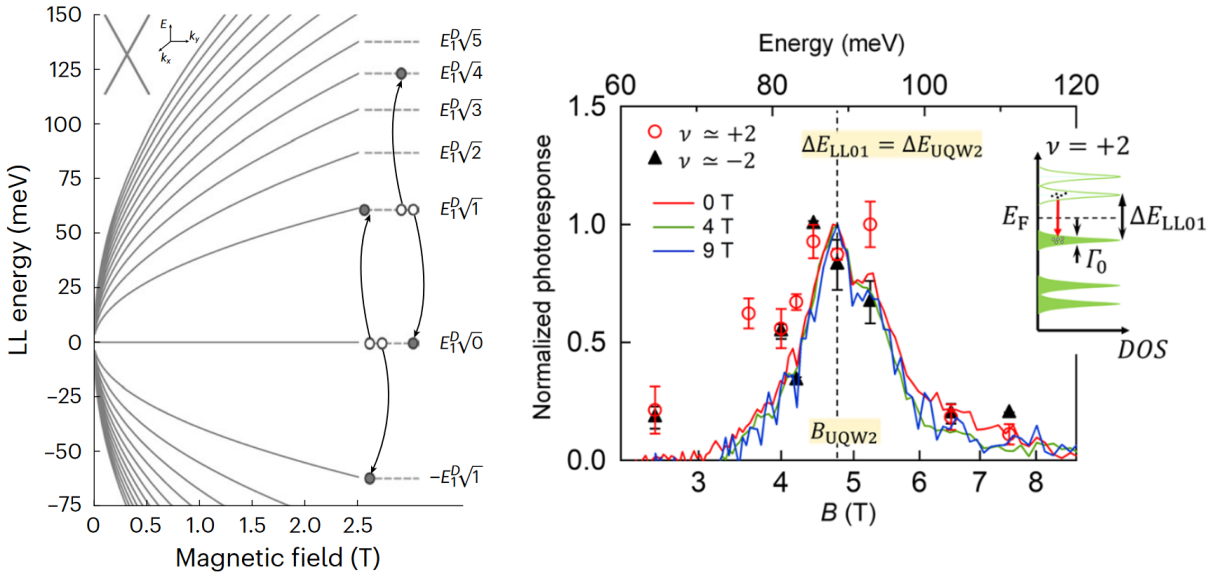

(a) (b)

Figure 1.9: (a) Representation of the LLs fan chart in graphene and illustration of two possible Auger processes, surviving due to the perfect square-root behavior of the LLs. Adapted from [33]. (b) Very recent Landau emission obtained in graphene. Adapted from [34].

Therefore, graphene does not seem to be the adequate candidate for the realization of a Landau laser.

However, one should still note that spontaneous Landau emission has been observed very recently by Inamura et al. [34] but the optical signal is extremely weak and thus it required a very sophisticated detection set-up. Moreover, the emission energy is around 90 meV so quite far from the THz technological gap (see Fig. 1.9b).

1.4.2 HgTe quantum well

We highlighted the fact that a purely square-root behavior of the LLs is not enough to overcome the Auger scattering process because it opens new diffusion channels. Therefore, an idea would be to find a material with an in-between band-structure. In the beginning of the 2000s, Bernevig et al. [41] predicted a Dirac fermion phase in HgTe-based quantum wells (QW), for specific growth parameters. For a critical thickness of the well, the material undergoes a topological phase transition and become a Quantum-Spin-Hall-Insulator (QSHI). This effect has notably been experimentally demonstrated the year after its prediction [42]. Figure 1.10a shows the structure of such a material, composed of a well of HgTe embedded in CdTe barriers. When the HgTe thickness is greater than a critical value, there is a band inversion, giving rise to a topological state. The corresponding band-structure of such a state is depicted Fig. 1.10b and features a 2D massive Dirac cone in the plane of the QW. Note that for the critical thickness value, the band-structure is a massless Dirac cone. It was computed thanks to a low-energy model developed in [41], called the Bernevig-Hughes-Zhang (BHZ) model and that we will present in the next chapter. As we will see later, the band-structures are composed of both linear and quadratic k-terms.

Figure 1.10c shows the LLs fan chart of those two structures. As expected, it has a behavior between a linear and a square-root evolution. On top of the lines are sketched two

Auger mechanisms that were existing in graphene and one can see that it is no longer possible due to the new LLs spacing. Therefore it is expected to be hard to find any subset of levels matching for Auger scattering and one can expect to see intense Landau emission out of these structures.

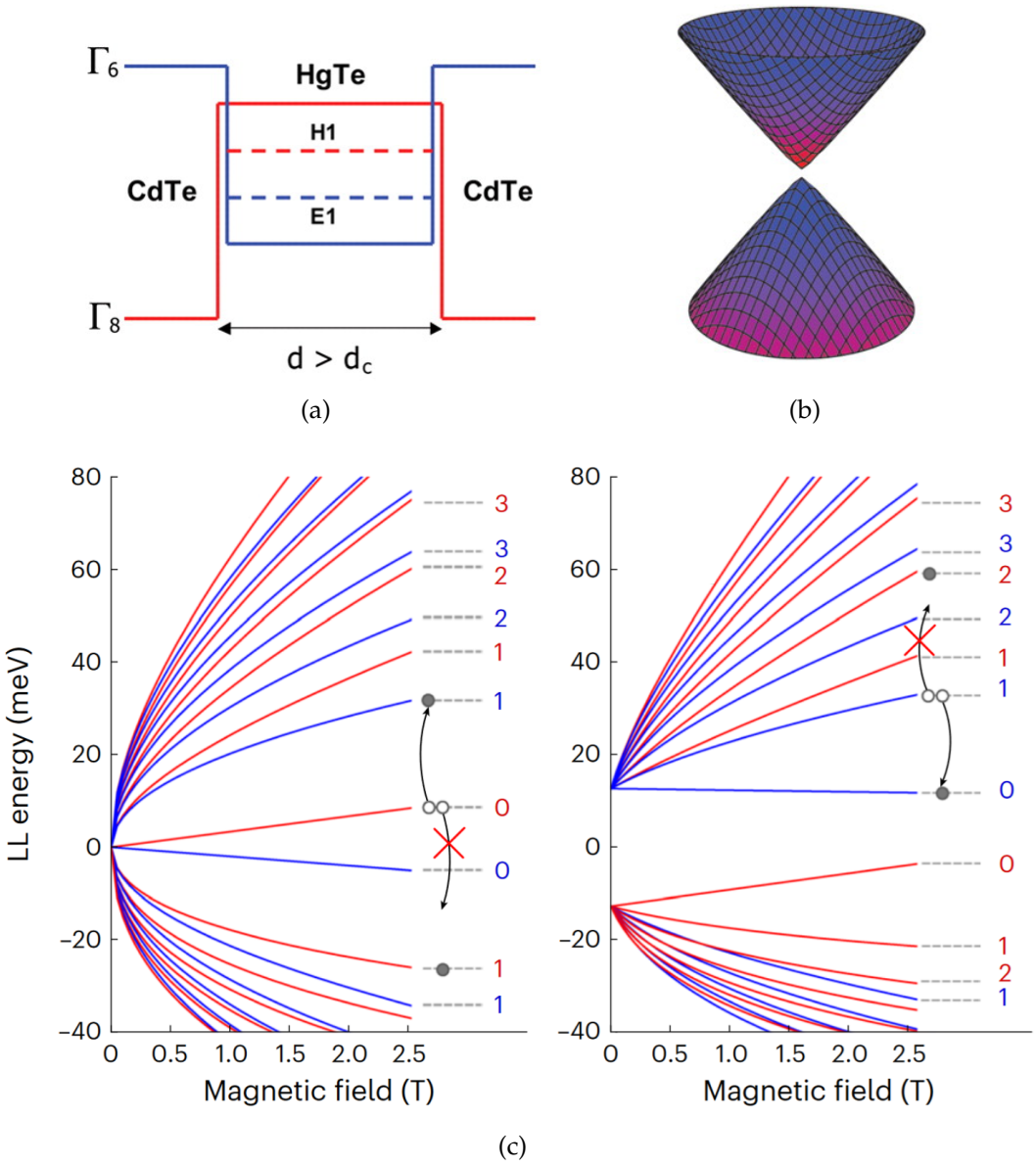

Figure 1.10: (a) Energy sketch of the well. (b) Corresponding band-structure, featuring a 2D Dirac cone in the plane of the well. Adapted from [41]. (c) LLs fan chart of HgTe QW for the critical thickness (left panel) and for a thickness greater that the critical value (right panel). Two suppressed Auger mechanisms are sketched to highlight the difference with the graphene LLs dispersion. Adapted from [33].

A very complete study has been performed in 2023 by Gebert et al. [33], showing that it is indeed possible to observe THz radiation from these structures. The QWs they studied have carrier densities close to $5\times10^{11}\text{cm}^{-2}$ and mobilities of the order of 100 000 $\text{cm}^2/\text{V/s}$. These quantities have a strong implication on the Landau energy landscape. Indeed, even though the Landau quantization is already present (it is notably confirmed by the existence

of Shubnikov-de Haas oscillations in the magnetoresistance), the different LLs still greatly overlap. The author define this specific regime as the "incipient regime" between a semi-classical and a fully quantized regime [33]. Therefore, the observable transitions are reduced to the semi-classical CR formula

$$E = \hbar \frac{eB}{m_c}, \tag{1.22}$$

where m_c is called the cyclotron mass and is defined as followed [43]:

$$m_c = \frac{\hbar^2}{2\pi} \frac{\partial A}{\partial E}, \quad \text{where} \quad A = \pi k_F^2, \tag{1.23}$$

with k_F being the Fermi wave-vector. In the case of a purely parabolic band we have $E = \frac{\hbar^2 k^2}{2m^*}$, giving $\frac{\partial E}{\partial A} = \left(\frac{1}{\pi} \frac{\partial E}{\partial k^2} \right)_{k=k_F} = \frac{\hbar^2}{2\pi m^*}$. Therefore, we obtain $m_c = m^*$ so the cyclotron mass would be constant and inherent to the material. On the other hand, for a purely linear band, $E = \hbar v_F k$ so $\frac{\partial E}{\partial A} = \left(\frac{1}{\pi} \frac{\partial E}{2k \partial k} \right)_{k=k_F} = \frac{\hbar v_F}{2k_F} = \frac{\hbar^2 v_F^2}{2E_F}$ which finally gives $m_c = \frac{E_F}{v_F^2}$. It is a general result for Dirac materials that the cyclotron mass depends on the Fermi level and it is also the case for HgTe QWs as we will see later. This gives another leverage of frequency tunability of the radiation. It is indeed possible to modulate the Fermi level position through the carrier density. This is exactly what has been demonstrated in [33], where they studied 8 different QWs featuring 8 different electron concentrations. Thanks to a unique Landau emission set-up (that will be described in details in the next chapter), they first showed that these structures can emit an intense THz radiation, tunable in magnetic field in great accordance with Eq. 1.22 (Figs. 1.11a and c). One can see that the frequency range covered by the emission is exactly in the THz gap as it extends from 500 GHz to more than 2.5 THz. Furthermore, they successfully demonstrated that the slope of the CR is different from one sample to another (Fig. 1.11c) and they could extract each corresponding cyclotron mass. Figure 1.11b shows a plot of these experimental cyclotron masses versus the carrier density of the QW (determined by analysis of the Shubnikov-de Haas oscillations in the magnetoresistance). It is compared with the theoretical prediction of the BHZ model and it shows an excellent agreement. It is a very important result because it opens the way to an electrically tunable CR THz source, based on these HgTe QWs. Indeed, it could be possible to directly modulate the carrier concentration in a single QW by the mean of a gate effect. This is one of the first results that I obtained during my thesis work and that I will present in chapter 3.

The authors evaluated the conditions required for the streaming motion regime to establish and a possible LLs population inversion to take place [33]. One express the optical phonon velocity and the time-of-flight for one carrier to reach the optical phonon energy as [44]:

$$T_{op} = \frac{V_{op} m_c}{eE} \text{ and } V_{op} = \sqrt{\frac{2\hbar\omega_{op}}{m_c}}, \tag{1.24}$$

where $\hbar\omega_{op} \simeq$18.5 meV in HgTe QWs and E is the electric field applied on the sample. As mentioned earlier, one should have $1 \leqslant \frac{V_{op}}{(E/B)} \leqslant 2$. This condition allowed the authors to estimate that a streaming motion could occur in their HgTe QW for a minimal value of E $\simeq$ 2 000 V/cm and a magnetic field value around 0.5 T. In order for the streaming motion to take place, we should also have $\tau \geqslant T_{op}$, where τ is the transport momentum relaxation

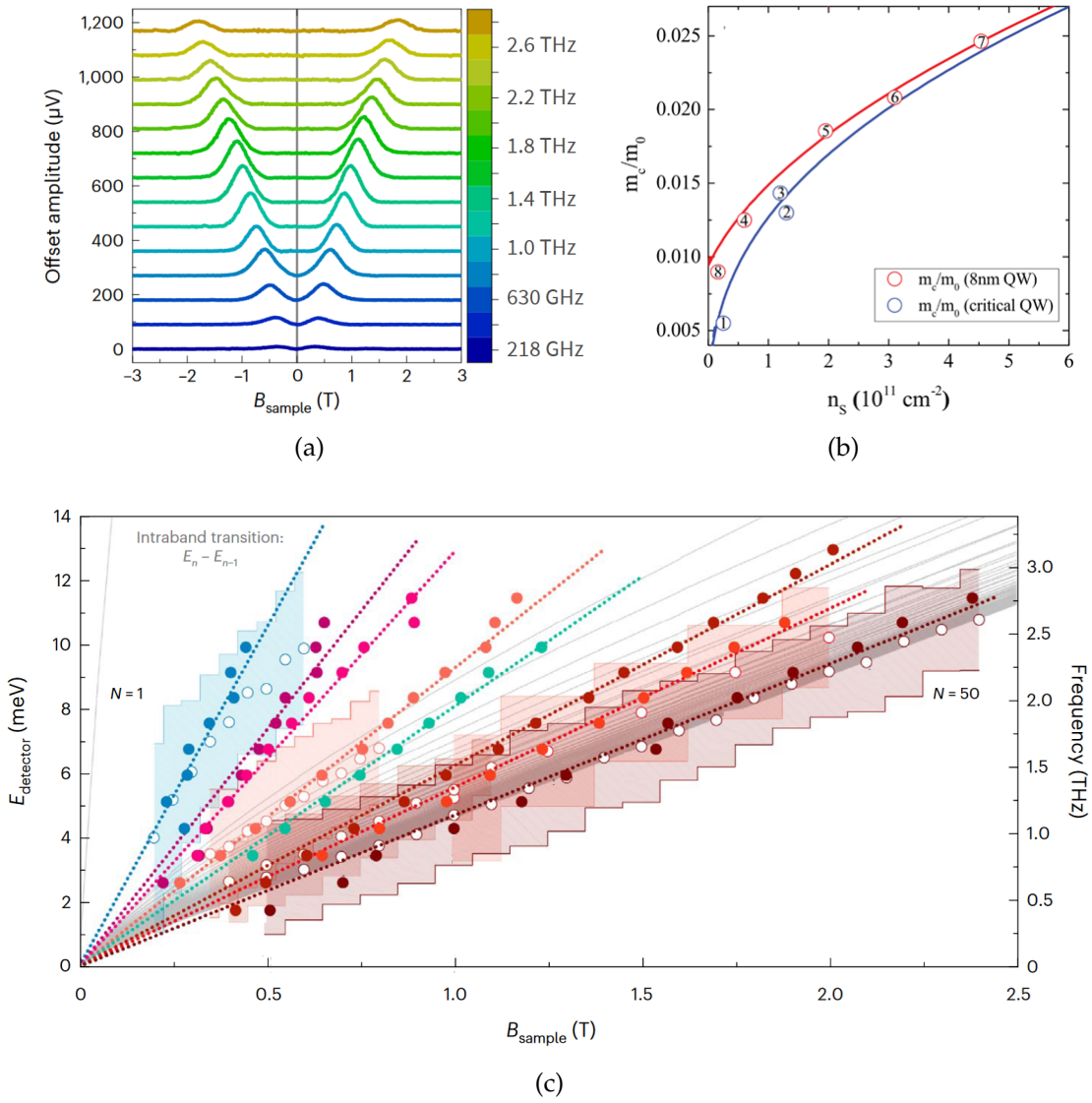

Figure 1.11: **Landau emission results obtained on HgTe QWs.**
(a) Waterfall plot of emission spectra obtain on one HgTe QW. The magnetic field is scanned while the detection energy is fixed. (b) Evolution of the cyclotron mass for two different well thicknesses (solid lines). Experimental points extracted for 8 different samples were plotted on top (numbered circles) for comparison. (c) Extracted emission maxima plotted in the energy/magnetic field plane, for the 8 different QWs. Adapted from [33].

time. This implies that the sample should have an electron mobility of the order of 2×10^5 $cm^2/(Vs)$, which is the case here. Even if the required electric field value is close to the substrate breakdown limit, it could still be achievable with an adapted processing like a submillimeter-sized grating [33].

One have to point out one very important drawback with the use of II-VI alloys. These are materials that are very sensitive to temperature. Indeed, due to its low boiling temperature, mercury atoms can migrate and create vacancies in the structure, hence totally changing the properties of the material. Moreover, the band-structure itself is temperature dependent. It has been shown that it is possible to close the topological gap of a bulk HgCdTe sample by increasing temperature [36]. This temperature sensitivity renders any

room-temperature applications impossible and complicates all cleanroom processes, as they must be carried out at temperatures below 80 °C. Therefore, it would be beneficial to investigate Landau emission in Dirac fermions hosted by another semiconductors family, like the III-V one where the temperature sensitivity is way lower and the technological process knowledge is mature.

1.4.3 The III-V familly

Less than five years after the discovery of the QSHI phase in HgTe QWs, it has been theorized [45] and experimentally evidenced [46] that a similar phase should take place in broken gap InAs/GaSb QWs. However, the topological gap remains very small compared to the one in HgTe and the effect is therefore very fragile. It is only in 2018 that researchers proposed a new geometry of III-V based QWs (namely trilayers QWs as depicted on Fig. 1.12a) which could host a QSHI phase with a large gap, reaching 60 meV [47]. In this paper, the authors also predicted the existence of a Dirac fermion phase, featuring a 2D Dirac cone for specific growth parameters (see Fig. 1.12b).

It has soon be experimentally confirmed that these III-V heterostructures can host a Dirac fermion phase, thanks to magneto-transport and magneto-absorption measurements [48, 49]. Moreover, the same team also demonstrated that the band-structure of these materials was not affected by temperatures up to 100 K [50], thus validating the robustness of these alloys compared to the II-VI ones. Therefore, the III-V semiconductor family seems to be very promising for Landau emission and we will see preliminary results in chapter 5.

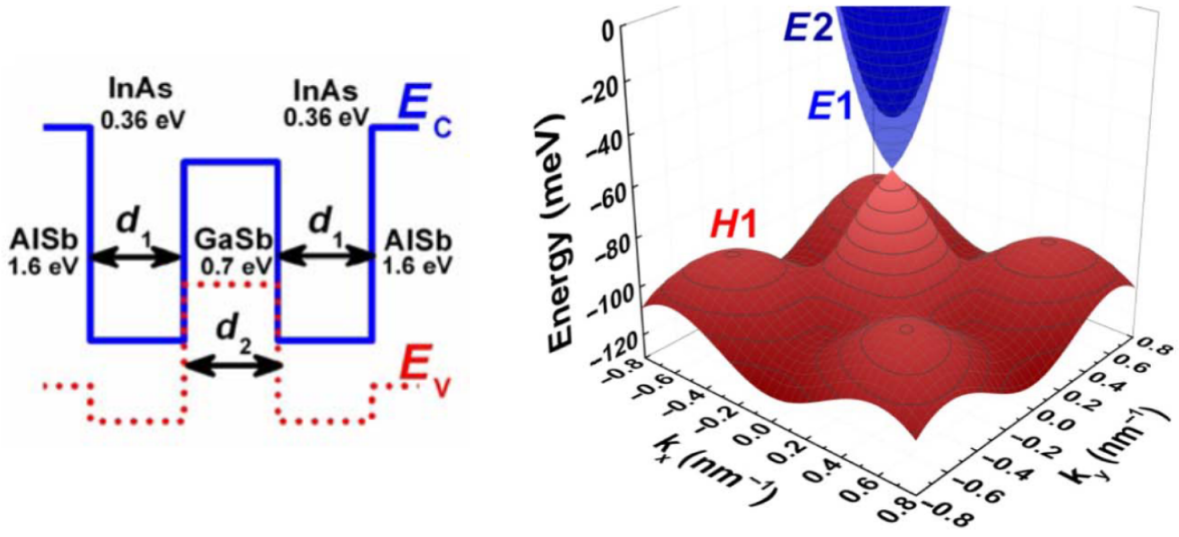

(a) (b)

Figure 1.12: (a) Sketch of the III-V based trilayer. It is composed of an InAs/GaSb/InAs well embedded in AlSb barriers. (b) 2D plot of the Dirac cone in the plane of the well. Adapted from [47].

1.5 A laser without population inversion: the polariton laser

In the previous section, we identified a certain numbers of difficulties to achieve a population inversion using a streaming motion effect. In particular, the need for high electron mobility devices and the use of intense electric fields are quite limiting. It is thus interesting to look for another physical mechanism that could lead us to a CR-based stimulated emission without facing these drawbacks. Therefore, the object of this section is to describe a totally different laser mechanism, which does not imply the use of strong electric fields.

It is based on strong light-matter coupling, namely polariton quasi-particles, and it does not involve a population inversion like with conventional Landau lasing effect.

1.5.1 Strong light-matter coupling

The strong coupling regime is characterized by a reversible exchange of energy between a material oscillator and an electromagnetic mode. In the weak coupling, light and matter interact in an irreversible way, meaning that after interacting, either the material or the electromagnetic mode dephases, though its environment, before eventually interacting again [51]. It is the case, for example, in a conventional laser where a photon is emitted from a material resonance, then dephase inside the cavity before interacting again with the amplifying medium. These situations are very well described by the well known Fermi Golden Rule (FGR) approximation [51].

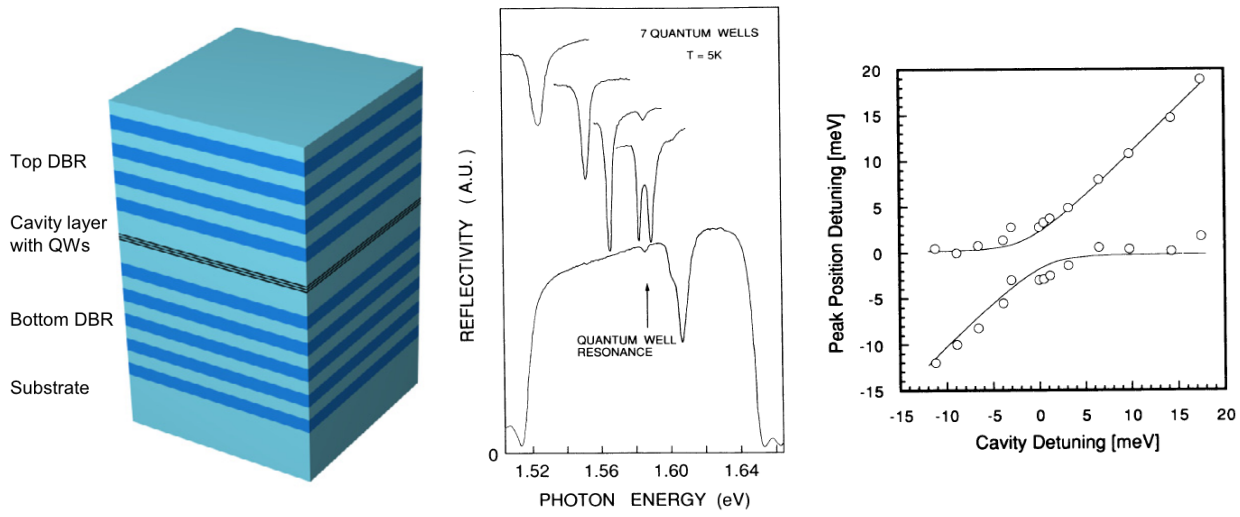

(a) (b) (c)

Figure 1.13: **Strong coupling between QWs' excitons and optical cavity mode.**
(a) Sketch of the device used to observe the strong coupling between an optical cavity mode and excitons in several QWs. Adapted from [51]. (b) Reflectivity spectra obtained on the sample, for different cavity detuning. (c) Extracted reflectivity minima plotted versus the cavity detuning, exhibiting a clear anti-crossing. Adapted from [52].

On the other hand, if a single material oscillator interact and a single electromagnetic mode interact in a reversible way, we enter what we call the strong-coupling regime [51]. It is possible if the energy exchange rate between light and matter (given by the coupling strength or Rabi frequency) is higher than the losses rates [53]. Therefore, the two systems

cannot be considered separately and the FGR is no longer the viable approach to describe the system. A full resolution of the problem is needed and it leads to new mixed eigenstates that we call polaritons [53]. To achieve this strong coupling regime, it is necessary to overcome as best as possible the losses and therefore high quality factor's cavities are needed.

One of its first experimental realization was done in 1992 between excitons confined in a QW and the optical mode of a cavity [52]. Figure 1.13a sketched the geometry of the sample used to demonstrate this strong coupling. It is made of several AlGaAs QWs embedded between two Distributed-Bragg-Reflectors (DBRs) made of the stacks of AlGaAs/AlAs layers. The authors took advantage of the growth in-homogeneity between the edge and the center of the cavity as a leverage of detuning of the optical mode compared to the QWs mode. Figure 1.13b shows different reflectivity spectra obtained for different detuning. The cavity mode is approaching the QW mode but it never cross, leading to what we call an anti-crossing (highlighted in Fig. 1.13c) which is one of the main characteristic features of the presence of a polariton. From this anti-crossing, one can extract the value of the Rabi splitting, which is given by the energy difference between the photon energy and the matter oscillator's one at resonance. In Fig. 1.13c one can estimate it to be around 4 meV and it is a way to quantify the strength of the coupling.

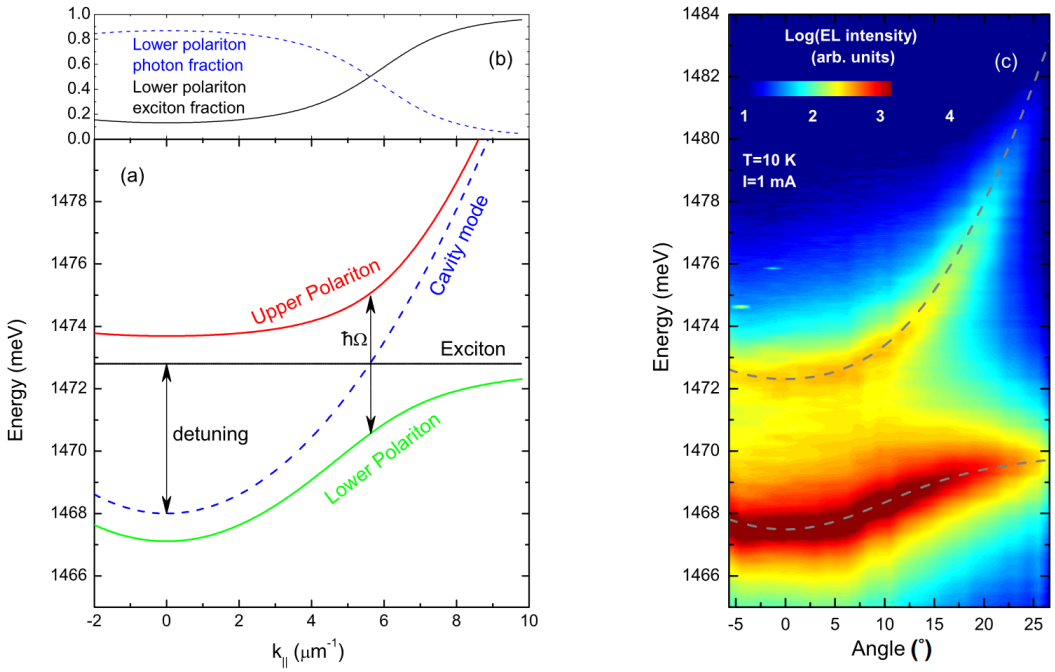

Figure 1.14: (a) Energy dispersion of the polariton branches, along with the bare exciton and cavity mode ones. (b) Evolution of the different matter/light fractions in the polaritonic branches. (c) Falsecolor mapping of the electroluminescence of the semiconductor microcavity depicted Fig. 1.13a. Adapted from [51].

A simpler way to tune the optical part is to change the angle of the incident light. Indeed it can be shown [51] that the planar cavity mode dispersion is given by

$$E_C = \frac{\hbar c}{n}\sqrt{\left(\frac{2p\pi}{L_{cav}}\right)^2 + k_{||}^2}, \tag{1.25}$$

where L_{cav} is the cavity length, n the optical index of the material, $p \geqslant 1$ an integer and $k_{||}$ the wave-vector component in the QW plane, which is linked to the incident light angle.

The energy dispersion of the polariton can be described by the following Hamiltonian [51]

$$H = \begin{pmatrix} E_X + i\gamma_X & \frac{\hbar\Omega}{2} \\ \frac{\hbar\Omega}{2} & E_C + i\gamma_C \end{pmatrix}, \tag{1.26}$$

where E_X is the exciton energy, Ω the Rabi splitting and γ_X (resp. γ_C) the linewidth of the exciton (resp. optical) resonance. This Hamiltonian can easily be diagonalized and it will give rise to two new eigenstates that we call Upper Polariton (UP) and Lower Polariton (LP) the dispersion of which is depicted on Fig. 1.14a. We retrieve the anti-crossing pattern with a gap given by the Rabi splitting. Figure 1.14c displays a falsecolor mapping of the electroluminescence of the AlGaAs-based microcavity and it shows an excellent agreement with the theoretical model.

What one can also derive is the light/matter fraction of each branch. Indeed, polaritons are mixed particles and we can therefore define a fraction of exciton or photon for each state. Figure 1.14b displays the computation for the lower branch and one can notice that the bottom of the LP branch is almost only photonic, which will play an important role in the polariton lasing effect.

1.5.2 Polariton laser

Exciton-polariton laser was first theorized in 1996 [54], the principle being sketched in Fig. 1.15a. The sample is first pumped, optically or electrically, at very high energies, well above the QW levels. It creates an electron-hole reservoir that will relax through phonon emission. The carriers will then start to populate the excitonic part of the LP branch and finally, by several mechanisms like phonon-polariton or polariton-polariton scattering events, they should relax towards the bottom of the LP branch [51]. Since polaritons are made of bosonic particles, it is itself a boson and hence obey the Bose-Einstein statistics. Therefore, the $k_{||}$=0 state population can potentially become very large as long as the pump is on and at the end, the polariton population can undergo a Bose-Einstein condensation in the bottom of the LP branch. We can see from Fig. 1.14b that the polariton states located around $k_{||}$=0 are mainly photonic, hence the polaritons mostly decay radiatively [51]. Therefore, we can observe light that is emitted coherently because all the photons collected emerge from the same polaritonic state.

The first polariton lasing effect was observed in CdTe-based microcavity in 2006 [55]. Figure 1.15b displays the main results of their study. It shows the far-field emission emerging from the microcavity, for three different input powers. Below the threshold power there is a broad and weak emission while it is intense and narrow above the threshold, witnessing a coherent emission. The authors also made a complete characterization of the emitted light, notably the spatial coherence, polarization and coherence lifetime [55].

To summarize, it is possible to obtain a coherent radiation out of a polaritonic system and this without the need of population inversion. Furthermore, it was shown in another paper [56] that the threshold power needed to achieve the lasing effect is lowered by more than one order of magnitude compared to a classical population-inversion laser (see Fig. 1.15c). In an electrically pumped system, it would be extremely useful because it would move the threshold bias away from the breakdown bias of the sample.

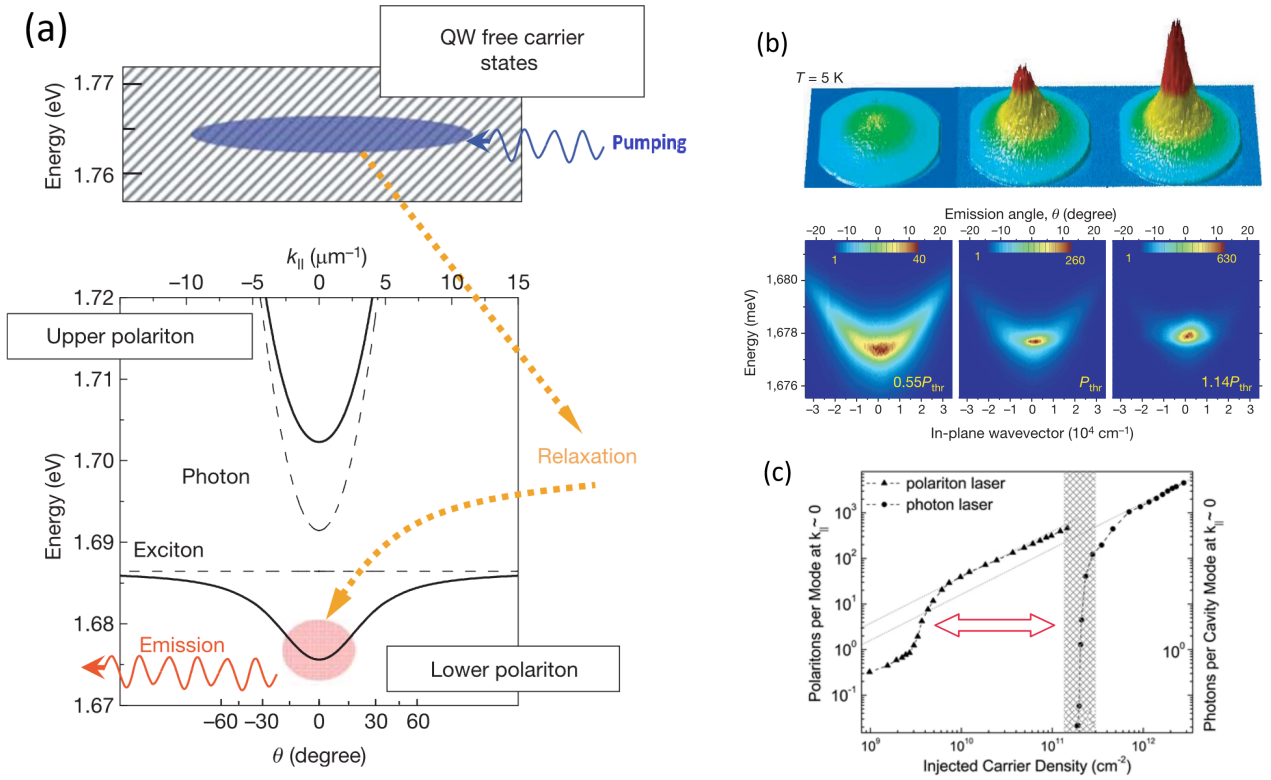

Figure 1.15: **First evidence of polariton lasing in a CdTe-based microcavity.** (a) Sketch of the polariton laser principle. (b) Far-field emission measured for different input powers, witnessing a condensation and a laser effect. Adapted from [55]. (c) Evolution of the populations of LPs (dark triangles) and photons (dark circles) of the lasing mode with respect to the injected carrier density. The inflections of the curves witness the respective lasing thresholds. Adapted from [56].

1.5.3 Landau polariton

So far, we have only been interested in polaritonic system emitting in the IR/visible energy range and composed of excitons as matter part. However it was proposed in 2010 [57] that a 2DEG CR coupled to a cavity resonator could also undergo a strong light-matter coupling, leading to what we now call a Landau polariton. It was experimentally demonstrated in various geometries, using meta-materials like split-ring-resonators (SRRs) [58] (see Fig. 1.16a) or conventional DBR-based micro-cavity more recently [59] (see Fig. 1.16c).

In these experiments, the magnetic field is used to tune the CR of a 2DEG. When it gets close to the resonator's energy, there is an anticrossing (see Fig. 1.16b and d), witnessing the presence of a polaritons. The initial idea of these studies was to reach a new light-matter interaction regime, the ultra-strong coupling [57], characterized by a Rabi splitting that is of the order of the light/matter excitations. Indeed, as seen on Fig. 1.16, the resonators are designed to have modes in the THz range and the Rabi splitting achieved are around several meV. Therefore, one can reach reduced Rabi splittings of almost $\Omega/\omega = 1$ [58–60], where ω is the resonator's frequency. This was made possible by significant technological advances that enabled the resonances of the resonators to be lowered to the THz range [61–63]. It also required ingenuity to adapt DBR-based microcavities to this energy range, using stacks of Silicon and air layers [59].

The Landau polariton presents characteristics that differ markedly from those of the ex-

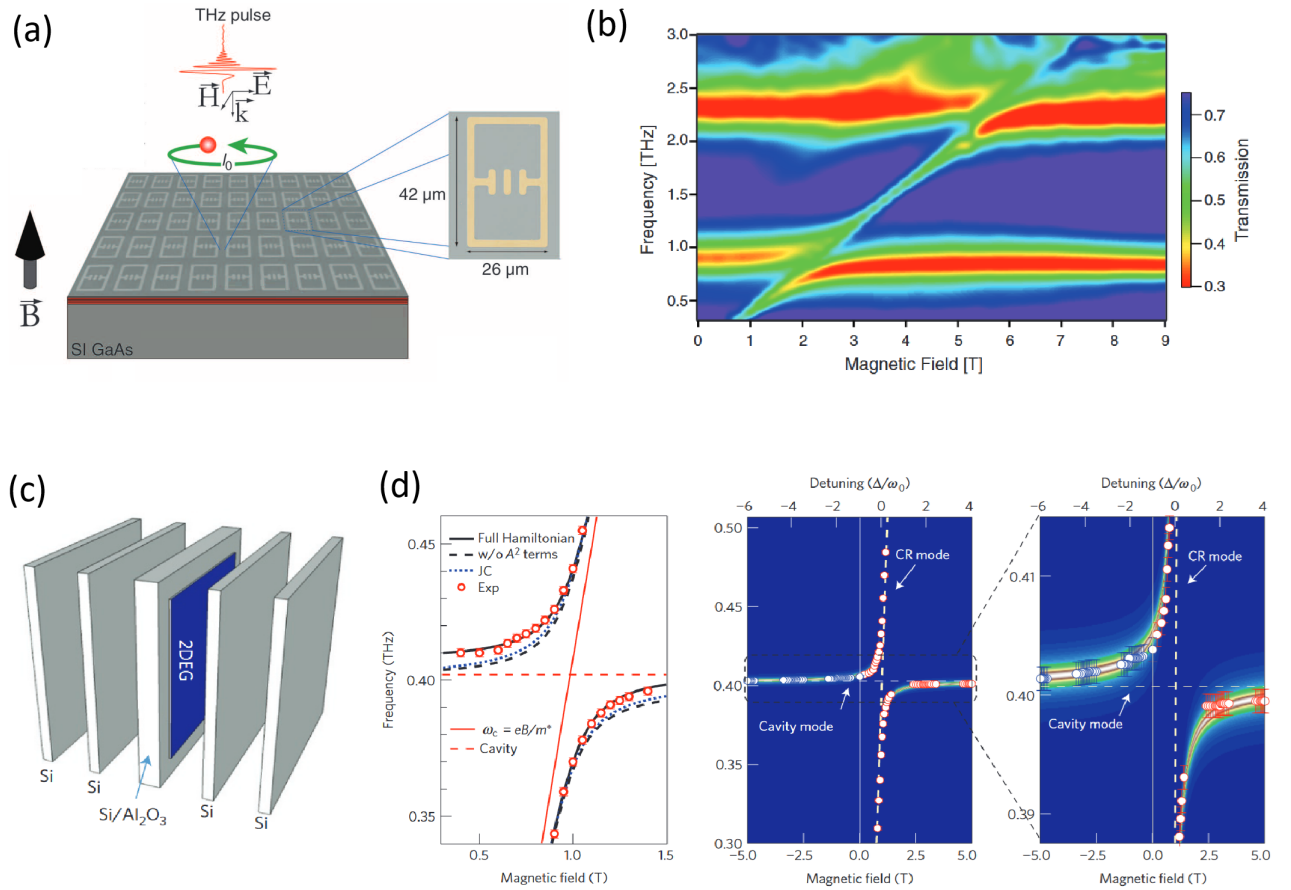

Figure 1.16: **Experimental signatures of Landau polariton in two different geometries.** (a) Sketch of the device which consist of a multiple GaAs QW on top of which is deposited a SSRs golden pattern that acts as a light resonator. (b) Time-Domain-Spectroscopy (TDS) magneto-transmission measurements highlighting the anti-crossing when tuning the magnetic field. Adapted from [58]. (c) Sketch of the device which consists in a 2DEG embedded in a DBR-based micro-cavity. (d) Magneto-transmission measurements also displaying an anti-crossing, along with a theoretical analysis. Adapted from [59].

citon polariton, in particular through the absence of a pronounced minimum in its energy dispersion. This distinctive feature implies that Bose–Einstein condensation and lasing phenomena may follow alternative mechanisms compared to conventional exciton–polariton systems. Interestingly, as shown in several studies, polariton accumulation and coherent emission can occur even away from an energy minimum. For instance, the well-known bottleneck effect, which arises at a minimum in the density of states due to the short radiative lifetime of polaritons compared with other scattering processes [64–67], can lead to polariton lasing away from the k = 0 point, forming so-called ring condensates [68]. More generally, various systems could lead to a polariton laser effect by optical selectivity, in a photonic bound states in continuum or topological photonic systems for example [69].

However, no polariton laser in the THz range was reported so far and we will explore this possibility in chapter 4.

1.6 Overview of the manuscript

This manuscript will be structured as follows. After detailing the experimental and numerical methods that I used during my PhD thesis (chapter 2), I will focus on the Landau emission in HgTe-based structures (chapter 3). In this chapter, I will demonstrate the possibility to have an electrically tunable cyclotron source, based on the Dirac nature of the material. I will also present results in a strong crossed electric and magnetic fields and show some limitations in the use of semiconductors of the II-VI family. In this sense, chapter 5 will explore many possibilities through different III-V materials, less sensitive to temperature. I will present results on an InSb-based QW which features high non linearity in its band structure, a GaAs-based QW which hosts a very high carriers mobility, before characterizing a 3D topological structure based on a InAs/GaInSb superlattice.

Finally, chapter 4 will be the core of this manuscript and aims at exploring the possibility of having a stimulated emission from these HgTe-based structures without the need of population inversion based on a strong electric field. In this chapter we show the electroluminescence of Landau polaritons and demonstrate that it is close to a lasing thresholds. We also propose several ways of improvement that could lead us towards a polariton stimulated emission.

I will naturally end this manuscript with a general conclusion and a summary of all the perspectives that were identified.

Chapter 2

Methods

Contents

The idea of this chapter is to detail the methods, both numerical and experimental, that were used during my PhD thesis. I will first present the well known Bernevig-Hugues-Zhang (BHZ) model, describing the band-structure of the HgTe-based QWs. I will then detail the magneto-spectroscopy experimental set-up that we used to characterize the samples. I will finish by presenting the unique Landau emission set-up that was central in my PhD work.

2.1 The BHZ model, a very useful tool

Initially developed by Bernevig, Hughes and Zhang in 2006 [41], the BHZ model is an effective four-band Hamiltonian that describes HgTe-based QWs. As we will see later on, it accurately describes the low-energy band structure and since it is analytic, it is a very useful tool to capture different other properties of the QW.

2.1.1 Band dispersion calculation

Starting from a six-band model, composed of the Γ_6 and Γ_8 atomic bands, it leads to two sets (spin up and spin down) of QW bands: $E1$, $H1$ and $L1$ [41]. It has been shown that the $L1$ band is separated from the two other and we can therefore neglect it, leaving an effective four-band model [41]. By symmetry considerations under a two-dimensional spatial reflection, it is possible to express the general form of the Hamiltonian, in the basis of $|E1, m_J = 1/2\rangle$, $|E1, m_J = -1/2\rangle$, $|H1, m_J = 3/2\rangle$ and $|H1, m_J = -3/2\rangle$, as

$$H_{BHZ}(k_x, k_y) = \begin{pmatrix} H(\mathbf{k}) & 0 \\ 0 & H^*(-\mathbf{k}) \end{pmatrix}, \tag{2.1}$$

where $H(\mathbf{k}) = (\mathcal{C} - \mathcal{D}k^2)\sigma_0 + (\mathcal{M} - \mathcal{B}k^2)\sigma_z + \mathcal{A}(k_x\sigma_x + k_y\sigma_y)$ can be written as:

$$H(\mathbf{k}) = \begin{pmatrix} \mathcal{C} + \mathcal{M} - (\mathcal{D} + \mathcal{B})k^2 & \mathcal{A}k_+ \\ \mathcal{A}k_- & \mathcal{C} - \mathcal{M} - (\mathcal{D} - \mathcal{B}))k^2 \end{pmatrix}, \tag{2.2}$$

with $\mathbf{k} = (k_x, k_y)$ being the in-plane momentum and $k_\pm = k_x \pm ik_y$. $\mathcal{A}, \mathcal{B}, \mathcal{C}$ and $\mathcal{D}$ are parameters depending on the growth parameters such as the QW width, the barriers composition or the strain [41]. The $\mathcal{M}$ is the mass or gap parameter which is the energy difference between the E1 and H1 bands at the center of the Brillouin zone. The diagonal form of the matrix comes from the inversion symmetry and axial symmetry of the material [41]. This

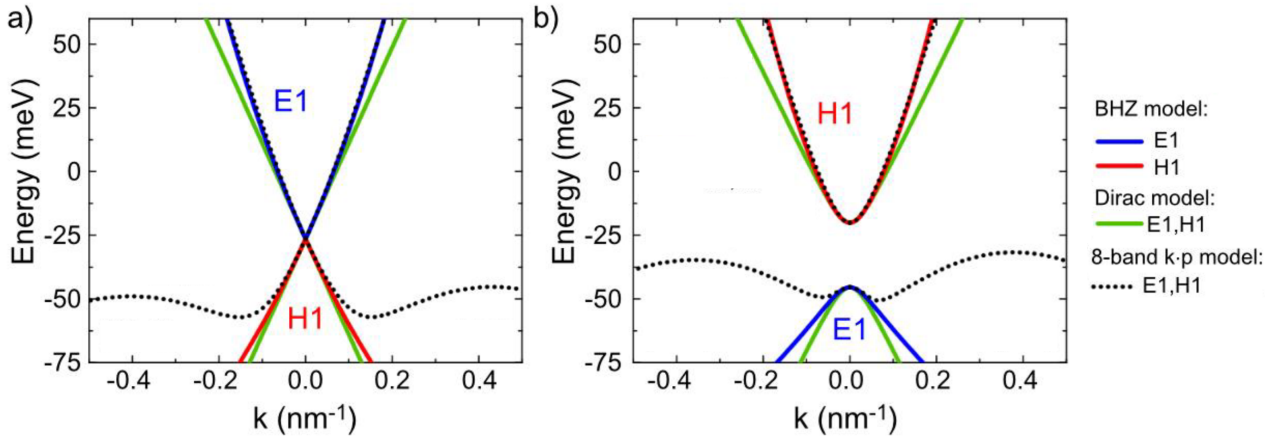

Figure 2.1: Results of the fitting procedure for (a) a gapless QW and (b) a gapped QW. The green curves were obtained by setting $\mathcal{B} = \mathcal{D} = 0$ from the BHZ model, in order to retrieve the Dirac model. Adapted from [33].

Hamiltonian can be exactly diagonalized and it gives the following eigenenergies

$$E_s(\mathbf{k}) = \mathcal{C} - \mathcal{D}k^2 + s\sqrt{(\mathcal{M} - \mathcal{B}k^2)^2 + \mathcal{A}^2k^2}, \tag{2.3}$$

where $s = +1$ (resp. -1) stands for the conduction (resp. valence) band, the two bands being spin-degenerated. One can notice that if we set $\mathcal{B} = \mathcal{D} = 0$, one retrieves the band dispersion of a massive Dirac fermion. Therefore, the quadratic terms of the BHZ model are specific to these HgTe QW and will play an important role as we will see later on.

A procedure has been developed in [33] to evaluate the BHZ parameters. The idea is to use a realistic 8-bands k·p calculation based on the six initial bands within the Kane model to compute the band-structure of the material. The parameters are then determined by fitting the obtained curves with equation 2.3. Figure 2.1 shows the results of the fitting procedure for one gapless and one gapped QW. One can see that the conduction band (CB) is very well reproduced by the model and that there is a good agreement at low energy for the valence band (VB). The corresponding parameters are summarized in Table 2.1 [33].

The BHZ can accurately reproduce the CB of HgTe QWs and as discussed in the Introduction, it features a highly non-parabolic dispersion, with additional quadratic terms compared to a purely graphene-like dispersion. As we will now see, this model allows us to compute other very useful quantities, namely the cyclotron mass and the LLs dispersion when a magnetic field is applied.

d [nm]	**x**	$\mathcal{C}$ [meV]	$\mathcal{M}$ [meV]	$\mathcal{A}$ [meV·nm]	$\mathcal{B}$ [meV·nm^2]	$\mathcal{D}$ [meV·nm^2]	g_e	g_h
6.2	0.65	- 26.5	0	375.8	- 634.4	- 451.6	59.15	2.43
8	0.8	- 32.8	-12.7	353.3	- 828.5	- 645.4	44.04	2.41

Table 2.1: BHZ parameters obtained from the fitting procedure described in the main text. x is the Cd content of the $Hg_{1-x}Cd_xTe$ barriers.

2.1.2 Cyclotron mass

As discussed in the Introduction, the high non-parabolicity of the HgTe QW's band-structure induces a large dependency of the cyclotron mass with the position of the Fermi level. Using

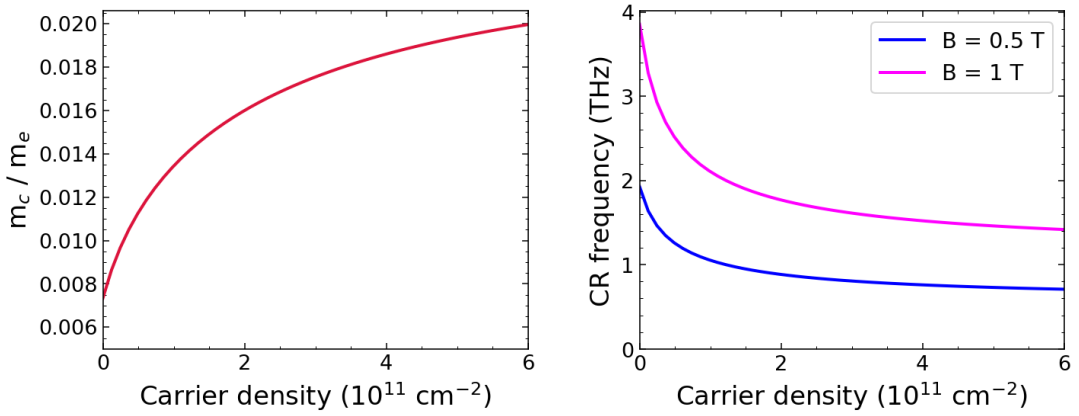

(a) (b)

Figure 2.2: **Predictions of the BHZ model.**
(a) Evolution of the cyclotron mass with the carrier density, for a gapped QW (second row of table 2.1). (b) Evolution of the corresponding CR frequency, for two magnetic field values.

equation 1.23, one can inject the BHZ formula 2.3 to compute the corresponding cyclotron mass. One easily obtains

$$m_c = \frac{\hbar^2\sqrt{(\mathcal{M}-\mathcal{B}k_F^2)^2+\mathcal{A}^2k_F^2}}{s\left[\mathcal{A}^2-2\mathcal{B}(\mathcal{M}-\mathcal{B}k_F^2)\right]-2\mathcal{D}\sqrt{(\mathcal{M}-\mathcal{B}k_F^2)^2+\mathcal{A}^2k_F^2}}, \tag{2.4}$$

where k_F is the Fermi momentum and can be computed as follow for a 2D system $k_F = \sqrt{2\pi n_s}$, n_s being the carrier concentration.

This formula was used to predict the evolution of the cyclotron mass of the 8 nm HgTe QWs with their respective electron densities in Fig. 1.11b. It is plotted in Fig. 2.2a for the gapped QW of table 2.1 and one can see that the mass increase is very large. For a carrier density ranging from 1 to $6\times10^{11}\text{cm}^{-2}$, the cyclotron mass would go from 0.01m_e to 0.02m_e. Figure 2.2b shows that it would imply a CR emitting frequency range from 1 to 4 THz for reasonably low magnetic field values, totally achievable with standard permanent magnets.

2.1.3 Landau-level calculation

It is also possible to compute the LLs fan chart with the BHZ model. To take into account the effect of a magnetic field oriented perpendicularly to the QW plane, one should perform Peierls substitution [33], namely $\mathbf{k} \rightarrow \mathbf{k} + \frac{e\mathbf{A}}{\hbar}$ where $\mathbf{A}$ is the vector potential so that $\mathbf{B} = \nabla \times \mathbf{A}$. As detailed in [70], it implies the following transformation:

$$k_+ \rightarrow \frac{\sqrt{2}}{l_B}\hat{a}^\dagger, \quad k_- \rightarrow \frac{\sqrt{2}}{l_B}\hat{a}, \quad k^2 \rightarrow \frac{2}{l_B^2}\left(\hat{a}^\dagger\hat{a}+\frac{1}{2}\right), \tag{2.5}$$

where $l_B^2 = \frac{\hbar}{eB}$ is the magnetic length and $\hat{a}^\dagger/\hat{a}$ are the standard ladder operators. One also have to take into account Zeeman splitting, with the following additional term

$$H_{Zeeman} = \frac{\mu_B B}{2}\begin{pmatrix} g_e & 0 & 0 & 0 \\ 0 & g_h & 0 & 0 \\ 0 & 0 & -g_e & 0 \\ 0 & 0 & 0 & -g_h \end{pmatrix}, \tag{2.6}$$

μ_B being the Bohr magneton and g_e and g_h the effective out-of-plan g-factors of the E1 and H1 bands. Finally, the LLs matrix takes the following form

$$H_{LL} = \begin{pmatrix} \mathcal{C}+\mathcal{M}-\frac{2(\mathcal{D}+\mathcal{B})}{l_B^2}\left(n+\frac{1}{2}\right) & \frac{\sqrt{2}\mathcal{A}}{l_B}\sqrt{n} \\ \frac{\sqrt{2}\mathcal{A}}{l_B}\sqrt{n} & \mathcal{C}-\mathcal{M}-\frac{2(\mathcal{D}-\mathcal{B})}{l_B^2}\left(n-\frac{1}{2}\right) \end{pmatrix} + H_{Zeeman}, \tag{2.7}$$

where $n > 0$ is the LL index. For the $n = 0$ term, the matrix becomes

$$H_{LL}^{(0)} = \begin{pmatrix} \mathcal{C}+\mathcal{M}-\frac{(\mathcal{D}+\mathcal{B})}{l_B^2} & 0 \\ 0 & \mathcal{C}-\mathcal{M} \end{pmatrix} + H_{Zeeman}. \tag{2.8}$$

Those two matrices can be analytically diagonalized and we obtain:

$$\begin{cases} \epsilon_n^{(\pm)} &= \mathcal{C} - \dfrac{2\mathcal{D}n \pm \mathcal{B}}{l_B^2} \pm \dfrac{g_e + g_h}{4}\mu_B \mathbf{B} \\ &\quad + s\sqrt{\left(\mathcal{M} \pm \dfrac{g_e - g_h}{4}\mu_B \mathbf{B} - \dfrac{2\mathcal{B}n \pm \mathcal{D}}{l_B^2}\right)^2 + \dfrac{2n\mathcal{A}^2}{l_B^2}} \\ \epsilon_0^{(+)} &= \mathcal{C} + \mathcal{M} - \dfrac{\mathcal{D} + \mathcal{B}}{l_B^2} + \dfrac{g_e}{2}\mu_B B \\ \epsilon_0^{(-)} &= \mathcal{C} - \mathcal{M} - \dfrac{\mathcal{D} - \mathcal{B}}{l_B^2} - \dfrac{g_h}{2}\mu_B B \end{cases} \tag{2.9}$$

Figure 2.3a displays the 40 first LLs of the CB and VB of a gapped HgTe QW. Unlike in graphene, there is a strong spin-splitting, coming from the large spin-orbit coupling in HgTe. As mentioned earlier in the Introduction, this LL fa chart has an in-between behavior between linear a square-rootish evolution in magnetic field. The $\epsilon_0^{(\pm)}$ levels are called "zero-mode Landau levels" and they have the particularity to disperse with magnetic field, compared to graphene. They are represented in grey on Fig. 2.3a. All these specificities participate in the Auger scattering suppression in these structures.

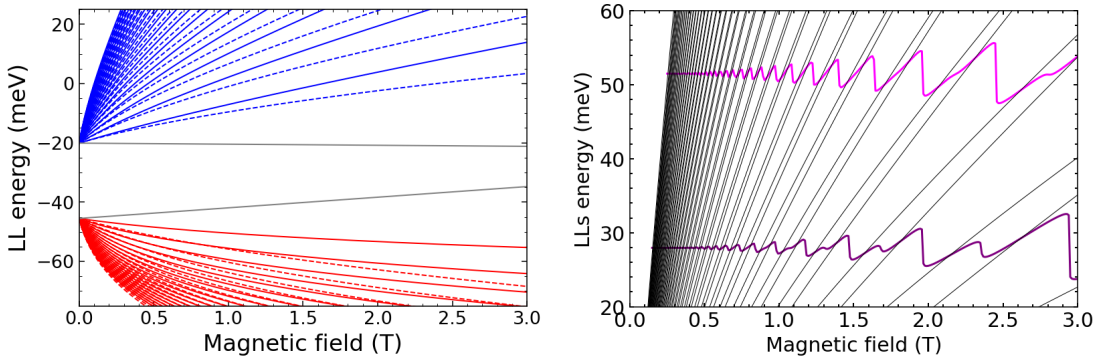

(a) (b)

Figure 2.3: **LLs fan chart computed via the BHZ model.**
(a) The 40 first LLs are computed. Spin up (resp. down) are plotted in solid (resp. dashed) lines and the CB (resp. VB) levels are plotted in blue (resp. red). The zero-mode LLs are plotted in grey. (b) Evolution of the Fermi energy with magnetic field for electron densities of 3×10^{11} cm^{-2} and 5×10^{11} cm^{-2} (resp. purple and magenta lines). The LLs of the CB are plotted in black thin lines.

2.1.4 Fermi level position

A standard information that we can access with the LLs fan chart is the position of the Fermi level with respect to the magnetic field. The first step is to compute the 2D Density of States (DOS) at a given magnetic field value. It can be approximated by modeling the LLs broadening by a Lorentzian function as

$$\mathcal{D}_{2D}(E) \equiv \frac{eB}{h}\sum_N \delta(E - E_N) = \frac{eB}{h}\sum_N \frac{\Gamma/2\pi}{(E - E_N)^2 + (\Gamma/2)^2}, \tag{2.10}$$

where the sum is made over all the LLs of the CB and Γ is the LLs broadening. From this we can compute the Fermi energy by minimizing the following quantity

$$f = n_{exp} - n(E_F) = n_{exp} - \frac{eB}{h}\nu(E_F), \tag{2.11}$$

where n_{exp} is the experimental carrier density and $\nu(E)$ the filling factor at a given energy , i.e., the number of LLs filled under an energy E. It is expressed as follows

$$\nu(E) = \frac{h}{eB}\int_{-\infty}^{E} \mathcal{D}_{2D}(E)dE = \sum_{N}\left[\frac{1}{2} + \frac{1}{\pi}\arctan\left(\frac{E - E_N}{\Gamma/2}\right)\right]. \tag{2.12}$$

Figure 2.3b shows the evolution of the Fermi energy with respect to magnetic field obtained by this method, for a broadening Γ = 1 meV and for two electron densities of 3×10^{11} cm^{-2} and 5×10^{11} cm^{-2}. Knowing the position and evolution of the Fermi level will prove to be very useful in the following.

2.2 The Transfer-Matrix-Method

In the following chapters, we will need to compute the energy position of optical cavity modes in a 2D planar vertical geometry. The Transfer-Matrix-Method (TMM) is very useful and easy to implement for this purpose. We will briefly detail it in this section and give some examples for simple cavity and Tamm cavities. The following description can be found in [71].

We consider a dielectric multi-layer environment, each layer n being characterized by its refractive index n_n. We work in one dimension, in the basis of the forward E_f and backward E_b electric field, of respective u_n and w_n complex amplitudes for the wave that enters the n^{th} layer. A sketch of the problem is represented on Fig. 2.4.

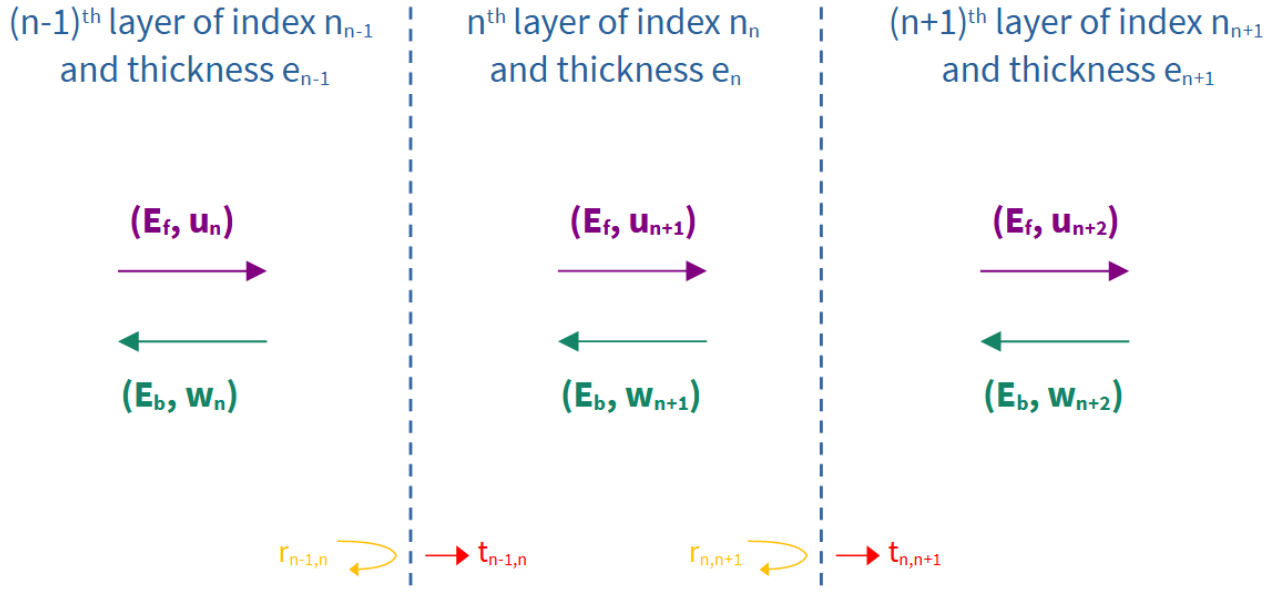

Figure 2.4: **Conventions for TMM calculations.**

We can then formulate the problem as follows

$$\begin{pmatrix} u_n \\ w_n \end{pmatrix} = M_n \begin{pmatrix} u_{n+1} \\ w_{n+1} \end{pmatrix}, \tag{2.13}$$

with M_n being the transfer matrix for the n^{th} layer. It is the product of a propagation matrix P_n and an interface matrix I_n which are given by:

$$P_n = \begin{pmatrix} e^{-ik_n e_n} & 0 \\ 0 & e^{ik_n e_n} \end{pmatrix} \quad \text{and} \quad I_n = \frac{1}{t_{n,n+1}} \begin{pmatrix} 1 & -r_{n+1,n} \\ r_{n,n+1} & 1 + r_{n,n+1} + r_{n+1,n} \end{pmatrix}, \tag{2.14}$$

where e_n is the thickness of the nth layer and $r_{i,j}$ and $t_{i,j}$ are respectively the reflection and transmission coefficients at the i/j interface and can be expressed (at normal incidence) as:

$$r_{i,j} = \frac{n_i - n_j - Z_0\sigma}{n_i + n_j + Z_0\sigma} \quad \text{and} \quad t_{i,j} = \frac{2n_i}{n_i + n_j + Z_0\sigma}, \tag{2.15}$$

where $Z_0 \simeq 377\ \Omega$ is the free space impedance, σ a possible surface conductivity at the in-

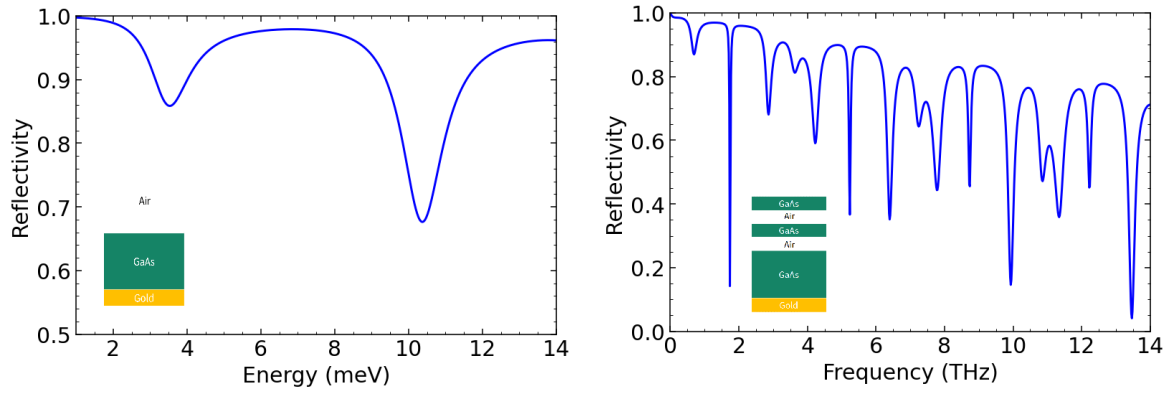

(a) (b)

Figure 2.5: **Example of reflectivity spectra computed with the TMM method.** (a) Spectrum computed for a simple cavity (see geometry in insert) composed of a 25 μm thick layer of GaAs on top of a gold layer. (b) Spectrum computed for a Tamm cavity which consists on a simple cavity on top of which is deposited a DBR-like mirror made of GaAs/air.

terface and $n_{i/j}$ the refractive index of the layer i/j. We can finally access the total reflectivity and transmission of the multi-layer by computing the total transfer matrix:

$$\begin{pmatrix} 1 \\ r \end{pmatrix} = M^{tot} \begin{pmatrix} t \\ 0 \end{pmatrix} \quad \text{with} \quad M^{tot} = I_0 \prod_1^N M_n, \tag{2.16}$$

I_0 being the incident intensity and therefore:

$$R = \left| \frac{M^{tot}_{1,0}}{M^{tot}_{0,0}} \right|^2 \quad \text{and} \quad T = \frac{n_{N+1}}{n_{air}} \left| \frac{1}{M^{tot}_{0,0}} \right|^2. \tag{2.17}$$

We can now compute the reflectivity spectrum for various cavity geometries, as summarized on Fig. 2.5 where a simple cavity geometry and a Tamm geometry were considered. This method will be very useful in chapter 4 when we will study the light-matter interaction in our structures.

2.3 Basic transport characterization

In this section we will briefly present the electrical transport methods that we used to determine basics properties of the samples, namely their carrier density and electron mobility. Figure 2.6 shows a sketch of the sample geometry used for these characterizations.

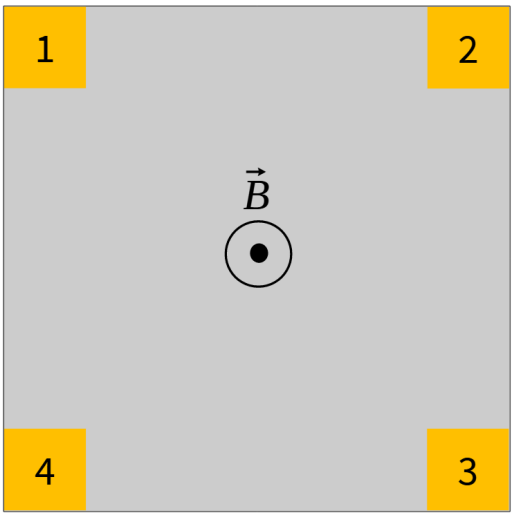

Figure 2.6: **Sketch of the sample's geometry for the transport characterizations.** Four Indium contacts (golden squares) are welded at the corners of the sample. The sample is then inserted in a cryofree cryostat, allowing to work at 10 K and under a magnetic field up to 0.5 T via the use of an electromagnet.

We first perform Hall effect measurement to determine the carrier type and density n_S. It is given by the following formula

$$n_S = \frac{B}{qR_H} = \frac{1}{qK_H}, \tag{2.18}$$

where q is the carrier charge, R_H the Hall resistance, B the magnetic field applied (0.5 T for our experiments), $K_H = \frac{R_H}{B}$ the Hall coefficient. To maximize the precision of the measurements, R_H was obtained by computing the mean of $R_{13,42}$ and $R_{24,13}$ with injection currents of ± 10 μA and ± 100 μA to suppress any thermo-electric effects (8 terms in total). The following convention was adopted: $R_{ij,kl}$ is the resistance between contacts i and j when the current is injected from k to l.

Another way to have access to the electron density is to study the quantum oscillations of the magnetoresistance, namely the Shubnikov-de Haas (SdH) oscillations. If we call Δ the period of these oscillations (in T^{-1}), the electron density is given by

$$n_S = \frac{2e}{h\Delta}, \tag{2.19}$$

where h is the Planck constant and for a spin-degenerated system.

We can then perform Van der Pauw (VdP) measurements to determine the QW sheet resistance. It is given by the following formula [72]

$$R_S = \frac{\pi R}{\ln 2}, \tag{2.20}$$

where R_S is the sample's sheet resistance (in $\Omega/\square$) and R the average value of $R_{14,23}$, $R_{43,12}$, $R_{32,41}$ and $R_{14,23}$ once again for four injection current values.

Finally, one can have access to the sample's mobility by combining the two last quantities

$$\mu = \frac{1}{qn_S R_S} = \frac{K_H}{R_S}. \tag{2.21}$$

One should note that no correction factor was introduced in the VdP formula to take into account the shape of the sample. Therefore, the mobility value should be taken as an order of magnitude more than a precise value.

2.4 Basic THz characterization

The most basic and easy-to-do optical characterization that we could perform is room-temperature Time-Domain-Spectroscopy (TDS), without magnetic field. We do it thanks to a commercial *Terapulse 4000* experimental set-up of the *Teraview* brand, that can be settled in a transmission or reflectivity mode. The TDS principle is sketched on Fig. 2.7. A broadband

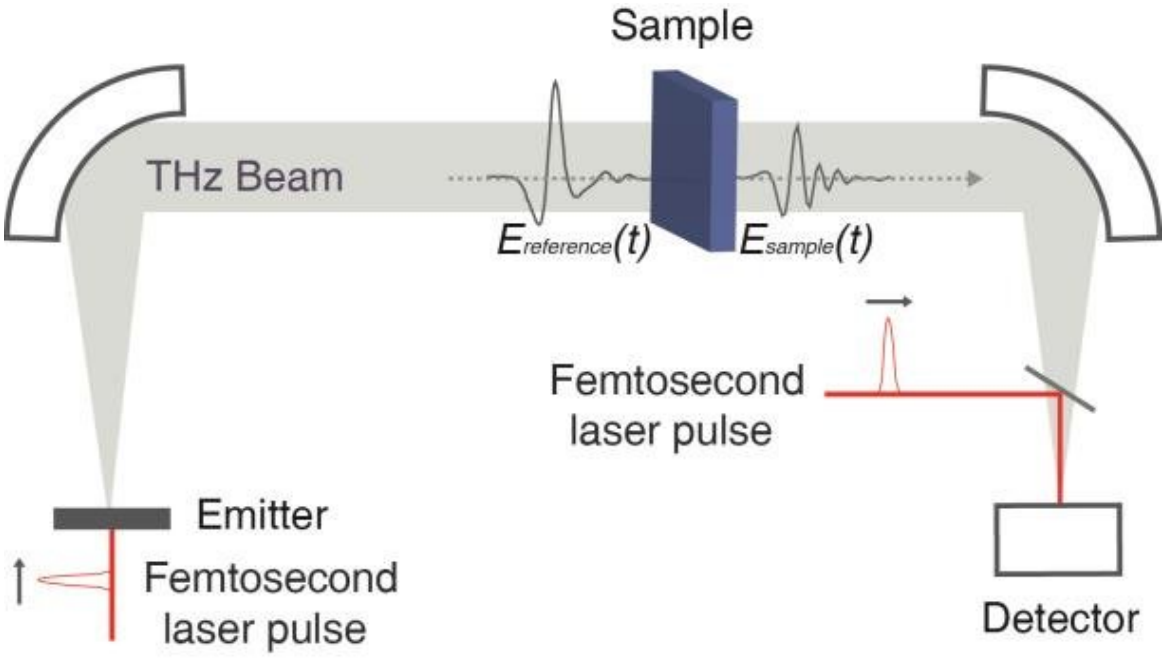

Figure 2.7: **Sketch of the Time-Domain-Spectroscopy experimental set-up in transmission mode.** Adapted from [73]

THz beam is generated from an emitter submitted to a femtosecond pulsed laser. The beam is then guided through the sample of interest and the signal emerging from it is in turn guided to a detector. Emitter and detector works on the same principle and are synchronized via the pulsed laser. Note that some additional mirrors are present when the set-up is in reflectivity mode. The absorbed spectrum is retrieved by taking the numerical Fourrier transform of the ratio $\frac{E_{sample}(t)}{E_{reference}(t)}$.

This set-up allows us to have rapid optical response of our samples and will prove itself very useful at characterizing the modes of our resonators (see following chapters).

2.5 Magneto-spectroscopy experimental set-up

The first experimental tool that is typically used to characterize the samples is a magneto-spectroscopy set-up. It allows one to have a very good understanding of the LLs energy landscape of the material and proves very useful in order to interpret further emission results. Measurements have been performed both in Montpellier at Charles Coulomb laboratory and in Grenoble where I was hosted by the National Laboratory of Intense Magnetic Fields (LNCMI). I will present the general principle of these set-ups, even though some characteristics may differ from one lab to the other.

2.5.1 Transmission configuration

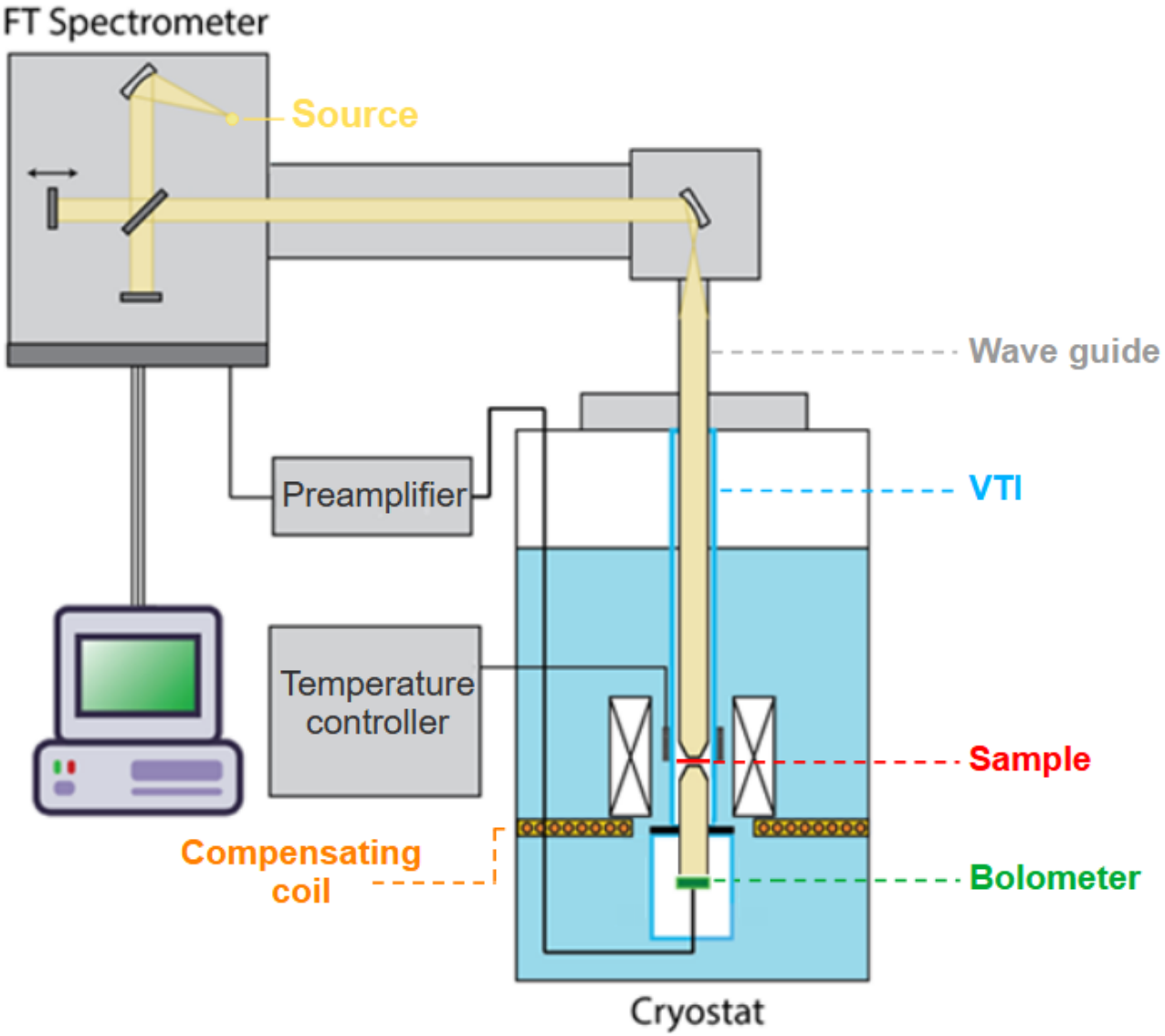

Figure 2.8: **Sketch of the magneto-transmission experimental set-up.**
The set-up is composed of a FTIR spectrometer coupled to a 16 T cryostat. The light is guided to the sample via a wave-guide. The transmitted light is detected by a bolometer located at the bottom of the cryostat.

To perform spectroscopy in the THz/MIR energy range, the Fourier Transform Infrared (FTIR) technique is widely used. It allows one to have a very broad range of spectroscopy. Figure 2.8 displays a sketch of a typical magneto-transmission FTIR-based set-up. It is composed of a Fourier Transform (FT) spectrometer and a source that will generate a THz/MIR radiation. This radiation is guided toward a wet liquid Helium (LHe) cryostat that hosts the sample and the superconducting coils. The sample is at the center of a first coil that creates the Landau quantization. The sample is inserted in the cryostat via a Variable Temperature

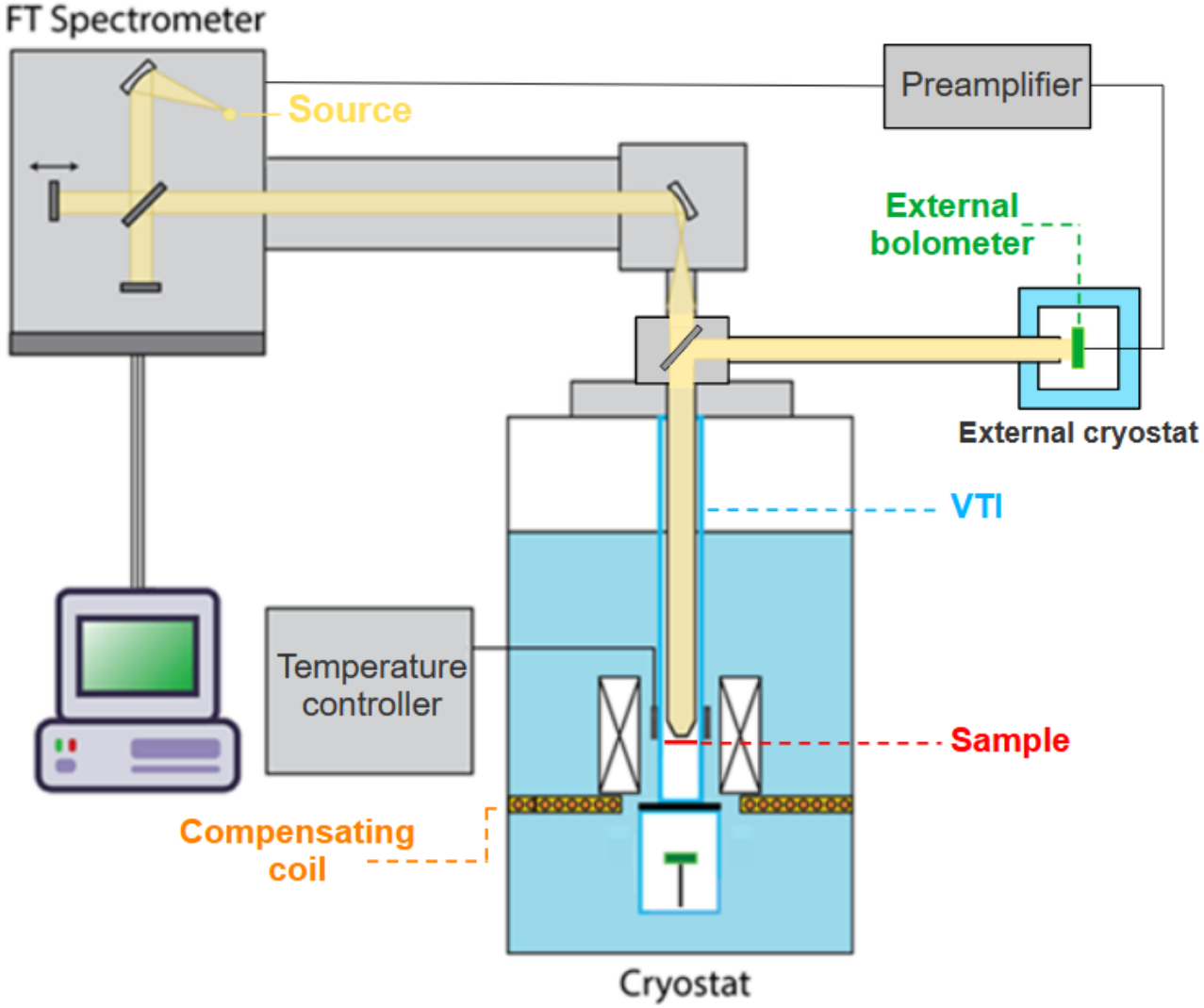

Figure 2.9: **Sketch of the magneto-reflectivity experimental set-up.**
It is composed of a FTIR spectrometer coupled to a 16 T cryostat. The light is guided to the sample via a wave-guide. The reflected light is guided outside of the cryostat thanks to an additional bean-splitter. The light is detected by an outside bolometer, cooled down by its own cryostat.

Insert (VTI) that allows to control the working temperature. The light goes through the material and hits a bolometer, separated from the rest of the cryostat by a diamond window. The bolometer is thus isolated from the VTI insert and stays at 4.2 K. It is also decoupled from the sample's magnetic field thanks to a compensating coil. The bolometer's output signal is then processed by the FT spectrometer and acquired by a software. Note that I also used the LNCMI-Grenoble laboratory facilities that owns a slightly different experimental

set-up. Namely, there is no compensating coil so the bolometer is influenced by the magnetic field, but this is taken into account in the data processing part.

To process the data we perform the following protocol. The transmitted output signal can be expressed as follows

$$T_{total}(\omega, B) = H(\omega) T_{sample}(\omega, B), \tag{2.22}$$

where $H(\omega)$ is only a function of frequency and represents the different contributions of the source, the experimental set-up or the bolometer's responsivity. The signal of interest is $T_{sample}(\omega, B)$, which is the transmission of the sample at a given frequency and magnetic field value. Therefore, it is very convenient to represent the following quantity

$$\hat{T}(\omega, B) = \frac{T_{sample}(\omega, B)}{T_{sample}(\omega, B = 0)}. \tag{2.23}$$

This way we have access of the normalized transmission of the sample for different frequencies and magnetic field values, without being bothered by frequency fluctuations of the source, the bolometer or any other component.

2.5.2 Reflectivity configuration

Transmission experiment are possible only when we deal with transparent or thin samples. When it is not the case, we can use the same spectroscopy set-up but in a slightly different operation mode. Figure 2.9 sketchs the experimental set-up in the reflectivity configuration. The only thing that differs from the transmission configuration is that we are now interested in the light reflected at the surface of the sample. It is guided outside of the wet crysostat via an additional beamsplitter and it finally goes into an external cryostat hosting a second bolometer.

2.6 Landau emission experimental set-up

The main experimental set-up that was used during my PhD is the Landau emission spectrometer, of the TEST team in Montpellier. It is a quite unique set-up, as it is one of the only ones remaining is the world. We will begin with a general overview of how the set-up, before detailing two critical components that are the detectors and the detection blocks.

2.6.1 General overview of the spectrometer

Figure 2.10 displays a sketch of the Landau emission experimental set-up. It is composed of three superconducting coils embedded in a wet LHe cryostat. Both the sample and the detector are mounted on the same insert that goes inside the cryostat. They are linked together by a copper-based wave guide. The sample is located at the center of a upper coil that creates the LLs dispersion. The detector is located at the center of a lower coil that is used to tune the energy window of the latter, as will be detailed in the following. The third and last coil is there to decouple the two first magnetic fields from each other. There are two possible operating configurations. The first is to sweep the magnetic field on the sample while keeping the magnetic field on the detector fixed. This way, we can have access to the magnetic field dependence of a phenomenon at a given energy. The second operating mode

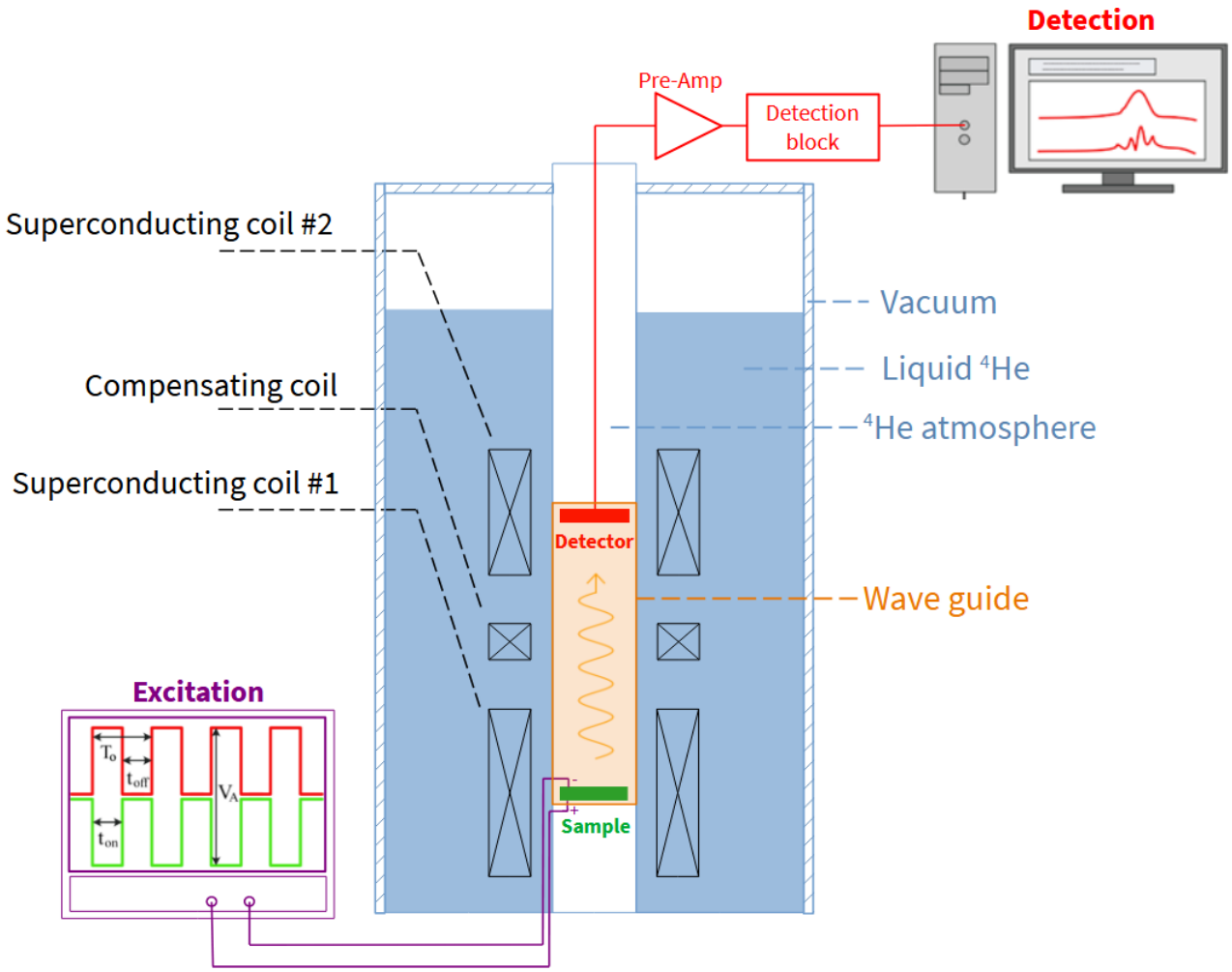

Figure 2.10: **Sketch of the Landau emission experimental set-up.**
It is composed of a three-superconducting-coil system, embedded in a wet LHe cryostat. The sample is excited with short electric pulses. The emitted light is guided through an inside bolometer. The signal is then amplified processed by a detection block.

consists in sweeping the magnetic field value on the detector while keeping the one on the sample constant. We have thus access to the full spectrum at a given magnetic field.

The sample is electrically excited by short voltage pulses, creating an out-of-equilibrium distribution of electrons in high index LLs, well above the Fermi energy. The typical width of the pulses is ranging from dozens of *ms* to dozens of μs, depending on the sample and the pulse's amplitude. The latter can be set from a few Volts to 200 V peak-to-peak thanks to two coupled *8114a Keysight Agilent* pulse generators. The samples are electrically bounded via Indium welding. It is a simple way to achieve good Ohmic contact as the Indium diffuses throughout the whole structure.

The output signal of the bolometer is send to a $\times 100$ *NF Electronic Instruments* low-noise pre-amplifier and then processed by the detection block. It can be either a lock-in amplifier block or a box-car-averager as we will detail later on. The final signal is acquired by a computer though a *Labview* software.

All the measurements are performed at liquid Helium temperature at 4.2 K.

2.6.2 Different detectors

During my PhD, we used two different detectors, one made of InSb and the other of GaAs. They are both photoconductive detectors and offer complementary characteristics in terms of resolution and detection range.

The first and mainly used detector is an InSb hot electron bolometer commercialized by *QMC Instrument Ltd*. Its photoresponse has widely been described in [74, 75] and is summarized Fig. 2.11. It displays the photoresponse of such a detector for two laser frequencies (blues lines) as a function of magnetic field and for 4.2 K. One can see two resonances, coming from an intraband LL transition and its associated impurity-level transition (see sketch

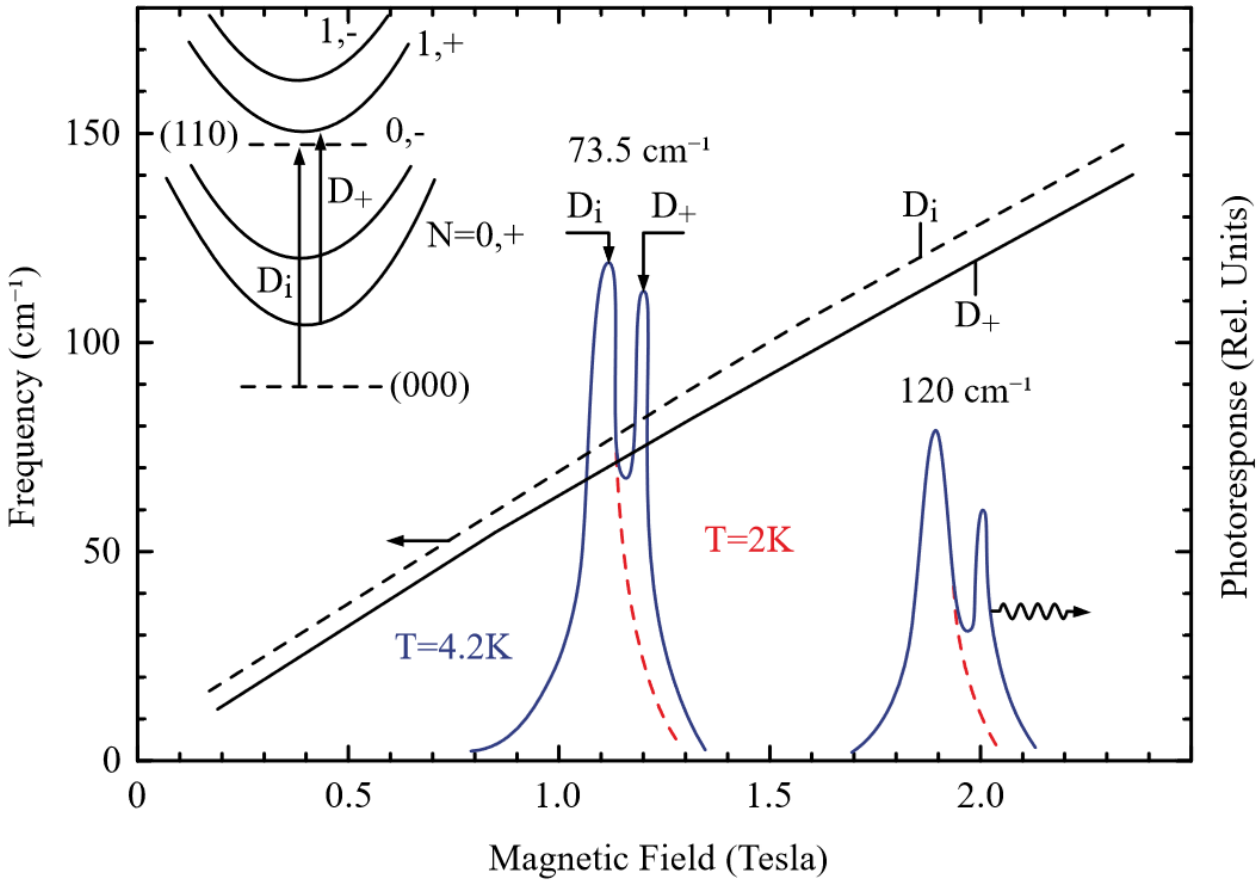

Figure 2.11: **Characteristics of the InSb detector used in Landau emission.** Photoresponse of the InSb detector as a function of the magnetic field (blue curves, right axis), for two different frequencies. The frequency dispersion with magnetic field is also plotted (black lines, left axis). The insert sketch the two intraband LLs transitions involved in the photoresponse, namely D_i and D_+. Adapted from [76].

in the insert). The magnetic field dependency of these two lines is also plotted on the left axis and one can see that it almost follows a linear behavior. Therefore, this InSb detector is easily magnetic field tunable between 1 and 18 meV (8 cm^{-1} to 150 cm^{-1}). The drawback of such a detector is inherent to the fact that two transitions exists. It limits the available resolution to 1 meV (8 cm^{-1}). One way to improve this is to reduce the working temperature. Figure 2.11 shows the photoresponse for 2 K (red dashed lines) and one can see that the D^+ transition becomes frozen, thus increasing the resolution to 0.25 meV (8 cm^{-1}). However,

since our set-up does not allow us to cool down to 2 K, this is not a viable solution. Another drawback to this detector is the the intrinsic Restshtrahlendband that hinders any detection above 22 meV [77, 78].

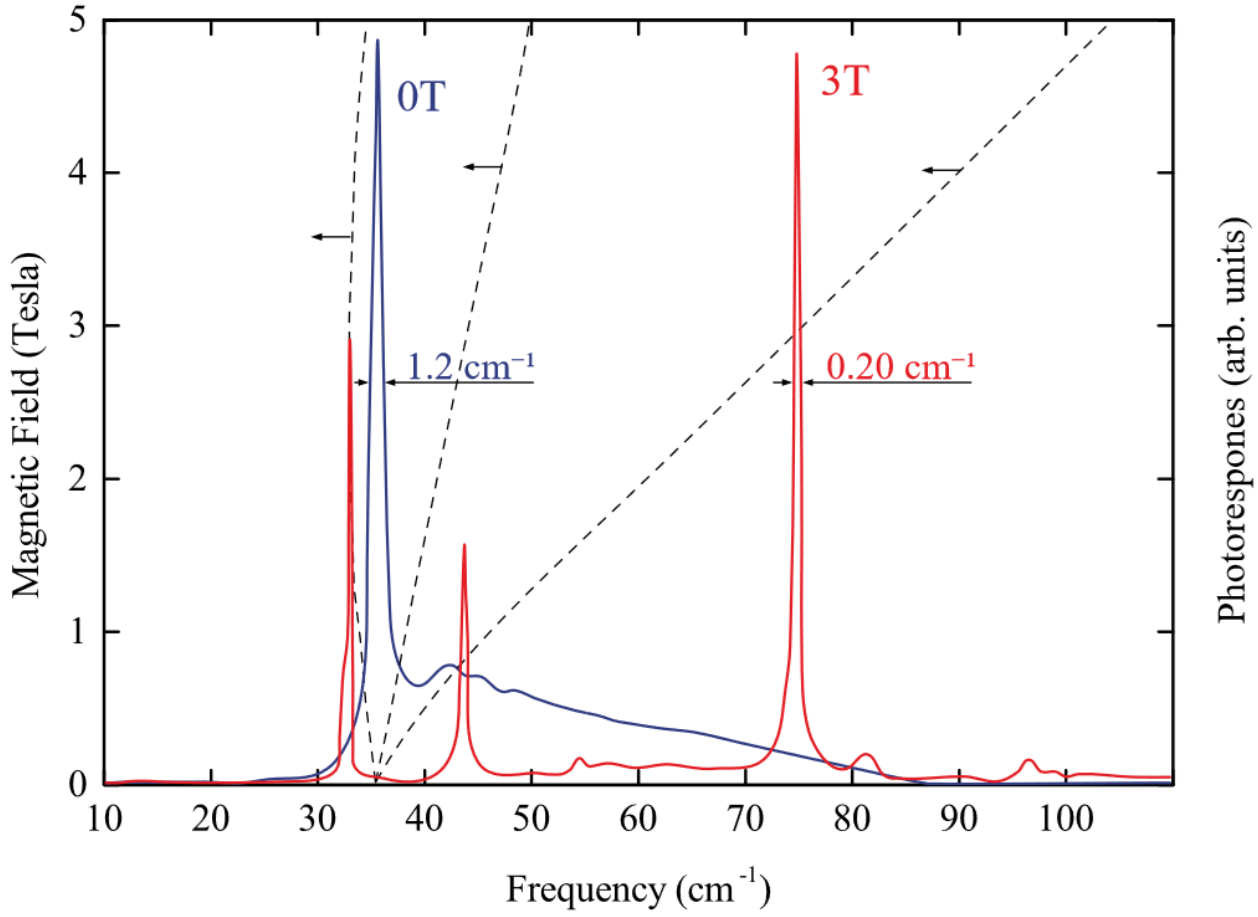

Figure 2.12: **Characteristics of the GaAs detector used in Landau emission.** Photoresponse of the GaAs detector as a function of frequency (blue and red lines, right axis), for two different magnetic field. The magnetic field dispersions of the three resonances are also plotted (dashed lines, left axis). Adapted from [76].

One way to cope with this low resolution is to use the other detector. Indeed, thanks to decades of studies and improvements, GaAs is the material that can reach the highest mobility at cryogenic temperatures [79]. Its photoresponse with magnetic field can be found in [80, 81], and Fig. 2.12 summarizes its main features. When submitted to a magnetic field (red curve), the dominant resonance splits into three peaks and the broad-band tail vanishes (see blue curve for the zero field response). One can see that the three transitions are really sharp, their linewidths reaching 0.025 meV (0.2 cm^{-1}). Figure 2.12 also depicts the magnetic field tunability of each peak, which is also linear, making GaAs suitable to a magnetic field detection energy control. However, since there are three resonances, this kind of detector is only suited to a range above 6 meV (50 cm^{-1}) where only the third peak is present. It was also shown that the transition can be followed only up to 14 meV (110 cm^{-1}).

To summarize, we use an InSb bolometer for a broad-range characterization but with a poor resolution while we switch to the GaAs detector to study fine spectral response but on a narrower energy window. Note that the sensitivity of the two detectors is comparable,

with a nominal value of 10^5 V/W at 4.2 K.

2.6.3 Different detection methods

Let us now present the detection block. Two main methods are used and depending on the injection conditions, it is preferable to use one or the other.

The first method is based on the well known lock-in detection principle. For that method we used a *EG&G Instrument* lock-in amplifier with a 127 Hz modulation frequency, also used as a reference for the pulse generators. Figure 2.13 displays a sketch of the principle of detection of such a method. The signal to analyze is multiplied by a reference sinusoidal signal and a low-pass filter is then applied to retrieve the amplitude and phase of the signal of interest. It is a very powerful detection technique and very easy to set in place. We used it as an exploratory tool, to get information on new samples. When using a lock-in detection technique, we typically send pulses of duration ranging from 4 to 1 ms (corresponding to duty cycle values of 50 to 1 % respectively) and amplitude up to 20 V peak to peak. All the emission information is typically contained in the phase signal.

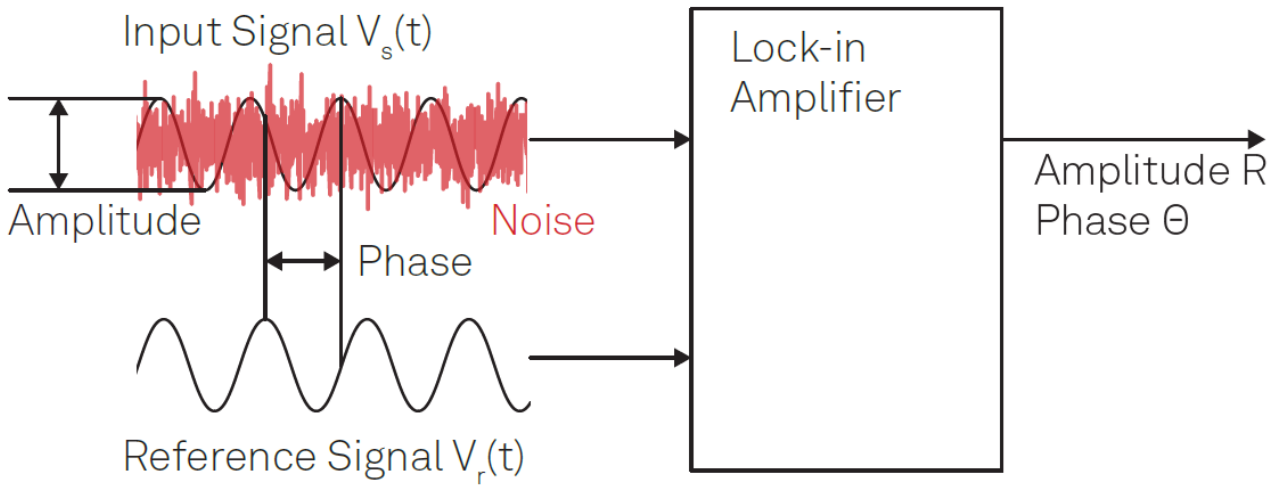

Figure 2.13: **Sketch of the principle of detection of a lock-in amplifier.**
The signal of interest is multiplied by a reference signal of the same frequency. After a low-pass filtering, it is possible to recover the amplitude and/or phase of the measured signal. Adapted from [82].

However, this technique has a major limitation when used on pulsed experiments. Indeed, the detection is made over the whole temporal range of the signal. Therefore, when working with low duty cycles, most of the integrated signal will be made of noise and it can be hard to extract the signal. Additionally, as we will see later on, when we increase the input voltage, the sample starts to heat quite significantly. Consequently, it is beneficial to reduce the time of the pulse in order to reduce the heating of the device. Therefore, at high input bias, we can't use a lock-in detection anymore as it becomes too noisy and we have to go to a more pulsed-experiment adequate detection device.

The second detection method is a boxcar averager. For that we used a *Stanford Research Instrument Inc.* boxcar. Figure 2.14 shows the principle of such a detection system. It consists in acquiring signal only during a certain time window (see center panel of Fig. 2.14). The

output signal is given by the average of the signal contained in the boxes over a high number of periods. It is really meant for pulsed experiments as it captures information only on the time ranges where the input pulse is on. It is therefore possible to work with pulses times below 1 *ms*. When acquiring with the boxcar averager, we typically use pulses of 3 μs (duty cycle of 0.04 %). This way, we can increase the input bias to 200 V peak to peak without heating too much the device. One very interesting option that can be provided by a boxcar

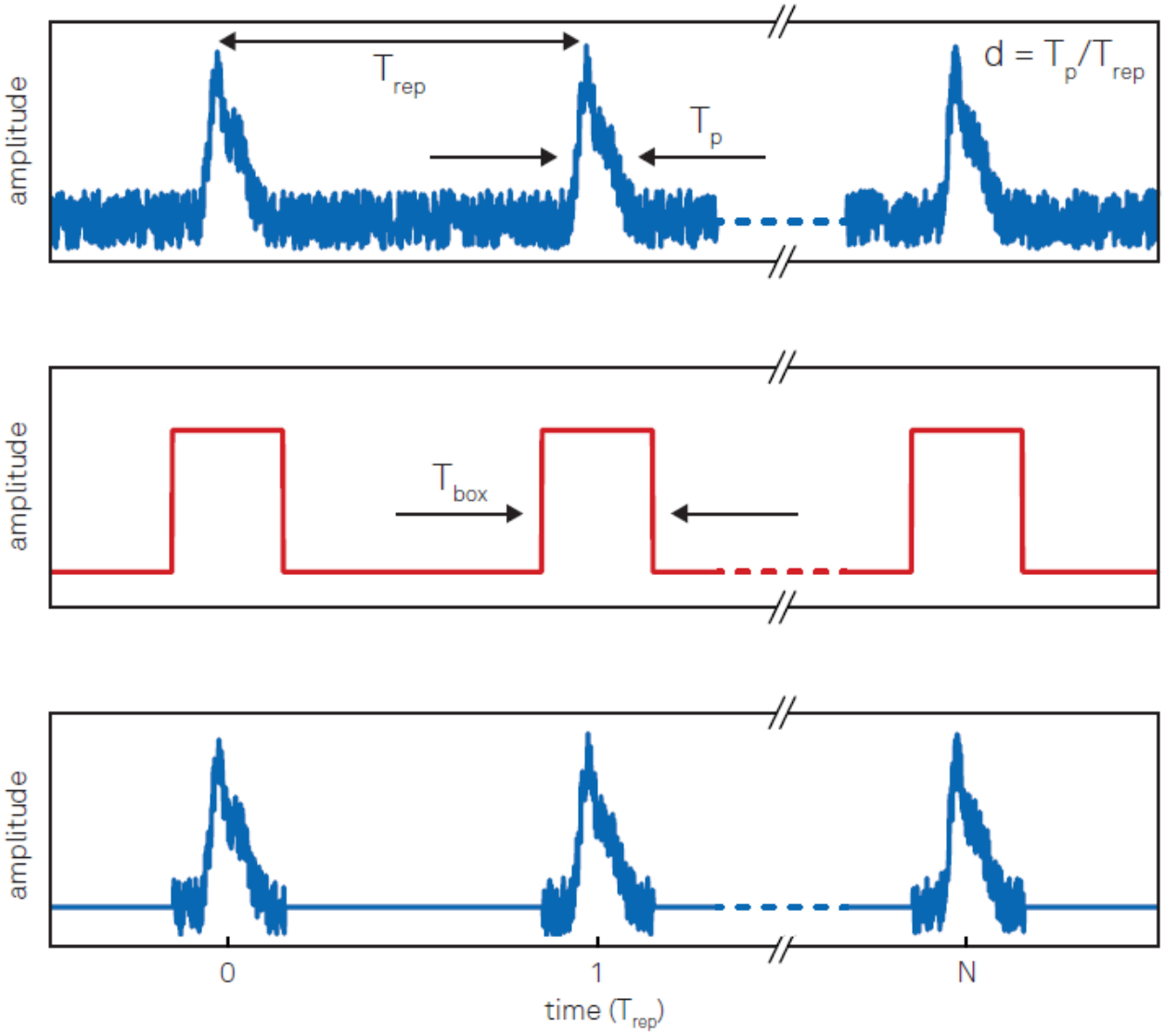

Figure 2.14: **Sketch of the principle of detection of a box-car averager.**
The signal of interest is convoluted with a box kind of signal and is being averaged over several periods. Adapted from [83].

averager is the background subtraction. It is possible to subtract any unwanted offset by opening a reference window in the time interval between pulses and to remove it from the signal of interest. This way, as we will see later, we could for example remove the heating part of the emitted signal.

2.7 Sample summary

In this section we will summarize the different samples measured and we will give some of their main characteristics.

2.7.1 HgTe-based QWs

During my PhD, two sets of HgTe QWs were studied. One was grown in the Institute for Physics of Microstructures of the Russian Academy of Sciences in Nizhny Novgorod, Russia (091222, see Table 2.2) and the other one was made by the CEA-LETI at the MINATEC Campus, DOPT in Grenoble, France (28104, see table 2.2). The two growths have been done by Molecular Beam Epitaxy (MBE) and have the same composition but are grown on different substrates (see Fig. 2.15a) for a sketch of the growth). It is composed of a buffer that is used to absorbs the strain relaxation between the substrate and the active layers, due to a mismatch of the mesh mismatch. Then comes the active layers namely a first HgCdTe barrier, a HgTe well and another HgCdTe barrier. The growth is closed with a CdTe cap layer to protect from any adsorption at its surface.

Table 2.2 summarizes different characteristics of the wells, obtained by the electrical characterizations presented earlier. One can note that the mobilities are comparable but that sample 28104 is less doped than sample 091222.

2.7.2 InSb-based QWs

I also measured an InSb-based QW which MBE growth has been made at the Purdue University in West Lafayette, USA. Figure 2.15b sketched the detailed growth which consists in a buffer, a first large AlInSb barrier and then the InSb well before the other barrier and a cap layer. A doping layer has been introduced in the second barrier to ensure the n-type of the QW.

Table 2.2 gives different characteristics of the sample. Its mobility is much lower than the HgTe ones but its electron density is comparable.

2.7.3 GaAs-based QWs

We also obtained GaAs-based QWs, grown by MBE at the Center for Nanotechnology and Nanoscience (C2N), Palaiseau, France. Its structure is sketched Fig. 2.15c and some transport characteristic are given in Table 2.2. This sample features a very high mobility compared to all the other ones ($> 2\,000\,000$ cm^2/Vs) and is therefore very interesting for Landau emission measurements.

Sample name	**Substrate**	**Carrier density [cm^{-2}]**	**Carriers mobility [cm^2/Vs]**
091222	GaAs	7×10^{11}	$\simeq 200\,000$
28104	CdTe	3×10^{11}	$\simeq 180\,000$
InSb QW	GaAs	7×10^{11}	$\simeq 50\,000$
GaAs QW	GaAs	3×10^{11}	$\simeq 2\,000\,000$

Table 2.2: Table summarizing the different samples' characteristics.

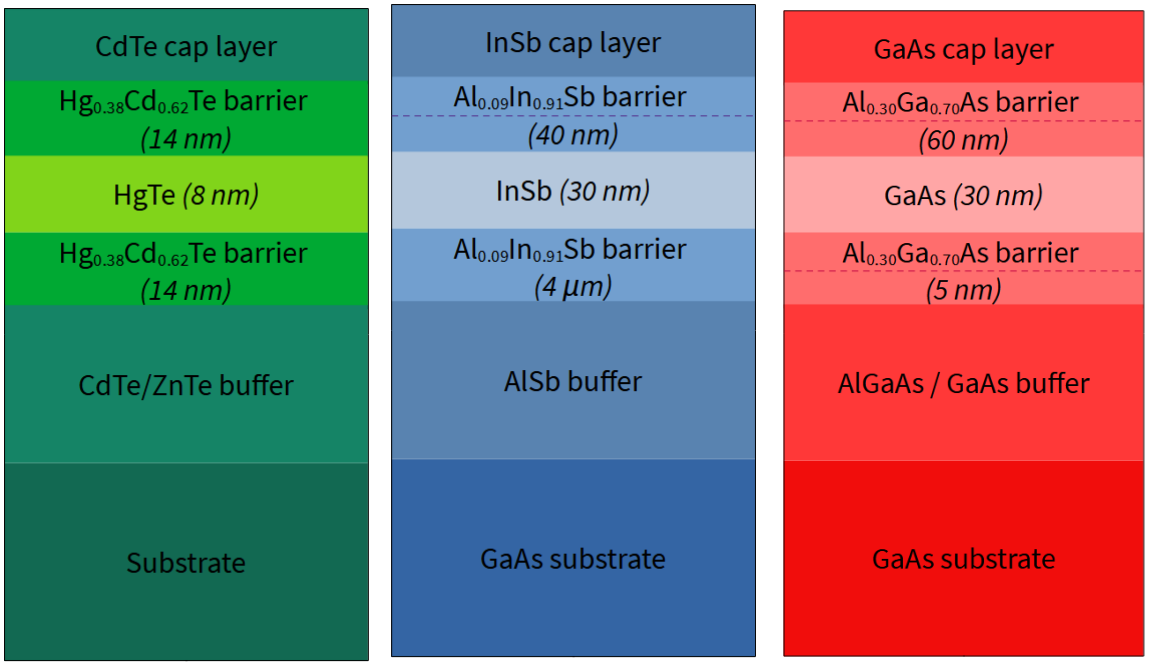

(a) (b) (c)

Figure 2.15: **Sketches of the growth of the HgTe-, InSb-, and GaAs-based QWs.**
(a) Sketch of the HgTe-based QW's growth. The substrate's nature depends on the QW (see Table 2.2). (b) and (c) Sketch of the InSb- and GaAs-based QW's growth respectively. The dotted lines are the Si doping levels incorporated during the growth.

Chapter 3

Landau emission in HgTe QW

Contents

3.1 Gate bias effect on the emission frequency

As mentioned previously, one of the peculiarities of Dirac fermions is the large dependence of the cyclotron mass with the Fermi level position. Thanks to the BHZ low-energy model we derived the precise evolution of the mass with the electron density, for HgTe QWs (see equation 2.4). We also saw in the Introduction that there is a perfect agreement between the experimental mass derived from the slope of the CR and the BHZ model, when studying different QWs with different electron densities [33]. The idea of this section is therefore to demonstrate the possibility to use this Dirac fermion special feature to develop a potential source, tunable over the whole THz gap with a reasonably low static magnetic field. Indeed, it is possible to control the carrier density within one single QW, by means of a gate voltage. All the results presented in this section have been published during my thesis and can be found in *Gate tunable terahertz cyclotron emission from two-dimensional Dirac fermions, B. Benhamou–Bui et al., APL Photonics 8, 116106 (2023) https://doi.org/10.1063/5.0168578*.

3.1.1 Device presentation

Due to the need for rather low (< 80 °C) working temperature to prevent atom migration, it is quite difficult to develop any technological process on Hg-based heterostructure. In addition to that, we need to let the surface of the sample uncovered to prevent any screening of the

emitted THz radiation. Therefore, a simple way to implement an electrical gate effect on a QW was proposed by Baenninger et al. [84]. The idea is to use the sample's semi-insulating substrate as a back-gate dielectric to modulate the electron density of the 2DEG. Figure 3.1 displays a sketch of the different steps to create the device. The backside of the sample is first polished to reduce the substrate's thickness down to approximately 100 μm. This part is achieved using a *Minitech 250 SP1* mechanical polishing machine, commercialized by *Presi* and was done on sample 091222 grown on GaAs (see Methods). The sample is then reported on a sample holder and glued using conducting silver paint to ensure good electrical contact.

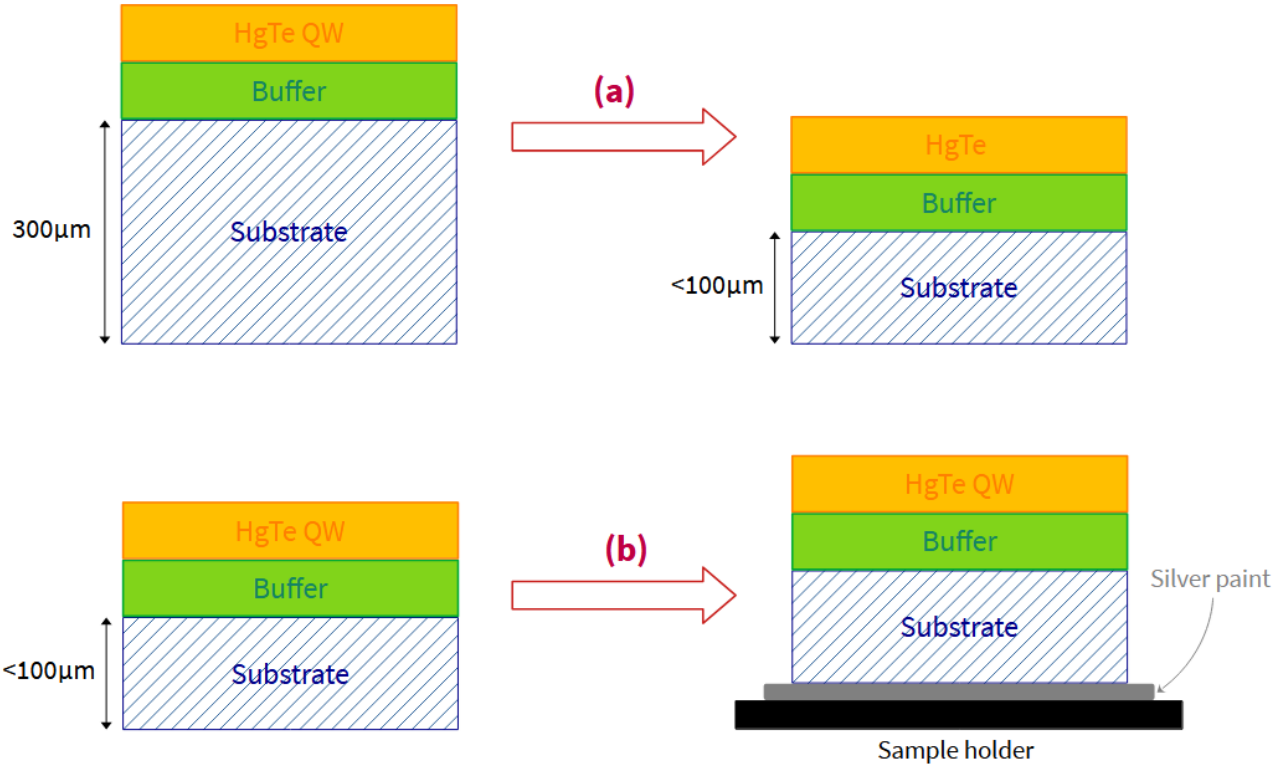

Figure 3.1: **Sketch detailing the different steps of implementation of the back-gate on the sample.**
(a) The substrate is thinned down to a thickness around 100 μm via mechanical polishing. (b) The sample is then reported on a sample holder and glued thank to a conducting silver paint.

3.1.2 Experimental results and discussion

Transport characterization

To reveal and quantify the gate effect on the QW, we first carried out magnetotransport measurements. Figure 3.2a displays 3 two-probe magnetoresistance curves obtained under different gate biases, ranging from -200 to +200 V. Clear SdH oscillations can be observed, which shift when the gate voltage is changed. From these quantum oscillations and using equation 2.19, one can extract each corresponding electron concentrations. It is plotted on Fig. 3.2b and it shows a clear density modulation from $3.3 \times 10^{11}\text{cm}^{-2}$ to $5.6 \times 10^{11}\text{cm}^{-2}$. It exhibits a linear dependence on the gate voltage, as expected for a planar capacitor. From

the slope, the surface capacity of the device can be extracted, and is found to be $C_{s,exp}$ = 0.9 μF/m^2. This value is coherent with a planar capacitor model that would give $C_{s,th} = \frac{l}{\epsilon_{GaAs}}$ = 1.1 μF/m^2, where ϵ_{GaAs} is the substrate permittivity (taken as 12.6) and l=100 μm its thickness. The discrepancy could arise from the thickness inhomogeneity of the substrate.

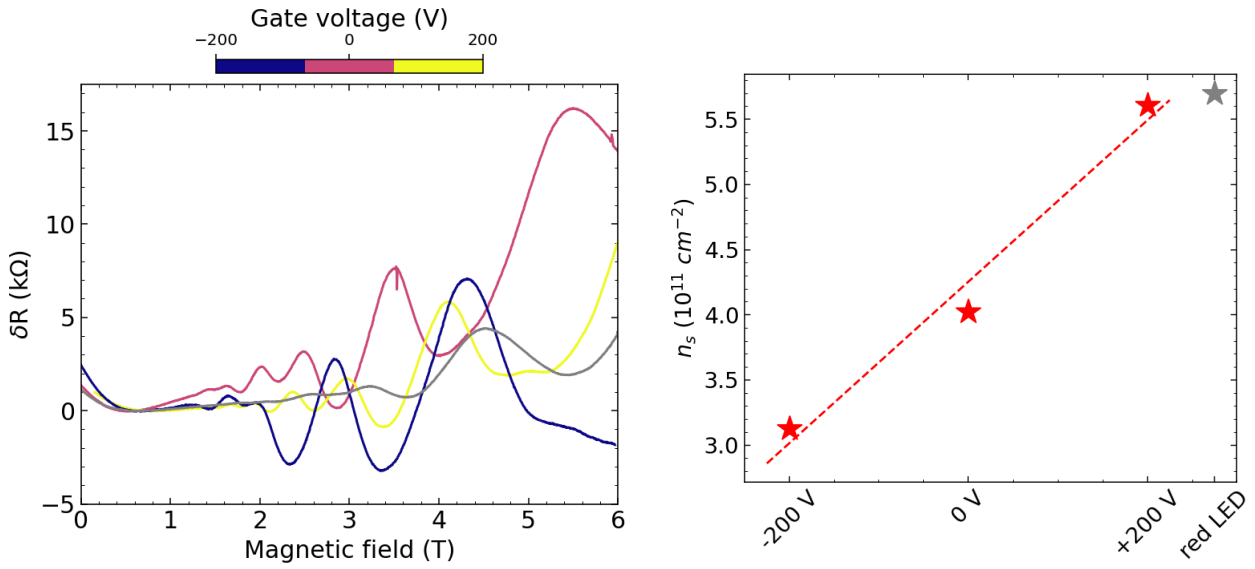

(a) (b)

Figure 3.2: **Transport characterization of the back-gate effect in the sample.**
(a) Magnetoresistance of the sample for different gate bias, displaying SdH oscillations. A linear background has been removed to emphasize the effect. The grey curve has been obtained with the red LED on. (b) Evolution of the electron density, extracted via the SdH oscillations, with the gate voltage value (red stars). A linear fitting is plotted on top (red dashed line) to extract the surface capacity of the device. The grey star has been obtained with the red LED on.

As a proof of concept, we employed an additional technique to modify the electron density in our system, namely the persistent photoconductivity (PPC). It has been demonstrated that a HgTe-based QW can have its electron concentration efficiently tuned when exposed to visible light [85]. The mechanism behind this doping effect is the generation of electron-hole pairs in the barriers, if the incident radiation has an energy higher than the barriers' gap ($\simeq$ 1.6 eV). Some of the excited electrons can then be dragged into the well by a small build-in electric field, thus increasing the carrier concentration of the latter [85]. We therefore mounted a 660 nm LED on the sample holder to further increase the QW doping. This additional point is displayed in grey on Fig. 3.2, when the LED is on. One can see that with this light-induced doping, one reaches carrier densities of almost 6×10^{11}cm^{-2}.

Finally, this transport characterization confirms the ability of our process to induce a gate effect on the QW. It allows an electron density modulation of about 40% using only an electrical effect. With a light-induced doping, the modulation can reach 45%.

Emission measurements

We then performed Landau emission spectroscopy on the device, using the Lock-In detection technique, typically with 5 to 10 V peak to peak amplitude and a 25% duty cycle

pulses. Figure 3.3a shows a typical result, obtained for a fixed gate bias. At a given magnetic field value on the sample, an intense emission peak is observed when scanning the detector's energy. This peak blue-shifts with increasing magnetic field, as expected for CR emission behavior. Figure 3.3b displays another representation of these results, in the form of a false-color map. The emission energy indeed exhibits a linear dispersion with magnetic field. From this we can extract the slope and then the value of the cyclotron mass (see pink

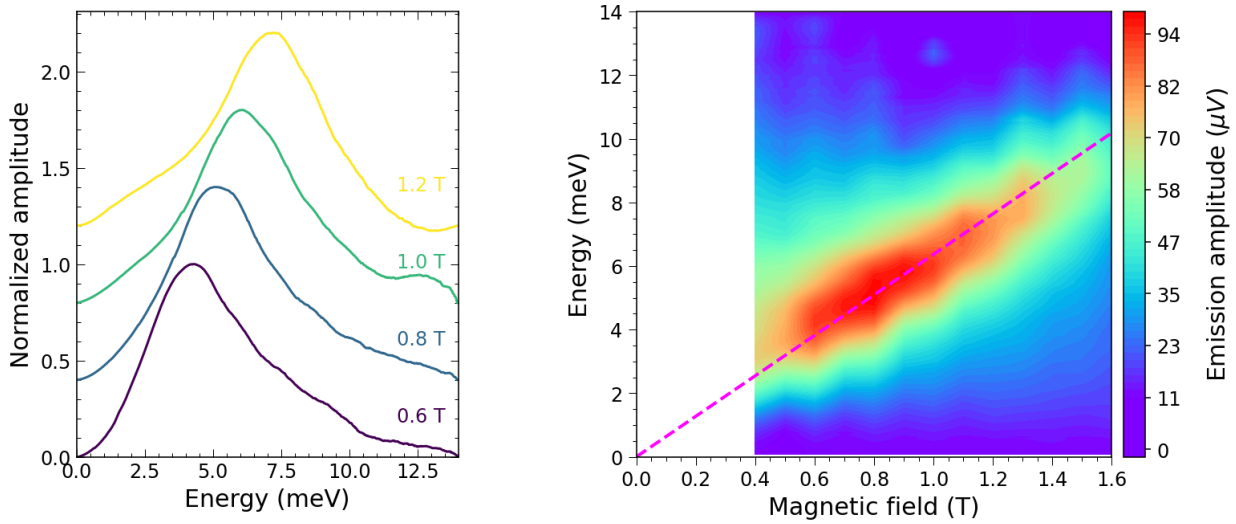

(a) (b)

Figure 3.3: **Landau emission spectroscopy results obtained on the device for zero gate bias.**
(a) Waterfall plots of emission spectra obtained for different magnetic fields applied to the sample. (b) False-color mapping of the emission amplitude withe respect to the energy and magnetic field. The pink dashed line is a linear fitting used to extract the CR mass of the sample.

dashed line) using equation 1.22. For example, results of Fig. 3.3 gives a cyclotron mass of 0.018 m_0. As mentioned previously, this mass is considerably lower than those in conventional semiconductors like GaAs (0.067 m_0 [86]) or p-Ge (0.047 m_0 [17]) which makes it possible to significantly lower the magnetic field required to cover the THz gap.

By performing such measurements for different gate voltage values, one can determine the evolution of the cyclotron mass with the electron density, obtained via the SdH oscillations. It is summarized on Fig. 3.4 where three representative points are plotted: -200 V, 0 V and +200 V. A fourth point was added using the PPC effet via a red LED. It can be seen that it accurately follows the BHZ model's prediction (black dashed line) detailed in the previous chapter.

Finally, as a proof of concept, we performed cyclotron emission measurements at a fixed low magnetic field of 1.5 T while sweeping the gate voltage value from -130 V to +150 V. The results are presented in Fig. 3.5a along with an additional spectrum obtained with the red LED turned on. The emission peak is clearly red-shifted when increasing the gate bias and thus the electron density, in accordance with the increase in cyclotron mass. With the combined effect of the electrical gate and the LED, the peak shifts by almost 1 meV corresponding to a 250 GHz displacement. This effect is better depicted in Fig. 3.5b where the peak frequencies are plotted with respect to the gate bias. It clearly shows that the

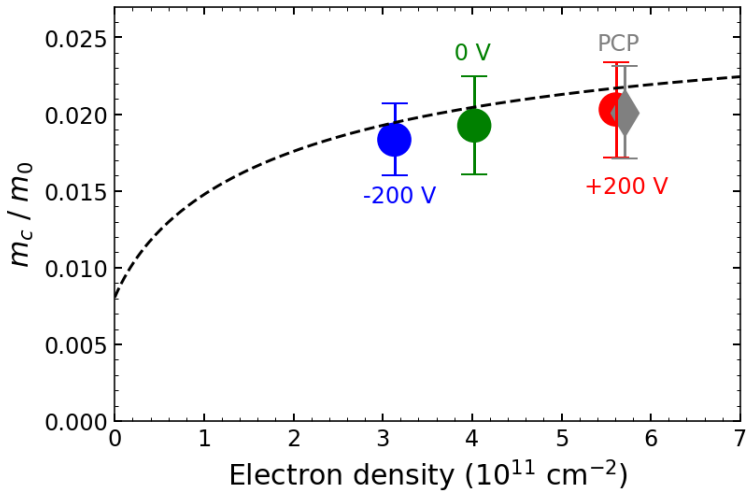

Figure 3.4: **Evolution of the cyclotron mass with electron density.**
Experimental CR mass, determined by Landau emission, plotted versus the electron density (colored points). The black dashed line is the BHZ model prediction (see chapter 2).

emission can be tuned from 2.3 to 2.15 THz, giving an electrical tunability of 536 MHz/V.

From the above results we conclude that we are able to produce cyclotron light within the THz gap, electrically tunable with a low static magnetic field (< 1.5 T). This new leverage of

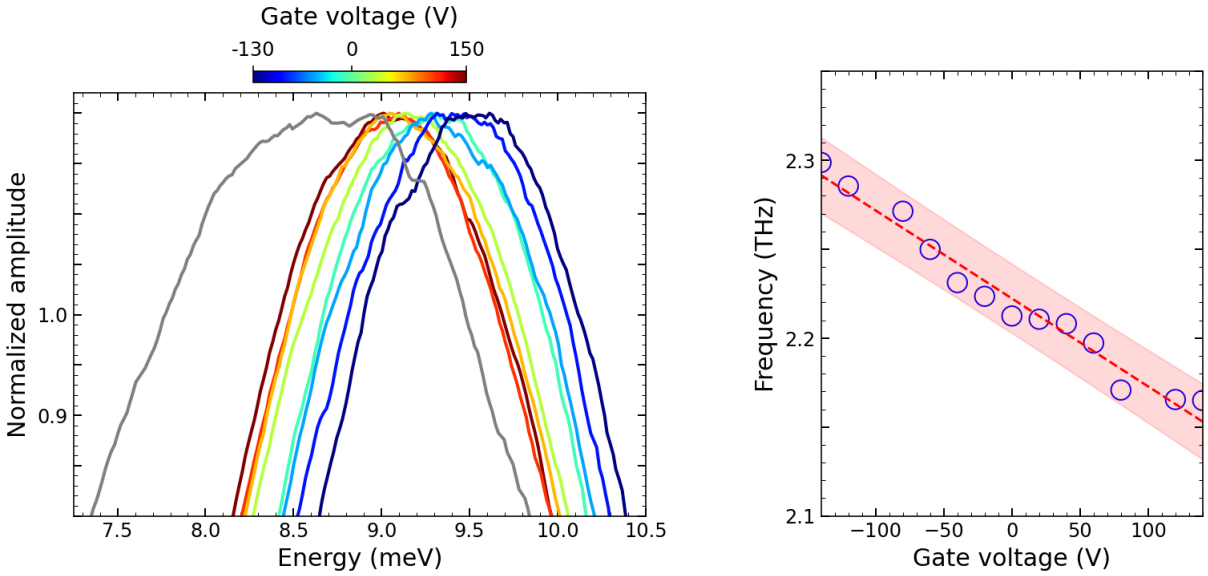

Figure 3.5: **Landau emission experiment for a fixed magnetic field and different gate bias.**
(a) Different emission spectra obtained for a fixed magnetic field of 1.5 T and gate voltage ranging from -130 to +150 V. The grey curve was obtained with the red LED on. (b) Extracted emission maxima plotted versus the gate bias.

tunability offers many advantages over magnetic field based tuning. Indeed, it is way easier to implement and more compact as it can be operated with a permanent magnet (750 mT to 1 T) rather than a superconducting coil. Last but not least, this electrical tunability offers the

possibility to modulate the output frequency at much higher speeds, eventually up to the GHz range, which is highly promising for potential telecommunication applications.

Discussion and perspectives

So far, our home-made device offers a limited tunability range. However, several improvement possibilities exist. A first way would be to increase the gate effect through a more advanced implementation. A semi-transparent gate (required to allow light emission from the structure),which have demonstrated large ranges of density modulation [87, 88], could be fabricated using NiCr alloys.

Another way to proceed would be to lower the HgTe QW intrinsic doping. This can be done by introducing Hg vacancies during the growth [84] . Indeed, as shown in Fig. 3.6, the BHZ model predicts a rapid change of the emitted frequency for low carrier densities (typically $< 2 \times 10^{11}\text{cm}^{-2}$). This is because the non-parabolicity of the HgTe QW band-structure is more pronounced at low energy and thus at low electron densities. The QW that we studied has a relatively high intrinsic doping (around $4 \times 10^{11}\text{cm}^{-2}$) and therefore, the density modulation effect on the emitted frequency is low. If we imagine having a QW with a zero bias density of $2 \times 10^{11}\text{cm}^{-2}$, then with the same range of modulation that we have here (around $\Delta n = 1.5 \times 10^{11}\text{cm}^{-2}$) we could have a much greater tunability. Indeed, it would result in a density modulation between $5 \times 10^{10}\text{cm}^{-2}$ and $3.5 \times 10^{11}\text{cm}^{-2}$ and if we look at the BHZ model's prediction (Fig. 3.6), for a magnetic field value of 1.5 T, it would correspond to a CR frequency ranging from 2.1 to 3.5 THz. This way, the tunability range is increased to 4.5 GHz/V which is ten times more than what we currently have. To conclude, we have

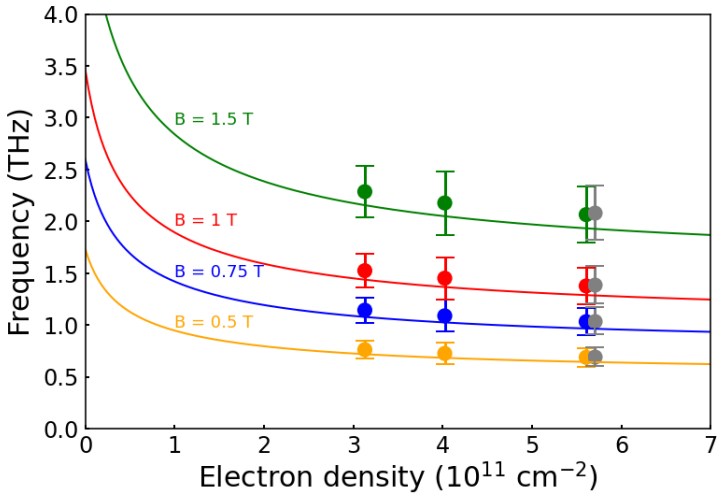

Figure 3.6: **Prediction from the BHZ model.**
Evolution of the frequency of the emitted light with the electron density, according to the BHZ model, for different magnetic field values (solid lines). The experimental points are added for comparison.

shown in this section that electrically tunable CR emission can be observed from HgTe QW, under a reasonably low magnetic field, thus allowing a fast frequency modulation and the use of permanent magnets. We also demonstrated that with some realistic improvements, this tunability range could be expanded to cover the whole THz gap.

3.2 Landau emission in strong crossed electric and magnetic fields

The Landau emission set-up we use has a crossed electric and magnetic fields geometry and so far, we have only applied relatively low electric fields. However, as discussed in chapter 1, if we aim to achieve a population inversion to obtain stimulated emission, we will need to increase the pulse amplitude to enter the streaming regime. The aim of this section is to present the interesting phenomena we observed when entering the regime of strong crossed electric and magnetic fields. Among other effects, we will see that the influence of the electric field on the LLs dispersion can no longer be neglected.

3.2.1 The hot carriers distribution

It is first important to understand how Landau emission works in the crossed fields configuration. A complete study has been done by *Chaubet et al.* to understand and model how light is emitted from a 2DEG submitted to crossed electric and magnetic fields [89]. The model they developed is based on a purely parabolic system, which is not the case for HgTe-based QW. However, by adopting HgTe representative parameters along with the use of the BHZ LLs, it gives interesting results in terms of interpretation.

The key ingredient is the interaction between electrons and acoustic phonons. It is through these scattering processes that electrons can populate higher-index Landau levels. If we consider a 2DEG in the (x,y) plane, submitted to a magnetic field in the z direction and an electric field in the x direction, then the authors showed that the LLs are tilted and disperse with k_y (see Fig. 3.7a). This way, through scattering, electrons from occupied LLs can jump into unoccupied states and then have a chance to de-excite radiatively.

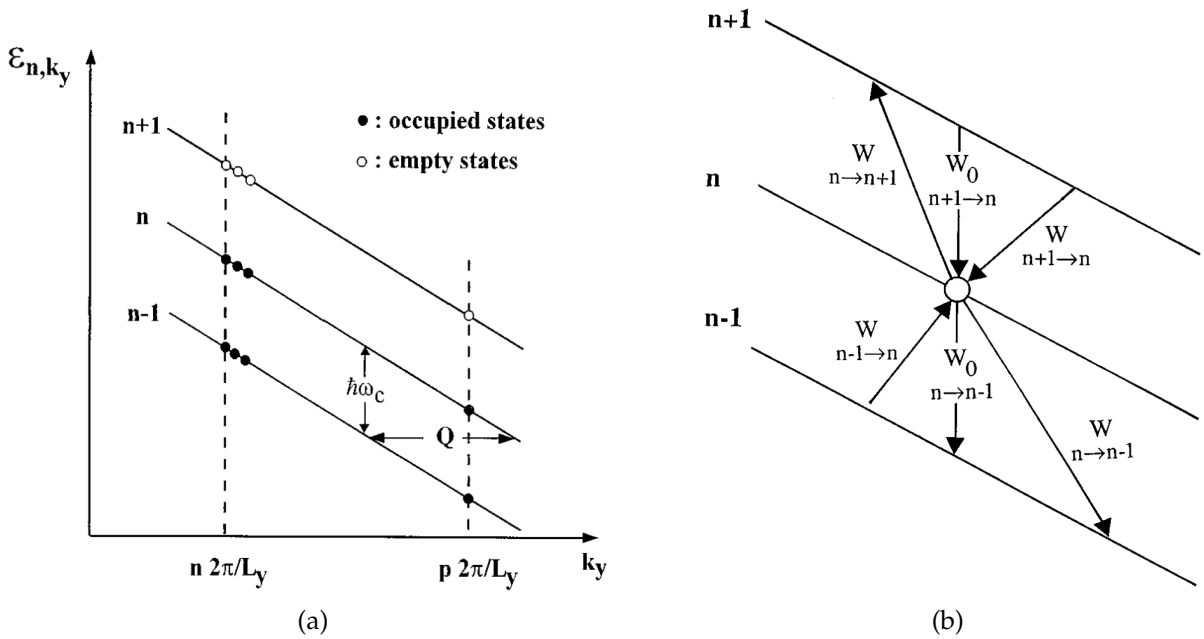

Figure 3.7: **Tilted LLs in a crossed electric and magnetic fields configuration.**
(a) In the presence of a strong electric field in the x direction, the LLs are tilted in the k_y direction. ω_c is the cyclotron frequency and Q is a characteristic distance which depends both on the electric and magnetic fields strengths. (b) The LLs population dynamic results in the balance of radiative (W_0) and non-radiative (W) processes. Adapted from [89].

The steady-state is given by the balance between radiative and non-radiative processes, summarized in Fig. 3.7b, and can be described by the following master equations, governing the population dynamics between different quantum levels [89]:

$$f_n = \frac{f_{n+1}\left(\underset{n+1\to n}{W} + W_0\right) + f_{n-1}\underset{n-1\to n}{W}}{(1-f_{n-1})\left(W_0 + \underset{n\to n-1}{W}\right) + (1-f_{n+1})\underset{n\to n+1}{W} + f_{n-1}\underset{n-1\to n}{W} + f_{n+1}\left(W_0 + \underset{n+1\to n}{W}\right)}, \tag{3.1}$$

where f_n is the n-th LL occupation, $W_{i\to j}$ is the non-radiative transition rate from level i to level j and W_0 the radiative transition rate which is given by $W_0(n,B) = \frac{e^4B^2\sqrt{\epsilon_r}}{2\pi\epsilon_0 c^3 m^{*3}}(n+1)$ [90]. Here we will consider that electron-phonon interaction is the dominant non-radiative process in play. It was modeled by the authors and they reveal that the electric field has a very large influence on the transition rate as it appears in the following exponential term

$$W_{i\to j} \propto e^{\frac{1}{2}Q^2 l_B^2} \propto e^{-\frac{e\hbar B^3}{2m^2E^2}}, \tag{3.2}$$

where $l_B^2 = \frac{\hbar}{eB}$ is the magnetic length and $Q = \frac{\omega_c B}{E}$ a characteristic distance in k_y which depends on both the electric and magnetic fields strengths (depicted in Fig. 3.7b). It is clear from this dependency and from picture 3.7b that a small increase of electric field will result in a larger tilt of the LLs and therefore a greater number of electrons scattered to high indexes levels.

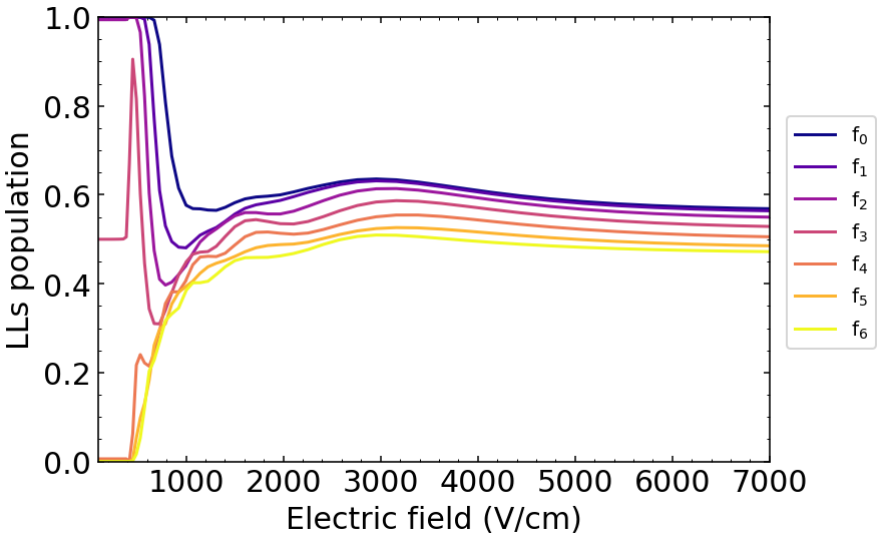

Figure 3.8: **Evolution of the LLs population with electric field, in HgTe-based QW.** Results of the numerical resolution of equation 3.1, for 7 LLs and a magnetic field of 1.5 T.

Equation 3.1 can be numerically solved and one can have access to the LLs populations for different electric field strengths. An example of resolution is plotted Fig. 3.8 where 7 LLs and a magnetic field of 1.5 T were considered. For this simulation, I used realistic parameters for HgTe, namely the speed of sound c_s = 2 000 m/s [91], the deformation potential E_1 = 3.7

eV [92] and the relative permittivity ϵ_r = 10.4 [93]. For low fields, (typically < 1500 V/cm), the initially filled LLs start to be depopulated and the higher ones starts to be filled. In this regime, we can make the assumption that the electrons are quickly thermalized at a temperature different from the lattice one. Therefore, we can still use the Fermi-Dirac (FD) distribution to describe this out-of-equilibrium situation, using the electronic temperature T_e:

$$f(\epsilon) = \frac{1}{1 + \exp\left(\frac{\epsilon - \mu}{k_B T_e}\right)}, \tag{3.3}$$

where ϵ is the energy, μ the chemical potential and k_B the Boltzmann constant. Figure 3.9a shows the evolution of this temperature with the electric field strength and Fig. 3.9b displays three distribution function examples. For very low fields, almost only the first LLs are populated and the electronic temperature is close to the crystal's one. When the electric field increases, so does the electronic temperature and the FD distribution starts to bend toward the higher LLs before becoming almost flat. At this point, the LL populations do not evolve much and the electronic temperature remains very high.

Note that this model does not aim at being quantitative, as it only considers scattering between electrons and acoustic phonons. However, it gives an interesting picture of the effect of the electric field on the LLs population. It also defines the notion of electronic temperature that is useful for understanding the electrons out-of-equilibrium distribution and we will reuse this quantity later on.

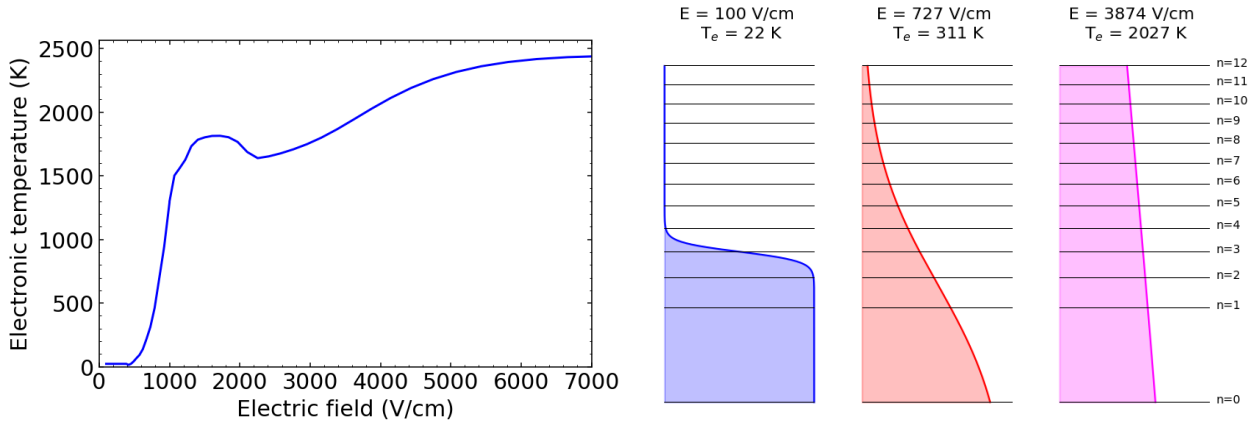

(a) (b)

Figure 3.9: **Electronic temperature evolution in HgTe-based QW.** (a) Evolution of the electronic temperature with respect to the applied electric field. (b) Plot of the FD distribution function for three different electric field strengths, superimposed on the BHZ LLs ladder.

One last thing we can estimate with this model is the emitted power. It can be expressed as [90]

$$P_{tot} = \sum_n P_n = \sum_n f_n(1 - f_{n-1}) W_0(n, B) \hbar \omega_c N, \tag{3.4}$$

where N is the density of electrons involved in the emission processes. This latter quantity is very difficult to estimate as it appears that the emission takes place only in "hot spots" localized around the current injection [94]. Therefore, we cannot simply replace N by the total electron density n_s. However we can have an estimation of the emitted power per electron,

which is depicted in Fig. 3.10. It is clear that an increase of the electronic temperature at relatively low electric field (typically < 1500 V/cm) implies an increase of the emitted power. When the saturation regime is reached (> 1500 V/cm) and all the LLs are equally filled, the total emitted power becomes almost constant with the electric field.

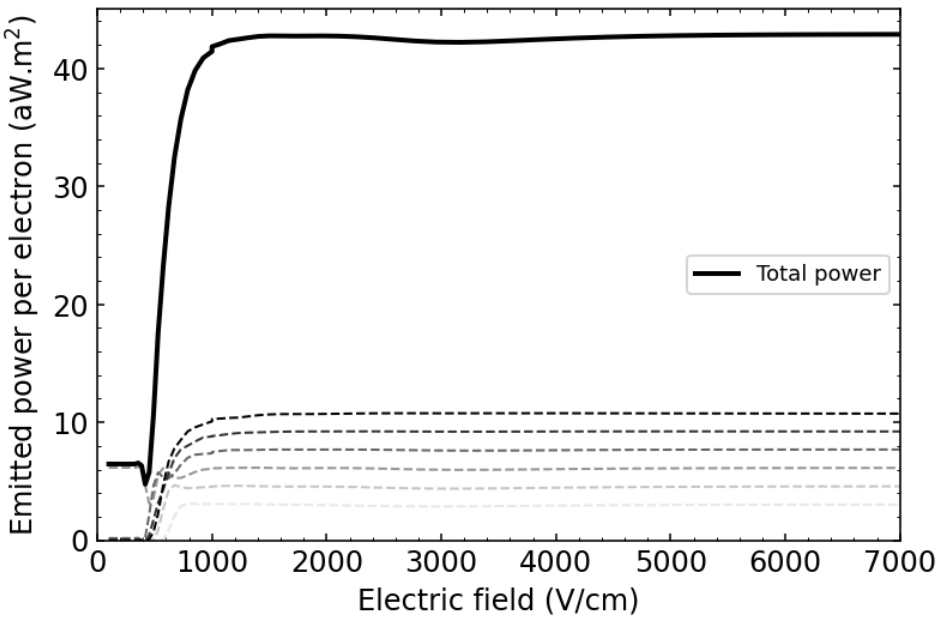

Figure 3.10: **Evolution of the emitted power per electron with respect to the electric field.** The total emitted power per electron is computed thanks to equation 3.4 and plotted versus the electric field strength (solid black line). The different LLs power contributions are also plotted as a comparison (dashed lines).

3.2.2 Crossed fields effect on the Landau levels dispersion

Up to now, the only influence of the electric field we considered was to bend the LLs, resulting in the hot-carrier distribution that we just discussed. However, for large drift velocities $v_d = E/B$, the LLs magnetic field dispersion itself is modified. This crossed electric and magnetic field effect was first studied by *Zawadzki et al.* and they showed that the LLs energy landscape was drastically affected [95]. We will detail these findings in a first subsection. These authors developed a fully quantized model suited for bulk InSb, which is a different system than HgTe-based QW as it features a much greater band-gap. Adapting this theory to our system is a complicated task and we will therefore present a semi-classical model that still demonstrate the effect of the crossed fields influence on the system.

Lorentz boost in InSb

Zawadzki et al. considered a narrow-gap semiconductor of gap energy ϵ_g and spin-orbit value $\Delta \gg \epsilon_g$ and they took into account one conduction band and two valence bands. They more precisely considered a 2DEG geometry subjected to a electric field in the gas plane and an magnetic field perpendicular to it. It can be shown that the LLs energies are

given by [95]:

$$E_n^{\pm}(k_x) = \hbar v_d k_x + \sqrt{1-\delta^2}\left[\left(\frac{\epsilon_g}{2}\right)^2 + \epsilon_g D_n^{\pm}\right]^{1/2}, \tag{3.5}$$

where

$$D_n^{\pm} = \hbar\omega_c\sqrt{1-\delta^2}\left(n+\frac{1}{2}\right) \pm \frac{1}{2}g_0\mu_B B, \tag{3.6}$$

and

$$\delta^2 = \frac{v_d^2}{\epsilon_g/2m^*}, \tag{3.7}$$

n being the LL index, g_0 a Landé factor and μ_B the Bohr magneton. With these formulas we retrieve that the LLs disperse along a direction perpendicular to the electric field. Therefore, the conclusions of the first subsection are still valid. However, we see that the magnetic field dispersion is now affected by the drift velocity and thus the electric field strength. In particular, we can identify an effective cyclotron frequency $\omega_{eff} = \omega_c\sqrt{1-\delta^2}$. For low drift-velocities, the LLs spectrum is weakly affected by the electric field and we can interpret the experimental results within the framework of the previous subsection. However, for large drift-velocities, ω_{eff} is significantly modified and so is the LLs dispersion. Eventually, if the electric field is strong enough so that $\delta^2 \geqslant 1$, the LLs spectrum collapses.

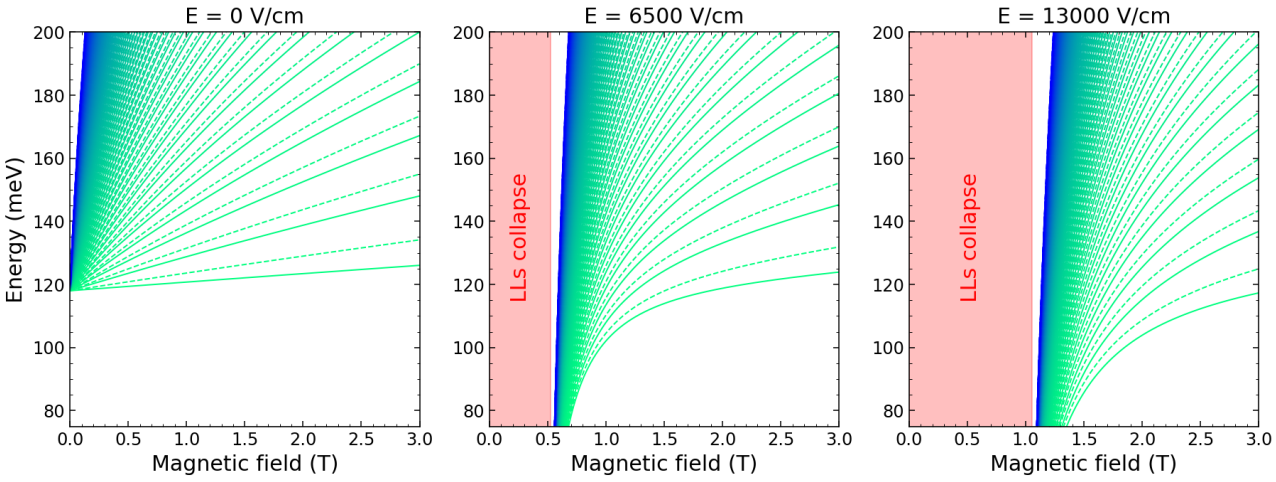

Figure 3.11: **Effect of the electric field on the LLs landscape in bulk n-InSb.** LLs fan-chart computed within the model described in the main text, for three electric field strengths. The solid (resp. dashed) lines are LLs for spin up (resp. down) and the pink area highlights the magnetic field range where the LLs collapse.

Figure 3.11 displays LLs fan-charts computed using equation 3.5, first with no electric field (left plot) and then with two different electric field strengths (two right plots). Bulk n-InSb parameters where taken, to illustrate the crossed fields influence: $m^* = 0.0136\ m_0$, $g_0 = -51.3$ and $\Delta = 236$ meV. It clearly highlights how the electric field distorts the LLs dispersion and how they collapse at low magnetic field (ie at high drift-velocity). In particular, this collapse implies a drastic increase of the cyclotron mass, as it can be defined like

$$m_c = \frac{\hbar eB}{E_{n+1} - E_n}. \tag{3.8}$$

This mass increase is plotted in Fig. 3.12, along with the experimental data obtained in [95]. In these experiments, the authors excite the $n = 1^+ \rightarrow n = 0^+$ transition of a bulk n-type InSb in a Metal-Oxyde-Semiconductor geometry for various crossed electric and magnetic field strengths. The data show a good qualitative agreement with the model described above and it shades light on the abrupt increase of the cyclotron mass at high drift-velocities.

This mass evolution with drift-velocity can be viewed as a semi-relativistic behavior of the conduction electrons in the material. This is more generally the case of all Dirac materials as their band-structure (without any influence of the fields) can be described in a pseudo-relativistic framework [96, 97]. In particular, it was shown by *Kane* that the energy-momentum of an electron in InSb and without electric field can be written as [98]:

$$E(p) = \sqrt{\left(\frac{\epsilon_g}{2}\right)^2 + \frac{\epsilon_g p^2}{2m^*}}. \tag{3.9}$$

It has the form of the energy-momentum relation of relativistic electrons in vacuum and one can thus make the following analogy:

$$\begin{array}{rcl} 2m_0c^2 & \leftrightarrow & \epsilon_g, \\ m_0 & \leftrightarrow & m^*. \end{array} \tag{3.10}$$

With this analogy we can deduce the maximum velocity for the conduction electrons in

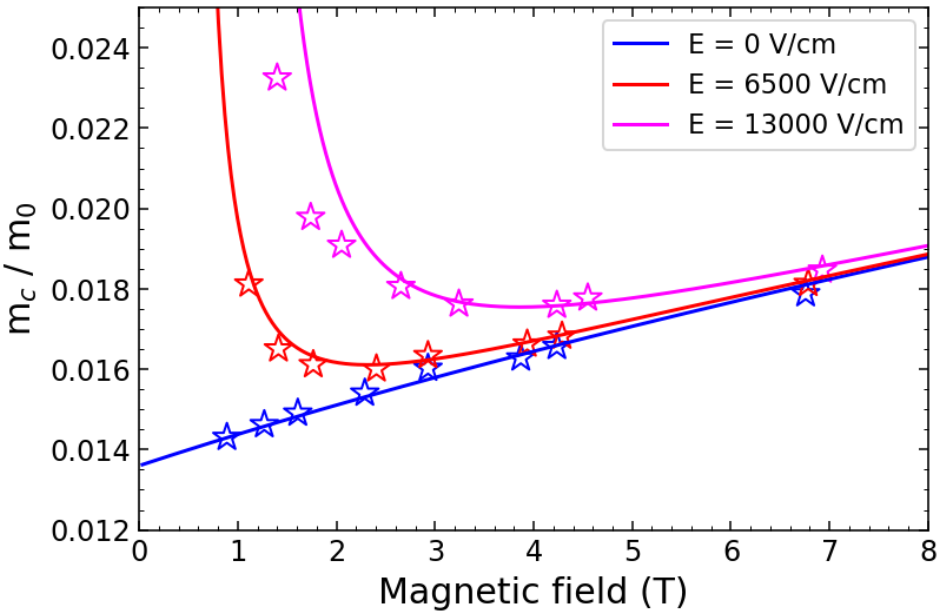

Figure 3.12: **Drastic increase of the cyclotron mass in bulk n-InSb.** Evolution of the cyclotron mass with magnetic field for different electric field strengths (solid lines). It is computed thanks to equations 3.5 and 3.8, for the $n = 1^+ \rightarrow n = 0^+$ transition. The markers are experimental data extracted from [95].

InSb: $u = \sqrt{\frac{\epsilon_g}{2m_0^*}} = 1.23 \times 10^6$ m/s. The Lorentz factor is then given by $\frac{1}{\sqrt{1 - \frac{v_d^2}{u^2}}} = \frac{1}{\sqrt{1 - \delta^2}}$ and by applying a Lorentz transformation, *Zawadzki et al.* showed that one can retrieve the exact spectrum of equation 3.5. Therefore, the increase of the mass with the drift velocity

can be seen as a relativistic accumulation of mass when the electron velocity approaches the material "speed of light" u. Figure 3.12 shows the experimental evolution of the cyclotron mass with magnetic field, for different electric field strengths. It witnesses the mass divergence when the drift velocity is increased. In particular, the maximum mass ($\simeq 0.023$ m_0) is reached for 13 kV/cm and 1.5 T, giving a drift velocity $v_d = 0.86 \times 10^6$ m/s = $0.7u$.

HgTe has a gap that it is one order of magnitude lower than InSb and a comparable zero-electric-field cyclotron mass. Therefore, the limiting speed u will be way lower in HgTe and we can therefore expect to see this "Lorentz-boost" effect for lower electric field strengths. Indeed, in HgTe we have $m_c = 0.02$ m_0 at zero electric field and a gap energy close to 28 meV. Therefore, for an electric and magnetic field strengths of 6.5 kV/cm and 2 T respectively, we obtain $\delta \simeq 0.93$, where it was only 0.26 in the same conditions in InSb.

Semi-classical model applied to HgTe-based QW

As mentioned earlier, it is quite hard to perform the same Landau level computation for the HgTe QW system, as its band-structure features both quadratic and linear in k terms. Therefore, to model the effect of strong drift velocities, we use a semi-classical approach, based on the optical conductivity (OC) computation. We will therefore not have access to the LLs of the material but we will be able to see the evolution of the cyclotron resonance when varying different parameters. This is relevant in our case because, as discussed earlier, due to the mobility of the carriers, the system is in the so-called incipient regime where LLs are formed but still strongly overlap, thus allowing a semi-classical treatment.

The calculations were made by Dr. *S. S. Krishtopenko* and I will only detail the main ingredients required to understand the model. A collection of charged particles in a static magnetic **B** aligned with the z direction and an oscillatory $\mathbf{E}_{tot} = \mathbf{E} + \mathbf{E}^{(\sim)}$ electric field along the y direction is considered. To compute the optical conductivity of the system, one needs to consider the Boltzmann kinetic equation, that will give access to the distribution function $f = f_0 + f_\sim$. After an ingenious change of variable from momentum (p_x, p_y) to angle-action coordinates (ϕ, $\mathcal{I}$) (can be found in [99]) and a first order approximation in $f_\sim/f_0$, it is possible to compute the distribution function. Once this is made, we can have access to the current densities

$$j_x^{(\sim)}(\omega) = g\,e \int_W dW \int_{-\pi}^{\pi} d\phi\, v(\phi, W) f_\sim(\phi, W, \omega) \cos\phi, \tag{3.11}$$

$$j_y^{(\sim)}(\omega) = g\,e \int_W dW \int_{-\pi}^{\pi} d\phi\, v(\phi, W) f_\sim(\phi, W, \omega) \sin\phi, \tag{3.12}$$

where g is a degeneracy factor equal to two for the spin, $W = \epsilon(p) + v_d p_y$ is the total energy and $v(\phi, W)$ the velocity distribution. The influence of the crossed-fields configuration is mostly contained in W, through the drift velocity and the bending of the band structures in the electric field direction. Finally, the OC can be obtained using the following relation:

$$\begin{pmatrix} j_x^{(\sim)}(\omega) \\ j_y^{(\sim)}(\omega) \end{pmatrix} = \sigma^{(\sim)}(\omega) \begin{pmatrix} E_x^{(\sim)} \\ E_y^{(\sim)} \end{pmatrix}. \tag{3.13}$$

By only considering the fundamental frequency and isotropic scattering, the velocity and $f_\sim$ terms can be greatly simplified and we finally obtain the following OC expression

$$Re\left[\sigma_{xx}(\omega)\right] = \pi g\, e^2 \int_{-\infty}^{\infty} \left(-\frac{\partial f_0(W)}{\partial W}\right) \frac{[V_0(W) + V_2(W)]^2}{2} \frac{\nu}{[\omega - \omega_c(W)]^2 + \nu^2}\, dW, \tag{3.14}$$

where $V_{0/2}(W)$ are the resonant velocity terms, whose expressions won't be detailed here, ν is a broadening parameter (assumed to be constant) and $\omega_c(W)$ the cyclotron pulsation. Its expression is given by

$$\omega_c = \frac{eB}{\hbar}\frac{2\pi}{\frac{\partial S(W)}{\partial W}}, \tag{3.15}$$

where $S(w)$ is the p-space area bounded by a trajectory for a given energy W. It is a very important quantity as it contains the bending of the band-structure with the applied electric field. It can be computed within the BHZ model and it yields

$$S(W) = \frac{\pi}{v_F^2}\frac{\alpha W^2 - (\alpha-\beta^2)\mathcal{M}^2}{(\alpha-\beta^2)\sqrt{\alpha(\alpha-\beta^2)}}, \tag{3.16}$$

where $\beta \equiv \frac{\hbar v_d}{\mathcal{A}} = \frac{v_d}{v_F}$ and $\alpha = 1 - 2\frac{\mathcal{D}W+\mathcal{B}\mathcal{M}}{\mathcal{A}^2}$, $\mathcal{A}, \mathcal{B}, \mathcal{D}$ and $\mathcal{M}$ being the BHZ parameter introduced in chapter 2.

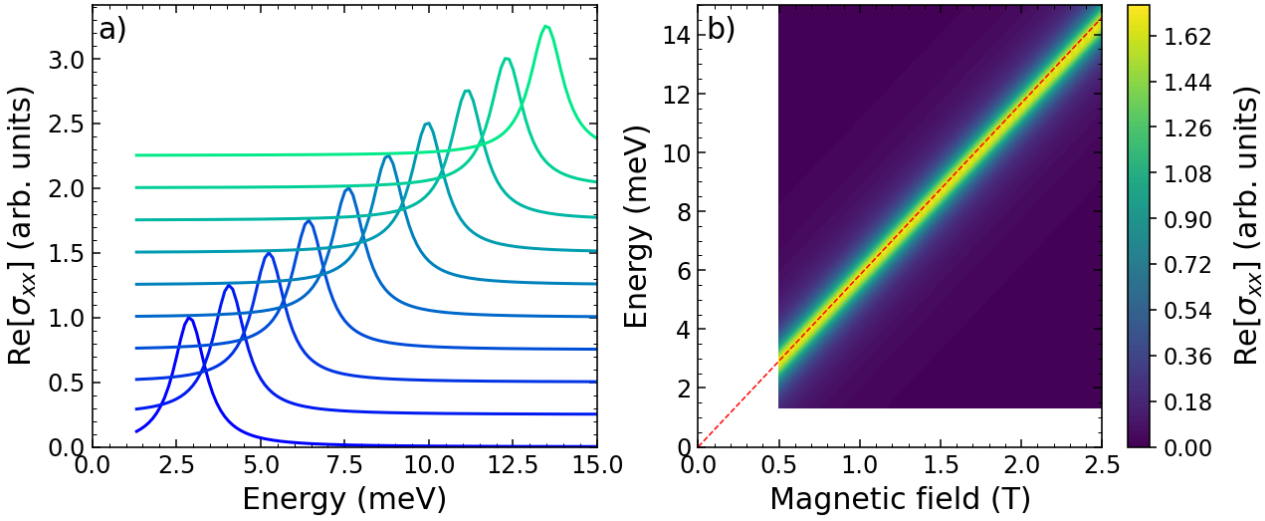

Figure 3.13: **Simulations of the CR for HgTe-based QW, without electric field.** (a) Waterfallplot of the real-part of the OC with respect to the emitted energy, for different magnetic field strengths ranging from 0.5 to 2.5 T. (b) False-color mapping of the same data, witnessing a linear evolution of the OC's maxima with magnetic field. The red dashed line is a linear fit used to extract the cyclotron mass value.

Due to rapid electron-electron interactions, the non-equilibrium distribution function f_0 can be considered stationary and written in the following form

$$f_0(W) = \frac{1}{\exp\left(\frac{W-\mu}{T_e}\right)+1}, \tag{3.17}$$

where μ is the chemical potential and is a function of the electronic temperature T_e though the following condition

$$n_s = \int \left[\frac{g}{(2\pi\hbar)^2}\frac{\partial S(W)}{\partial W}\right] f_0(W)dW, \tag{3.18}$$

where n_s is the electron concentration.

To summarize, the optical conductivity is the product of three terms: (i) a Lorentzian function, of width ν, emerging from the isotropic collisions and resonant around the CR pulsation, (ii) a temperature dependent term made of the derivative of the distribution function, narrowing the integral around the chemical potential and (iii) a velocity form factor. The main parameters are the electronic temperature and β, that is given by the drift velocity. Note that this quantity is the same as the δ found in the Lorentz-boost model developed for InSb.

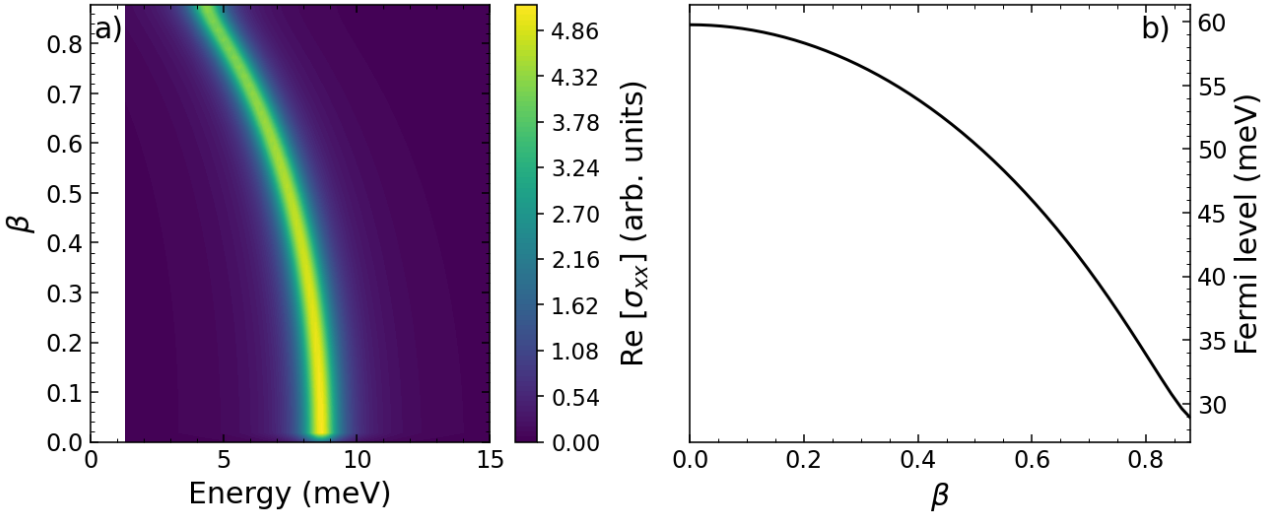

Figure 3.14: **Simulation of the influence of β on the optical conductivity in HgTe-based QW.** (a) False-color mapping of the real-part of the OC with respect to the energy and when varying the electric field strength at a fixed magnetic field value. (b) Evolution of the chemical potential with respect to the electric field strength.

We can first verify that the model correctly reproduces the cyclotron resonance behavior when increasing the magnetic field strength. The simulation's results are shown in Fig. 3.13, for an electronic temperature of 4 K and a carrier concentration of 3×10^{11} cm^{-2}. We took $\nu = 1/\tau \simeq 0.9$ ps, where $\tau = \frac{\mu_e m^*}{e}$ is given by the Drude formula, μ_e being the electron mobility estimated to be around 10^5 cm^2/V/s. The OC's real part exhibits a Lorentzian shape which maximum is blue-shifting when increasing the magnetic field strength (see Fig. 3.13a). It is better depicted in Fig. 3.13b where the OC's energy maximum linearly evolves with the field (see red dashed line). A linear fit of this behavior gives a cyclotron mass of 0.02 m$_0$ which is coherent with our structure, thus validating the simulation.

We can then study the influence of the electric field, at a fixed value of magnetic field. This is included by changing the value of the β parameter and an example is plotted on Fig. 3.14a, for 1.5 T, an electronic temperature of 4 K and a carrier concentration of 3×10^{11} cm^{-2}. When β varies from 0 to 0.9, attesting from an increase of the electric field, a clear redshift of the cyclotron resonance is observed, from 8.5 to almost 4 meV. We retrieve here the Lorentz boost effect at strong drift velocities that was previously observed in InSb. Indeed, a diminution of the CR energy directly implies an increase in the cyclotron mass. Figure 3.14b also depicts the evolution of the chemical potential, recalculated at every step of the simulation. It is clear that it decreases, by more than a factor of two, when the electric field gets stronger. This is coherent with the interpretation of a LLs collapse as the energy of the last filled level should also collapse and so will the chemical potential.

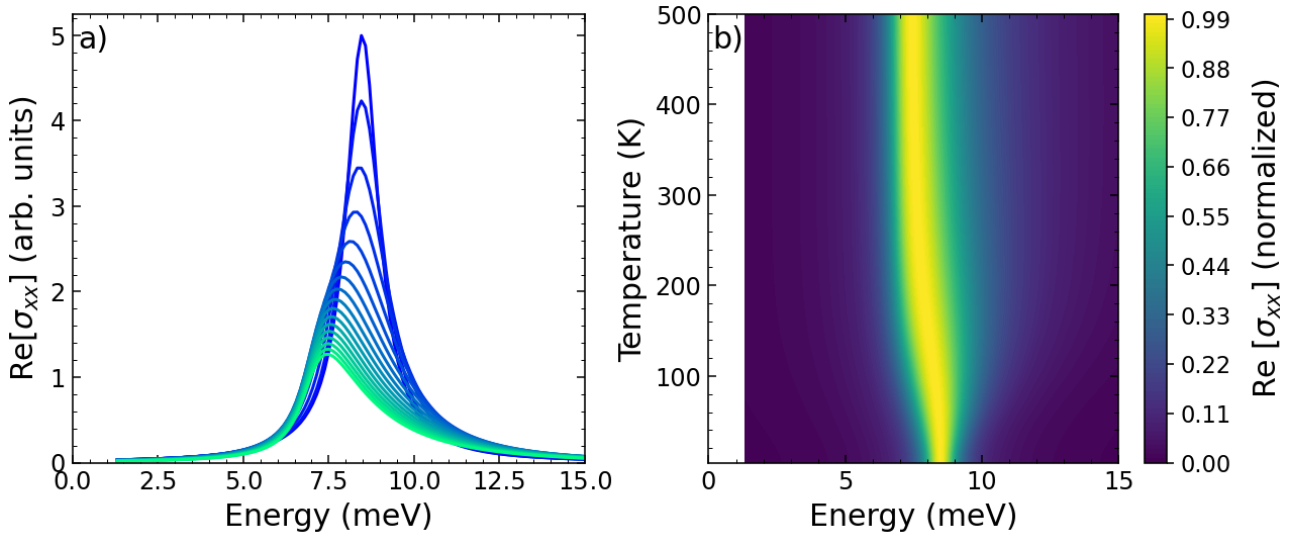

Figure 3.15: **Simulation of the influence of the electronic temperature on the optical conductivity.** (a) OC's spectra for different electronic temperatures, ranging from 4 to 500 K. (b) False-color mapping of the real-part of the OC with respect to the energy and when varying the electronic temperature at a fixed magnetic field of 1.5 T and zero electric field.

Finally, we can study the influence of an increase of the electronic temperature. Indeed, we saw in a previous section that one of the effects of the crossed electric and magnetic field was to populate empty high energy LLs, resulting in an electronic temperature increase, well above the crystal one. We can therefore use the previously derived model to study the influence of such an increase on the CR spectrum. The results for a magnetic field of 1.5 T and zero electric field are shown in Fig. 3.15. When increasing the electronic temperature from 4 to 500 K, we can see that the OC's energy maximum is red-shifting. This is better depicted in Fig. 3.15b where the normalized spectra are plotted as a false-color mapping where a shift of 1 meV is observed. We can also notice a broadening of the spectra as the temperature rises, along with the appearance of a slight disymmetry towards high energies. These findings can be interpreted by the fact that, when increasing the electronic temperature, the distribution function gets flattened. Therefore, higher indexes LLs get populated and since the system is highly non-parabolic, the spacing of these high energy LLs is reduce. This leads to a decrease of the resonance energy as well as an inhomogeneous broadening since more transitions with different energies are now involved.

We can study this red-shift and broadening effect for different magnetic field strengths. The results are summarized in Fig. 3.16, where the cyclotron mass and the full width at half maxima (FWHM) are plotted. It doesn't seem that the temperature rise is magnetic field dependent, as the three curves almost perfectly overlap, up to numerical precision. The mass witnesses a 13 % increase as the electronic temperature range from 4 to 500 K. On the other hand, the spectral broadening is magnetic field dependent. The three curves feature the same behavior as they increase until 200 K before saturating. The FWHM's increase ranges from 60 to almost 70 % when the field is changed from 1.5 to 2.5 T.

3.2.3 Landau emission experiments in a crossed-fields configuration

Armed with this knowledge, we will now study the influence of a strong electric field on the cyclotron emission, in crossed fields configurations. We performed Landau emission

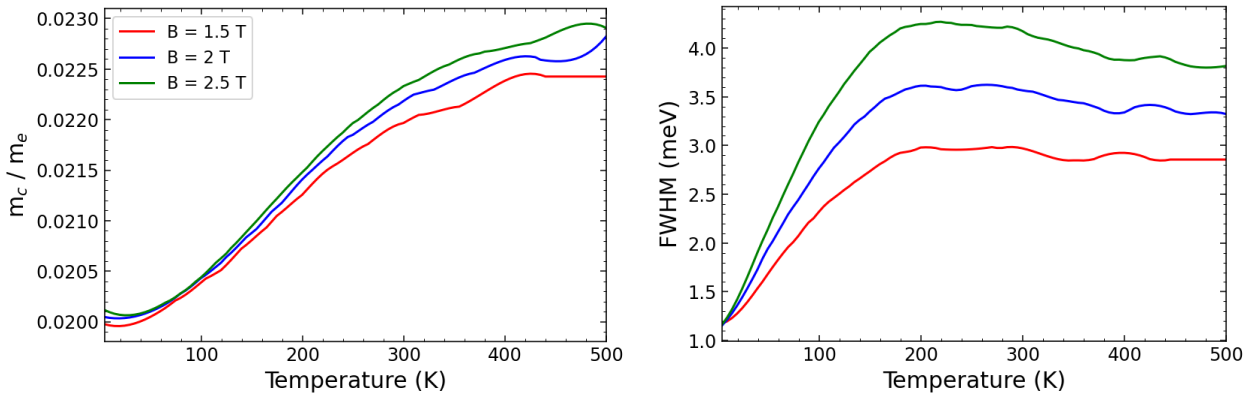

(a) (b)

Figure 3.16: **Evolution of the mass and FWHM with the electronic temperature.** Evolution of (a) the cyclotron mass, (b) the FWHM of the spectra, with the electronic temperature and for the three different magnetic field values.

experiments on HgTe QWs at different values of injection bias V_{pp}. Here we used the Box-car detection method because we want to apply high voltages on the sample. Therefore, if we want to avoid any damage, a solution is to decrease the pulse ratio (typically down to 0.5 %) and the Lock-in detection is no longer suited for this very short pulses detection.

Since the current is injected through Indium contacts, the current lines are not well controlled and therefore it is very difficult to accurately estimate the value of the electric field within the sample. We will thus refer to the bias rather than the electric field and we cannot expect our results to be quantitative with respect to the preceding subsection. Implementing a clean-room process to control the sample geometry (into a H-bar or Hall-bar for example) would be a valuable improvement for future work.

Low bias regime

Figure 3.17 shows an example of Landau emission spectra obtained at fixed magnetic field of 1.5 T and increasing injection bias (typically below 100 V peak-to-peak). The first noticeable feature is that the maximum amplitude of the spectrum increases with the bias, suggesting a corresponding increase of the emitted power increases. This is coherent with the conclusions of the simple statistic model developed earlier. Indeed, as the electric field is increased, the LLs become more tilted, leading to the occupation of higher levels and, consequently, to an increase of the total emitted power.

High bias regime

Beyond the increase in amplitude with the bias, Fig. 3.17 also reveals a slight red shift of the spectra's maximum. We increased the injection voltage to higher values to probe how significant this shift can become. We also performed the experiment at different magnetic field strengths to investigate any additional dependencies. It is summarized on Fig. 3.18 where we reached 150 V peak-to-peak for 1.5, 2 and 2.5 T.

We first note that the emitted amplitude continues to increase with the applied bias, even at larger values. Therefore, it seems that we never reach the saturation regime identified in the previous section, where all the LLs are equally populated.

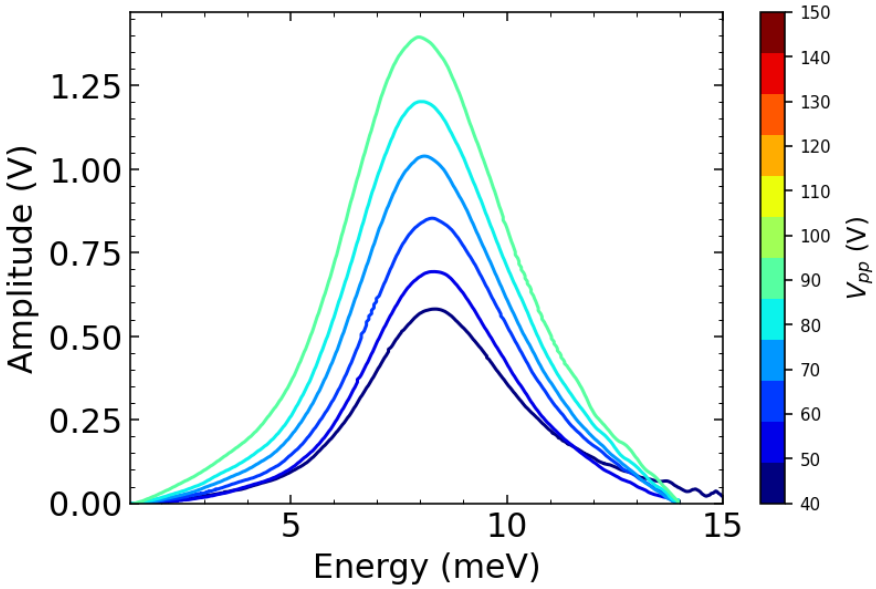

Figure 3.17: **Landau emission spectra at low bias.** Experimental spectra obtained in HgTe QW, for a magnetic field strength of 1.5 T and low increasing peak-to-peak excitation bias.

For high values of bias, in addition to the cyclotron emission peak, we start to see a shouldering whose position does not depend on the magnetic field strength. We associate this secondary emission to the black-body radiation. When a strong current flows through the sample, the Indium contacts and the material itself start to heat-up and therefore emit in the THz range according to the Planck's law [100]. We can estimate the position of the black-body radiation's maximum to be around 4 meV (see Fig. 3.18). Using the Wien displacement law, one can estimate the corresponding black-body temperature to be around 10 K, which seems plausible given the high values of bias applied.

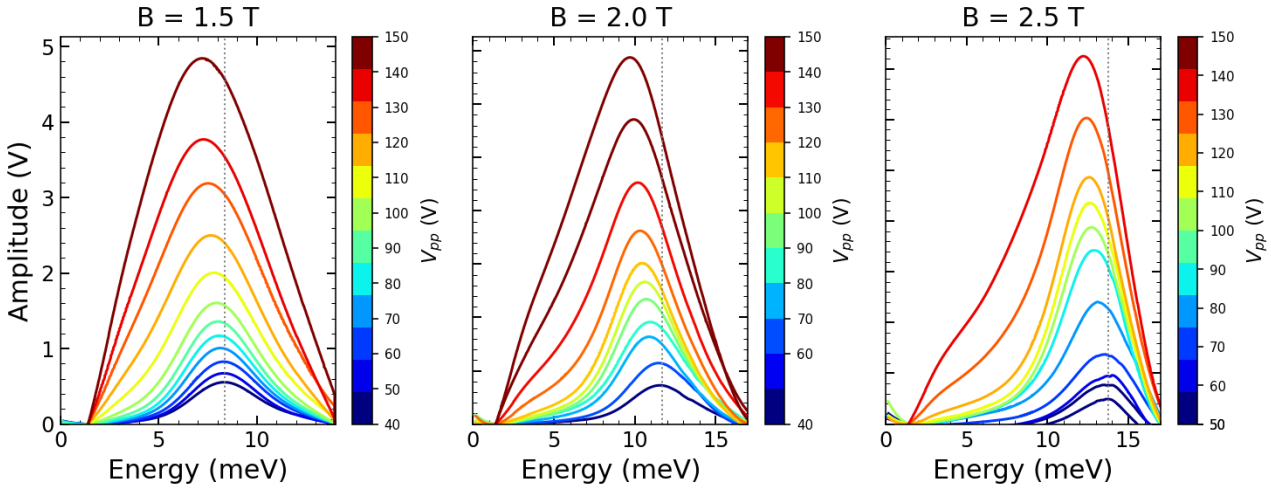

Figure 3.18: **Landau emission spectra at high bias.** Experimental spectra obtained in HgTe QW, for different magnetic field strength and high increasing peak-to-peak excitation bias. The grey dotted line is a guide for the eye pointing the low field energy position of the CR.

The most notable effect of the strong injection bias is the previously mentioned red shift, which becomes more pronounced for voltage exceeding 100 V peak-to-peak. Figure 3.19

displays the evolution of the emission maxima with respect to the applied bias, for the four different magnetic field values. The red-shift is rather weak at 1 T (around 1 meV) and increases with the magnetic field strength. In particular it reaches almost 2 meV at higher fields. We now discuss whether this shift can be attributed to a Lorentz-boost effect or a potential streaming effects described in the previous subsections.

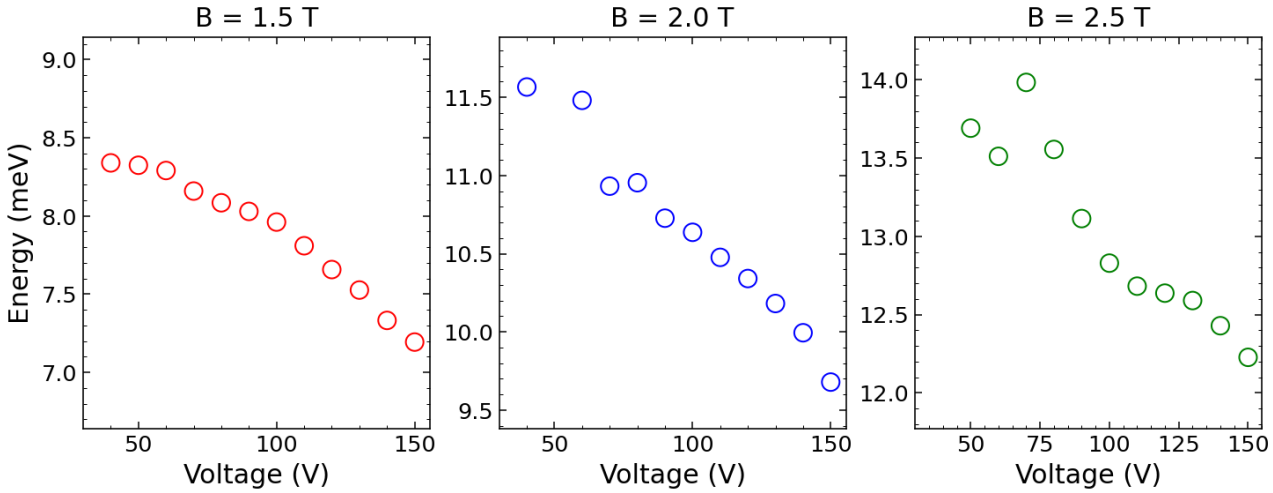

Figure 3.19: **Red-shift of the emitted energy with increasing electric field.** The emitted energy is extracted from Fig. 3.18 and plotted with respect to the peak-to-peak injection bias.

To investigate the influence of the crossed electric and magnetic fields, it is interesting to plot the cyclotron mass rather than the energy of the emission maximum. It is done on the left panel of Fig. 3.20a, where I used equation 1.22 to compute the mass. There is a clear increase of the cyclotron mass with the applied bias, of nearly 20 %.

This mass change could be due to an increase of the lattice temperature due to the high applied voltage. Indeed, it was shown that HgTe-based QWs undergo a topological phase transition with temperature, from an inverted to a conventional phase, leading to the closing of the gap for a critical temperature [101]. Therefore, the more the lattice temperature is increased, the closer the system gets from a purely linear band-structure and, for a fixed Fermi level position, the cyclotron mass should thus decrease. Since we observe a increase of the mass with the applied bias, we can then discard this explanation.

Additionally, this increase remains almost magnetic field independent. Since the Lorentz-boost effect depends on the drift velocity and thus on the magnetic field, the mass increase is expected to be bigger when decreasing magnetic field. However, this is not observed experimentally, as the mass increase with electric field remains the same for all magnetic field values. This finding rules out the Lorentz-boost effect as the origin of the red shift in the Landau emission observed under crossed-field conditions. We can try to estimate a favorable situation for the observation of this relativistic effect, based on the previously derived Zawadzki model. In order to avoid at best the influence of the black-body radiation, we should work at at relatively high magnetic field strength (2 T for example) to increase the magnetoresistance of the sample. We can then consider that we start to see a Lorentz-boost effect when δ is of the order of 0.25 (see discussion at the end of subsection 1.2.2). Therefore, the minimal electric field strength required in HgTe would be approximately 1.8 kV/cm. Regarding our device, the Indium contact can be placed at best at 1 mm from one another. If we assume that the electric field is homogeneous between the two probes, it would give

an electric field of 1.5 kV/cm for a 150 V bias applied.

It is clear with this very optimistic estimation that we currently do not apply a strong enough electric field to observe a Lorentz-boost in our sample. However, the implementation of very close electrical contacts could allow us to further increase the electric field strength and see this relativistic effect.

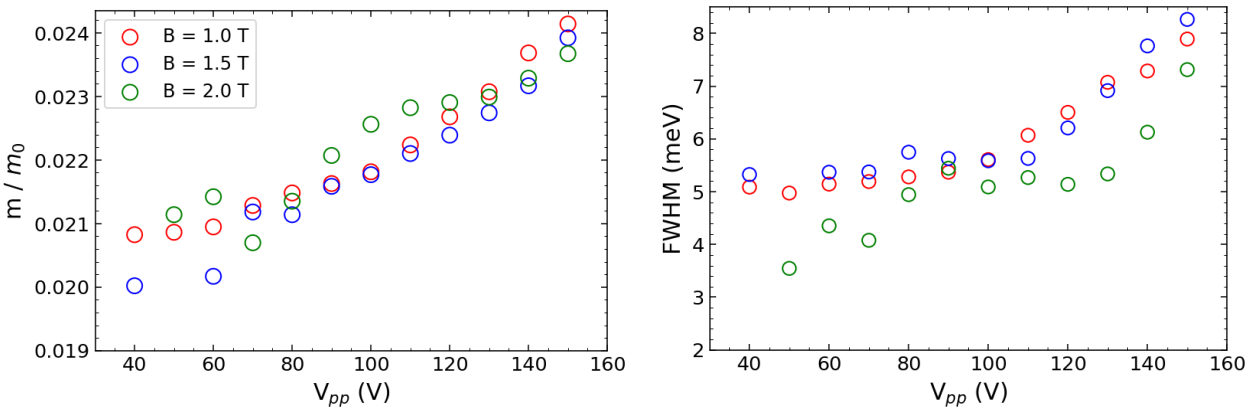

(a) (b)

Figure 3.20: **Evolution of the mass and FWHM with the applied bias.** Evolution of (a) the cyclotron mass, (b) the FWHM of the spectra, extracted from Fig. 3.19, with the applied voltage and for the three different magnetic field values.

Finally, although this relativistic phenomenon does not account for the observed red shift, the effect might still be interpreted within the framework of pseudo-special relativity. Indeed, we can understand this mass increase as follow. As discussed earlier, one effect of the electric field, fundamental to Landau emission, is to heat the carriers. As a consequence, the electrons populate higher index LLs. Since HgTe-based QWs feature a highly-non parabolic band-structure, its LLs fan-chart is therefore strongly non-equidistant. As the carriers are driven to higher energies, the spacing between the LLs they experience becomes progressively smaller, and thus the cyclotron mass increases. The experimental increase of the mass that we measured can therefore be seen as the manifestation of the non-equidistance of the LLs fan-chart of the material.

In addition of being red-shifted, the spectra are also broadened. The peaks are becoming asymmetrical, probably due, at least partially, to the additional black-body contribution, and it is therefore difficult to fit them with a Gaussian-like function. We can nonetheless estimate the width by taking the definition of the FWHM. The evolution of the spectra's FWHM with the injected bias is plotted on Fig. 3.20b. This broadening of the spectra at high bias could be due to an approaching streaming regime, as described in [44] and detailled below. However, as mentionned earlier, it could also be due to the black-body emission that artificially enlarge the spectra. Finally, it could be due to the heating of the carriers. Indeed, through the optical conductivity simulations, we saw previously that the spectra get broadened when increasing the electronic temperature. However, a saturation of the broadening was observed so it can not solely be attributed to this phenomenon. This evolution is still not yet well understood and under investigations.

The mass increase and the spectra's broadening put together, it strongly suggests that we observe the beginning of a streaming regime. Indeed, *Komiyama et al.* observed the same behavior in many crystals like p-Ge or AgBr [44] and they also interpreted this situation by

a flattening of the distribution function and thus a population of the high indexes LLs. In their study, when they increase the electric field further, they observe clear signatures of a streaming regime.

3.2.4 Summary and perspectives

In this section we presented two effects of the crossed fields configuration on the Landau emission. The first one results from the bending of the LLs by the electric field, which induces the filling of higher-index LLs. This leads to an increase of the emitted intensity, which we observed experimentally. In our case, this hot-carrier regime also revealed an increase of the cyclotron mass as it probes the non-equidistance of the HgTe QW Landau levels, which are quite peculiar.

The second effect occurs for high drift velocity values (strong electric field or low magnetic field). Similarly to the special relativity Lorentz-boost, the crossed fields strongly modify the LL dispersion, inducing a mass accumulation. However, we could not observe this effect experimentally. Indeed, if we want to avoid the emission to be enlarged by the blackbody radiation, we should work at relatively high magnetic fields (typically at least 1.5 T). Therefore, to reach a sufficiently high drift velocity we should apply strong electric fields.

We are thus currently limited by the contacting technique that we use which only allows the generation of few kV/cm. As discussed previously, a perspective would be to implement very close contacts or even intertwined grating contacts to apply stronger fields without heating the sample too much. Most importantly, this could also allow us to reach the streaming regime mentioned earlier, and eventually induce a population inversion and a lasing effect as demonstrated in p-Ge. At the end, we would obtain a compact and electrically tunable cyclotron source, capable of covering the whole THz technological gap.

Chapter 4

Electroluminescence from Landau polariton

Contents

In this chapter, as mentioned in the Introduction, we will explore another way to obtain stimulated emission without the need of a population inversion. The idea is based on the remarkable properties of the hybrid particles known as Landau polaritons, created by the strong interaction between the cyclotron resonance (CR) excitation of a 2DEG and an optical cavity mode. I will first describe how we induced THz cavity modes in the HgTe-based QWs. I will then present the magneto-reflectivity data confirming the presence of Landau polaritons in our structures. I will conclude with the electroluminescence of these polaritons and an estimate of how close our devices are to a lasing threshold.

4.1 Device presentation

4.1.1 Cavity fabrication

Our strategy for inducing a cavity effect is to use the substrate as a planar resonator, like in a Fabry-Perot vertical cavity. At frequencies around 1.5 THz, the substrate's thickness should be below $\frac{\lambda_{1.5THz}}{n}$ where n is the substrate's optical index, which gives a critical thickness of 55 μm for GaAs ($n \simeq 3.6$) and 62 μm for CdTe ($n \simeq 3.2$).

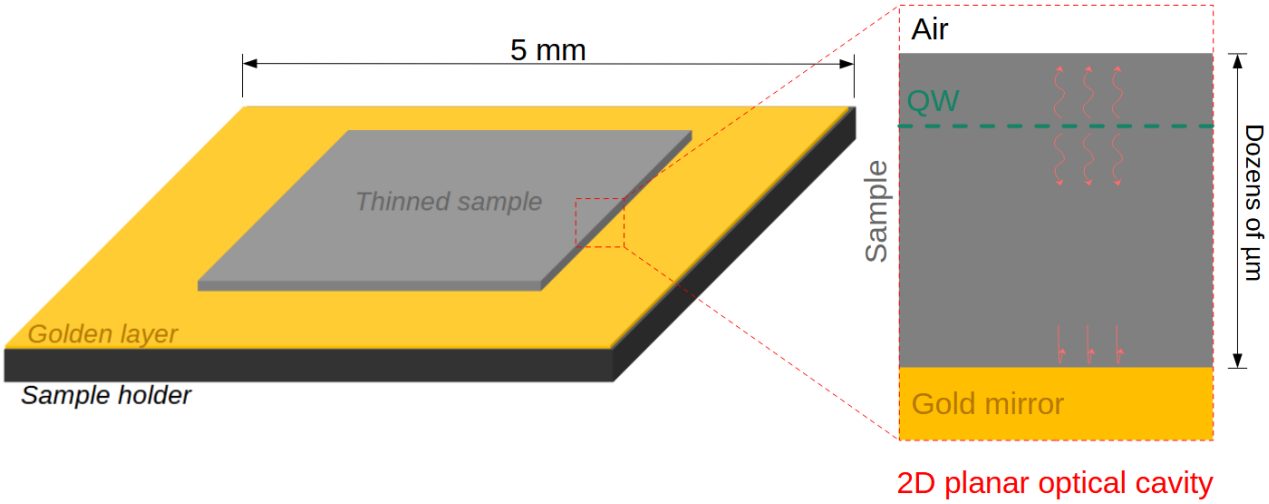

Figure 4.1: **Sketch of the cavity geometry at the end of the process.**
The mechanically and chemically thinned sample is glued on a golden sample-holder, forming a Fabry-Perot cavity.

The first step of the process is identical to the one used earlier in chapter 3. Mechanical thinning can produce substrate thicknesses close to 50 μm but below this, the sample becomes too fragile for standard mechanical polishing. To further reduce thickness we apply chemical/ plasma etching using an inductively coupled plasma reactive ion etcher (*Oxford* ICP-RIE machine located at the IES laboratory, Montpellier) with a $BCl_3/Cl_2/Ar$ gas mixture at about 2 mTorr total pressure. Under our conditions we remove roughly 500 nm of GaAs per minute. Combining mechanical and chemical etching allowed us to obtain GaAs substrates below 30 μm. A different approach was used to further thin the CdTe-based samples.

Sample name	Substrate	Final thickness	Thinning process
091222-50um	GaAs	50 μm	Mechanical thinning
091222-32um	GaAs	32 μm	Mechanical thinning + ICP-RIE ecthing
091222-28um-A	GaAs	28 μm	Mechanical thinning + ICP-RIE ecthing
091222-28um-B	GaAs	28 μm	Mechanical thinning + ICP-RIE ecthing
28104-80um	CdTe	80 μm	Mechanical thinning
28104-64um	CdTe	64 μm	Mechanical thinning
28104-40um	CdTe	40 μm	Micrometric rotary saw

Table 4.1: Table summarizing the different measured devices.

It was performed at the CEA-Leti laboratory in Grenoble, where a micro-metric rotary saw

was used to etch the substrate out of the sample. By this method, the substrate thickness was reduced down of about 40 μm.

The second step involves placing the thinned sample onto a gold substrate, which acts as a perfect backside mirror. The sample/air interface closes the cavity from the top, due to the refractive index mismatch. In the end, we obtain a vertical Fabry-Perot cavity as illustrated on Fig. 4.1.

4.1.2 Thickness homogeneity

It is important to assess the thickness homogeneity of the samples at the end of the process. Indeed, the position of the optical modes is highly dependent on the cavity size, therefore any inhomogeneities could lead to a spectral broadening. To achieve this, we performed optical profilometry measurements which provided access to the height profile of the samples.

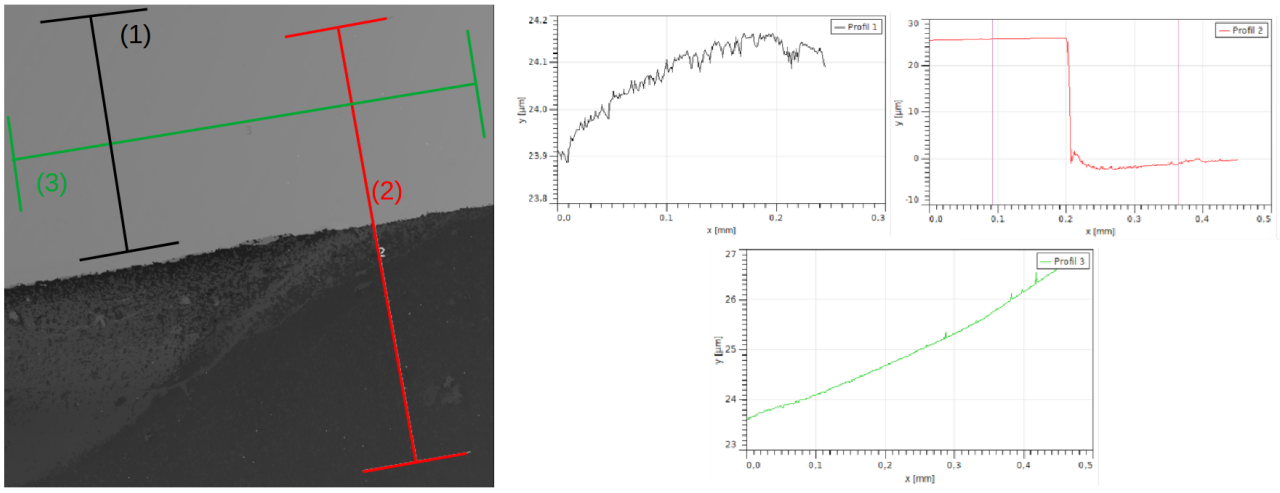

Figure 4.2: **Example of a profilometry characterization.**
The light grey surface is the top of the sample and the dark surface is the golden sample-holder. Three profiles were measured to have an idea of the thickness of sample 091222-28um-A (2) and of its inhomogeneities along the two directions (1 and 3).

Figure 4.2 shows an example of such a characterization on one of the thinnest samples we obtained (sample 091222-28um-A). We can see one extremity of the sample's surface (in light grey) on top of the golden sample-holder (dark area). Using the *Gwyddion* software, it is possible to measure height profiles from the image. This was done to estimate the total thickness of the device (profile 2, red) and it gives an average step of 28 μm. Thickness inhomogeneities can also be assessed by drawing profiles along the surface of the sample, in two directions (profiles 1 and 2, black and green). It shows that there is a rather large deviation from the mean thickness, which can reach several μm per millimeter. This thickness variation can be correlated with energy mode variations using the TMM method developed in chapter 2. Figure 4.3 shows an example of such a calculation, for a sample close to sample 091222-28um-A (ie a GaAs substrate on top of a gold layer). It reveals that a 2 μm change in the cavity size leads to a shift of 200 GHz (resp. 600 GHz) of the first (resp. second) optical mode's energy. For the simulations, I took a real refractive index of 3.6 for GaAs and the following frequency dependency for Gold [102]

$$n_{Gold}(\omega) = n_1(\omega) + i\, n_2(\omega), \tag{4.1}$$

where

$$n_1(\omega) = \frac{\sqrt{2}}{2}\frac{\omega_P}{\sqrt{\omega\omega_\tau}}\left(1 - \frac{\omega}{2\omega_\tau}\right) \quad \text{and} \quad n_2(\omega) = \frac{\sqrt{2}}{2}\frac{\omega_P}{\sqrt{\omega\omega_\tau}}\left(1 + \frac{\omega}{2\omega_\tau}\right), \tag{4.2}$$

with $\omega_P = 1.4 \times 10^{36}$ rad.s^{-1} and $\omega_\tau = 4.5 \times 10^{13}$ [102].

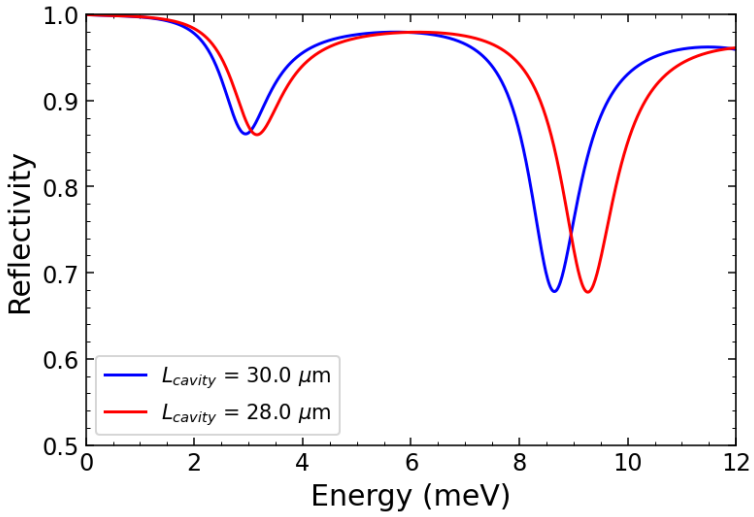

Figure 4.3: **Influence of the cavity's thickness.**
TMM calculations for a GaAs substrate, of width 30 μm (blue curve) and 28 μm (red curve), on top of a gold layer.

This large thickness inhomogeneity is due to the initial mechanical thinning which is performed manually. One way to improve this would be to rely exclusively on chemical etching, but this would require a very long etching time (close to a day). An acid-based etching process could be a possible solution to this issue.

4.1.3 Optical modes characterization

Time Domain Spectroscopy

A first approach to characterizing the optical response of the cavities is to use TDS in reflectivity mode (see chapter 2). The left panel of Fig. 4.4 shows two spectra obtained from two different cavities. They feature several absorption modes located in the 0.5 - 3 THz range. The minima are extracted and plotted with respect to an arbitrary index (see right panel of Fig. 4.4) along with a TMM computation. It shows an excellent agreement with the experimental data, confirming that the reduced thickness of the substrate indeed induces an optical cavity effect in the sample. Thanks to a Gaussian fitting, the width of the resonances could be estimated as 2κ = 1 meV.

Landau emission

Another way to highlight the presence of the cavity is to perform emission spectroscopy at zero magnetic field. Indeed, in these conditions, the only detectable light comes from the black-body radiation of the sample or its electrical contacts, both heated by the electrical pulses.

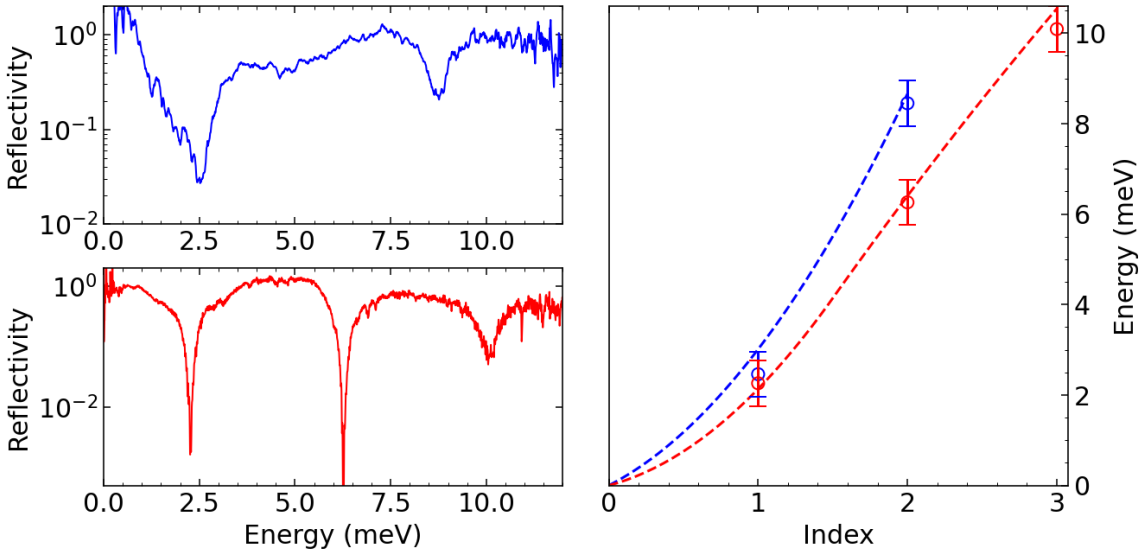

Figure 4.4: **TDS characterization of two cavities.**
(Left panel) TDS reflectivity spectra measured for two different cavities, one on sample 091222-28um-A (blue curve) and the other on sample 28104-40um (red curve). (Right panel) Transmission minima extracted and plotted against an arbitrary index (empty circles). A TMM-based prediction (dashed lines) is overlaid, showing excellent agreement with the experimental data.

Figure 4.5 displays three spectra obtained from thinned samples along with one from a bare sample for comparison (top panel). A mode structuration is visible on the processed samples (dashed lines), featuring additional maxima compared to the unprocessed sample. The grey dashed lines indicate the position of the modes that are visible only at finite magnetic field strengths. We can see that the Planck-shape spectrum is strongly modified by the presence of the cavity and becomes convoluted with the optical modes. This modification of the emitted spectrum compared to the ideal Planck curve has already been reported some years ago on sub-wavelength objects and is very well understood, opening a new field in the thermal radiation physics [103, 104].

When extracted, these emission maxima are once again in very good agreement with the predictions of the TMM model. Figure 4.6 demonstrates that the samples' thicknesses measured by profilometry are very close to those estimated with the model and the zero-field emission spectra. In particular, the right panel of Fig. 4.6 shows a perfect agreement with the red curve of Fig. 4.4 as they correspond to the same cavities. We can now confirm that reducing the substrate thickness enables the formation of an optical mode landscape in our samples. We will now see how it behaves when coupled to the cyclotron resonance of the 2DEG as the magnetic field is tuned.

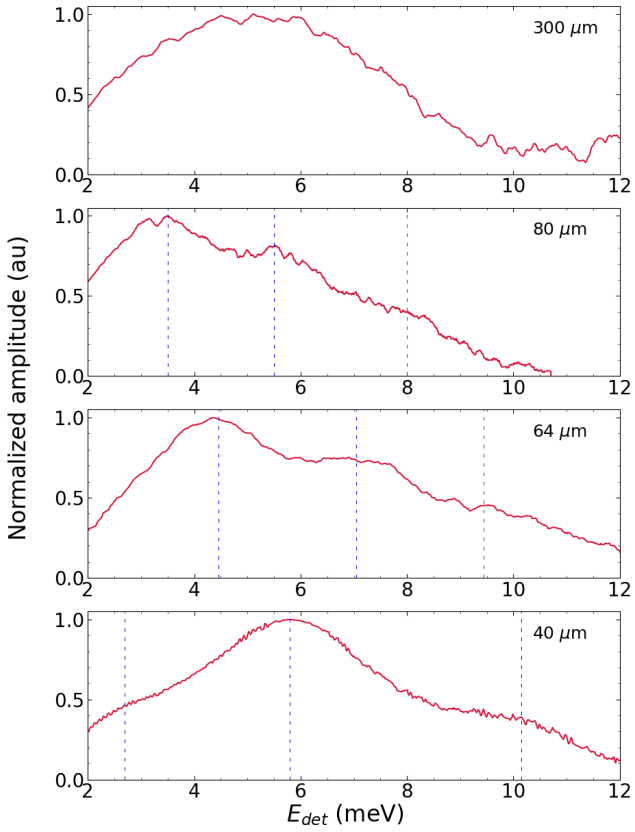

Figure 4.5: **Zero magnetic field emission spectra obtained on different cavities.** On the bare sample (300 μm), the spectrum exhibits no structuration. When the substrate thickness is reduced below 100 μm (sample 28104-80um, 28104-64um and 28104-40um), additional extrema (blue dashed lines) emerge, indicating a cavity effect. Notably, the 8 meV line in sample 28104-80um and the 9.5 meV line in sample 28104-64um (grey dashed lines) are barely visible at $B = 0$ T but become observable through cyclotron resonance at finite magnetic fields.

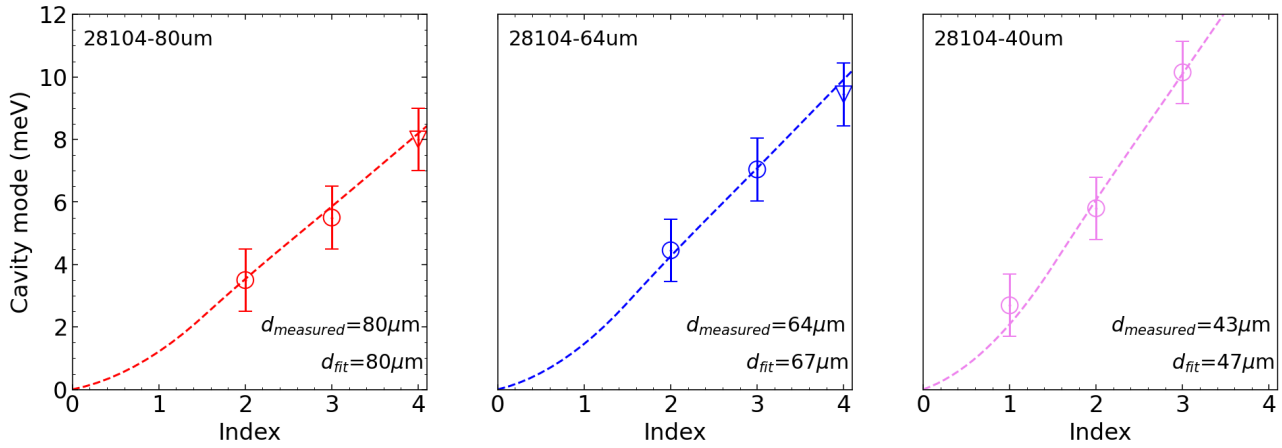

Figure 4.6: **Evolution of the cavity mode energies extracted from the zero field emission spectra.** Triangular markers correspond to data obtained at high magnetic fields. The energy values were deduced from the $B = 0$ T emission spectra. A TMM prediction (dashed lines) is overlaid, showing excellent agreement with the experimental data.

4.2 Evidence of the Landau-polaritons presence

To highlight the presence of Landau polaritons in our systems, we used the magneto-reflectivity spectroscopy technique. These experiments were performed at the Laboratoire National des Champs Magnétique Intenses in Grenoble (LNCMI-G), where I was hosted in Milan Orlita's group.

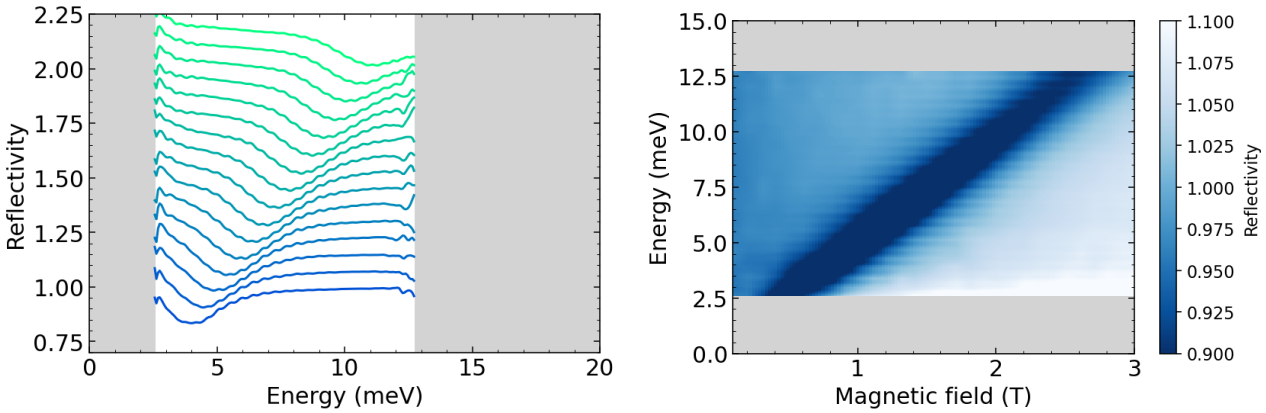

(a) (b)

Figure 4.7: **Magneto-spectroscopy experiment on a raw QW.**
(a) Waterfallplot of the different spectra obtained when tuning the magnetic field strength. (b) False-color map of the reflectivity signal with respect to energy and magnetic field. The light grey areas are energy ranges corresponding to the Reststrahlen bands of either the substrate or the beam-splitter, giving no signal at the end.

Before investigating the samples featuring a THz cavity, it is useful to recall how a bare CR appears in such an experiment. Figure 4.7a displays a waterfallplot of several spectra obtained by magneto-reflectivity and for different magnetic field strength. It shows a minimum of reflectivity blue-shifting when increasing the field. It is the same resonance previously observed in emission mode in chapter 3. Figure 4.7b shows the same results but in the form of a false-color map and exhibiting a clear linear behavior with magnetic field, characteristic of the cyclotron resonance. The width of the bare CR absorption could be estimated as $2\gamma = 2.9$ meV, thanks to a Gaussian fitting.

Figure 4.8 now presents the results obtained when performing magnetospectroscopy on samples processed to include a cavity effect. A clear difference with the raw sample mapping can be observed, as the straight CR line is no longer visible. We can see instead several diamond-like shapes centered around well defined energies. As discussed in the Introduction, this is one of the signatures of the presence of a Landau polariton. A closer look reveals that these diamonds are in fact anti-crossings, typical of interacting systems. We can notice that the energies at which the anti-crossings occur correspond exactly to those previously identified as the THz cavity modes (see Fig. 4.4 and Fig. 4.6 right panel).

It is better depicted on Fig. 4.9 where raw spectra are plotted for magnetic fields around the anticrossings of sample 091222-28-A. For each region, two absorption minima are visible. These minima are getting closer in energy as we approach the anticrossing (0.65 T for the lower mode and 2.2 T for the upper one) before going further away. The green and blue dashed lines truly emphasize the avoided crossing performed by the two modes. Taken together, these results strongly suggest that we have successfully induced light-matter cou-

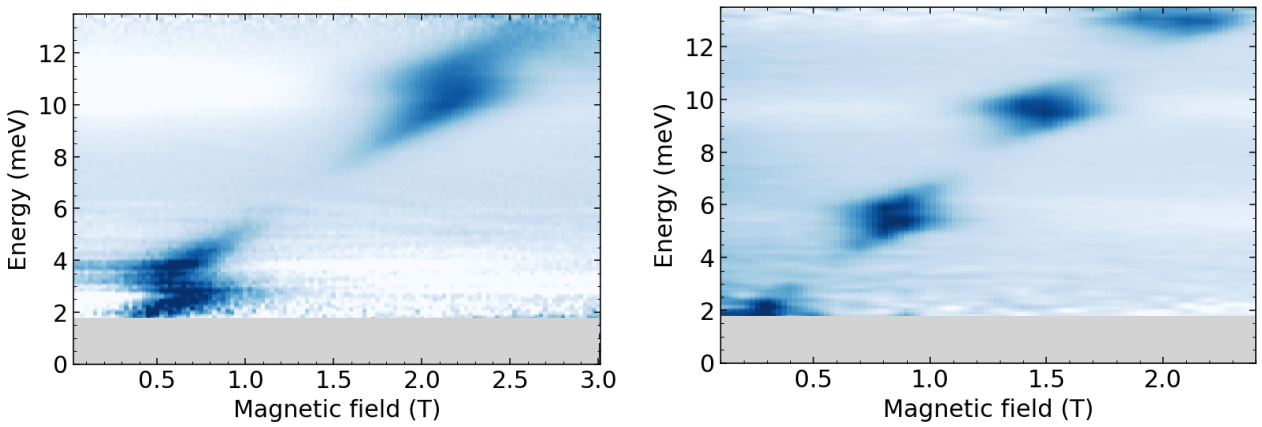

(a) (b)

Figure 4.8: **Magneto-spectroscopy experiment on QW with a cavity process.** False-colors map of the reflectivity spectra obtained when tuning the magnetic field strength for (a) sample 09122-28um-A and (b) sample 28104-40um.

pling in our QWs, leading to the formation of Landau-polaritons.

We can determine the coupling strength of the interaction by using the model developed in [57] and later adapted in [58]. It is based on the following total Hopfield Hamiltonian

$$H = H_{cavity} + H_{Landau} + H_{int} + H_{dia}\,, \tag{4.3}$$

where H_{cavity} is the bare Hamiltonian of the cavity, H_{Landau} describes the collective cyclotron excitation of the electrons occupying the Landau levels, H_{int} is the paramagnetic light-matter interaction, while H_{dia} is the diamagnetic contribution. This Hamiltonian can be exactly diagonalized using a Hopfield transformation and the polariton excitations can be obtained by finding the eigenvalues the following Hopfield-Bogoliubov matrix [57]

$$M_j(B,\chi_j) = \hbar \begin{pmatrix} \omega_c & \chi_j\sqrt{\omega_c} & 0 & \chi_j\sqrt{\omega_c} \\ \chi_j\sqrt{\omega_c} & \omega_j + 2\chi_j^2 & \chi_j\sqrt{\omega_c} & 2\chi_j^2 \\ 0 & -\chi_j\sqrt{\omega_c} & -\omega_c & -\chi_j\sqrt{\omega_c} \\ -\chi_j\sqrt{\omega_c} & -2\chi_j^2 & -\chi_j\sqrt{\omega_c} & -\omega_j - 2\chi_j^2 \end{pmatrix}, \tag{4.4}$$

where

$$\chi_j = \frac{\Omega_j}{\sqrt{\omega_c}} \tag{4.5}$$

is a fitting parameter, independent of the magnetic field, Ω_j being the collective polariton coupling (Rabi) frequency for the electromagnetic mode j. By diagonalizing this Hamiltonian, we can access the theoretical polaritonic branches, labelled $\omega_j^{UP}(B,\chi)$ (resp. $\omega_j^{LP}(B,\chi)$) for the upper branch (resp. lower branch). Therefore, we can extract the coupling strength by minimizing the following root mean square deviation (RMSD) quantity

$$RMSD_j(\chi) = \sqrt{\frac{\sum_{\chi}^{N_{exp}} \left[\left(\omega_{j,\eta}^{UP} - \omega_j^{UP}(B_\eta,\chi)\right)^2 + \left(\omega_{j,\eta}^{LP} - \omega_j^{LP}(B_\eta,\chi)\right)^2 \right]}{2N_{exp}}}, \tag{4.6}$$

where N_{exp} is the number of experimentally measured points.

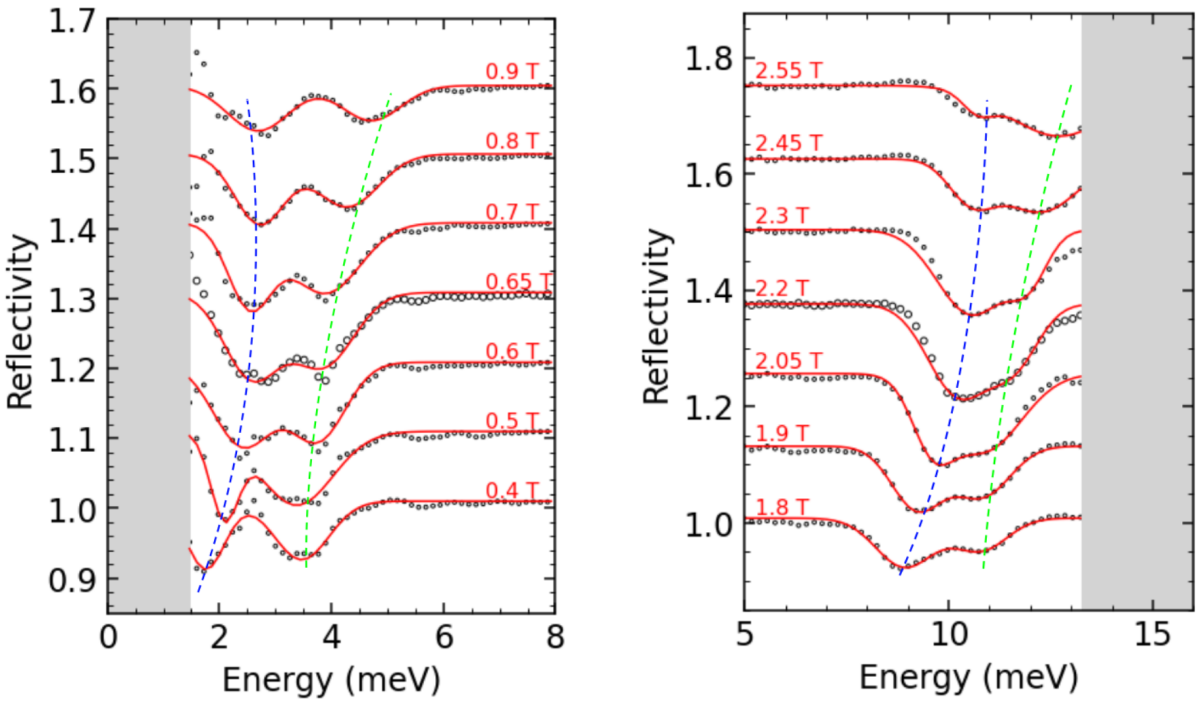

(a) (b)

Figure 4.9: **Highlighting of the anti-crossings of sample 091222-28um-A.** Waterfall plot of the magneto-reflectivity spectra obtained for different magnetic field strengths (empty black circles), around the (a) first and (b) second anti-crossing of sample 091222-28um-A. The red lines are double Gaussian fitting to highlight the positions of the lower and upper polaritons. The blue and green dashed lines are guide for the eye to emphasize the evolution of the anti-crossings.

Figure 4.10a shows an example of this minimization procedure, applied to sample 09122-28um-A. The minimum of each curve gives us the optimal χ parameter of each anti-crossing (see Fig. 4.10b for the correspondence) and thus the coupling strength. Figure 4.10b shows that the model provides an excellent fit to the reflectivity data, giving $\frac{\Omega_1}{\omega_1} = 0.21$ and $\frac{\Omega_2}{\omega_2} = 0.06$ with $g_1 = \frac{1}{2}\hbar\Omega_1 = 0.65$ meV and $g_2 = \frac{1}{2}\hbar\Omega_2 = 0.62$ meV for the first and second anti-crossings respectively. The fitting also allows us to confidently identify the polaritonic branches which we will refer to as UP1/LP1 and UP2/LP2.

At this point, we can assess several figures of merit of our system. The first one is the commonly used $\frac{2g}{\gamma - \kappa}$ quantity, where g is the coupling strength and γ and κ the width of the matter and cavity modes respectively, when there is no coupling. We can estimate this quantity for sample 091222-28um-A and we find $\frac{2g_1}{|\gamma - \kappa|} \simeq 1.44$ and $\frac{2g_1}{|\gamma - \kappa|} \simeq 1.38$. The fact that $2g > |\gamma - \kappa|$ means that light and matter exchange energy faster than any decay mechanisms, therefore profoundly modifying the system into what is called the strong coupling regime [105]. The other aspect of this regime is that for mode one, $\frac{\Omega_1}{\omega_1} = 0.21$, meaning that the Rabi splitting is a significant fraction of the cavity mode (typically greater than 10 %). This is the signature of ultra-strong coupling and a drastic change of the ground-state

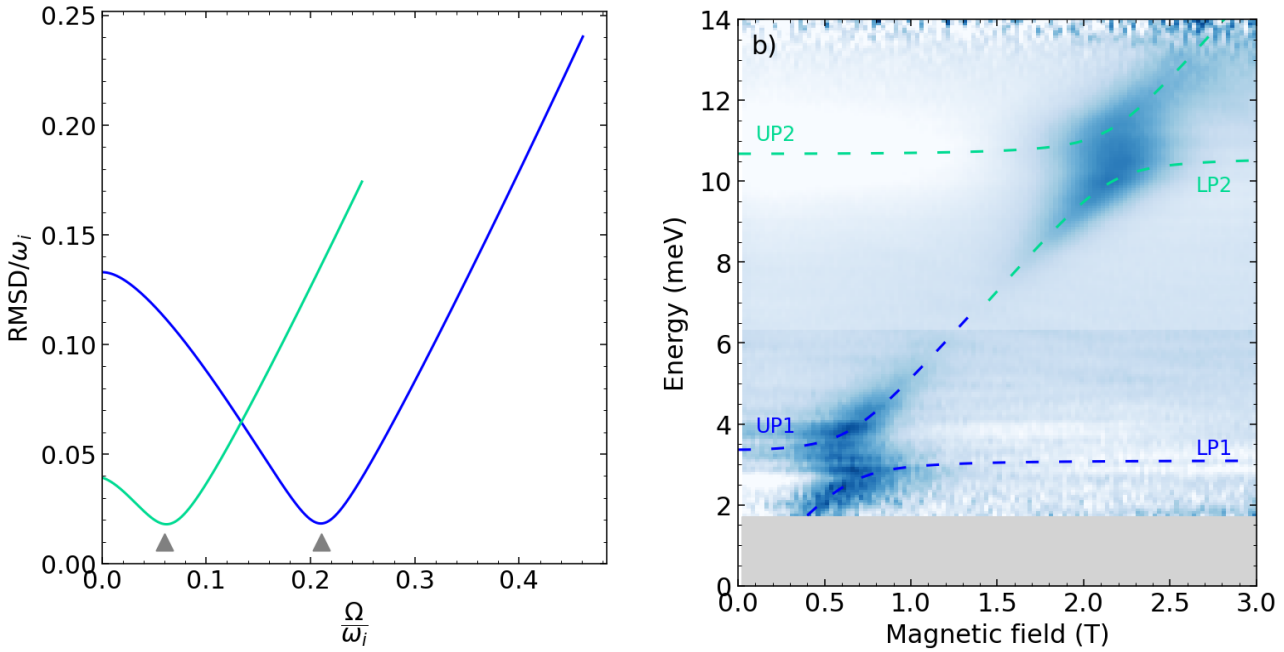

(a) (b)

Figure 4.10: **Example of fitting of the polaritonic branches.**
(a) Example of the minimization of the RMSD quantity (see main text) applied to sample 09122-28um-A. The blue (resp. green) curve corresponds to the lower (resp. higher) mode anti-crossing. (b) False-color map of the reflectivity obtained on the same cavity. The result of the fitting described in the text is superimposed and shows excellent agreement with the experimental data. The corresponding polaritonic branches are labeled in accordance.

properties is to be expected in this situation [57].

These magnetoreflectivity measurements have successfully confirmed the presence of Landau-polaritons in our QWs when processed inside a THz cavity. Let us now see if these structures can emit light when subjected to electric pulses.

4.3 Landau polariton electroluminescence

We performed Landau emission spectroscopy on the same two samples previously measured in magneto-reflectivity and for different cavity thicknesses. Figure 4.11 shows the results obtained, plotted as a waterfallplot for the different magnetic field strengths applied. A typical CR feature plotted again in the two left panels (bare samples) for comparison. As soon as the substrate thickness falls below a critical value (identified in a previous subsection) the magnetic dispersion of the emission peak starts to deviate from the CR classical evolution.

Indeed, one no longer observe a single peak blue-shifting as the magnetic field strength is increasing. Instead we now observe several discrete peaks that are almost not moving with magnetic field. The peaks slightly blue-shift on specific magnetic field ranges and finally merge with the one just above in energy. The positions of the discrete peaks is consistent with the one of optical modes identified with previous techniques, the thinner the cavity, the widely spaced the modes become, strongly suggesting the presence of anti-crossings.

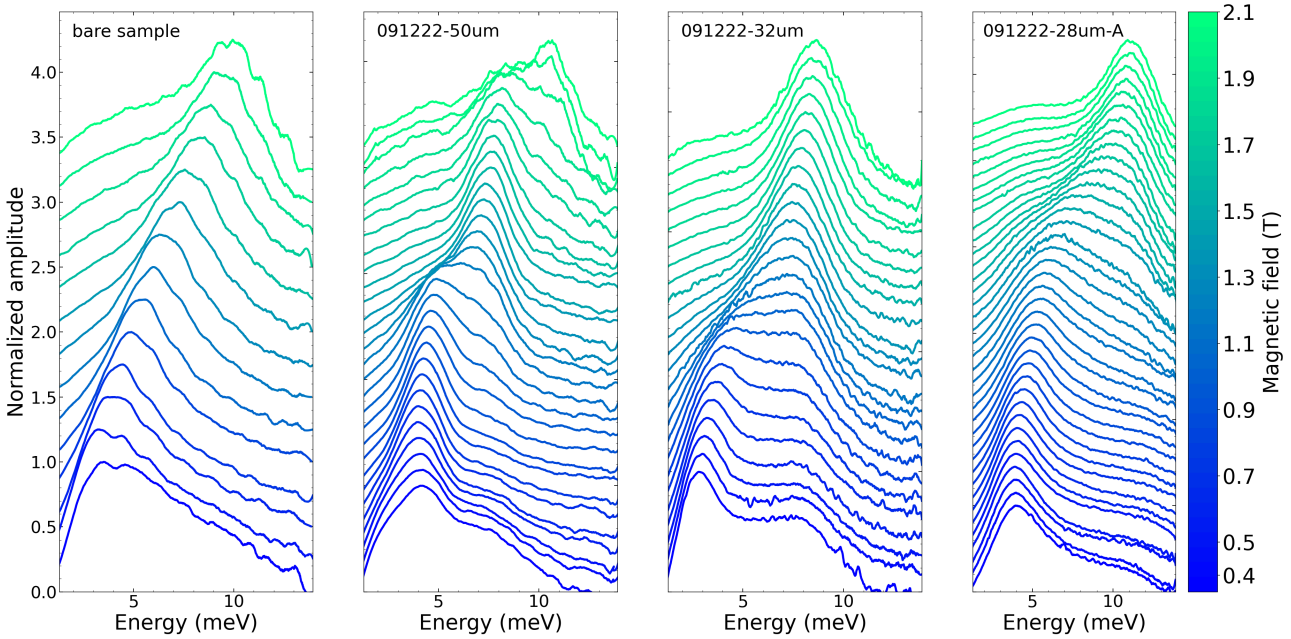

(a)

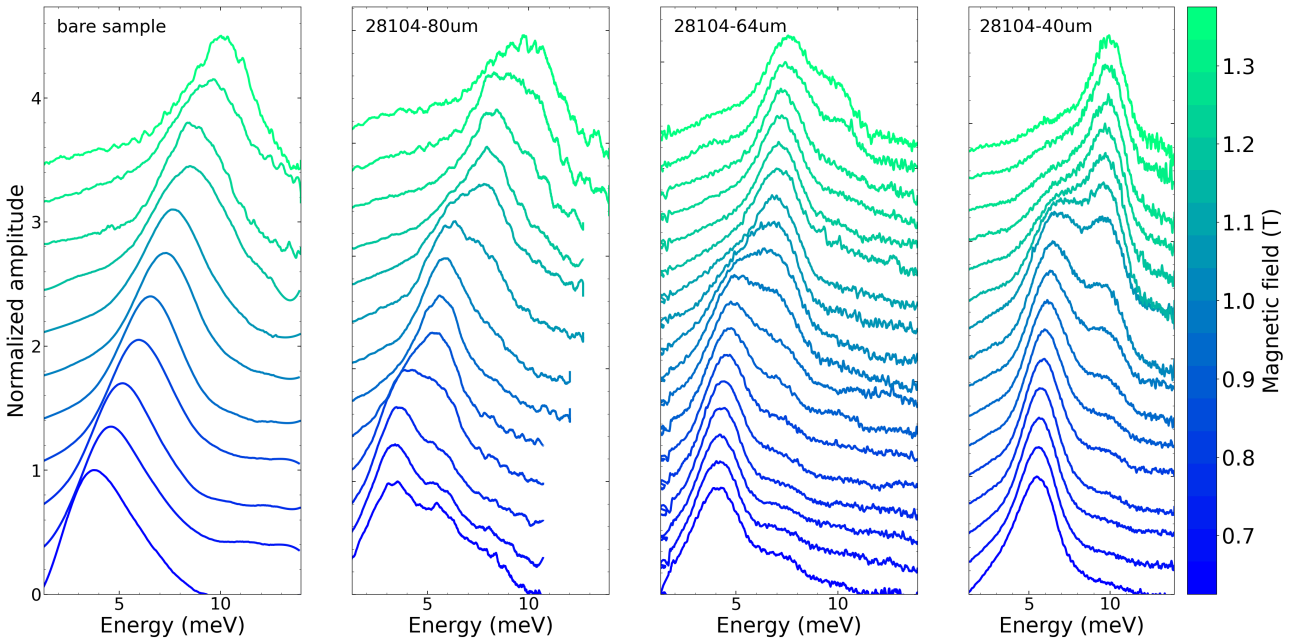

(b)

Figure 4.11: **Electroluminescence of Landau polaritons for different cavities.** Waterfallplot of Landau emission spectra obtained on different cavities and when tuning the magnetic strength for (a) 091222 and (b) 28104 growths. The two left plots are obtained for bare samples without cavity.

This is confirmed when extracting the emission maxima's positions. It was done for sample 09122-28um-A and 28104-40um, which exhibit the strongest shift. It is plotted on Fig. 4.12 along with the corresponding magneto-reflectivity mapping in the background for comparison. We can see that the emission data perfectly follow the previously identified upper branches. This provides clear confirmation of the electroluminescence of Landau polaritons in our structures.

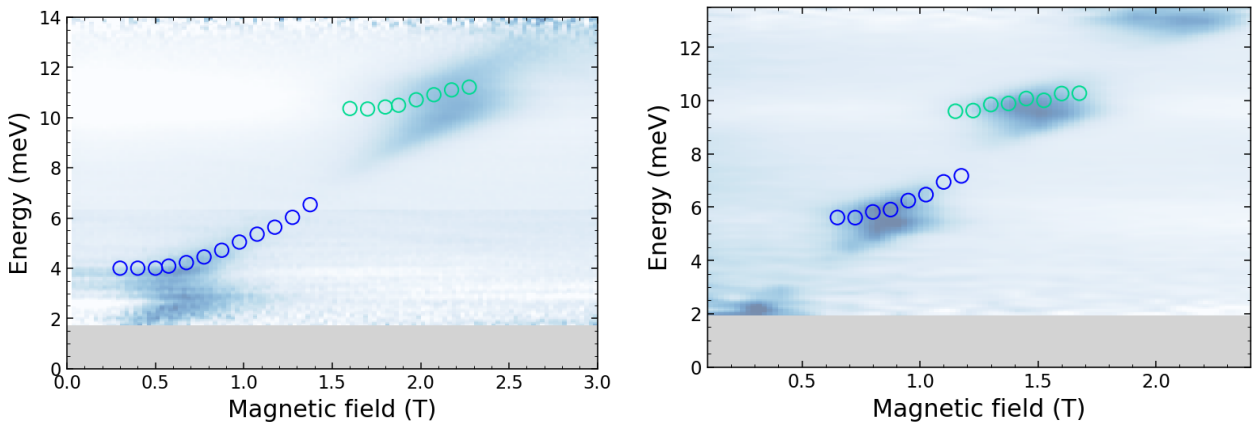

(a) (b)

Figure 4.12: **Electroluminescence and magneto-reflectivity comparison** Emission maxima's energy plotted with respect to the magnetic field for sample (a) 091223 thinned down to 28 μm and (b) 28104 thinned down to 40 μm. The corresponding false-color magneto-reflectivity map is plotting behind as a comparison.

Indeed, the higher polariton branch dominates in our emission spectra. This may result from a bottleneck effect that strongly inhibits the redistribution of polaritons from the upper to the lower branches [55]. Such a bottleneck arises from a complex interplay of relaxation mechanisms, including polariton-phonon, polariton-carrier, and polariton-polariton scattering, as well as intrinsic radiative and non-radiative losses. While near-infrared exciton-polaritons typically relax efficiently toward the lower branch, our Landau-quantized system exhibits the opposite trend, with electroluminescence predominantly emitted from the upper branches. A possible explanation lies in the combined influence of non-equidistant Landau levels and the non-equilibrium carrier distribution generated by electrical injection, as discussed in a previous chapter, especially carriers occupying high-energy states above the Fermi level. These electrons can absorb energy at lower scales due to the reduced spacing between Landau level. This effect may be further amplified by the presence of crossed electric and magnetic fields, which cause higher energy levels to shift downward more rapidly than lower ones. In addition, Coulomb interactions may enhance this process by enabling the conversion of polaritons into electron-hole excitations at similar energies through interactions with non-equilibrium carriers. A deeper understanding of these relaxation mechanisms calls for further experimental and theoretical investigation, both in this system and in other Dirac materials.

4.4 Estimation of the Landau population

From the magneto-reflectivity and electroluminescence results, we can have an estimation of the Landau polaritons population. This information is particularly valuable to have as it allows us to know whether or not we are close to a potential lasing threshold. Indeed, as discussed in the Introduction, polariton lasers are based on the accumulation of quasi-particles into one state thus generating a coherent emission. Therefore, the polariton population in this state should become macroscopic, thus serving as a reliable indicator of how far the system is from the lasing point.

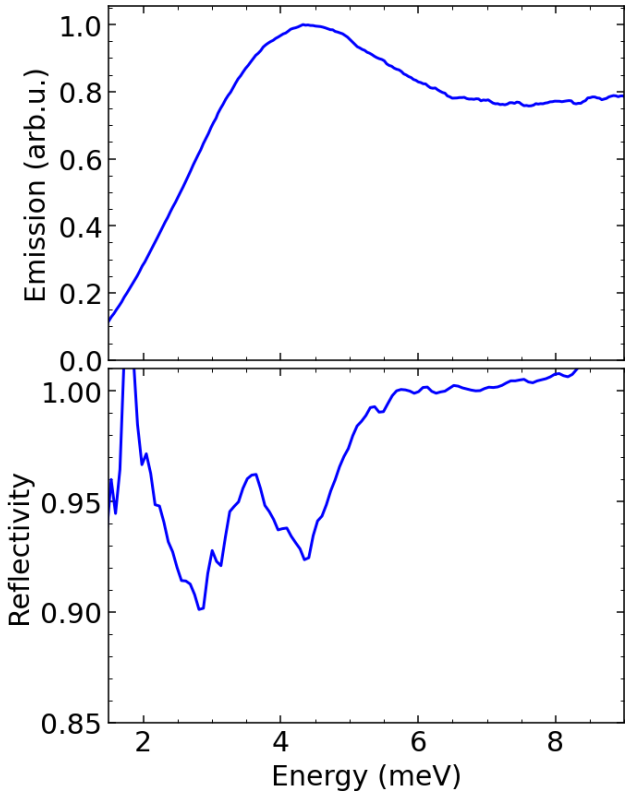

Figure 4.13: **Comparison of the raw reflectivity and emission spectra.**
(Top panel) Emission spectrum obtained on sample 091222-28um-A and a magnetic field value of 0.75 T, positioning it in the first anti-crossing. (Bottom panel) Corresponding magneto-reflectivity spectrum, displaying the two polaritonic resonances.

In this section we will therefore develop three methods that allow us to estimate the polariton population. This was made possible with the precious help of Pr. Cristiano Ciuti of MPQ laboratory in Paris. A first one will be derived considering that all available states are populated. Since it is a very unlikely scenario, it will provide a lower bound of the population. On the other hand, in the second method, we consider a single populated mode. This will thus give an upper bound for the population. Finally, in a third method based on the width of the emission spectra, we will derive a realistic estimation of the polariton population, coherent with the two first methods.

4.4.1 Lower bound estimation

Let us consider the cavity energy dispersion

$$E_{cav}(\mathbf{k}) = \frac{\hbar c}{n}\sqrt{k_z^2 + k^2}, \tag{4.7}$$

where c is the speed of light, n the refractive index of the substrate, z is the direction perpendicular to the 2D material. For small in-plane wave vectors, the cavity dispersion can be approximated as parabolic, namely

$$E_{cav}(\mathbf{k}) = \frac{\hbar c}{n}k_z\sqrt{1 + \frac{k^2}{k_z^2}} \simeq E_{cav}(0)\left(1 + \frac{1}{2}\frac{k^2}{k_z^2}\right). \tag{4.8}$$

The density of photonic states is

$$\begin{aligned}\mathcal{D}(E) &\simeq \frac{A}{(2\pi)^2}\int d^2k\,\delta(E-E_{cav}(\mathbf{k}))\\ &= \frac{A}{2\pi}\int kdk\,\delta(E-E_{cav}(\mathbf{k}))\,,\end{aligned} \tag{4.9}$$

where A is the area of sample where there is emission. Since $dE_{cav} = E_{cav}(0)\frac{kdk}{k_z^2}$, then $kdk = \frac{k_z^2}{E_{cav}(0)}dE_{cav}$ and therefore

$$\mathcal{D}(E) \simeq \frac{A}{2\pi}\frac{k_z^2}{E_{cav}(0)}. \tag{4.10}$$

The polariton density of states is comparable to the photonic density of states, which will be used for our estimate of the number of polariton modes involved in the emission process

$$\mathcal{N}_{mode} \simeq \mathcal{D}(E)\,\Delta E_{emission} = \frac{A}{2\pi}k_z^2\frac{\Delta E_{emission}}{E_{cav}(0)}, \tag{4.11}$$

where $\Delta E_{emission}$ is the emission linewidth. Given the experimental nominal parameters, we can take $A \simeq 1\,mm^2$, $k_z = \frac{\pi}{L_{cav}} = \frac{\pi}{30\mu m} = 10^5\,m^{-1}$ and $\Delta E_{emission} = 3\,\text{meV}$ we have $E_{cav}(0) \simeq 3\,\text{meV}$ we get $\mathcal{N}_{mode} \simeq 1500$. Finally, we can estimate the number of polariton via the emitted power

$$\mathcal{P}^{emission} \simeq N_{pol}\,\gamma_{rad}^{avg}\,\hbar\omega_{pola}^{avg}, \tag{4.12}$$

where N_{pol} is the number of polaritons in the steady state, γ_{rad}^{avg} the average radiative rate and $\hbar\omega_{pola}^{avg}$ the average photon emission energy. By injecting the experimental values $\mathcal{P}^{emission} \simeq 10$ nW, $\hbar\omega_{pola}^{avg} \simeq 3\,\text{meV}$ and $\gamma_{rad}^{avg} \simeq \frac{\Delta E_{emission}}{h} = \frac{3\,\text{meV}}{h} \simeq 0.7\,ps^{-1}$ we get: $N_{pol} \simeq 30$. Finally, we get the lower bound:

$$\frac{N_{pol}}{\mathcal{N}_{mode}} > 2\cdot 10^{-2}. \tag{4.13}$$

4.4.2 Upper bound estimation

The upper bound for the polariton occupation number is obtained by assuming that all the polaritons are occupying the same polariton mode. This is certainly not the case, but together with the lower bound calculated above, it will allow us to have a decent estimate of the polariton occupation numbers. Assuming that only one mode participates in the emission, we can assess the polariton population from the non-linear dependence of the emission amplitude with respect to the injected electrical power. This can be calculated via the simple rate equation

$$\frac{dN_{pol}}{dt} \simeq -\gamma N_{pol} + \eta P_{elec}(1+N_{pol}), \tag{4.14}$$

where γ is the polariton loss rate and η is unknown. The steady-state solution reads

$$N_{pol} = \frac{\eta P_{elec}}{\gamma - \eta P_{elec}}. \tag{4.15}$$

From this equation we can see that for $P_{elec} \to P_{elec}^{(thresholds)} = \frac{\gamma}{\eta}$ then $N_{pol} \to +\infty$. Below threshold, we can Taylor-expand the previous solution as follows

$$N_{pol} = \frac{\eta P_{elec}}{\gamma} \frac{1}{1 - \frac{\eta P_{elec}}{\gamma}} \simeq \frac{\eta P_{elec}}{\gamma}(1 + \frac{\eta P_{elec}}{\gamma}) \simeq \frac{\eta P_{elec}}{\gamma} + \left(\frac{\eta P_{elec}}{\gamma}\right)^2. \tag{4.16}$$

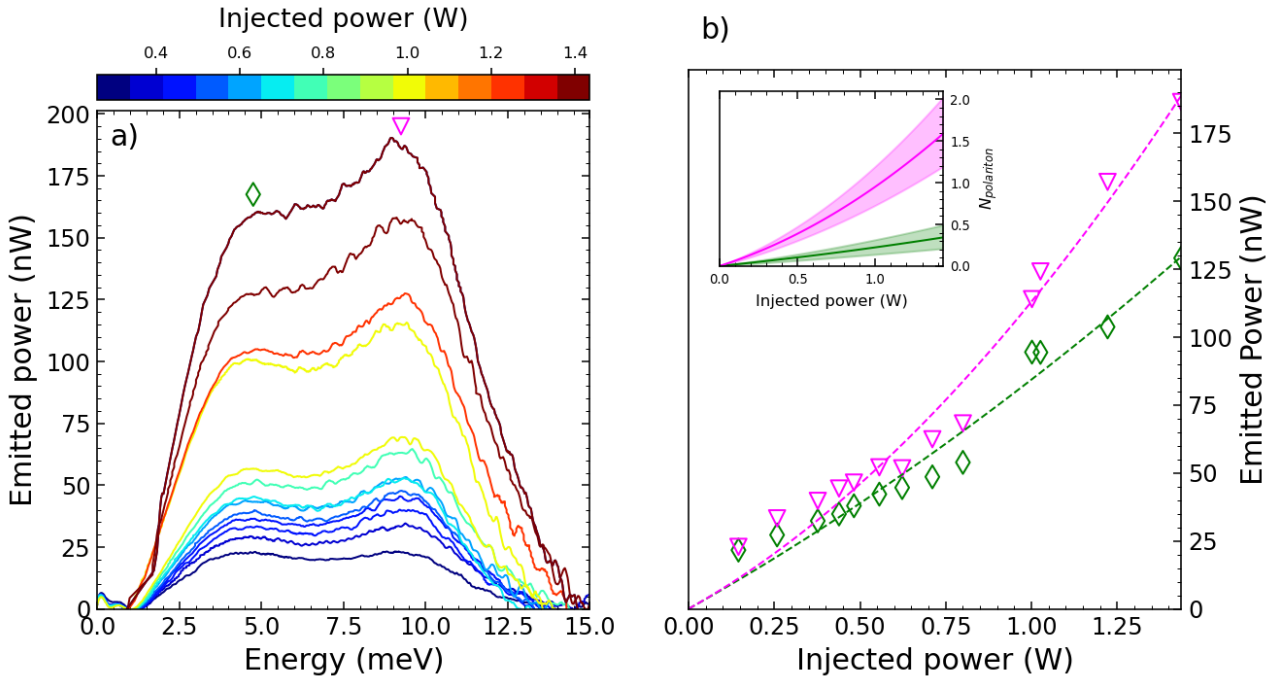

Figure 4.14: **Evolution of the emitted power with the injection power for sample 091222-28um-B.**
(a) Plot of several emission spectra, obtained for a fixed value of magnetic field of 0.9 T, when increasing the injected electrical power from 0.15 to 1.45 W (corresponding to electric fields ranging from 300 to 1000 V/cm). (b) Evolution of the emitted power with the injected electrical power, for the two polaritonic branches identified on panel (a) with the marker styles and colors. The dashed lines are quadratic fittings used to compute the corresponding polariton population (shown in insert) according to the model derived in the main text.

Therefore, we now have the dependence of the emission power on the electrical power, namely

$$P^{emission} \simeq N_{pol}\, \gamma_{rad}^{avg}\, \hbar\omega_{pola}^{avg} \simeq \gamma_{rad}^{avg}\, \hbar\omega_{pola}^{avg} \left[\frac{\eta P_{elec}}{\gamma} + \left(\frac{\eta P_{elec}}{\gamma}\right)^2\right] = a_1 P_{elec} + a_2 P_{elec}^2, \tag{4.17}$$

where $a_2/a_1 = \gamma/\eta$. We can therefore have access to the polariton population by fitting the curve corresponding to the measured emitted power versus the electrical injected power, as shown in Fig. 4.14 for sample 091222-28um-B. For the considered sample, the polariton population would reach more than one for an electrical injected power of 1.5 W (obtained for an electric field of 1 kV/cm).

From the two scenarios developed above, we can conclude that the polariton occupation from the most populated mode in our system is bound as follows:

$$2 \cdot 10^{-2} \leq \frac{N_{pol}}{\mathcal{N}_{mode}} \leq 1. \tag{4.18}$$

4.4.3 Realistic estimation via the losses

Another approach to estimating the polariton population is to study the evolution of the emission peak spectral linewidth (full width at half maximum, FWHM) as the electrical injection bias increases. Figure 4.15b shows that the UP2 emission peak spectrally narrows when increasing the electrical power P and reaches a minimum around 0.5 W. Increasing P further, the linewidth increases and for power exceeding 0.8 W, there is net broadening with respect to the low-power regime. This could be attributed to non-linear polariton losses caused by scattering processes [106], where a polariton is converted into an excitation of carriers in higher-energy Landau levels. We can model in a general way the power-dependent emission linewidth with the following formula

$$\Gamma(P) = \frac{\Gamma(0)}{1 + N_{pol}(P)} + \Gamma_{NL}(P), \tag{4.19}$$

where $N_{pol}(P)$ is the polariton occupation number and $\Gamma_{NL}(P)$ is a power-induced additional broadening. This formula includes both Schawlow-Townes narrowing produced by stimulated scattering due to the polariton final-state population [107] and nonlinear losses. At the lowest order in the power, $N_{pol}(P) \simeq \mathcal{N}P$ and $\Gamma_{NL}(P) \simeq \eta P$, since both quantities vanish for $P \to 0$. With this formula we achieve an excellent fit of the experimental linewidth versus power, as shown in Fig. 4.15b with the fitting parameters $\Gamma(0) = 5.65$ meV, $\mathcal{N} = 2.0$ W^{-1} and $\eta = 3.1$ meV/W. For a power $P = 0.5$ W, the estimated polariton occupation number is 1, which is consistent with the previous discussed bounds.

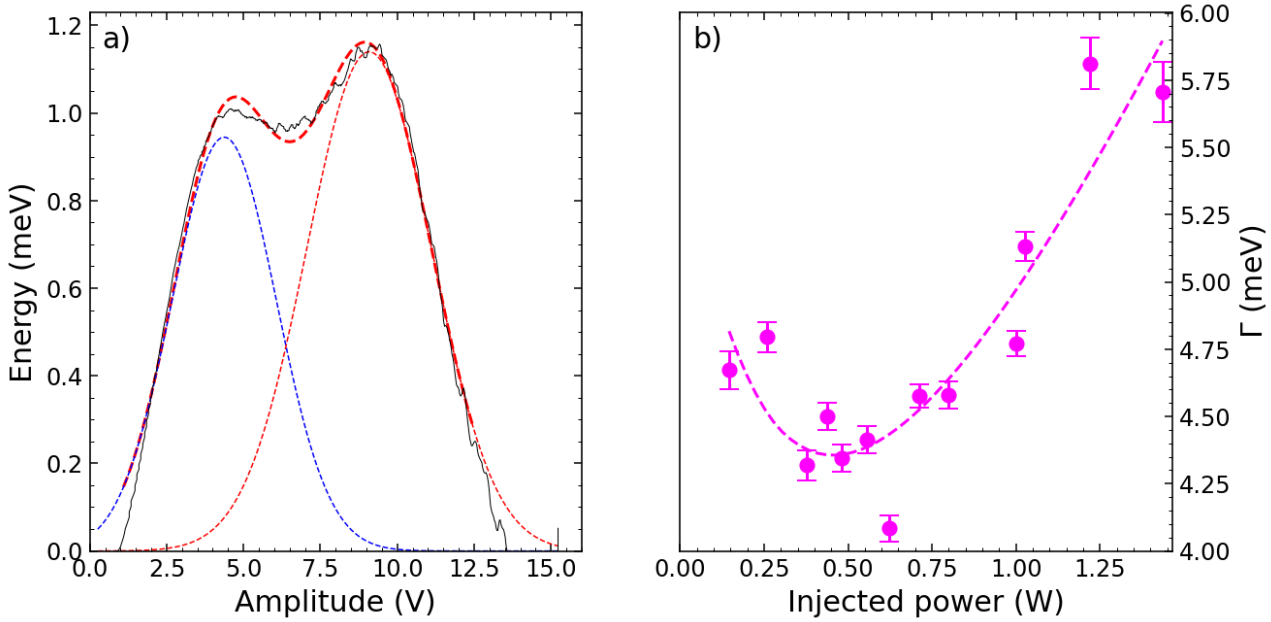

Figure 4.15: **Evolution of the FWHM with the injection bias.**
(a) Example of double-Gaussian fitting used to extract the emitted amplitude and FWHM. (b) Evolution of the FWHM of the UP2 branch when increasing the injection bias (pink markers). The pink dashed line is a fit using the loss-inclusion model described in the main text and showing great accordance with the experimental data.

4.4.4 Discussion

One point needs to be addressed carefully. Indeed, the last subsections demonstrated that the system is close to a lasing thresholds. In particular, it seems that the higher energy peak UP2 is the most likely to reach this state. However, all the experiments were conducted at 0.9 T, which favors the low energy anticrossing. In practice, because sample 091222-28um-B has a lower carrier density, it exhibits a smaller cyclotron mass and therefore a steeper cyclotron slope. Consequently, the anticrossing between the CR and the second cavity mode occurs at lower magnetic fields in sample 091222-28um-B than in sample 091222-28um-A. In other words, at 0.9 T we are closer to this second anticrossing in sample 091222-28um-B than in sample 091222-28um-A, although, still not exactly within the theoretical anticrossing region. Nevertheless, since the CR is intrinsically broad in emission in the absence of the cavity (see Fig. 4.16b and c), the second mode is already activated at lower magnetic fields. This behavior is also evident in Fig. 4.16a, which presents a waterfall plot of spectra at different magnetic fields; in particular, at 0.9 T, the peak associated with the second mode becomes visible. Thus, the signal observed on this mode does not arise from thermal emission but originates from the broadened cyclotron resonance coupled to the cavity mode. We therefore emphasize that our interpretation in terms of nonlinear electroluminescence from Landau polaritons remains valid for the UP2 mode, even if the emission does not occur exactly at the theoretical anticrossing position.

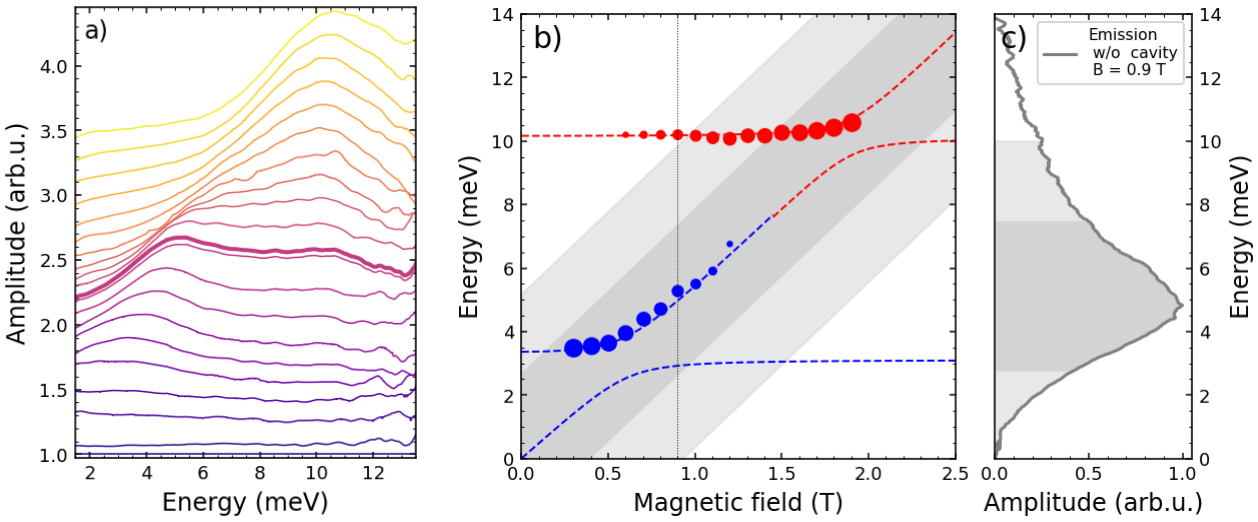

Figure 4.16: **Evolution of the FWHM with the injection bias.**
(a) Waterfall plot of raw emission spectra from sample B with increasing magnetic field (0 - 1.9 T). At 0.9 T (bold curve), two peaks are visible, corresponding to the first and second cavity modes. (b) Extracted emission maxima (solid circles) corresponding to the two UP branches of panel (a). The circle size reflects the amplitude of the corresponding emission spectrum. Fits based on the Hopfield model are also shown (dashed lines). The black dotted vertical line marks the point B = 0.9 T. The dark gray (resp. light gray) shaded regions denote the energy ranges over which the bare CR extends, corresponding to the FWHM (resp. twice the FWHM) of the curve in panel (c). (c) Bare CR emission obtained without the cavity at a magnetic field of 0.9 T.

4.5 A way to make it better: improving the quality factor

We just demonstrated that our system is close to a potential polariton-lasing threshold. Our devices were made using a basic, homemade process that could largely be improved. We will now discuss the main leverage of improvement and the technological solutions that we could implement as perspectives for future studies.

The lower polariton population estimation, based on a pessimistic situation where every mode is occupied, gives an interesting result in terms of how does the population behaves. Indeed, combining equations 4.11 and 4.12, we can deduce that

$$N_{pol/state} \propto \frac{1}{\Delta E_{em}^2}, \tag{4.20}$$

where ΔE_{em} is the emission linewidth. This formula indicates that the narrower the emitted spectrum, the higher the polariton population. Therefore, it may be possible to reach the lasing threshold before non-linear losses become too important (like in Fig. 4.15b).

4.5.1 Overcoming the thickness inhomogeneities

Currently, the quality factor of our cavities can be estimated around 3 with a linewidth of about 1 meV in reflectivity mode (see Fig. 4.13). As a comparison, the linewidth is 4 or 5 times larger in emission mode (see Fig. 4.15b). This is primarily attributed to the involvement of additional inter-level transitions in the emission process compared to the reflectivity one, due to the hot-carrier distribution and the Stark effect on ionized impurities. However, in systems with optical cavities, these are not the only contributing factors. As discussed in a previous section, the thickness inhomogeneities of the cavities are critical here. The typical magneto-optic spot-size is around 500 μm whereas the emitted area, determined by the size of the contacts, is at least on the order of mm^2. Moreover, the emitted radiation will spread over the whole sample through multiple reflections in the cavity. Therefore the emission process is way more sensitive to the thickness inhomogeneities of the sample, resulting in a larger inhomogeneous broadening than in optical spectroscopy.

A way to reduce these thickness variations would be to get rid of the mechanical thinning step. Since it is done manually, it is a large source of inhomogeneities that propagates through the rest of the process. A first option would be to thin the substrate exclusively using plasma etching, but this would require a very long processing time, imposing multiple runs to maintain consistent machine conditions for reproducibility. Another option would be to use chemical etching. It was demonstrated in several papers [108, 109] that a H_2O_2/NH_4OH based solution is very efficient at etching GaAs substrates, in a much faster way than with a plasma. These two options would eliminate the need for manual etching, thus drastically reducing thickness inhomogeneities.

4.5.2 Upgrading the cavity

Another approach to increasing the cavity's quality factor is to reduce the photonic losses. They could come from absorption processes in the substrate or light diffusion from impurities or due to the surface roughness. However, a dominant source of losses could be that too many photons are escaping the device without interacting with the cavity. Indeed, in our system, the optical cavity consists of a first gold mirror at the back of the sample but it lacks a true second mirror to complete the cavity. The top part of the cavity is made of the high

refractive index gradient at the sample (n $\simeq$ 3.6) / air (n $\simeq$ 1) interface. A simple calculation based on the Fresnel coefficient gives us

$$T = 1 - \left(\frac{n_{GaAs} - n_{air}}{n_{GaAs} + n_{air}}\right)^2 \simeq 0.7, \tag{4.21}$$

meaning that almost 70% of the light escapes the cavity after a single round trip. Therefore this intrinsically leads to a poor quality factor. A simple yet effective modification to

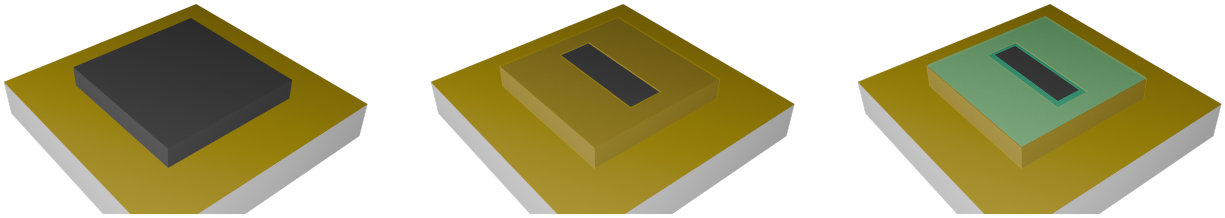

(a) (b) (c)

Figure 4.17: **Sketch of the enhanced cavity process.** (a) The thinned sample is glued on the golden sample holder via the SU8 resin technique. (b) A photolithography is then performed on the sample to delimit the area to open. The gold is then deposited and lifted off the surface of the sample. (c) A layer of oxide is deposited on the device to isolate the sample. Another photolitography is then made to delimit the area to etch in order to open the central rectangle.

improve this cavity design would be to close the cavity with a gold layer on the top and around the sample. The process that we implemented is illustrated in Fig. 4.17. The first step is to perform a photolithography on the sample to define the shape of a gold-free area on the surface. Indeed, since the Indium contacts are welded on the surface, an opened area without gold is required. We chose a rectangular shape with a width of 700 μm and a height of 3.2 mm. Once the lithography is done, we then deposited 150 nm of a Ti/Au alloy and performed a lift-off in an acetone combined to ultrasound bath. Figure 4.17b shows what we obtain at this stage of the process. In order to prevent any current leakage from the contact to the top gold layer, we added an extra step, involving the deposition of a protective oxide layer. For that purpose we deposited a thick layer of SiO_2. We then performed another step of lithography to shape a slightly smaller rectangle (500 μm $\times$ 3 mm) and we finally etch the oxide by mean of the ICP RIE machine previously presented. At the end of the process, the device should look like Fig. 4.17c.

Figure 4.18a displays a photo of the device at the end of the fabrication process. The grey area corresponds to the QW's surface, the yellow one indicates the deposited gold and a pink area represents the deposited dielectric layer. We then covered the lateral surface of the sample with silver paint and welded two Indium balls on the surface (see Fig. 4.18b). Finally, we performed Landau emission spectroscopy and the results are shown on 4.18c. Unfortunately, no clear amelioration is visible. Indeed, the width of the emission peaks are still as wide as before and the coupling (blue-shift) remains low. This could be due to the fact that a large uncovered portion of the sample still remains between the two electrical contacts and therefore a majority of photons escape without seeing the rest of the cavity. Therefore, it could be necessary to look for a cavity design that is able to include the contacts inside the resonating volume. A certain number of geometry exists but the one that seem to be suited for our purpose is the so-called Tamm cavity. We will now detail its functioning and present some preliminary results.

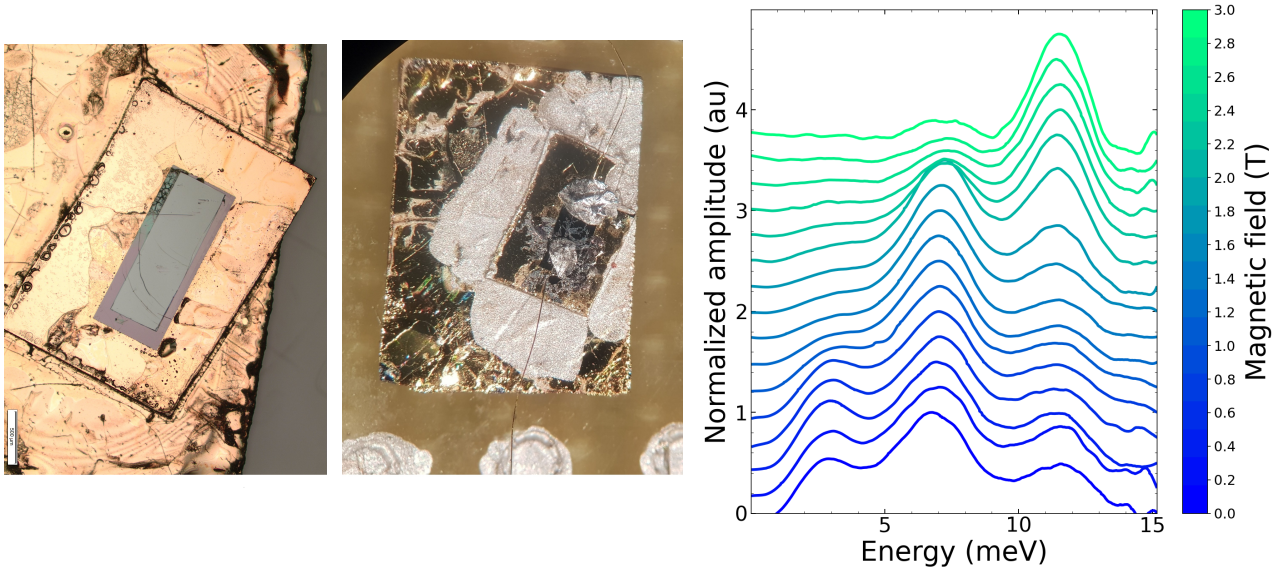

(a) (b) (c)

Figure 4.18: **Photos of the enhanced cavity at the end of the process.** Photo of the sample after the process developed in the main text, (a) and after we welded the Indium contacts in the opened area (b). The sample's contours have been covered with silver paint to prevent from any photon leakage from the sides. (c) Waterfall plot of the emission spectra obtained on the enhanced cavity, for different magnetic field strengths.

4.5.3 Toward high-tech cavities: the Tamm cavity

Presentation

Tamm electromagnetic modes take place at the interface between a periodic stack of materials featuring highly different optical indexes (distributed Bragg reflector, DBR) and free space. It was theorized in 1996 [110] and rapidly applied to visible/IR systems due to the availability of high-quality AlGaAs/GaAs stacks [111, 112]. To adapt this technology to the THz range, it is necessary to have thicker layers in the DBR thus disabling the use of molecular beam epitaxy for its growth. Therefore Tamm cavities have been realized using stacks of silicon layers (n $\simeq$ 3.42) of thickness close to 25 μm, spaced with air layers (n $\simeq$ 1) of approximately the same thickness. In particular, these DBR have been applied to the p-Ge laser as efficient semi-transparent THz mirrors [113]. More recently it has been shown that Tamm cavities can reach very high quality factor (> 200) for a resonant frequency of 1 THz when coupled to a gold mirror [102].

The geometry of such a THz Tamm cavity is sketched on Fig. 4.19a. The layers typically used are GaAs or silicon, with air spacers as previously mentioned. To size the air layer, spacers are used, typically made of scotch tape, GaAs or silicon. The sample of interest is inserted in the cavity by being placed at the interface with the DBR. Its bottom is covered with a gold layer, thus closing the cavity. Figure 4.19b shows a TMM calculation of the reflectivity spectra for such a structure, when varying the number of GaAs/Si/air layers. It was obtained considering 13.6 μm of GaAs as a DBR layer and 50 μm of air. When the periodicity of the DBR is increased, the resonance width decreases as its strength diminishes (see insert of the plot). In particular, the quality factor of the Tamm cavity ranges from 10 to 74 for DBRs from 1 to 3 periods. For comparison, the reflectivity of the bare cavity (namely only

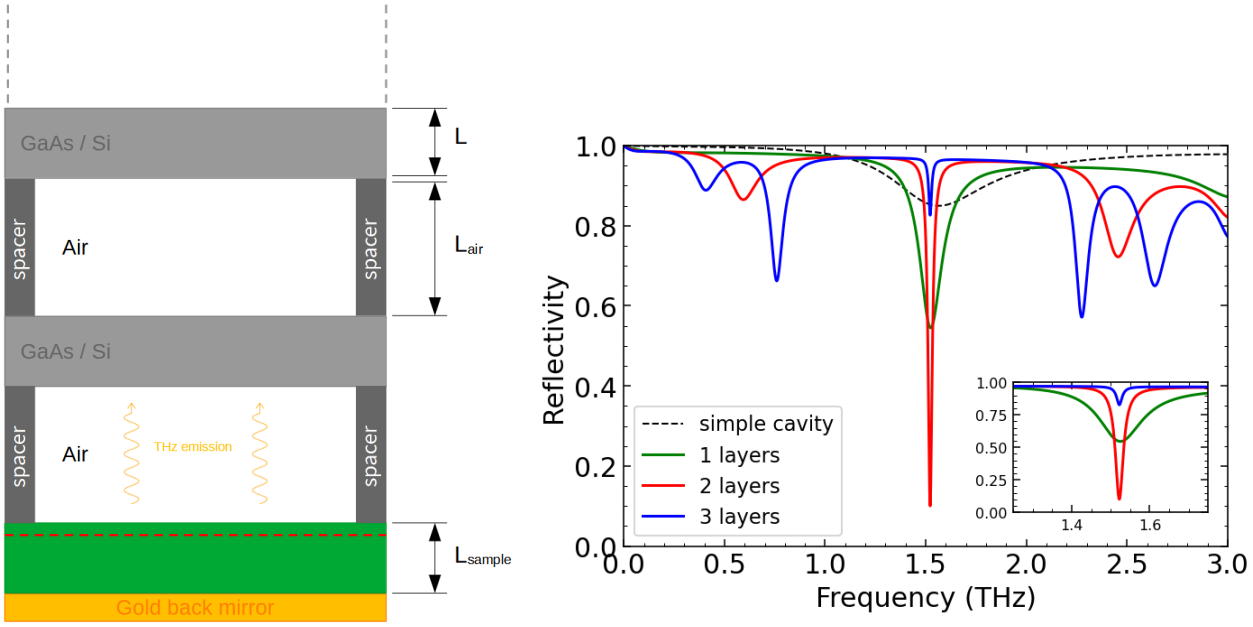

(a) (b)

Figure 4.19: **Sketch of a THz Tamm cavity.** (a) Side view of a THz Tamm cavity, composed of a DBR stack made of either GaAs either silicon layers separated by air and closed with a gold mirror, positioned at the back of the sample of interest. A zoom around 1.5 THz is plotted in insert. (b) Reflectivity spectrum, computed by the mean of the TMM method (see Methods), obtained for these structures for different number of GaAs/Si/air layers. A simple cavity (ie just the thinned sample) spectrum is plotted on top for comparison.

the thinned sample) is plotted, clearly demonstrating that the Tamm cavity design brings a great improvement in the quality factor. From Fig. 4.19b, it seems that having a two periods DBR is a good trade-off between high quality factor and intense resonance.

TDS characterization

We characterized two Tamm cavities using room temperature TDS measurements. The first cavity was built by my myself and it is made of 150 μm thick scotch spacers and a 50 μm thick undoped GaAs layer. The sample originates from the 091222 growth and its substrate has been thinned down to 50 μm. It is glued on golden holder (see insert of Fig. 4.20a). The second cavity was provided by Pr. Jun Kono's group of Rice University, USA. It was fabricated by Alan Covarrubias and consists of a 28104 sample thinned down to 160 μm, with two layers of Si (50 μm thick)/air (173 μm thick). The whole cavity is encapsulated with a PTFE cover (see insert of Fig. 4.20b).

Figure 4.20 displays the TDS reflectivity spectra obtained on the two Tamm cavities. In both cases, it features several resonances, much narrower than the one obtained with the bare cavities. Indeed, the linewidth of the home-made cavity is typically of 70 GHz compared to 42 GHz for the Rice device, whereas it exceeded 250 GHz for the simple cavity (see Fig. 4.4). The higher quality factor of the American's cavity is most likely due to the fact that it features two stacks where the homemade only has one. Nonetheless, these TDS results already demonstrate that Tamm cavity could greatly improve the quality factor of the system.

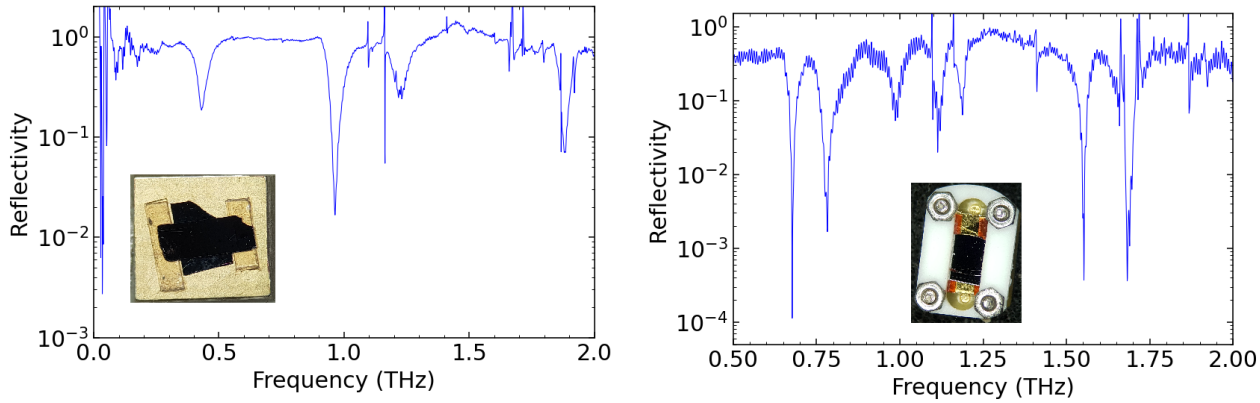

(a) (b)

Figure 4.20: **TDS characterization of the two Tamm cavities.** TDS reflectivity spectrum obtained on (a) the homemade Tamm cavity and (b) the Tamm cavity provided by Pr. Kono, Rice University. A photo of each device is shown in insert.

Magneto-reflectivity measurements

I measured these two samples at the LNCMI-G laboratory to probe their optical magneto-reflectivity. It is shown in the left panel of Fig. 4.21, plotted as a false-color map. It features several anti-crossings whose positions are in good agreement with the previous TDS characterization, even though only the more pronounced modes appear to be visible in magneto-optics. It means that we successfully induced light-matter coupling in our samples, in the form of Landau polaritons.

The coupling seems to be relatively low and can be roughly estimated at below 10% (around 5% for the American and 9% for the homemade cavity). However, when we look at the raw spectra on the right panel of Fig. 4.21, it is clear that the resonances are significantly narrower than previously (see red curve for the comparison with the simple cavity). Indeed, the UP/LP modes of the homemade (resp. the American) cavity exhibits linewidths of 100 GHz (resp. 50 GHz) compared to 210 GHz for the simple cavity, corresponding to quality factors of 10 (resp. 16) versus 3 previously. We finally succeeded at enhancing the quality factor of the resonator by more than a factor 3 by implementing a Tamm cavity design.

The quality factor Q characterizes the lifetime of a resonant mode, while the coupling strength g quantifies the intensity of the light-matter interaction. These two quantities are governed by different parameters: Q depends on losses, whereas g is determined by the local field strength, and thus by the effective mode volume. In our case, the new cavity exhibits a higher quality factor, indicating reduced losses. However, the coupling strength remains unchanged or it is even slightly lower. This suggests that, despite better energy confinement in time (i.e., lower losses, higher Q), the electromagnetic field is not more tightly confined in space. In other words, the cavity concentrates the field less efficiently, which weakens the local light-matter interaction and therefore reduces the coupling strength g. Improving g is essential to reach the strong coupling regime. However, once this regime is achieved, progressing toward Bose-Einstein condensation relies primarily on enhancing the quality factor Q. A higher Q leads to longer polariton lifetimes, which facilitates more efficient relaxation into the ground state and increases the likelihood of condensation.

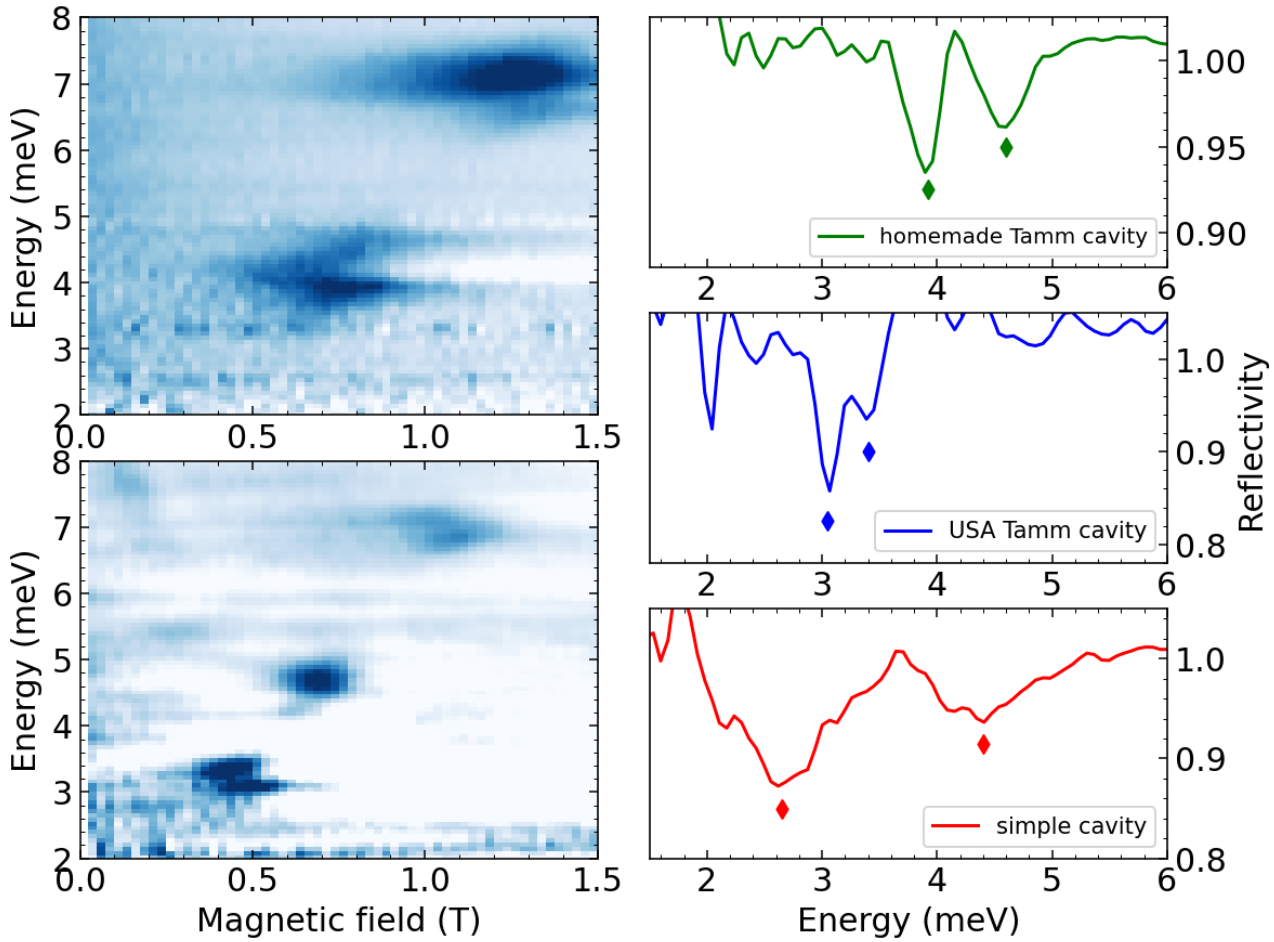

Figure 4.21: **Magneto-reflectivity obtained on the two Tamm cavities.** (Left panels) False-color magneto-reflectivity mapping obtained on the homemade (upper plot) and American (bottom plot) Tamm cavity. (Right panels) Raw reflectivity spectra displaying the different polaritonic modes. The spectrum obtained with a simple cavity on 091222 is added for comparison. The diamond markers point at the different polaritonic branches.

Emission measurements

Finally, we aim to determine whether Landau emission can be obtained from these two structures, with narrower resonances. The results are plotted on Fig. 4.22. The first observation is that there is no effect of the optical modes with the USA Tamm cavity. Indeed, we can only see a classical CR blue-shifting when increasing the magnetic field strength. This absence may be attributed to the electrical contacts, located outside of the cavity, thus preventing the emitted light from coupling to the electromagnetic modes.

On the other hand, the emission obtained with the homemade cavity exhibits some optical modes. The positions of the modes seem to be in good accordance with the ones previously observed in TDS and magneto-reflectivity (see figures 4.20 and 4.21). However, the coupling is really weak as no clear deviation from one mode to the other is visible. Therefore, we don't induce any polaritonic phase in the system. This is nonetheless an encouraging result as for this cavity as an effort to weld the Indium contact inside the cavity have been made, resulting in the coupling of the emitted light with the cavity modes.

Overall, the emission and magneto-reflectivity results are very different. The fact that we loose the light-matter coupling may be due to the increased interaction volume when probing the emission. Indeed, as discussed earlier, while the magneto-optic radiation is well focused on the sample, thus probing a small and homogeneous part of the cavity, the emission case is quite different. For the American cavity, the light could escape the sample without being affected by the cavity as the electrical contacts lay outside of it. In the homemade cavity, it could be due to a guided propagation towards the sides of the sample, both leading to an inhomogeneous broadening and an increase of the interaction volume, thus destroying the light-matter coupling.

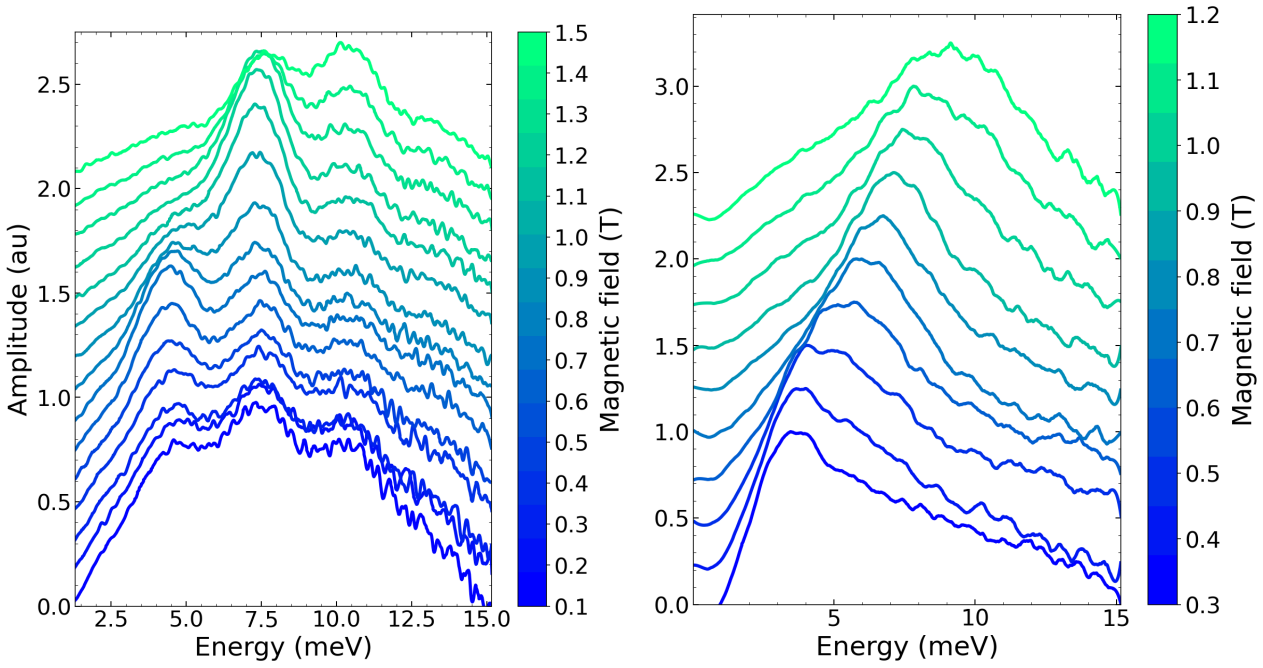

Figure 4.22: **Landau emission spectroscopy of the two Tamm cavities.** Landau electroluminescence spectrum obtained on (a) the homemade Tamm cavity and (b) the Tamm cavity provided by Pr. Kono, Rice University. It was obtained for different magnetic field strength and plotted as a waterfall plot with a constant amplitude offset.

In summary, it is necessary to consider a new cavity design that provides better spatial confinement of the electromagnetic field in the active material region, while improving the quality factor. Several complementary approaches can be considered to improve the performance of the cavity. To enhance the light-matter coupling, one should employ structures with strong spatial confinement of the field, position the emitters at the maxima of the electric field, and increase the number of coupled emitters, for instance by integrating multiple quantum wells [57]. To increase the quality factor Q, it is essential to reduce all sources of losses that limit the mode lifetime. This involves minimizing radiative losses through higher mirror reflectivity and optimized cavity geometry, as well as reducing material losses by selecting low-absorption materials and operating at suitable wavelengths. Finally, fabrication quality plays a crucial role: precise control of layer thicknesses, minimal surface roughness, and high uniformity of the deposited layers are key to suppressing scattering and significantly enhancing Q.

Chapter 5

III-V-based heterostructures

Contents

The objective of this chapter is to present some preliminary results obtained on samples of the III-V semiconductors family. Indeed, as it was mentioned in the Introduction, these materials' band structures are less temperature sensitive compared to the II-VI family and benefit from an advanced technological process knowledge, making them mature for potential applications. Results on InSb- and GaAs-based quantum wells will be presented, followed by an investigation of the magneto-optical properties of a superlattice structure composed of InAs/GaInSb alloys.

5.1 InSb-based quantum wells

5.1.1 Landau emission experiments

One of the first system where Landau emission was observed are bulk structures of n-type InSb [114–117]. It was already known that InSb is a narrow-gap semiconductor and thus features a non-parabolic band-structure. It was evidenced that, under electric excitation, electrons are excited from impurity states to conduction Landau levels and then recombine radiatively. However, it was shown that, due to strong electron-electron interactions, a population inversion was hard to achieve in these structures[23]. Additionally, bulk materials offer poor leverage of tunability as it is impossible to tune the carriers concentration. Since no Landau emission results where reported in InSb-based QWs, it is interesting to go towards this research direction. The InSb-based QW sample were provided to us by the group

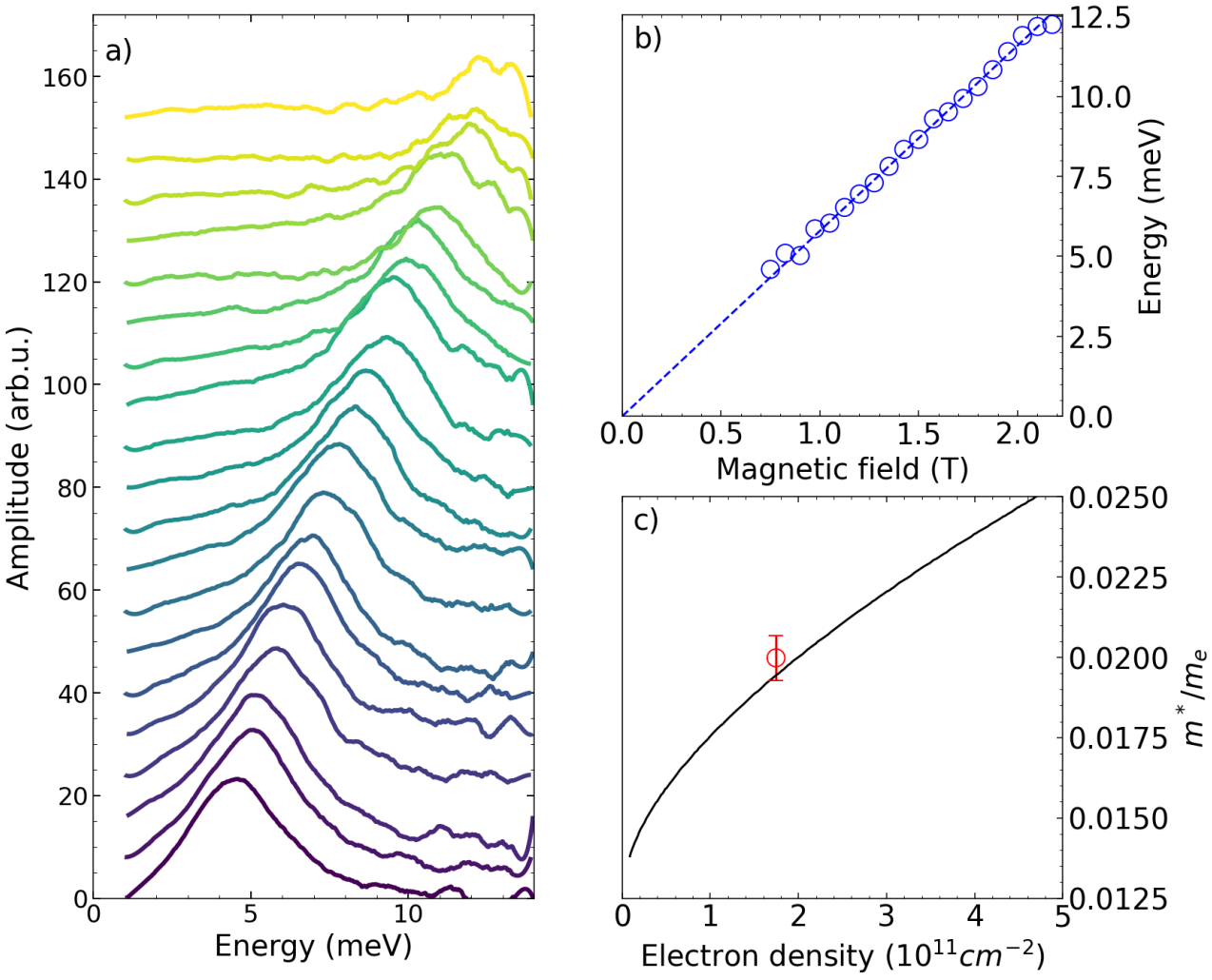

Figure 5.1: **Landau emission experiments on InSb QW.** (a) Waterfall plot of the Landau emission spectra obtained when varying the magnetic field strength. (b) Extracted spectrum maxima plotted against the magnetic field. The dashed line is a linear fit used to extract the cyclotron mass value. (c) Cyclotron mass for the given electron density of the sample (red star). Multi-bands Kane models prediction is plotted for comparison (black line), showing good agreement [118].

of Pr. Manfra of Purdue University, West-Lafayette, USA. The detailed growth as well as some characteristics are summarized in the previous chapter. We performed Landau emission spectroscopy measurements on this structure and the results are shown on Fig. 5.1. We can see an intense emission ranging from 5 to 13 meV when tuning the magnetic field strength from 0.8 to 2.3 T (Fig. 5.1a). When extracted, the positions of the spectra's maximum align well with a linear-in-magnetic-field behavior, characteristic of the cyclotron resonance (Fig. 5.1b). The cyclotron mass deduced from the slope of a linear fit is estimated to be 0.02 m_e, which is in good agreement with the Kane model [118], for the measured electron density (Fig. 5.1c).

5.1.2 Towards engineered ohmic contacts

As discussed in the Introduction, one of the advantages of the III-V semiconductors' family is the extended available knowledge regarding fabrication processes. Therefore, ohmic contacts were fabricated on this InSb-based structure. It is indeed important to find an alternative to the Indium-ball contacting method as it does not allow a precise control of the electric field lines inside the sample. In this subsection, the work carried out to achieve this goal will be detailed. The adopted geometry is a Van der Pauw (VdP) 2.5 mm×2.5 mm square (see Methods) with contact pads' width of 500 μm.

The key step is the etching process. Indeed, accessing the well requires the local removal of the 40 nm-thick barrier, followed by the deposition of a metal layer to establish contact with the well. To perform this step, I used a well established wet etching technique, based on a citric acid/H_2O_2 solution [119–122]. Since it does not require any heavy equipment, unlike dry-etching techniques, it has the advantage of being easy to implement.

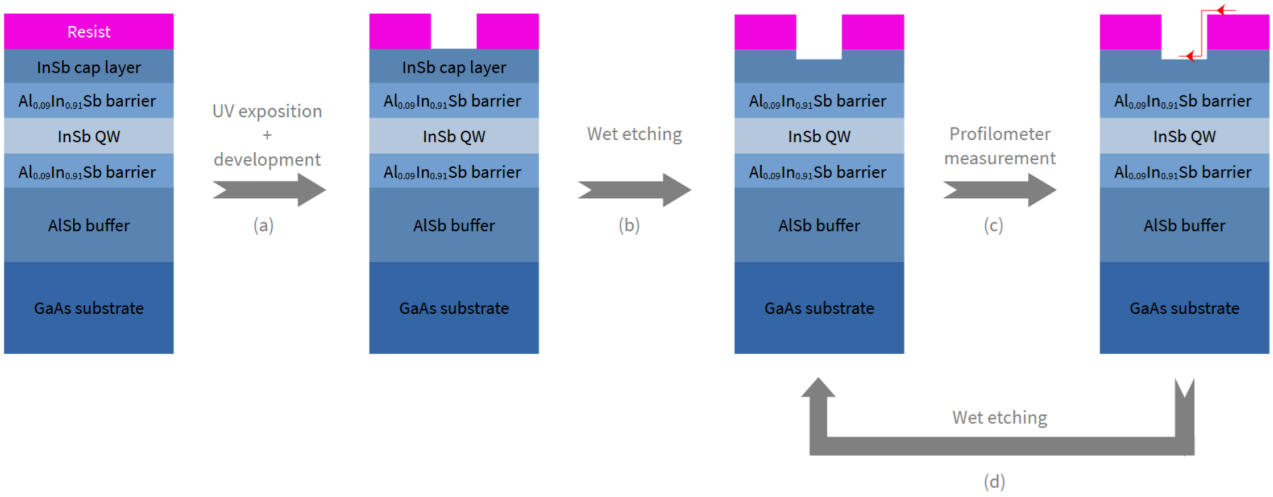

Figure 5.2: **Sketch of the etching protocol.** (a) The deposited resist is exposed to UV light through a Chrome mask with the VdP shape. It is then developed in an acetone bath. (b) The sample is then plunged inside the citric acid/H_2O_2 solution for a defined time. (c) The sample is then measured by the mean of a profilometer. The red line shows the path of the tip that allows us to estimate the etched depth. (d) The sample is then plunged again in the solution until the desired depth is reached.

Before etching the sample, I performed tests on pure InSb wafers to establish an efficient recipe and an associate etching speed. The protocol is the following: after a UV lithography to pattern the VdP shape (see step (a) of Fig. 5.2), the sample is plunged inside the citric

acid/H_2O_2 with a 50:1 ratio (based on [120]) to start the etch the material (see step (b) of Fig. 5.2). After a certain defined time, the sample is removed from the solution, rinsed and the etched depth is measured by the mean of a profilometer (see step (c) of Fig. 5.2). I then repeat the etching and depth measuring steps for around 20 min to have an estimation of the etching speed. As a result, the etched depth exhibits an evolution with etching time that is nearly linear (see Fig. 5.3b). When comparing with Chang et al.'s work [120], the etching speed that we obtain is much larger. Indeed, after removing the resist, a final measurement of the etched step was carried out. I find 1328 nm which gives an etching speed of 66 nm/min compared to 16 nm/min in Chang's work. This could be explained by the difference in the etched material, the slightly different temperature of operation (22°C against 18 in [120]) or the state of the chemical solution (concentration, freshness etc...). This test allows us to have an estimation of the etching time needed to reach the InSb QW, located 40 nm below the surface of the sample (see Methods).

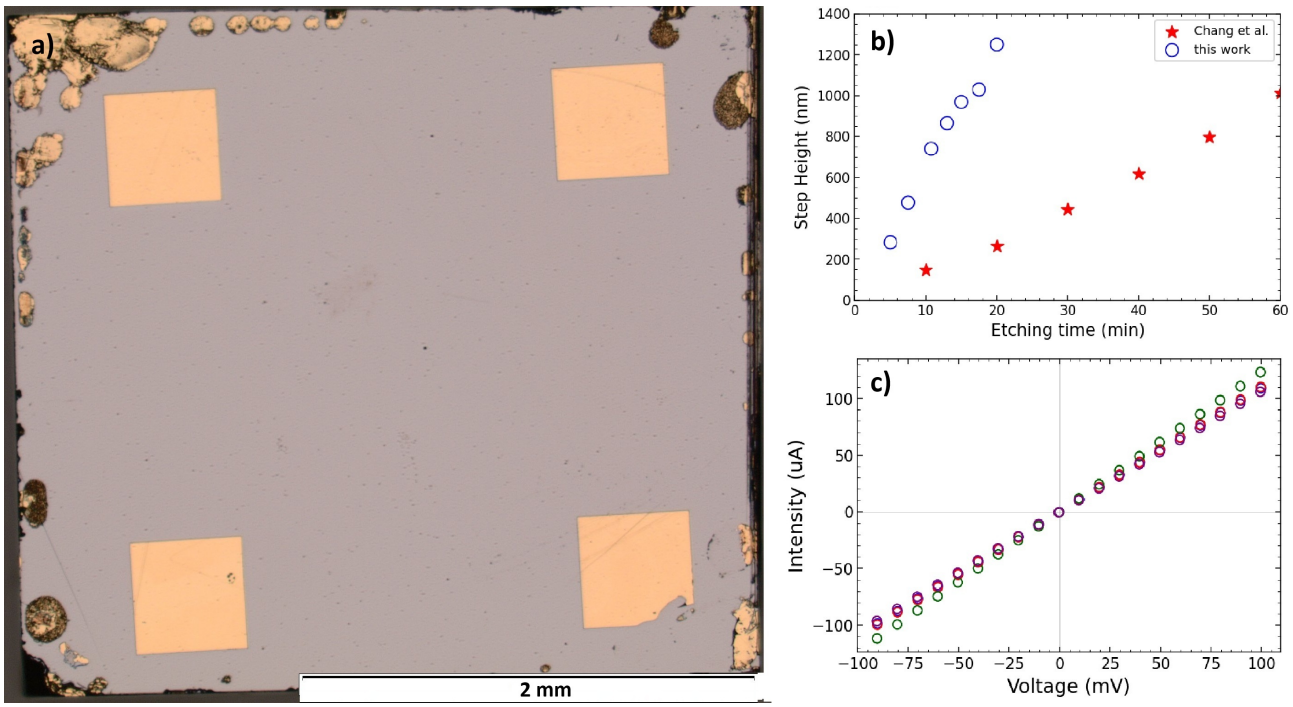

Figure 5.3: (a) Optical photo of the final device obtained after the etching process and the metal deposition. (b) Etched depth evolution with time for our work (blue empty circles) compared to Chang et al.'s work [120] (red stars). (c) I(V) curves obtained, at room temperature, on four two-probes configurations of the sample.

Figure 5.3a shows an optical photo of the processed sample, after the etching and the metal deposition. A simple Ti / Au (10/50 nm) metallic alloy was deposited to contact the well. We then performed I(V) characterizations, at room temperature, on four different two-probes configurations and the results are plotted in Fig. 5.3c. It displays a perfect linear behavior, giving an average resistance of 893 Ω. Although these room-temperature results are encouraging, they are not sufficient, as the contact resistance increases drastically when the temperature is lowered to that of liquid nitrogen. This means that a Schottky barrier is formed at the interface between the metal and the semiconductor [123] and therefore the QW is not properly contacted. A way to improve this would be to perform an thermal annealing to break this barrier or to change the metal alloy towards a composition that can diffuse inside the structure, like AuGeNi [119, 122].

5.1.3 Towards light-matter coupling

InSb QWs have been used to study the influence of band structure's non-parabolicities on the light-matter coupling [124]. The use of these metamaterials has the benefit to be quite straightforward, compared to the thinning process, as it only require one step of lithography and a step of metal deposition and a lift-off. It also offers an easily tunable platform since, as we will see later, the resonance frequency is determined by its size. It is therefore a very promising platform to study Landau polaritons [58, 124].

Small introduction to the split-ring resonators

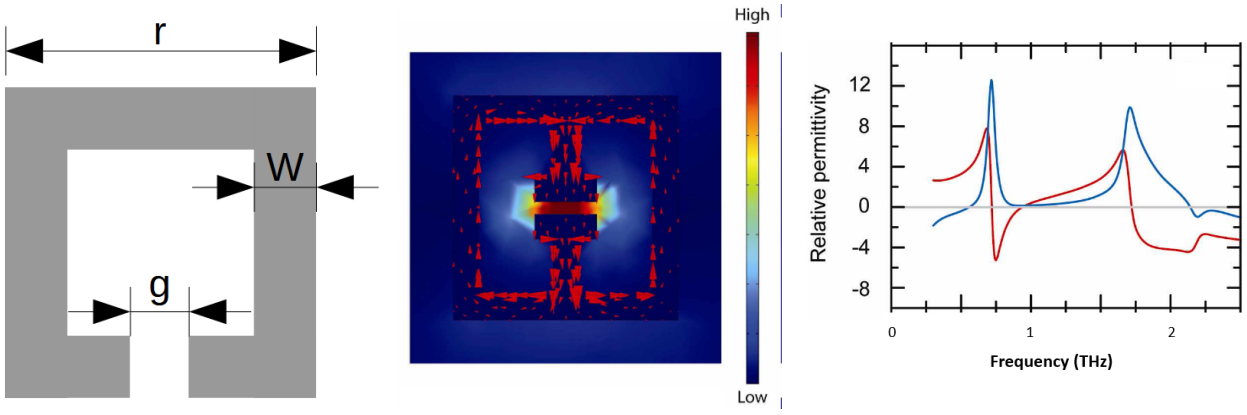

(a) (b) (c)

Figure 5.4: (a) Sketch of the typical geometry of a SRR. (b) Electromagnetic simulation and (c) associated real (resp. imaginary) part of the computed permittivity (red resp. blue line). Adapted from [125].

Figure 5.4a shows the typical geometry of a SRR. It is usually made by a metal of thickness t, of width W, lateral length r and features a slit of size g. Its resonator mechanism can be understood, in a first approximation, as a miniature LC circuit. The metallic loop plays the role of an inductance, while the gap introduced in the ring behaves as a capacitance. Together they form a resonant oscillator whose natural frequency is determined by the combination of these two elements. When an electromagnetic wave illuminates the resonator, the magnetic field perpendicular to the loop induces a circulating current through Faraday's law, and the electric field parallel to the gap drives a build-up of charges across it. The result is a resonant excitation that efficiently converts the incident field into localized oscillations of currents and charges.

This mechanism provides an interface between light and matter: the incoming light couples to a photonic mode confined by the geometry of the split-ring. When the split-ring is placed close to a semiconductor material subjected to a static magnetic field, the relevant matter mode is the cyclotron resonance. When the natural frequency of the LC circuit formed by the split-ring coincides with the cyclotron frequency, the interaction between the two becomes resonant. The localized field in the resonator's gap acts as an extremely efficient antenna, capable of forcing the carriers to oscillate at the imposed frequency. This way, it is possible to induce strong light-matter coupling and the formation of Landau polaritons, like previously observed in [58, 124].

We can have an estimation of the SRR resonance frequency with the following formula

$$f_0 = \frac{1}{2\pi\sqrt{LC}}, \tag{5.1}$$

where L and C are the inductance and capacitance of the equivalent circuit representing the system. In practice, it is hard to have a precise value of these two quantities and full electromagnetic simulation are required to determine the resonance frequency. However, we can still have an estimation of it using basic formula for L and C. Indeed, in a very simple model we can approximate the inductance of a thin loop with

$$L \simeq \mu_0 r \left(\log \frac{8r}{W} - 2 \right), \tag{5.2}$$

where μ_0 is the vacuum permeability. We can also use a planar model to estimate the capacitance of the gap:

$$C \simeq \epsilon_0 \epsilon_r \frac{W \times t}{g}, \tag{5.3}$$

where $\epsilon_0\epsilon_r$ is the substrate permittivity. By taking t = 100 nm, W = 5 μm, r = 50 μm and g = 2 μm, we find $f_0 \simeq 2.4$ THz. It is a very brutal estimation because it neglects the sides effects but it has been shown with both simulations and experiments that these dimensions typically give rise to resonances in the THz range [62, 125–127] (see Fig. 5.4b and c for example).

Clean-room realization and TDS characterization

Therefore, I designed a Chromium mask featuring several SRRs patterns, of various characteristic sizes. These structures have shown to be resonant in the THz range when the size of the gap is typically on the μm order and that the resonance frequency red-shifts when the motif is scaled up [126]. Figure 5.5 shows a sketch of the mask, detailing the different SRRs geometries, inspired from [62, 125–127].

After several conclusive tests on Silicium and GaAs to find the correct lithography recipe, I processed an InSb-based QW sample with the (c) SRRs pattern. I deposited a standard Ti / Au (10/50 nm) metallic layer on top to shape the resonators and the results is shown on Fig. 5.6a. Most of the patterns are well defined and the size of the gap is around 1.1 μm and one expects a resonance frequency at 1.5 THz, based on the study made by O'Hara et al. [62]. I performed room-temperature TDS characterization to confirm the THz resonance in the meta-material. The transmission spectra are plotted on Fig. 5.6b, for two polarization configuration indicated on Fig. 5.6a. The spectra were obtained by taking the Fourrier transform of the time-truncated electric field signal, to filter the interference arising from the Fabry-Perot effect in the substrate.

The gap in the ring works like the capacitor of the LC circuit, and its orientation decides whether the incoming electric field can excite the resonance. If the field is polarized across the gap, no voltage builds up and nothing resonates. If the field is polarized along the gap, charges pile up at its edges, the circuit is driven, and a clear resonance around 1.5 THz appears. The resonance's width is quite important as it is estimated to be around 440 GHz for a resonance frequency of 1.45 THz, giving a quality factor around 3.5. This value is below the one obtained in [62], where they measure a resonance's quality factor around 10. This discrepancy could be attributed to the fact that in their study, the authors designed

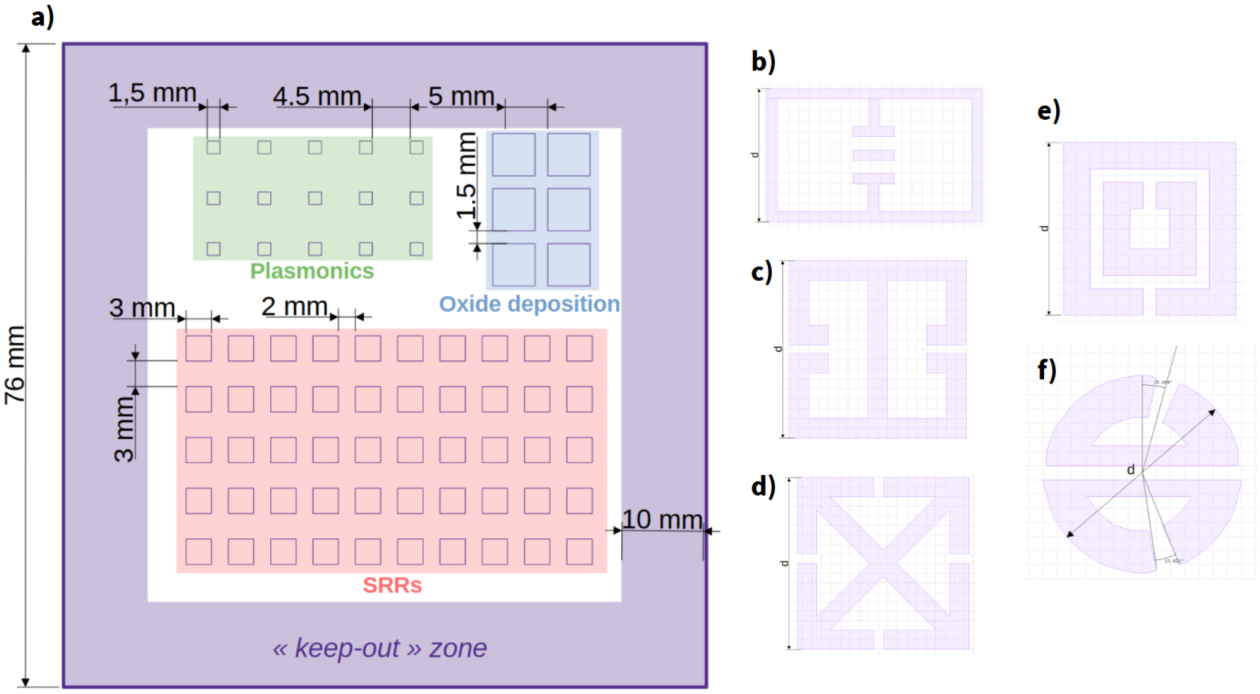

Figure 5.5: **Split-ring resonators for THz light-matter coupling.** (a) Sketch of the designed Chromium mask. It also includes plasmonics and oxide deposition patterns that are not presented in this manuscript. (b to f) Different SRRs geometries, adapted from [62, 125–127].

SRR resonating around 600 GHz. To shift this resonance towards higher frequency, it was necessary to reduce the size of the split-ring pattern. It leads to a 2 μm gap, which dimension is close to the UV lithography limit. Therefore, the quality of the patterns is affected and an inhomogeneous broadening is expected.

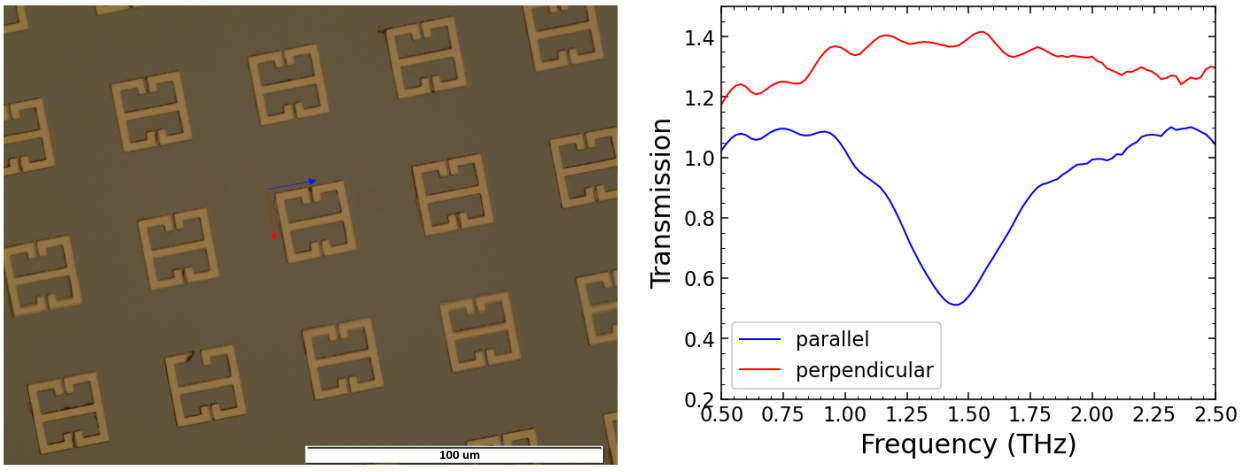

(a) (b)

Figure 5.6: **TDS characterization of the SRRs device.** (a) Optical photo of the processed device. The red (resp. blue) arrow indicate the polarization of the incident TDS beam, perpendicular (resp. parallel) to the split-ring gap. (b) TDS transmission spectra obtained on the sample, for the two polarization configurations.

The next step is to characterize the sample in the presence of a magnetic field, in order to verify the presence of a coupling between the meta-material and the InSb 2DEG.

Magneto-absorption characterization

The magnetoabsorption measurements were performed at the LNCMI-G laboratory, by Mr. *Kassa Krystof* and the results are shown on Fig. 5.7. The false-color mapping reveals an anti-crossing around 6 meV and 1.1 T, as expected given the TDS characterization. Using the same procedure detailed in the previous chapter, the polariton branches and the coupling strength could be determined. I find a Rabi spitting $\hbar\Omega$ = 0.6 meV giving a coupling ration of 9 %. It confirms that we successfully induced a strong light-matter coupling in the InSb QW using a SRRs meta-material.

In the future, Landau emission experiments on this structure could be interesting as it features a greater quality factor than with the Fabry-Perot devices, thus offering a promising asset for Landau polariton lasing.

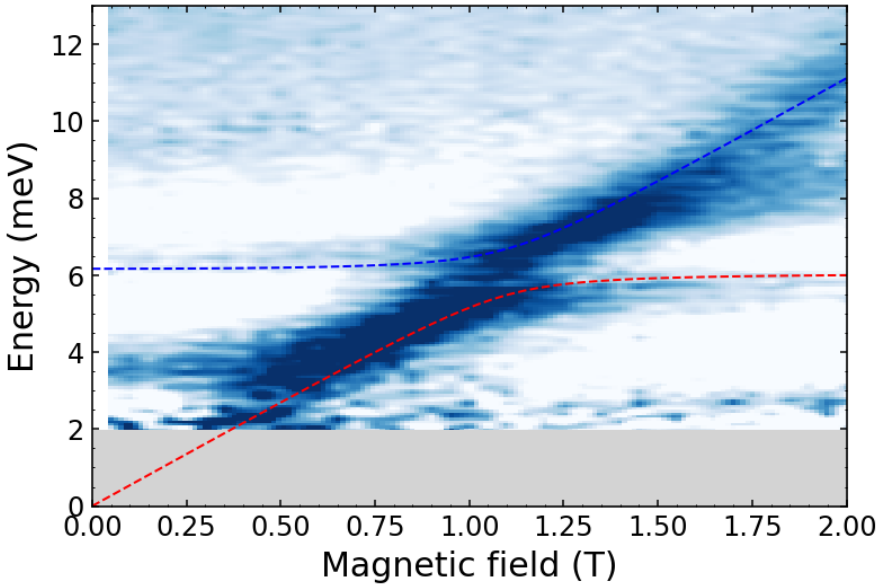

Figure 5.7: **Magneto-absorption characterization of the SRRs device.** False color mapping of the magneto-absorption spectra when varying the magnetic field strength. It exhibits an anti-crossing around 6 meV and 1 T. The dashed lines are Hopfiled fittings (see chapter 4 for the detail of the procedure).

5.1.4 Summary and perspectives

In this section, we investigated an InSb-based QW, through magneto-absorption and cyclotron emission experiments. We showed for the first time that this structure can emit THz radiation. We tried to implement ohmic contacts to better control the current injection. This was not successful and we should try to understand why.

We also attempted at inducing a light-matter coupling in the structure, through the use of Split-Ring resonators. We successfully demonstrate the presence of Landau polariton by the mean of magneto-optics experiments. As a perspective, we would like to observe Landau emission emerging from this strongly coupled system.

5.2 Landau emission in GaAs-based QWs

5.2.1 Transport characterization

I also had the occasion to measure GaAs-based QWs samples. It was given to us by Dr. U. Gennser from the C2N laboratory, Palaiseau. Even if this structure features a parabolic bandstructure, making it highly sensitive to Auger scattering, it holds a very high carrier mobility. Indeed, the growth is supposed to have an electron mobility of the order of 2×10^6 $cm^2/(Vs)$ which is one order of magnitude higher than what we can achieve in the HgTe QWs presented in this manuscript. Therefore, it makes the study of this material very interesting because, as we saw in the Introduction, a higher mobility makes it easier to reach a streaming regime and thus a potential cyclotron lasing effect. The structure of the growth is sketched in chapter 2.

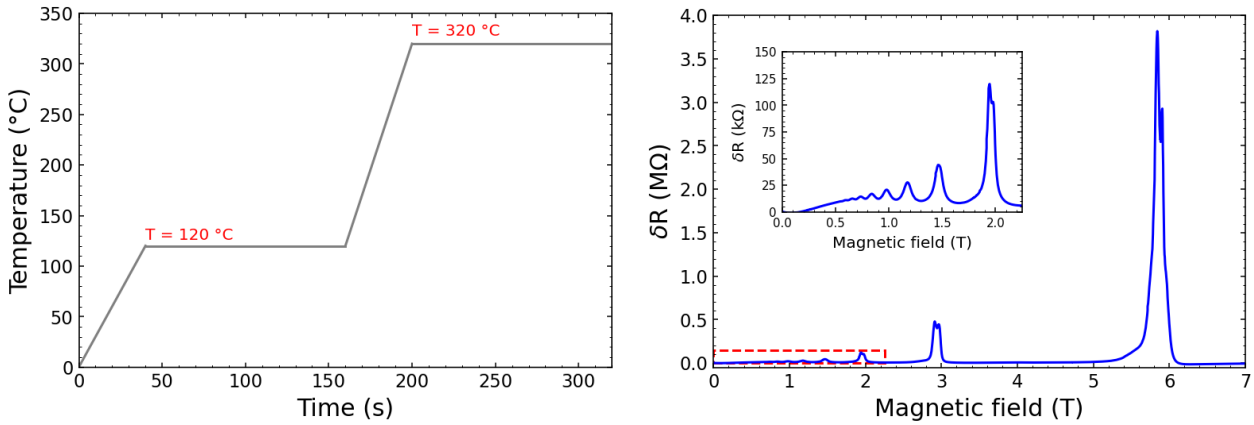

(a) (b)

Figure 5.8: (a) Temperature profile used for the Indium contact annealing. (b) Two-probe magneto-resistance evolution of the GaAs-based QW. The start of the quantum oscillations is plotted in insert, which range is indicated with the red dashed box.

In order to implement electrical contacts on the sample, it is necessary to perform an annealing of the Indium balls. Figure 5.8a displays the temperature profile used and implemented in an *Annealsys* oven. It allowed us to create good ohmic contact and perform electrical measurements. Figure 5.8b shows the evolution of the two-probe magnetoresistance of the sample. It shows well defined quantum oscillations, that starts at rather low magnetic field values (see insert) witnessing the high carrier mobility. The SdHO's period allow us to estimate the carrier density to be around 1.38×10^{11} cm^{-2}.

We can notice the presence of a splitting of the quantum oscillations for magnetic fields larger than 2 T. It was observed several times before [128, 129] and it could indicate that we start to resolve the spin splitting of the material at high magnetic fields. Note that this behavior was not systematically observed on all samples, witnessing inhomogeneities in the growth.

5.2.2 Landau emission experiments

We then performed Landau emission experiments. Figures 5.9a and c shows the spectra obtained when increasing the magnetic field strength. Even if Landau emission has already

been observed in GaAs-based structures [90], it is the first time that it is observed in a QW structure. The FWHM of the spectra is estimated to be around 2 meV, which is less than the width typically obtained in HgTe-based QWs (around 3 meV). This is most probably due to the fact the electron mobility is higher in GaAs thus reducing the LLs broadening. Once extracted, the spectrum maxima's position give a perfectly linear CR and a cyclotron mass of 0.0703 m_e (see fitting of the black experimental points in Fig 5.9c), way larger than in HgTe, as expected, and coherent with the literature [86].

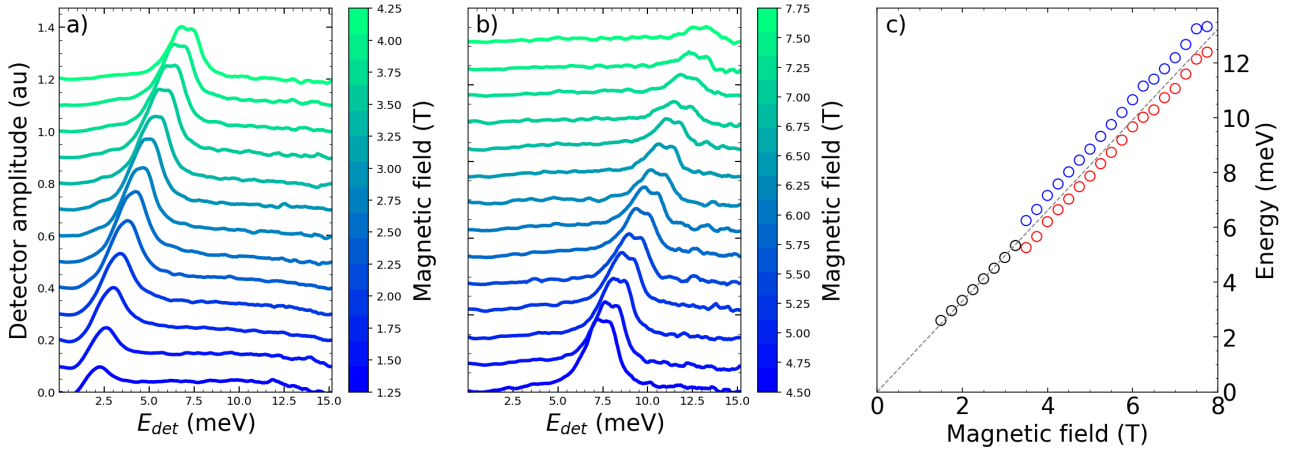

Figure 5.9: **Landau emission experiments on GaAs-based QW.** (a and b) Emission spectra waterfallplot for different magnetic field strengths. (c) Extracted emission maxima plotted with respect to the magnetic field value (empty circles). The black points are extracted from the spectrum only showing one maximum, and is used to determine the cyclotron mass thanks to a linear fitting (see grey dashed line). The blue and red circles are extracted from the spectra featuring a dedoubling of the emission peak.

We can notice that, for magnetic field strengths above 3.5 T, a cyclotron resonance doublet is observed, separated by around 1 meV. This is neither a conventional nor an expected result, and it requires discussion. Certain explanations can be excluded rapidly. A first possibility would be that the doublet reflects the occupation of two electronic subbands. In wide GaAs quantum wells, the second subband can indeed be populated [130]. However, the cyclotron frequency in the two subbands differs only through band non-parabolicity, which is weak in GaAs, and should therefore induce a mass difference far smaller than the values observed here.

Two other possibilities are more directly connected to the breakdown of Kohn's theorem under strong non-equilibrium conditions. The first is that the doublet originates from a purely nonlinear response. In the linear regime, Kohn's theorem ensures that the cyclotron resonance energy in a parabolic band is unaffected by electron-electron interactions [131]. Under intense terahertz driving, however, these conditions no longer apply: *Maag et al.* showed that strong-field THz pulses drive the 2DEG beyond Kohn's protection, revealing anharmonic Landau-level ladder climbing and distinct extra peaks that are nonlinear sidebands rather than independent equilibrium CR lines [132].

A second, closely related possibility is that the doublet reflects interaction-driven spin effects under non-equilibrium conditions. In a simple single-particle picture, the two same-spin cyclotron transitions are degenerate. Even with electron-electron interactions, as long as Kohn's theorem applies, this degeneracy is preserved and only the spin splitting of Lan-

dau levels is enhanced [128, 129]. To actually separate the two cyclotron transitions in energy requires going beyond Kohn's theorem. In our experiments, the system is driven far from equilibrium by a strong electric field, so that the cancellation mechanism that protects the resonance energy may fail. In this case, dynamic correlation effects can shift the two transitions differently, leading to a measurable splitting. This second scenario would be consistent with the previous magneto-transport results since it seems that the spin splitting is resolved.

Testing this scenario requires complementary magneto-absorption experiments at thermal equilibrium, where only a single resonance should be visible if this interpretation is correct. It has been done at the LNCMI laboratory and the results are shown in Fig. 5.10a, as the form of a false-color mapping of the magneto-absorption of the material. It displays a perfectly linear CR over the full 16 T range, which cyclotron mass is coherent with the previously deduced emission one. A raw spectrum is shown in Fig. 5.10b, witnessing that the cyclotron resonance is not splitted and thus strengthening the previous hypothesis of a splitting induced by the breakdown of Kohn's theorem due to the hot carrier regime in the Landau emission configuration.

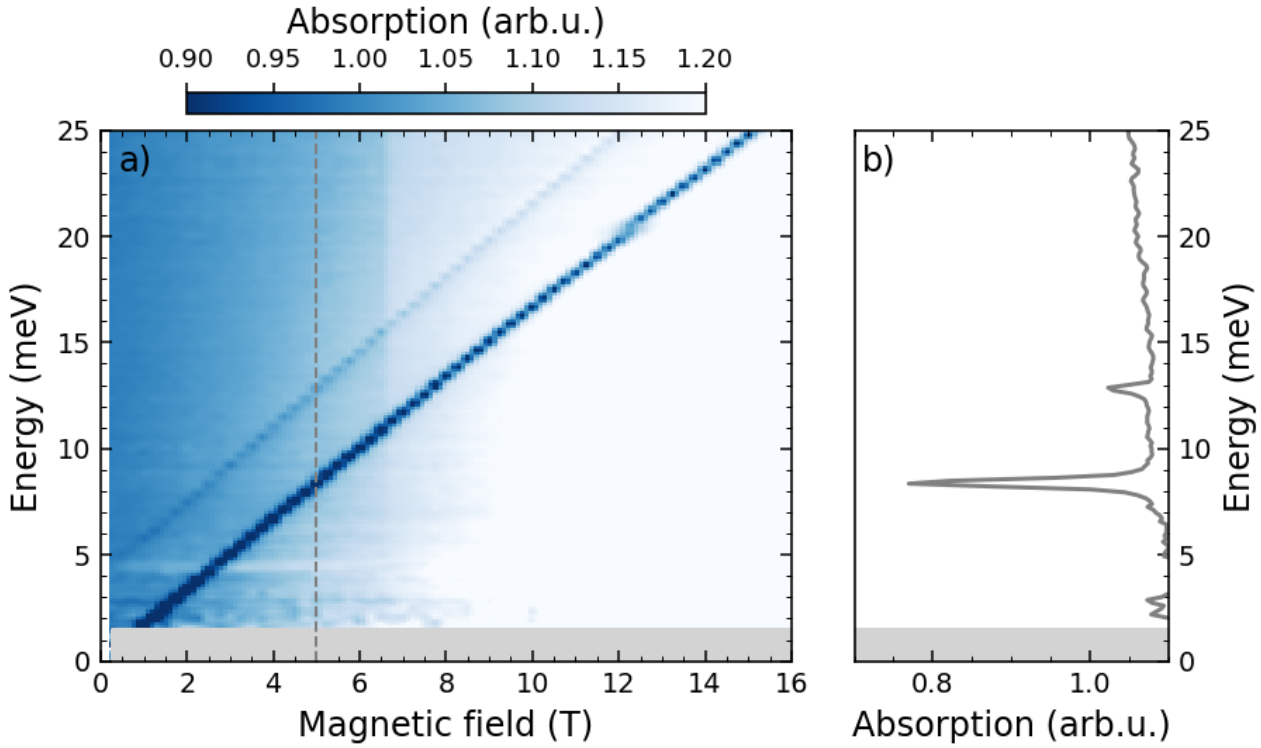

Figure 5.10: **Magnetoabsorption experiments on GaAs-based QW.** (a) False-color mapping of the sample's absorption spectra when tuning the magnetic field strength. (b) Raw spectrum, obtained at 5 T, highlighting the presence of two resonances.

We can notice the presence of a second linear resonance, approximately 4 meV above the cyclotron line. This resonance is too low to be attributed to an inter-band transition between two electronic subbands. We think it can be explained by the presence of charged impurities in the QW. These could come from the doping layers outside the well and that would have diffuse inside the 2DEG, as explained in [133]. These impurities create additional states below the 2DEG LLs and therefore allow new transitions to be visible. It has been extensively studied in GaAs heterostructure [133–135] and the binding energy's order of magnitude of

4 meV is coherent with Silicon doping. The exact nature of the impurity levels involved as well as the magnetic field dependence of the transition is still to be addressed and is part of an ongoing investigation.

5.2.3 Emission in strong crossed electric and magnetic fields

We finally increased the injection bias at a fixed magnetic field. The amplitude first increases and then saturates (see Fig. 5.11a). When V_{pp} reaches 140 V, the emission spectrum becomes highly distorted, transforming from its usual Gaussian shape into a sequence of peaks (see Fig. 5.11b). Equally spaced peaks are observed, and multi-Gaussian fitting (red dashed line of Fig. 5.11b) reveals an energy spacing of 470 μeV. Since the sample is not shaped to embed any optical cavity, a possible explanation is that the substrate itself plays the role of a a Fabry-Perot cavity. With this reasoning, the energy spacing that we just measured might be the Free Spectral Range (FSR) of the cavity. From this value, we can extract the length of the cavity. Taking the refraction index of GaAs $n_{GaAs} = 3.6$, we find a cavity length $l_{cav} = \frac{c}{2n_{GaAs}\Delta E_{FSR}} = 368 \pm 76$ μm. When we compare with the substrate's thickness of 300 μm, the hypothesis of a cavity effect is plausible.

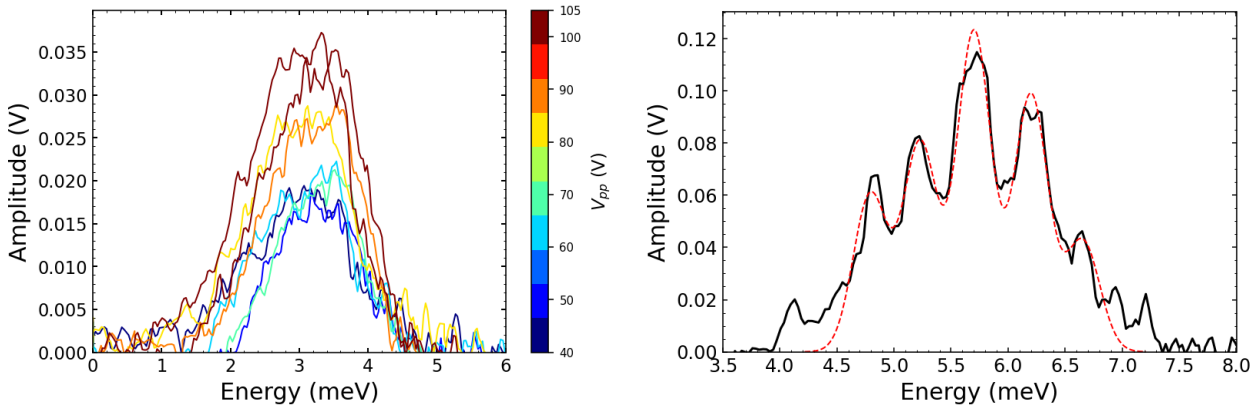

(a) (b)

Figure 5.11: **Landau emission in GaAs-based QW at high electric field.** (a) Emission spectra for fixed magnetic field of 2 T and for various increasing values of injection bias. (b) Emission spectrum obtained for a magnetic field strength of 3.5 T and a injection voltage of 140 V peak-to-peak (black solid line). The red dashed line is a multiple-Gaussian fit to extract the positions of the peaks.

However, unlike the case of Landau polaritons observed in HgTe quantum wells, this structuring of the emission spectrum does not appear for all values of the applied electric field. It emerges only above a relatively high threshold field, beyond which the emission becomes unstable and the spectrum is radically deformed. This threshold behavior and specific structuring resemble the emission spectrum of a frequency comb laser. In this scenario, however, the only possible lasing mechanism involves population inversion through a streaming motion effect, as described in the Introduction. Given the high mobility of the sample, the electron have time to reach the optical phonon energy before being scattered. Indeed, in GaAs $\hbar\omega_{op} \simeq 37$ meV [44] giving an optical phonon speed of $V_{op} = \sqrt{\frac{2\hbar\omega_{op}}{m_c}} =$

4.3×10^5 m.s^{-1} with the experimental mass previously determined. Therefore, the minimal electric field at which a carrier reaches the optical phonon energy before being scattered is $E_{min,1} = \frac{V_{op}\, m_c}{e\tau} \simeq 43$ V/cm if we take a scattering time of $\tau = \frac{m_c\, e}{\mu} \simeq 40$ ps corresponding to a mobility $\mu = 10^6$ cm^2/(Vs). This electric field is very low and largely achieved at 140 V over 1 mm distance between the contacts, therefore corresponding to 1400 V/cm.

However, we saw in the Introduction that the other required condition for a streaming motion to establish is $\frac{E_{min,2}}{B} \simeq \frac{V_{op}}{2}$. As a reminder, this situation corresponds to the limit when the orbit of motion of the carrier is tangent to the optical phonon's speed. Taking B = 3.5 T like in Fig. 5.11b situation, it reads $E_{min,2} \simeq 7.5$ kV/cm. If we compare to the most optimistic estimation of the electric field in Fig. 5.11b which gives 1.4 kV/cm (140 V between 1 mm-spaced contacts), we see that we are one order of magnitude too low for the streaming regime to be established. The most plausible explanation at this stage is that, owing to the absence of shaping (such as in a Hall bar), the current distribution within the sample cannot be controlled. Therefore, it is possible that locally, there is a tightening of the current lines and thus a local increase of the electric field. This makes it impossible to reproduce the result without more elaborate technological processing of the sample. Therefore, there is a need to shape the sample to better control the electric field.

5.2.4 Summary and perspectives

In this section we investigated a GaAs-based QW through magneto-transport, absorption and cyclotron emission. It revealed a quite unusual behavior as it showed a splitted CR line that we want to attribute to a splitting emerging from the hot carrier distribution in the sample, thus breaking the Kohn's theorem.

Strong crossed electric and magnetic field emission experiments showed that we could have reached a streaming regime in the material, leading to the onset of the laser effect. Unfortunately, due to the poor electric field control in our structure, these results could not be reproduced.

It is therefore natural to seek for professional process to shape the sample and control the field applied. Grating contacts could allow us to apply strong electric fields and reach a potential Landau lasing threshold. As a second perspective, we would like to implement a cavity pattern like introduced in the previous chapter. Indeed, this GaAs-based QW features a high electron mobility and thus the emission linewidth is reduced, compared to the one obtained in HgTe-based samples. Therefore, we can expect the threshold of a potential Landau polariton laser to be achieved at lower electric field strengths.

5.3 Toward a small gap and bulk III-V material

This section aims at presenting preliminary results on a superlattice (SL) structure made of stacks of InAs and GaInSb layers. This material was proposed with the purpose of obtaining a three dimensional system exhibiting a very rich topological phase diagram. Indeed, only by varying the respective InAs/GaInSb layers thicknesses, it was shown that is is possible to obtain a state of matter ranging from a trivial to a 3D topological insulator and a Dirac semimetal phase. It was achieved in II-VI materials [136, 137] where the authors could observe clear signatures of the Dirac nodes along with surface states, one of the characteristics

of 3D topological insulators. However, additionally to the fact that this semiconductor's family is highly sensitive to temperature rises, these structures are only 60 nm thick so it is hard to consider it as being truly three dimensional. Therefore this InAs/GaInSb SL aims at offering a true topological platform, more robust against high temperatures.

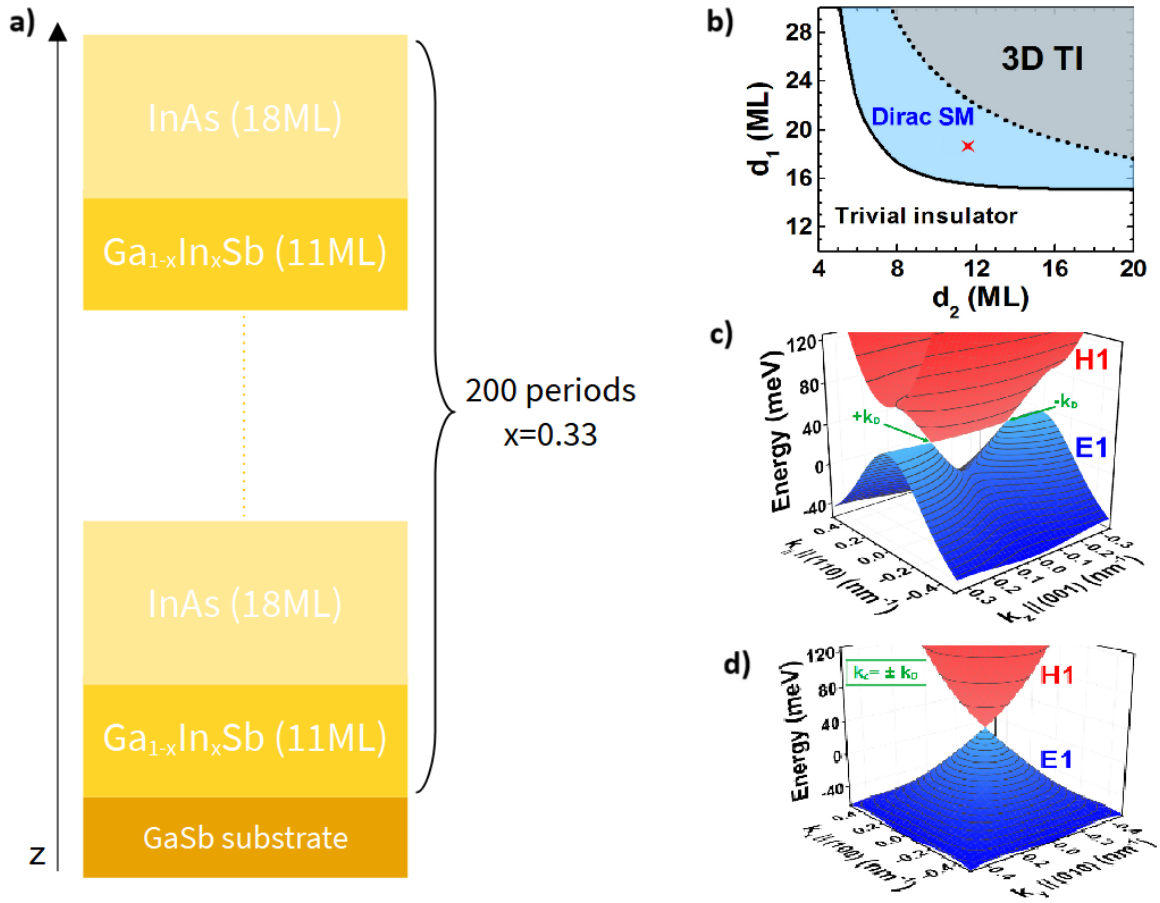

Figure 5.12: **Presentation of the InAs/GaInSb SL structure.** (a) Sketch of the epitaxial growth, made at the IES laboratory in Montpellier. ML stands for mono-layer. (b) Theoretical phase diagram obtained by the mean of k·p calculations. It displays three different phases (trivial, Dirac semi-metal and three dimensional topological insulator), accessible by varying the InAs (resp. GaInSb) thickness d_1 (resp. d_2). The red star locates the studied growth. (c) Theoretical bandstructure in the $k_{\parallel}/k_z$ plan (z being the direction of the growth and $\parallel$ standing for either x or y). The $\pm k_D$ identify the k_z values for which the two bands are touching. (d) Theoretical band-structure in the k_x/k_y plan for $k_z = \pm k_D$, displaying a Dirac cone.

5.3.1 Presentation of the structure

The SL was made at the IES laboratory in Montpellier and was grown on a GaSb substrate. It consists of the alternation of a $Ga_{1-x}In_xSb$ layer and an InAs layer where x = 0.33 (see Fig. 5.12a for a sketch of the structure). The SL's number of periods (ie the number of GaInSb/InAs bilayers) is 200. 8-bands k·p calculations where performed in the team to determine the bandstructure of this sample, depending on the layers thicknesses that can be summarized on the phase diagram displayed on Fig. 5.12b. Depending on the respective

thicknesses of the GaInSb and InAs layers, it leads to a different state, from a trivial insulator with a normal band ordering to a Dirac semimetal phase and finally a three dimensional topological insulator with an inverted band-structure. The structure examined here comprises a stack of 11 GaInSb monolayers and 18 InAs monolayers, yielding thicknesses of 3.3 nm and 5.4 nm, respectively. The red star of the diagram indicates the theoretical position of the considered growth and we therefore expect signatures of a Dirac semimetal. Figure 5.12c shows the theoretical bandstructure of this structure in the $k_{\parallel}$ (k_x or k_y) / k_z plan, where z is the growth direction. One can see that for the particular values $k_z \simeq \pm 0.118\ nm^{-1} \equiv \pm k_D$, the two bands are touching. The in-plane corresponding bandstructure is then plotted on Fig. 5.12d. At $k_z = \pm k_D$, the dispersion takes the form of a Dirac cone, which justifies the term Dirac semimetal phase. Therefore, this structure would be particularly well suited for Landau emission due to its strongly non-parabolic band structure.

5.3.2 Low-energy magneto-spectroscopy

Experimental results

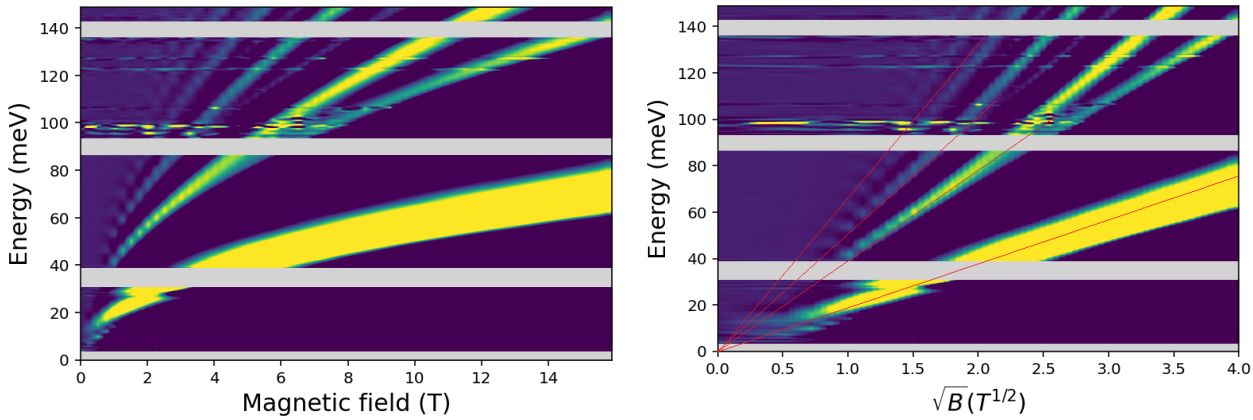

(a) (b)

Figure 5.13: **Magneto-transmission measurements obtained on the SL.** False-color mapping of the magneto-transmission spectra, obtained when tuning the magnetic field strength. It was plotted with respect to the (a) magnetic field and (b) square-root value of the magnetic field. The red solid lines are linear guides for the eye and the grey bands are absorption bands of either the substrate or the different optical component of the experimental set-up such as the beam-splitter or the different lenses.

To characterize the band structure of the SL, we performed transmission magneto-spectroscopy measurements. The results are shown in Fig. 5.13 as the form of false-color mappings of the transmission spectra. It displays four sets of very bright transitions, that evolves in a square-root-like behavior when increasing the magnetic field (Fig. 5.13a). It is evidenced more clearly on Fig. 5.13b where the same mapping is plotted as a function of the square-root of the magnetic field. It then exhibits a linear behavior, emphasized by the red solid lines that are guides for the eye.

A second noticeable aspect is that all the transitions are converging towards a small energy value (< 10 meV) when the magnetic field is extrapolated to zero. This suggests that we are observing inter-band LL transitions, from a system presenting a narrow gap in its

band structure. This is consistent with the previous observations of [35], where they studied a 3D topological insulator, featuring an almost flat hole band. The authors showed that the almost non-dispersive band pins the Fermi level in its vicinity. In our system, the E1 band is almost flat along the k_z direction and we can thus expect to have the Fermi energy lying close to the Dirac points.

We can also notice that the higher energy transitions are vanishing for magnetic fields below 1 T. This is another indication that the Fermi level is positioned slightly above the Dirac node, thus disactivating certain transitions at low field because of the filing of the upper LL involved in the transition. A better estimation will be done later on when looking at the precise LL dispersion. Finally, we can see that the LLs transitions are asymmetric in

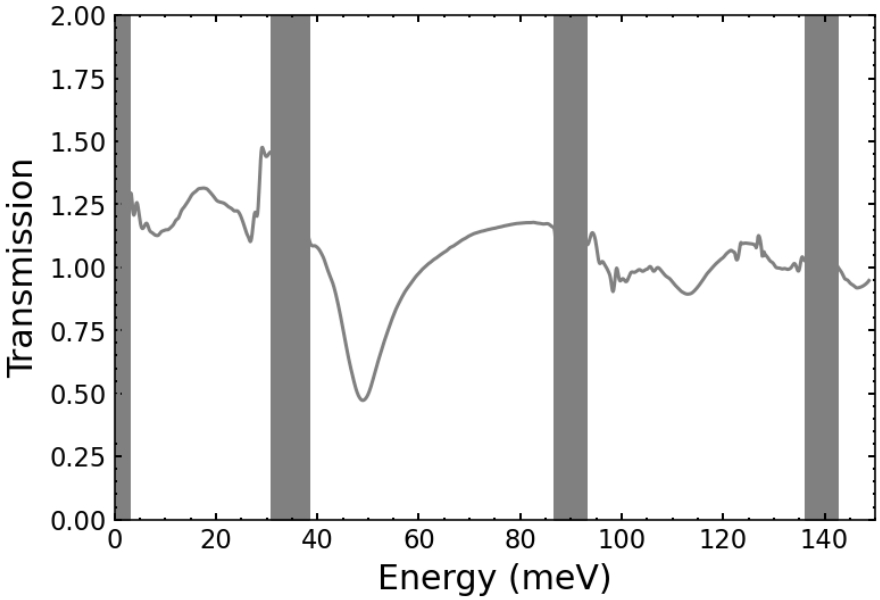

Figure 5.14: **Raw transmission spectrum obtained at 7.5 T.** It features an asymmetric minimum around 50 meV, typical from a 3D system absorption.

energy. Indeed, the first bright transition has a sharp low energy ending whereas it features a high energy tail. It is evidenced more clearly on the raw spectrum of Fig. 5.14, showing an asymmetric transmission minimum around 50 meV. This behavior, explained by the joint density of states and the shape of the Landau bands, is typical from 3D absorption as it has already been characterized in previous works [35].

Taken together, these observations strongly suggest that we are probing a low n-doped 3D Dirac system with a small energy gap, possibly arising from spin-orbit coupling associated with symmetry breaking. We will now try to interpret this within an 8-bands k·p framework.

Comparison with an 8-band k·p calculation

The first thing that we investigated is the joint density of state (JDOS) of the k_z dispersion. It is given by the following formula [138]

$$JDOS(\hbar\omega) = \sum_{k_z} \sum_{k_x,k_y} \delta\left(\hbar\omega - E_{cv}\right), \tag{5.4}$$

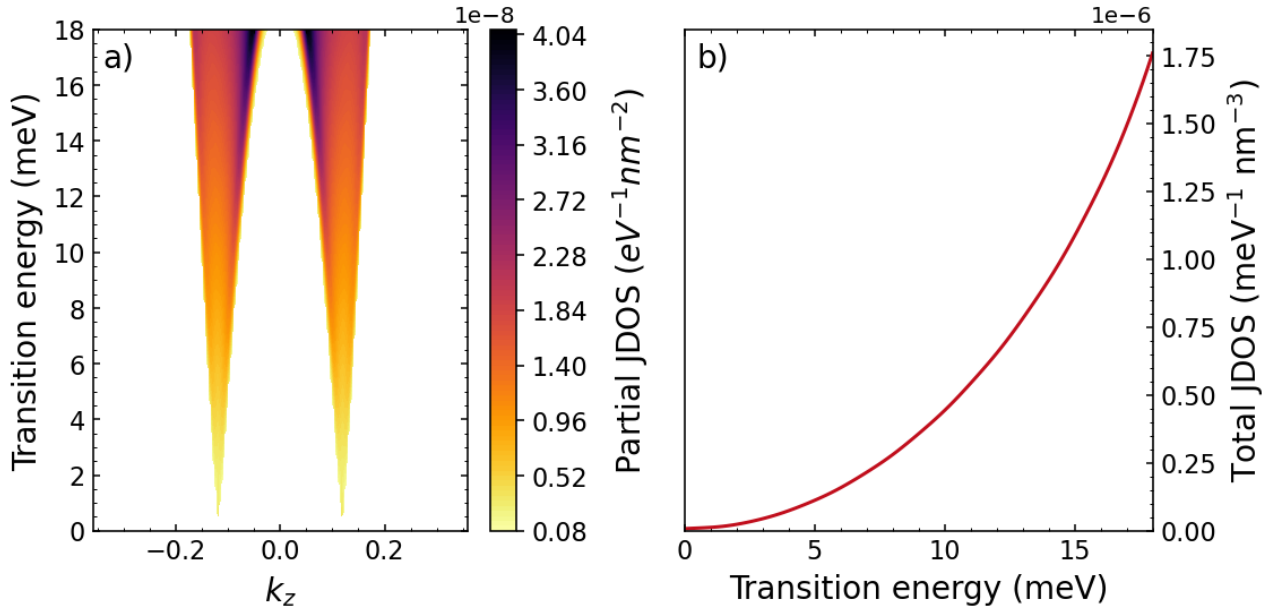

Figure 5.15: **Theoretical optical transitions.** (a) False-color mapping of the partial JDOS for different k_z and excitation energy values. (b) Evolution of the total JDOS with the excitation energy.

where $\hbar\omega$ is the excitation's energy and $E_{cv} \equiv E_c - E_v$ is the energy difference between the conduction and valence bands. The result at low energy is plotted on Fig. 5.15a as a false-color mapping of the partial JDOS, defined as the JDOS for a fixed value of k_z. If the total JDOS (Fig. 5.15b) does not exhibit any particular behavior, it is clear from Fig. 5.15a that the major contributions arise from k_z values close to k_D. This is valid only at low excitation's energies but when looking at the magneto-absorption mapping, we continuously follow the transitions towards low energy. Therefore, by continuity, we can assume that these emerge from $k_z \simeq k_D$ LLs.

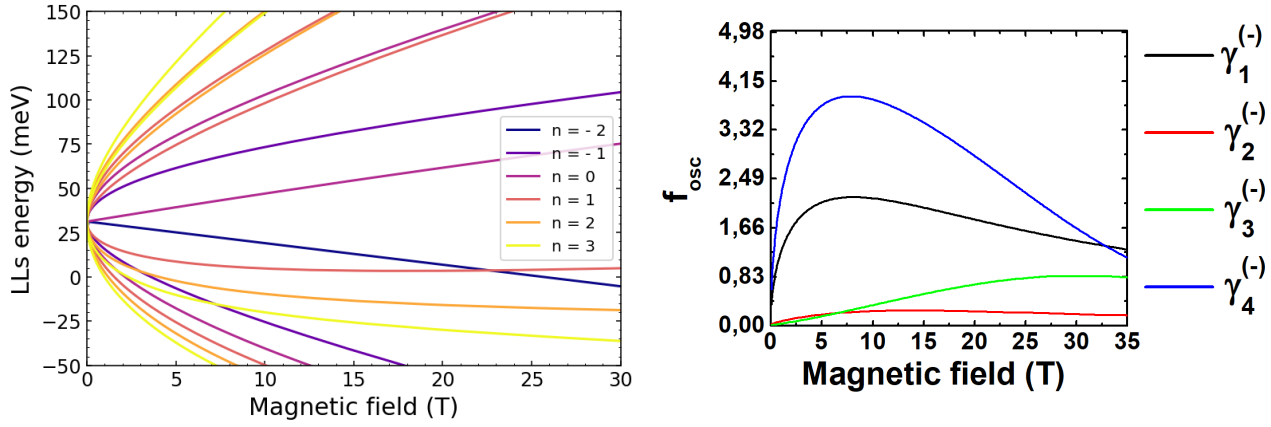

(a) (b)

Figure 5.16: **LLs fan-chart and oscillator strength.** (a) Theoretical Landau-level fan chart for $k_z = \pm k_D$. (b) Example of oscillation strength calculation for the $\gamma^{(-)}$-type transitions.

The above argument tends to attest that we can capture most of the optical properties of the material by computing the Landau levels only at the particular $k_z = k_D$ point of the band structure (see Fig. 5.16a).

From the LLs fan chart we can now try to determine which transitions come to play. Since linear polarized light was used, it is natural to consider $\Delta n = \pm 1$ transitions where n is the index of the Landau level. From all these possible transitions, we can select only the strongest ones by evaluating their respective oscillator strength, defined as follow [138]

$$f_{osc}^{n\to m} = \frac{2m_0}{\hbar^2} \frac{\left|\langle m|\frac{\partial \hat{H}}{\partial k}|n\rangle\right|^2}{E_m - E_n}, \tag{5.5}$$

where $\langle n|$ (resp. $\langle m|$) is the wave function of the initial (resp. final) state involved in the transition, associated with the LL energy E_n (resp. E_m). Figure 5.16b shows an example of

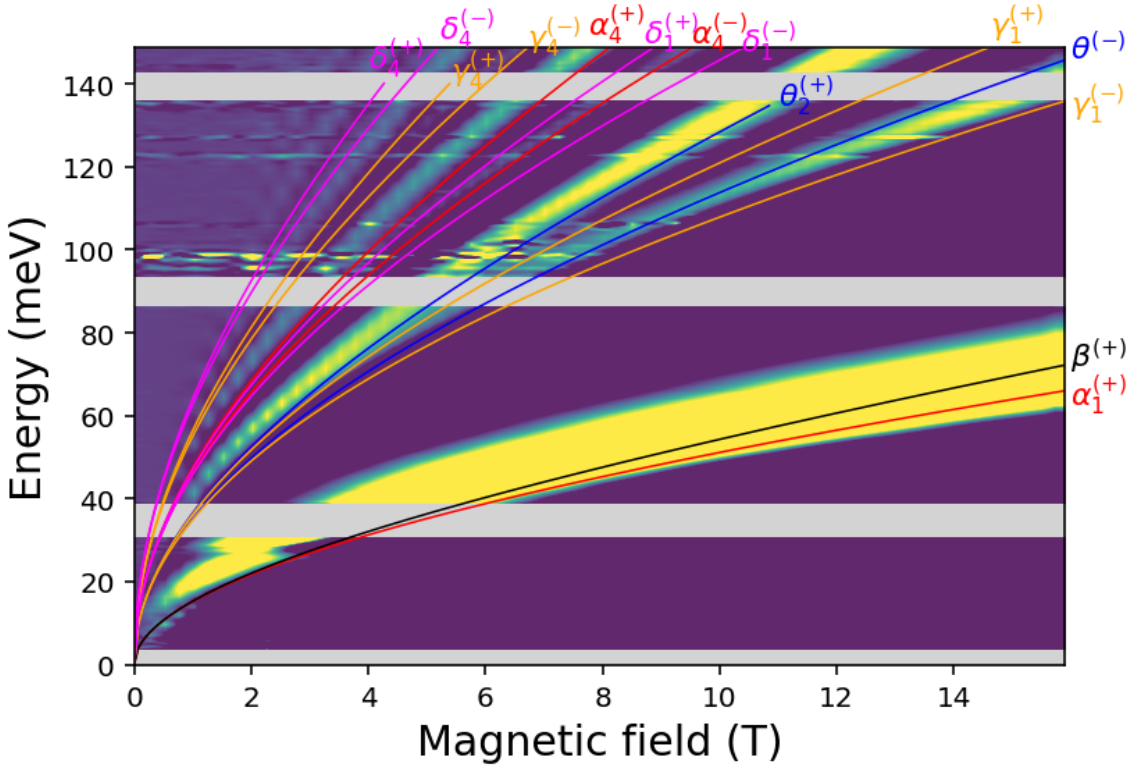

Figure 5.17: **Theoretical optical transitions and comparison.** Theoretical transitions previously selected considering there oscillator strengths (solid colored lines). The false-color magneto-transmission mapping is plotted in the background for comparison.

such a calculation for the $\gamma^{(-)}$-type transitions (n = 2 → m = 1), for a wide range of magnetic fields. One can identify two strong transitions, that are $\gamma_1^{(-)}$ and $\gamma_4^{(-)}$, where the two others are rather weak. We can therefore select only the two strong ones. Table 5.1 explains how the transitions labels were chosen. Figure 5.17 shows the final results compiling the experimental mapping along with the theoretical selected transitions. One can see that there is an overall very good agreement between experiment and theory, strengthening the idea that we have a Dirac phase inside the superlattice.

It also shows that what we previously interpreted as splittings were actually energy close transitions. Indeed, all the identified transitions are giving slightly different energies be-

tween Δn = +1 et Δn = -1 cases, reflecting the electron-hole asymmetry in the structure. Finally, it is noticeable that all the theoretical lines lie below the experimental ones. This could be due to the fact that no gap was taken into account in the model. As mentioned earlier, all the transitions are extrapolating at a finite energy at zero magnetic field thus witnessing the presence of a gap. The consideration of this narrow gap further improve the accordance between theoretical and experimental results.

One last thing that we can deduce is the Fermi level position. As mentioned previously, the higer energy transition vanish for magnetic fields below 1 T. These transitions are now identified and looking at Fig. 5.16a, the only way to continuously see transitions $\alpha_1^{(+)}$ or $\beta^{(+)}$ but not the other ones is to have the Fermi level lying around 50 meV.

Label	α	β	θ	γ	δ
$\mathbf{n \leftrightarrow m}$	n = 0, m = 1	n = -2, m = -1	n = -1, m = 0	n = 1, m = 2	n = 2, m = 3

Table 5.1: Transition labeling conventions. An exponent (+) (resp. (-)) is added to indicate a transition $n \rightarrow m$ with n < m (resp. n > m).

5.3.3 High-energy magneto-spectroscopy

To further investigate the structure, we then performed magneto-transmission experiments at the LNCMI-G laboratory, in M. Orlita's group. Their unique facilities allowed us to reach higher energies and magnetic field up to 35 T.

The results are presented on Fig. 5.18 as a false-color mapping. In addition to the previously identified square-rootish transitions, we can now observe resonances at higher energies. This set of transitions evolve linearly when increasing the magnetic field strength and all extrapolate at the same energy value of around 309 meV at zero field. This suggests that these resonances come from a conventional semiconductor system with a gap value close to 300 meV.

A way to understand this set of transitions is to look at the full band-structure of the super-lattice. Indeed, in addition to the E1 and H1 bands, there is a third band of light-holes LH1 that lies far below the two first in terms of energy. When we look at the gap between LH1 and H1 for the considered structure, we find 257 meV at $k_z = 0$. However, this value was obtained using k·p calculations with a model that does not include any interface inversion asymmetry (IIA). It was indeed shown that this asymmetry plays an important role in these kind of heterostructures [139, 140] and this could be exacerbated in MBE-grown superlattices where the interfaces are very sharp and are present in large numbers. This IIA term induces a spin splitting of the bands into two subbands thus implying an increase of the effective gap at $k_z = 0$. This symmetry breaking could also explain the previously identified gap when extrapolating the low-energy transitions to zero magnetic field. Therefore, including this IIA term into the model could allow us to fully describe the magneto-transmission mapping obtained on this SL.

Another potential explanation would be that these transitions are emerging from the InAs cap layer. Indeed, these transitions are crossing the ones of the SL, indicating that there is no interactions between the two systems. We also saw that all the lines are extrapolating at 309 meV at zero magnetic field, value that is not too far from the gap value of InAs at low temperature (around 400 meV [141, 142]). Even though the InAs band gap value is rather far, it would still be interesting to measure this sample again, after having the cap removed.

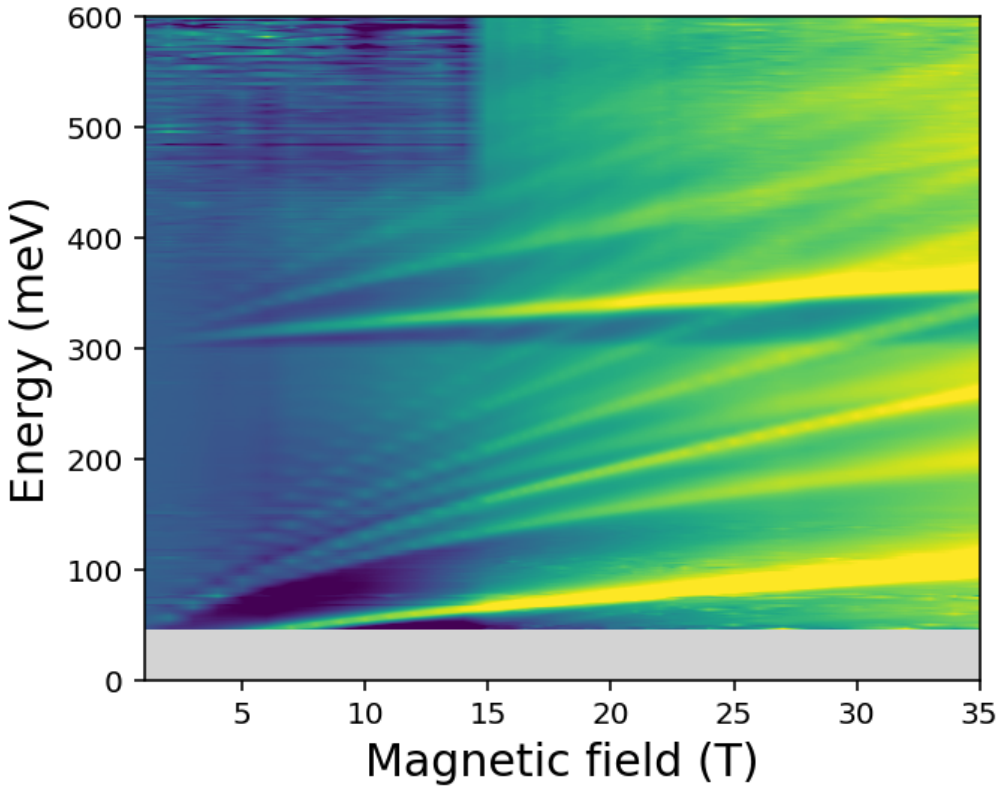

Figure 5.18: **High-energy magneto-transmission measurement on the SL.** False-color mapping of the magneto-transmission measurements obtained on the studied SL. It was performed using a Silicon beam-splitter to reach high energies. The magnetic field could be tuned up to 35 T thanks to the LNCMI-G facilities.

5.3.4 Magneto-transport measurements

We also performed magneto-transport measurements on this superlattice structure. In addition to providing interesting characteristics of the material, it is a powerful tool to probe the nature of the band-structure.

Low-temperature magneto-transport

I first carried out magneto-resistance measurements at low temperature. It was done using an Helium 3 insert that allows us to reach 300 mK. The sample was contacted by soldering Indium balls at its surface, in a Van der Pauw geometry. Figure 5.19a displays the evolution of the resistance when tuning the magnetic field strength, perpendicular to the sample's surface. It features clear Shubnikov-de Haas oscillations (SdHO) on top of a monotonic background evolution of the longitudinal resistance. This background could result from the fact that, given the VdP geometry with non-ideal contacts, an increase of the magnetic field induces a longer path for the carrier to travel and thus a higher resistance [143]. Another possible explanation is the presence of multiple carriers that induces a quadratic magnetoresistance increase [144]. When looking at the behavior of the Hall effect on Fig. 5.19b, two different slopes are evidenced, indicating that two n-type carriers are present in the system thus making the second explanation plausible.

Nonetheless, SdHO are visible attesting for the good quality of the sample. We can ex-

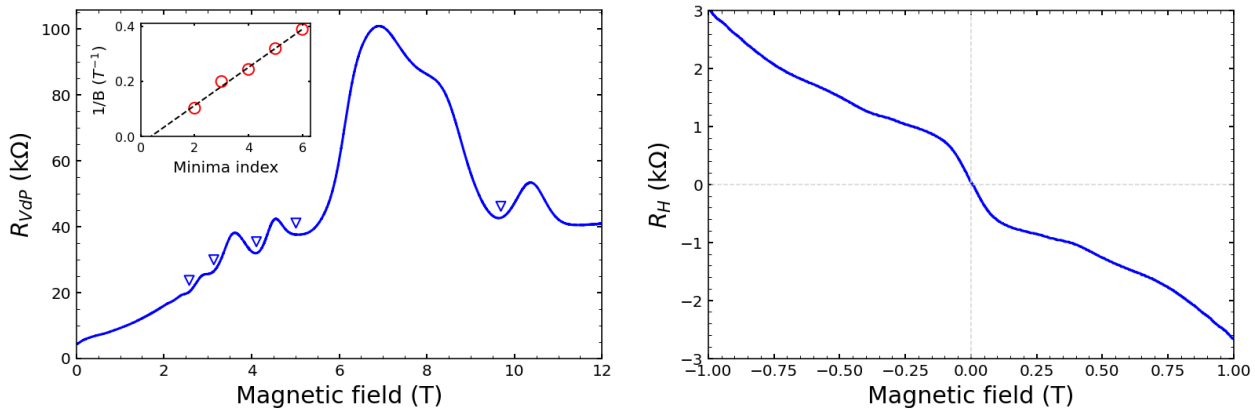

(a) (b)

Figure 5.19: **Magneto-transport measurements on the SL at 300 mK.** (a) Four-probe Van der Pauw longitudinal resistance measured when tuning the magnetic field value, perpendicular to the sample's surface. In insert in plotted the extracted inverse magnetic field corresponding to the minima of the oscillation, used to determine the carrier density. (b) Corresponding low-field Hall resistance.

tract a carrier density via the position of the minima's position (see insert of Fig. 5.19a) and we found n = 3.5 $\times$ 10^{11} cm^{-2}. This density seems really high and not coherent with the previous magneto-transmission results. Indeed, the overall evolution of the Hall resistance on Fig. 5.19b gives us a negative slope which for this measurement corresponds to a n-type of carriers. According to the density value that we just extracted, it would mean that for a magnetic field value of 1 T, $\nu = \dfrac{n}{eB/h} \simeq 15$. However, if we look at the lowest energy transition on Fig. 5.16b, it is either $\alpha_1^{(+)}$ or $\beta^{(+)}$. Thus, it implies that the LLs number 2 or 3 should be empty for the transitions to be possible. A possible density for the $\beta^{(+)}$ transition to be visible at 1 T would be 5 $\times$ 10^{10} cm^{-2}. Therefore the density extracted from the transport measurements is way too large to be coherent with the optical experiments.

Temperature dependence of the SdHO

To further characterize the sample, we then performed temperature dependent magneto-resistance measurements. For this purpose we used a Variable-Temperature-Insert (VTI) that allowed us to tune the temperature from 3 to 40 K. The results are presented in Fig. 5.20a, where only the curves from 8 to 25 K are presented. We can see that the amplitude of the SdHO is damped when the temperature rises. From this evolution we can extract the effective mass of the material, using the Lifshitz-Kosevich (LK) formula [145]

$$\frac{\Delta R(T,B)}{\Delta R(T_{ref},B)} = \frac{T\ \sinh(2\pi^2 k_B T_{ref} m^*/\hbar eB)}{T_{ref}\sinh(2\pi^2 k_B T m^*/\hbar eB)}, \tag{5.6}$$

where $\Delta R(B,T)$ is the SdHO amplitude at a magnetic field B and temperature T, k_B the Boltzmann constant, T_{ref} a reference temperature taken in the data-set and m^* the effective mass of the material.

We extracted the amplitude for two sets of oscillations, around 5 and 7 T (see black and red points on Fig. 5.20a), and the results are plotted in figures 5.20b and c, along with the

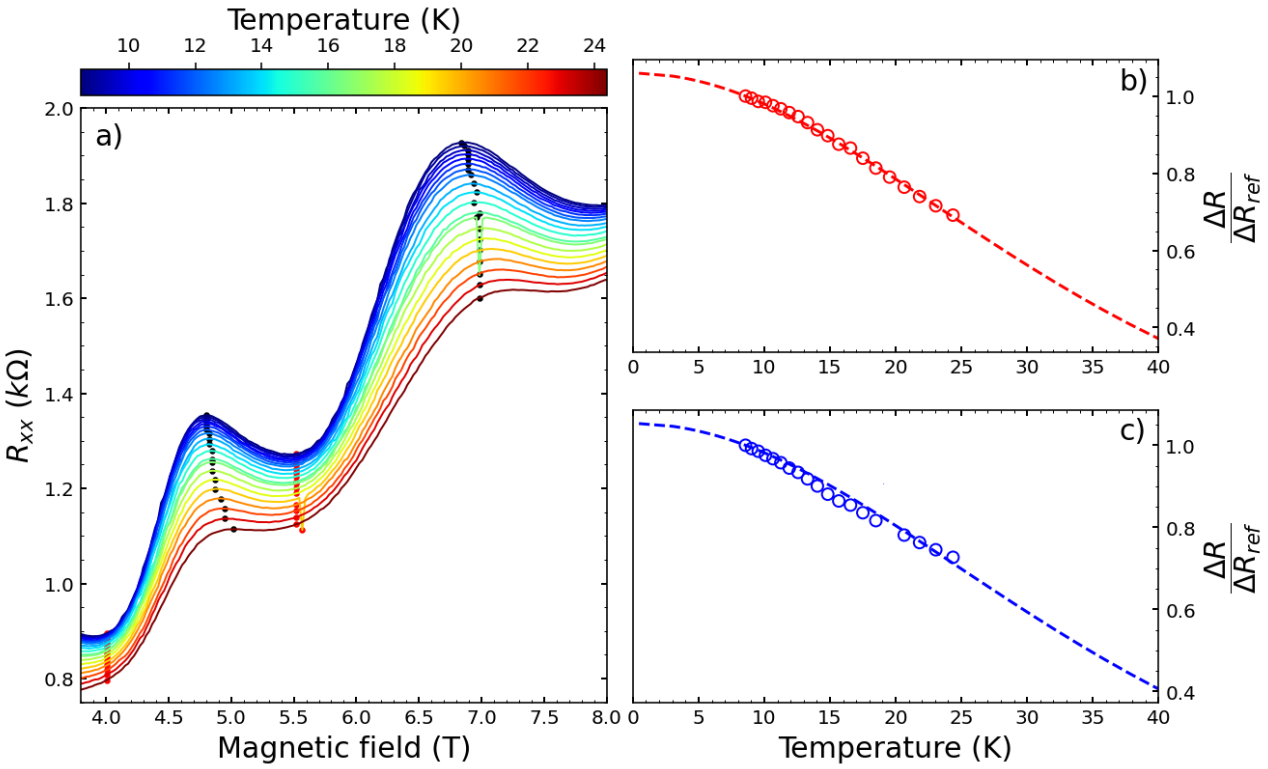

Figure 5.20: **Temperature dependence of the SdHO.** (a) Longitudinal magneto-resistance for temperature values ranging from 8 to 25 K. The black (resp. red) points shows where the maximum (resp. minimum) value of resistance was taken for each temperature. (b) (resp. (c)) Evolution of the amplitude of the considered peak around 5 T (resp. 7 T) when tuning the temperature. The dashed line is the result of the LK fitting.

best fit using formula 5.6 with T_{ref} = 8.5 K. The fittings are good and gives an average mass value of m^* = 0.0268 m_0 (0.0237 m_0 at 5 T and 0.0298 m_0 at 7 T). Given the strong magnetoresistance background, it is hard to evaluate the true amplitude of the SdHO. Therefore, this mass value is to be taken as an order of magnitude more than a precise value. At this stage, it is worth noting that this value is really close to the value of 0.026 m_0, expected for a pure InAs system [141, 142]. Combined to the fact that we see two sets of SdHO in the magneto-transport experiments, it strongly suggests that the InAs cap layer brings an important contribution in the measurements.

Magneto-transport in a titled field

Finally, we performed magneto-transport measurements for various angle of the magnetic field. This is is a very useful way to have insights on the nature (2D or 3D) of the structure that we probe. Indeed, the period of the SdHO is given by the extreme cross-sections of the Fermi surface in the plane normal to the magnetic field [43]. Therefore, by rotating the magnetic field direction and determining each SdHO period, it is possible to reconstruct the Fermi surface and have information on the band-structure of the material. An example of 3D Fermi surface is plotted in Fig. 5.21. It has a rugby ball shape and therefore, if we go from a situation where the magnetic field direction is aligned with the growth direction (Fig. 5.21a) to a situation where the field is in the plane (Fig. 5.21b), we expect an increase of the Fermi cross-section and thus a decrease of the SdHO's period.

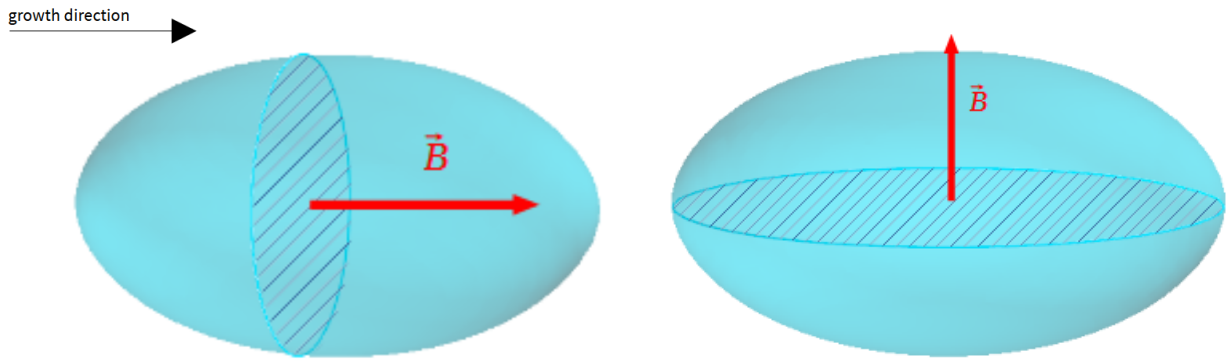

(a) (b)

Figure 5.21: **Probing the Fermi surface via titled-field measurements.** Example of 3D Fermi surface (cyan surface). Two extreme magnetic-field configurations are represented: (a) the field is perpendicular to the sample's growth direction and (b) the field is is the plane of the sample. The dashed area are the extreme cross-sections of the Fermi surface, determining the SdHO's period.

Figure 5.22a shows the measured longitudinal magnetoresistance for field directions ranging from 0° to 80°, where the angle is taken with respect to the normal of the the sample. We can see that the SdHO remains as we increase the field direction's angle. Figure 5.22b shows the evolution of the density, extracted from the SdHO's period, as a function of the angle. The prediction for a pure 2D system is plotted as a comparison (black dashed line). Indeed, in the latter case, the density is constant and the SdHO's period should be

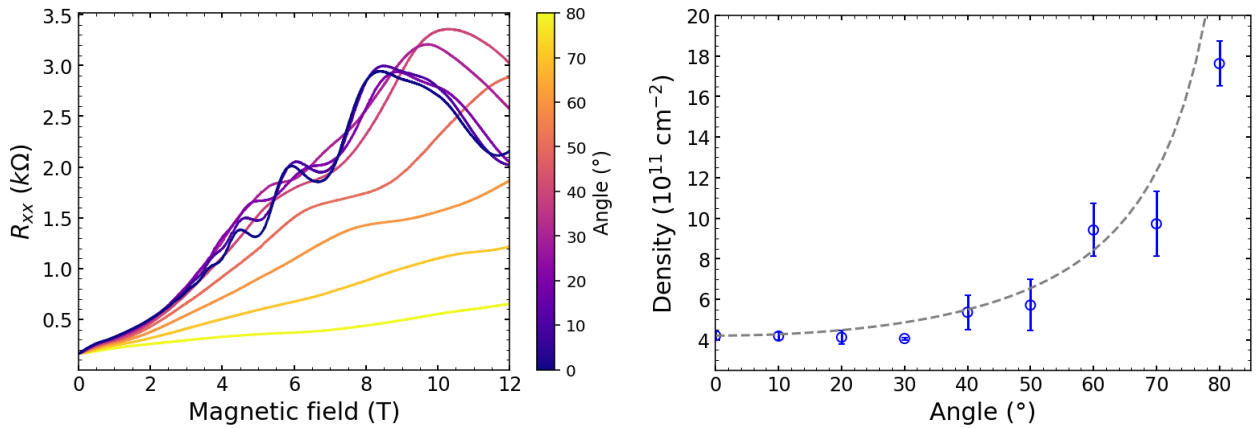

(a) (b)

Figure 5.22: **Magneto-transport experiments at various field angles.** (a) Longitudinal magneto-resistance evolution for a field direction varying from 0 to 80°. (b) Evolution of the SdHO-extracted density with respect to the field direction (blue empty circles). The uncertainties are given for 3 sigmas. The grey dashed line is the predicted evolution for a pure 2D system.

only determined by the perpendicular component of the magnetic field. Therefore it reads:

$$n_{2D} = \frac{e}{h \cdot \Delta\left(\frac{1}{B_\perp}\right)} = \frac{e}{h \cdot \Delta\left(\frac{1}{B\cos\theta}\right)} = \frac{e}{h \cdot \Delta\left(\frac{1}{B}\right)} \cos\theta = n(\theta)\cos\theta \tag{5.7}$$

where θ is the magnetic field direction's angle, $B_\perp$ is the field projection on the normal direction of the sample, n_{2D} is the system's density, also equal to the density at $\theta = 0$ and $n(\theta)$ is the density extracted from the SdHO. The good accordance of the experimental data with the 2D prediction strongly suggest that the system that we are probing has a 2D band structure. This is another indication that we could be probing the InAs cap layer. Therefore, we tried to remove this protecting layer and perform these measurements once again.

Magneto-transport after removal of the cap layer

The InAs cap layer was removed by wet chemical etching, performed by Dr. Salah Benlemqwanssa, using a $H_3PO_4/H_2O_2/H_2O$ solution in a 2:1:2 ratio. For InAs, the etching rate was approximately 1.1 μm/min. The etching duration was approximately 10 s, so the cap layer is certainly removed. After etching, the sample was contacted using the same procedure as described previously.

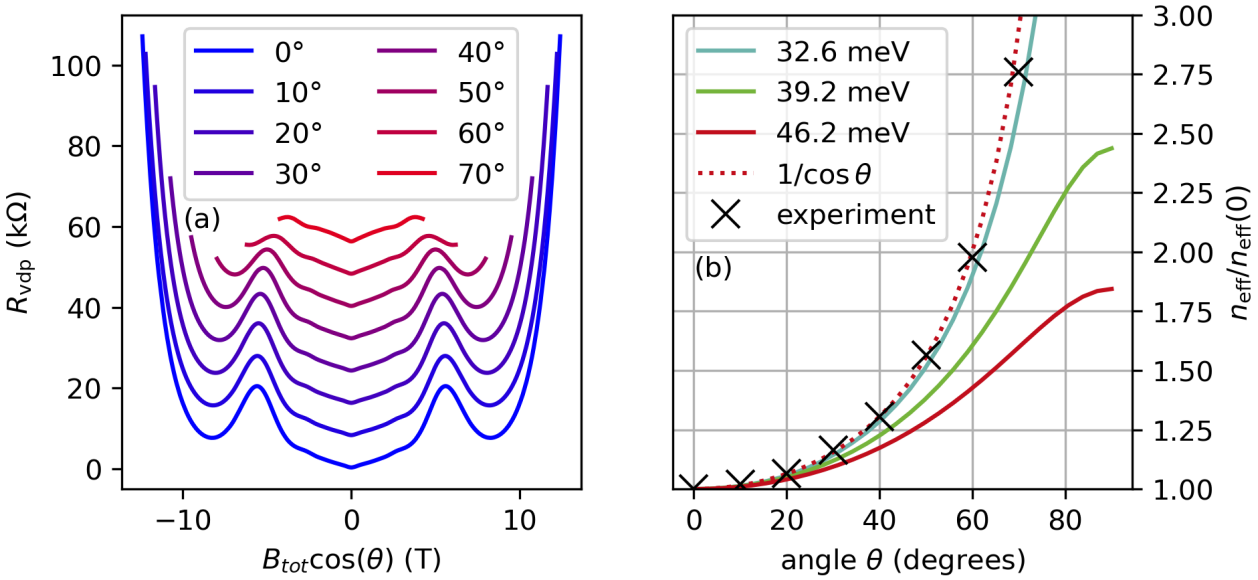

Figure 5.23: **Angle dependence of the SdHO without cap layer.** (a) Magnetoresistance as a function of $B_{\text{tot}}\cos(\theta)$, where θ is the angle of the magnetic field with respect to the z direction. The curves have been shifted vertically for clarity. (b) Calculated normalized effective carrier density $n_{\text{eff}}(\theta)/n_{\text{eff}}(0)$, for three different values of the Fermi energy reported in Fig. 5.24. The experimental values $n_{\text{eff}}(\theta)/n_{\text{eff}}(0)$ extracted from the SdHOs shown in (a) are reported as black crosses.

Figure 5.23a presents magnetoresistance measurements obtained after removal of the cap layer. A key observation is that the fast component of the SdHOs previously observed in R_{vdp} has disappeared, leaving only the slower oscillations (see 0° curve of 5.23a). This strongly suggests that the doped InAs cap layer was successfully removed. Nevertheless, a detailed inspection of the Hall resistance (not shown here) still indicates the presence of at least two types of carriers.

In the following, we restrict the analysis to the main SdHO peaks observed in R_{vdp}. From the positions of the resistance maxima at $B \approx 2.5$ T and $B \approx 5.5$ T, we extract an effective

electron sheet density of

$$n_s = \frac{e}{h}\left[\Delta(1/B)\right]^{-1} \approx 1.1 \times 10^{11}\,\mathrm{cm}^{-2}. \tag{5.8}$$

This density is in better agreement with the low Fermi energy values previously deduced from magneto-transmission experiments. To interpret these results, Fig. 5.24 shows the calculated band structure of the SL in reciprocal space, together with representative Fermi surfaces. The band structure was evaluated from a k·p calculation. For different assumed Fermi energies, we evaluated the effective 2D carrier density that would be inferred from SdHO measurements with the magnetic field applied along B_z. In this configuration, the SdHOs probe the Fermi surface cut at $k_z = 0$.

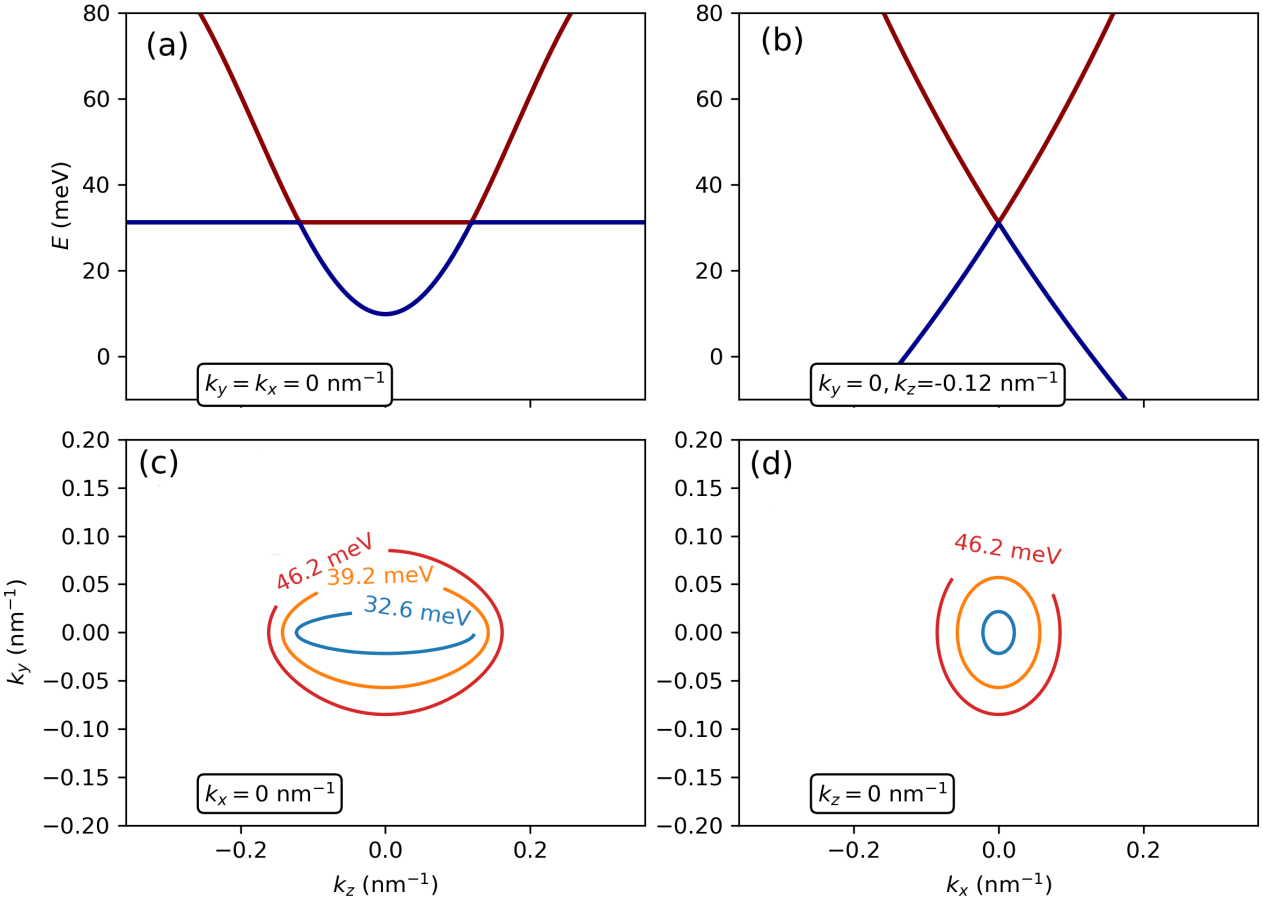

Figure 5.24: **Iso-energy at the Fermi level for different field directions.** (a) Band dispersion along k_z at $k_x = k_y = 0\,\mathrm{nm}^{-1}$. (b) Band dispersion along k_x at $k_z = 0.12\,\mathrm{nm}^{-1}$, which corresponds to the zero-gap location. (c) Slices of the Fermi contour at three different values of the Fermi energy: $E = 46.2$ meV (red), 39.2 meV (orange), and 32.6 meV (blue), at $k_x = 0\,\mathrm{nm}^{-1}$. The conduction band edge is at 31 meV. (d) Similar slices at $k_z = 0$.

For $E_F - E_c^{\min} = 1.4$ meV, 8 meV, and 15 meV ($E_c^{\min} = 31.2$ meV being the bottom of the

conduction band, at $k_{\parallel} = 0$ and $k_z = \pm k_D$), the calculated densities are

$$n_s = 7.4 \times 10^9 \,\mathrm{cm}^{-2}, \tag{5.9}$$
$$n_s = 5.2 \times 10^{10} \,\mathrm{cm}^{-2}, \tag{5.10}$$
$$n_s = 1.15 \times 10^{11} \,\mathrm{cm}^{-2}, \tag{5.11}$$

respectively. The highest value is close to the experimentally observed SdHO periodicity. The corresponding 3D carrier density is numerically estimated as $n \approx 5 \times 10^{16}$ cm^{-3}.

We then simulated the evolution of the Fermi level with increasing B_z for this concentration. The calculation could be performed as the k·p band structure was first fitted by a BHZ Hamiltonian, whose parameters depend on k_z (see Appendix A). The electrochemical potential $\mu(B)$ is shown in Fig. 5.25 as an orange line. At low fields, $\mu(B)$ follows the Landau levels (LLs) near $k_z = 0$ (dashed red lines), consistent with semi-classical expectations. At higher fields, $\mu(B)$ becomes strongly pinned to a zero-mode LL of hole character, whose energy decreases with B_z, due to the large density of states in this region. Around $B \approx 8$ T, $\mu(B)$ crosses the second zero-mode LL. This should produce an additional SdH peak. At

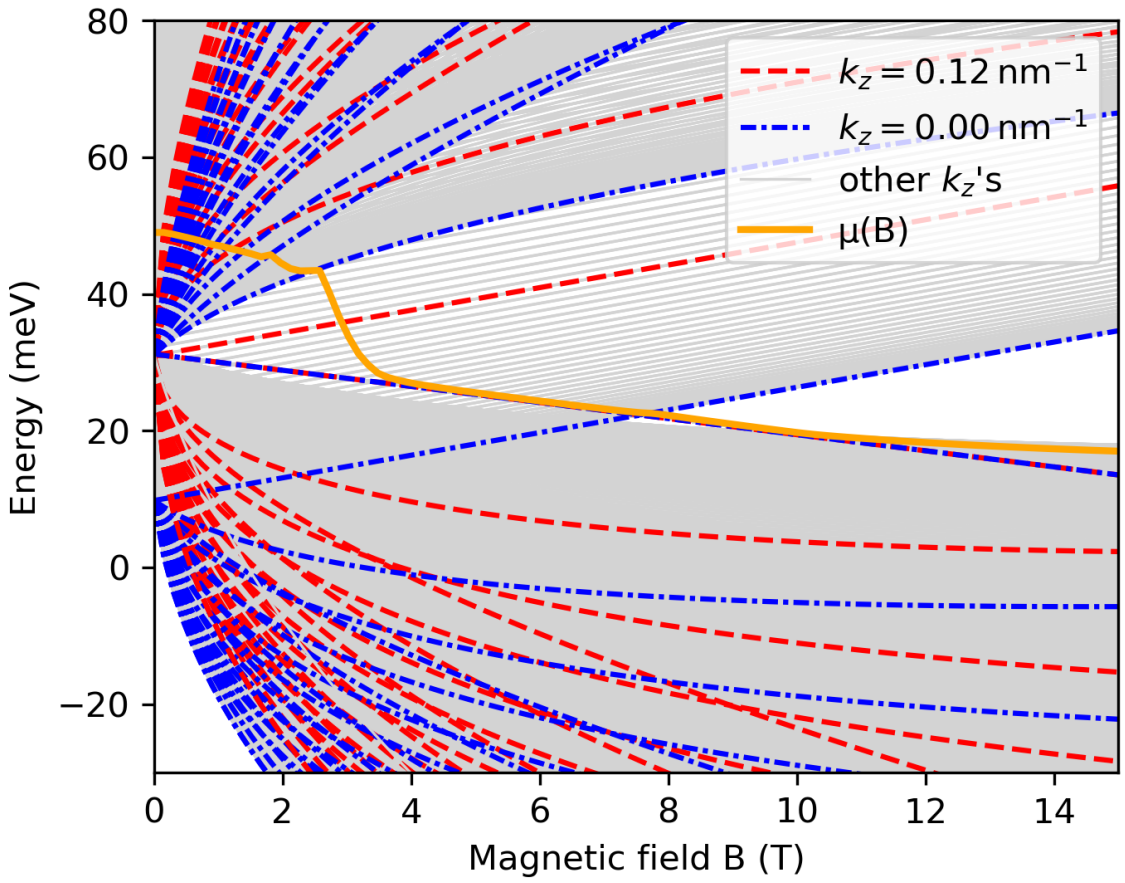

Figure 5.25: **Chemical potential evolution with magnetic field.** Energy of the Fermi level $\mu(B)$ as a function of the magnetic field applied along the z direction. The Landau level (LL) dispersion at specific slices of the k_z momentum are highlighted: in blue for $k_z = 0\,\mathrm{nm}^{-1}$, and in red for $k_z = 0.12\,\mathrm{nm}^{-1}$ (the zero-gap position), showing the pinning of $\mu(B)$ at the $k_z = 0$ density of states. The other LLs at different k_z values are shown in grey, evidencing the pinning of $\mu(B)$ in a normal gap above $B = 8\,\mathrm{T}$.

still higher fields, $\mu(B)$ enters a trivial insulating gap, and $\mu(B)$ becomes pinned due to a high degeneracy of states on the low energy side of that gap. The absence of available states in this region is illustrated in Fig. 5.25 (grey lines), showing the LL dispersion at all k_z with a step $\Delta k_z \approx 0.015\,\mathrm{nm}^{-1}$.

Within this simple model, we approximately reproduce the positions of the last two observed SdHO peaks (2.5 T for the first, and around 8 T versus the experimental 5.5 T for the second). Moreover, the model naturally explains the clear magnetic-field-induced metal-insulator transition seen experimentally. In view of Fig. 5.25, this transition has the character of a topological metal-insulator transition.

To further test this interpretation, SdHO measurements were performed with the magnetic field tilted by an angle θ. The effective carrier density was extracted from the oscillation period as

$$n_{\mathrm{eff}} = \frac{e}{h}\left[\Delta(1/B)\right]^{-1}. \tag{5.12}$$

We find that $n_{\mathrm{eff}}(\theta)/n_{\mathrm{eff}}(0)$ follows very closely a $1/\cos\theta$ dependence (Fig. 5.23b), which is characteristic of a 2D electronic system, rather than a quasi-3D bulk state. For comparison, Fig. 5.23b also shows the calculated $n_{\mathrm{eff}}(\theta)$ for the three Fermi energies considered above. For the case $n_{\mathrm{eff}}(\theta = 0) \approx 1.15 \times 10^{11}\ \mathrm{cm}^{-2}$, the calculation predicts a strong deviation from the $1/\cos\theta$ trend, which should have been experimentally observable.

We cannot conclude on the exact origin of the SdHOs at this stage. On the one hand, the used semiclassical model is not valid in strong magnetic field, and especially cannot reproduce the peculiar crossing of the zero-mode LLs. Thus an apparent 2D $1/\cos(\theta)$ behavior could possibly be explained by an adequate model taking into account the real evolution of the band structure in tilted magnetic field. On the other hand, a possible way to interpret these results would be the presence of surface states at the top of the SL. Indeed, it was extensively demonstrated that semiconductor superlattices can host Tamm states [146–148]. These states have a 2D nature and could explain these unexpected results.

5.3.5 Summary and perspectives

In this subsection we performed magneto-absorption and transport measurements on a InAs/GaInSb superlattice. We managed to show that this sample is hosting an exotic topological phase in which lies massive 3D Dirac fermions. The 2D nature of the SdHOs is nonetheless quite puzzling and could be interpreted as surface electronic states. Further theoretical investigations are needed. Finally, the presence of a gap in the system is still unclear, but including a symmetry breaking term in the Hamiltonian could help us understand this aspect.

On the other hand, what is more disappointing is the total absence of observable emission from this system. Since this SL hosts a highly non-parabolic band structure, we were expecting this system to be a good candidate for Landau emission experiments. More generally, we never observed any THz emission from ternary III-V alloys such as GaInSb or InAsSb. This absence of emission is still an open question at the moment.

Chapter 6

Conclusion and perspectives

During my PhD work, I first had the opportunity to continue the study initiated by *S. Gebert et al.* on Landau emission in HgTe-based quantum wells [33]. I confirmed that these II–VI structures constitute an excellent platform for investigating cyclotron emission. The strong non-parabolicity of their band structure leads to a pronounced dependence of the cyclotron mass on the electron density. As a result, I demonstrated that the emitted frequency can be tuned through a back-gate bias in a single quantum well and at relatively low magnetic fields. On this basis, the first continuously electrically tunable THz light emitting diode was designed and fabricated. This result establishes a new approach for achieving voltage-controlled THz emission in solid-state systems. A natural next step would be to implement a more efficient gating scheme on a device with lower intrinsic doping.

I also investigated the effect of strong crossed electric and magnetic fields. The purpose of these experiments was twofold: to explore the possible onset of a streaming regime, and to probe potential relativistic-like effects in these structures as the Lorentz boost. A clear shift of the cyclotron emission was observed with increasing electric field, originating from the pronounced non-parabolicity of the band structure. As carriers gain energy and occupy higher states in the conduction band, the Landau levels become more closely spaced and the transition energy decreases. This effect can be interpreted as an increase in the effective mass of hot electrons, resulting in the measured redshift of the cyclotron emission. This study once again emphasized the need for improved control over the applied electric field, as well as the ability to increase it sufficiently to reach regimes such as carrier streaming or Lorentz boost.

The main objective of my PhD was to explore an alternative route to achieving a lasing effect, without relying on population inversion and the associated strong electric fields. We discovered that, by reducing the substrate thickness below the emitted wavelength, an intrinsic optical cavity effect can be induced within the device. Through magneto-reflectivity experiments, we demonstrated that these optical modes efficiently couple to the cyclotron resonance of the two-dimensional electron gas, leading to the formation of Dirac Landau polaritons. This strong light–matter coupling was observed and thoroughly characterized across multiple samples, confirming the robustness of the phenomenon. Most importantly, these hybrid quasiparticles were found to emit in the THz range. The position of the emission maxima shows excellent agreement with the reflectivity spectra, providing compelling evidence that the observed signal corresponds to the electroluminescence from Dirac–Landau polaritons. Using three different complementary models, each relying on distinct experimental findings (namely the emitted power evolution with the injected power and the spec-

tral narrowing), we were able to estimate the polariton population, showing that our system operates close to the lasing threshold. The natural continuation of this work is therefore the development of a more efficient optical cavity, combining great quality factors and small effective mode volumes. Although several approaches for improvement were explored, the performance of our current cavities could not be significantly enhanced. Ongoing collaborations are expected to provide access to highly efficient cavity designs capable of coupling more effectively to the cyclotron radiation.

I concluded this manuscript with an exploratory chapter dedicated to the potential of the III–V material family. In this last part, I demonstrated that Landau emission can be observed from InSb-based quantum wells, which also exhibit a strongly non-linear band structure. I developed and tested several approaches to achieve ohmic contacts on these structures. I then explored the possibility of inducing light–matter coupling in this system using a metamaterial approach, which appears promising for further studies. In addition, I demonstrated cyclotron emission from GaAs-based quantum wells. Although this material exhibits a parabolic band structure, its high carrier mobility makes it a compelling platform for investigating population inversion through streaming effects. Interestingly, when increasing the applied electric field, a structuring of the emission line was indeed observed. This feature resembles a comb-like pattern that could be attributed to stimulated emission, which would only occur if the actual electric field inside the device were significantly higher than our estimated values. Further optimization of the electrical injection is therefore required to confirm these preliminary observations. In addition, integrating a Fabry–Perot cavity or a Tamm cavity would be highly beneficial for studying Landau polariton emission. The simpler processing technology of these III–V structures, combined with their higher carrier mobility, could lead to cavities with larger quality factors than what was obtained in HgTe QW-based systems. This would open the way to probing Bose–Einstein condensation and stimulated emission in the strong coupling regime. Finally, I investigated a three-dimensional superlattice material exhibiting a highly exotic band structure. Magneto-optical characterization revealed that this system hosts a Dirac semimetal phase. However, transport and emission measurements indicated that the electrical contacts do not efficiently probe the entire structure. Advanced processing techniques will therefore be necessary to fully access and explore the rich physical properties of this promising material.

Appendix A

BHZ fitting of the SL band structure

The idea is to develop a BHZ-like toy model in order to describe, qualitatively but in an easy way, the physics of InAs/GaInSb-based superlattices. The goal is to evaluate the parameters of the low-energy model from the 8-bands k·p calculations.

Near the center of the Brillouin zone, one can show that it is possible to write the Hamiltonian of the system in the following form

$$H_{SL} = H_{\parallel}(k_x, k_y) + H_z(k_z), \tag{A.1}$$

where the first term is a typical BHZ Hamiltonian which describes the material at k_z constant. The second term describes the dispersion of the bands in the growth direction and can be written as

$$H_z(k_z) = \begin{pmatrix} A_z k_z^2 & 0 & 0 & 0 \\ 0 & B_z k_z^2 & 0 & 0 \\ 0 & 0 & A_z k_z^2 & 0 \\ 0 & 0 & 0 & B_z k_z^2 \end{pmatrix}. \tag{A.2}$$

Therefore, the total Hamiltonien can be casted as: where $C_z = C_0 + \left(\frac{A_z + B_z}{2}\right) k_z^2$ and $M_z = M_0 + \left(\frac{A_z - B_z}{2}\right) k_z^2$. One can see that we have here a BHZ-like Hamiltonian to describe the system. In order to reproduce the periodicity of the SL along the z direction, one can do the following transformation:

$$H_{SL} = \begin{pmatrix} C_z + M_z - (D+B)k_{\parallel}^2 & Ak_+ & 0 & 0 \\ Ak_- & C_z - M_z - (D-B)k_{\parallel}^2 & 0 & 0 \\ 0 & 0 & C_z + M_z - (D+B)k_{\parallel}^2 & -Ak_- \\ 0 & 0 & -Ak_+ & C_z - M_z - (D-B)k_{\parallel}^2 \end{pmatrix}, \tag{A.3}$$

$$k_z^2 \to \frac{2}{L^2}\left(1 - \cos k_z L\right), \tag{A.3}$$

where L is the period of the SL. Finally, given this hamiltonian, one can show that the eigenvalues are given by the following formula:

$$E_{SL}^{(+/-)} = C_z - Dk_{\parallel}^2 + s\sqrt{A^2 k_{\parallel}^2 + (M_z - Bk_{\parallel}^2)^2}, \tag{A.4}$$

where $s = \pm$ stands for conduction/valence band and (+/-) for the spin. With such an Hamiltonian, we have a fully spin degenerated system. The eigenvectors can be written as:

$$\Psi^{(+)}_{SL,c}(k_x,k_y,k_z) = \begin{pmatrix} \cos\theta_c^{(+)} \\ \sin\theta_c^{(+)} \\ 0 \\ 0 \end{pmatrix} \quad \text{where} \quad \tan\theta_c^{(+)} \equiv \frac{Bk_\parallel^2 + \sqrt{A^2k_\parallel^2 + (M_z - Bk_\parallel^2)^2} - M_z}{Ak_+}, \tag{A.5}$$

for the conduction band. For the valence band, we have:

$$\Psi^{(+)}_{SL,v}(k_x,k_y,k_z) = \begin{pmatrix} \cos\theta_v^{(+)} \\ \sin\theta_v^{(+)} \\ 0 \\ 0 \end{pmatrix} \quad \text{where} \quad \tan\theta_v^{(+)} \equiv \frac{M_z + \sqrt{A^2k_\parallel^2 + (M_z - Bk_\parallel^2)^2} - Bk_\parallel^2}{Ak_-}. \tag{A.6}$$

For the spin (-), we have the same expressions but with the non-zero and zero components reversed:

$$\Psi^{(-)}_{SL,c}(k_x,k_y,k_z) = \begin{pmatrix} 0 \\ 0 \\ \cos\theta_c^{(-)} \\ \sin\theta_c^{(-)} \end{pmatrix} \quad \text{and} \quad \Psi^{(-)}_{SL,v}(k_x,k_y,k_z) = \begin{pmatrix} 0 \\ 0 \\ \cos\theta_v^{(-)} \\ \sin\theta_v^{(-)} \end{pmatrix}. \tag{A.7}$$

Dispersion along k_z

In order to obtain the values of A_z and B_z, one have to fit the k·p curves for $k_\parallel = 0$. In these conditions, $H_\parallel$ can be written as

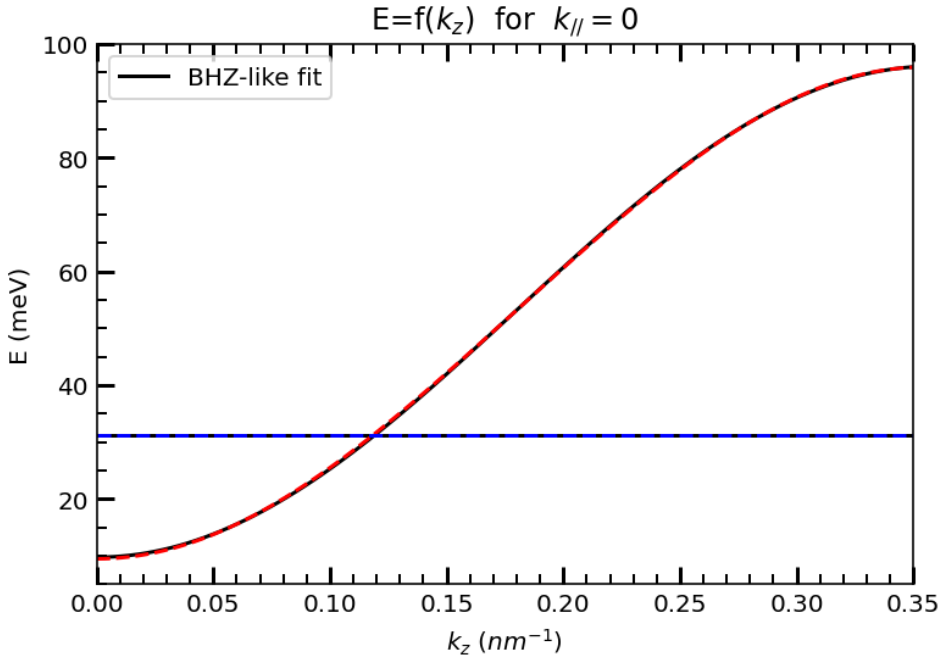

Figure A1: Solid lines: low-energy fitting. Dashed lines: k·p calculations.

$$H_{\parallel}(k_{\parallel}=0)=\begin{pmatrix} C_0+M_0 & 0 & 0 & 0 \\ 0 & C_0-M_0 & 0 & 0 \\ 0 & 0 & C_0+M_0 & 0 \\ 0 & 0 & 0 & C_0-M_0 \end{pmatrix} \tag{A.8}$$

And therefore one finds:

$$\begin{cases} E_1(k_{\parallel}=0,k_z)=C_0+M_0+A_zk_z^2 \\ H_1(k_{\parallel}=0,k_z)=C_0-M_0+B_zk_z^2 \end{cases} \tag{A.9}$$

Figure A1 shows that the model reproduces quite well the full k_z dispersion. One finds the following parameters:

$\boxed{A_z=1657.1\,meV.nm^2\ et\ B_z=-0.01\,meV.nm^2}$ et $\boxed{C_0=20.5\,meV\ et\ M_0=-10.7\,meV}$.

In-plane BHZ parameters

Let's now evaluate the BHZ paremeters A, B and D. For this, one will fit the k.p energy dispersions at $k_z=k_D$. At this particular point, $M_z=0$ (by definition of the Dirac node) so we directly have:

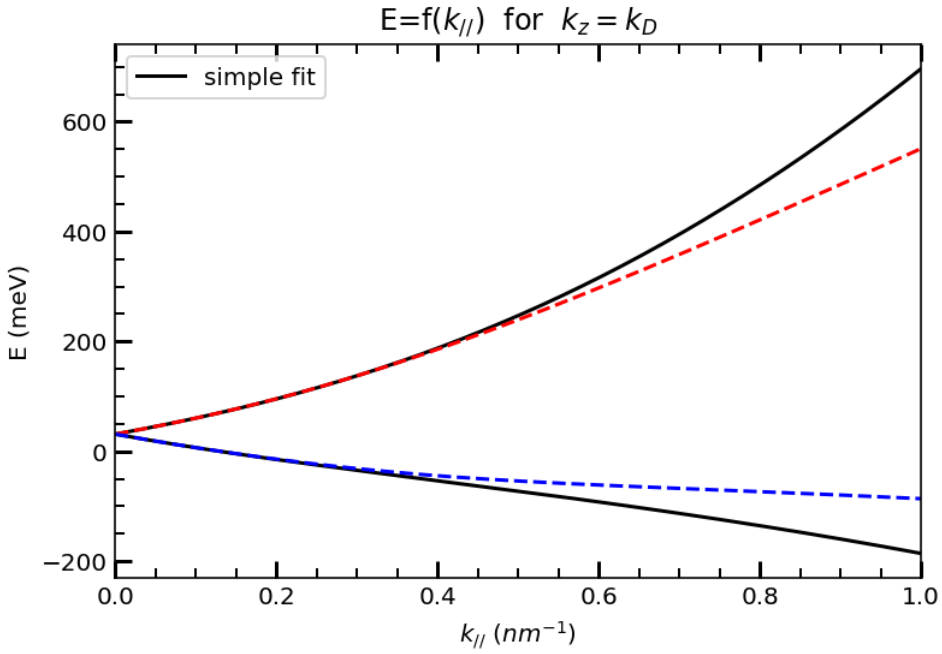

Figure A2: Solid lines: low-energy fitting. Dashed lines: k.p calculations.

$$\begin{cases} E_1(k_{\parallel},k_z=k_D)=C_z(k_D)-Dk_{\parallel}^2-\sqrt{B^2k_{\parallel}^4+A^2k_{\parallel}^2} \\ H_1(k_{\parallel},k_z=k_D)=C_z(k_D)-Dk_{\parallel}^2+\sqrt{B^2k_{\parallel}^4+A^2k_{\parallel}^2} \end{cases} \tag{A.10}$$

which can be written as:

$$\begin{cases} \dfrac{E_1(k_{\parallel},k_z=k_D)+H_1(k_{\parallel},k_z=k_D)}{2}=C_z(k_D)-Dk_{\parallel}^2 \\ \left(\dfrac{E_1(k_{\parallel},k_z=k_D)-H_1(k_{\parallel},k_z=k_D)}{2}\right)^2=B^2k_{\parallel}^4+A^2k_{\parallel}^2 \end{cases} \tag{A.11}$$

These two equations allow us to obtain the BHZ parameters. Figure A2 shows that the model can correctly fit the k·p calculations around $k_{\parallel} = 0$. I obtained the following parameters:

$\boxed{A = 266.9\, meV.nm,\ B = -351.1\, meV.nm^2\ et\ D = -223.9\, meV.nm^2}$.

Landé factors

The last parameters that we have to know are the Landé factors. Indeed, if one wants to compute the Landau Levels of the material, one have to add a Zeeman term and therefore Landé factors. To do so, one will fit the k·p zero-mode LLs computed at $k_z = k_D$. After a Peierls substitution, one knows from the BHZ model that the zero-mode LLs can be writen as followed:

$$\begin{cases} E_0^{(+)} = C_z(k_D) - \dfrac{D+B}{a_B^2} + \dfrac{g_e}{2}\mu_B\mathcal{B} \\ E_0^{(-)} = C_z(k_D) - \dfrac{D-B}{a_B^2} - \dfrac{g_h}{2}\mu_B\mathcal{B} \end{cases} \tag{A.12}$$

where $\mathcal{B}$ is the magnetic field applied and $a_B^2 = \dfrac{\hbar}{e\mathcal{B}}$ is the magnetic length. Here, only g_e and g_h are unknown. Figure A3 shows that the low-energy model can well reproduce the zero-mode LLs for low magnetic field values. I obtained the following Lande factors values:

$\boxed{g_e = 27\ et\ g_h = 34}$.

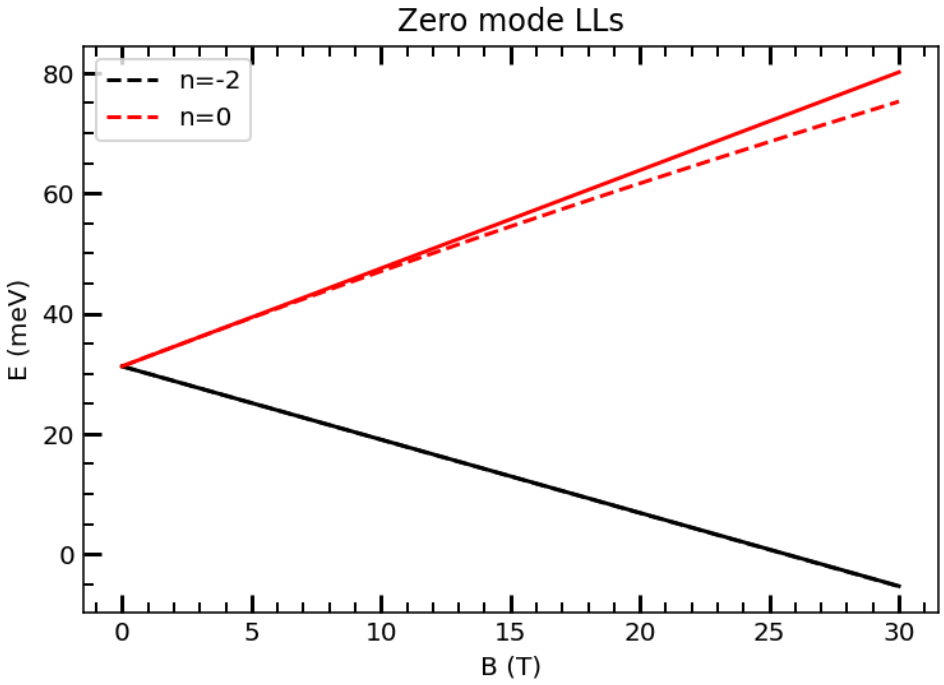

Figure A3: Solid lines: low-energy fitting. Dashed lines: k.p calculations.

Appendix B

Influence of the strong-coupling regime on the zero-mode LLs anti-crossing

As mentioned in the Introduction, 8 nm HgTe-based QWs are the first topological insulators in which Quantum Spin Hall effect (QSHE) has been experimentally demonstrated [41, 42]. One of the specificity of this topological phase, that results from the inverted band structure, is the magnetic field dispersion of the peculiar zero-mode LLs (LL0s). These levels emerge from the band edges, the one coming from the CB decreasing with magnetic field and the one rising from the VB increasing with the field. Therefore, these LLs0 are crossing

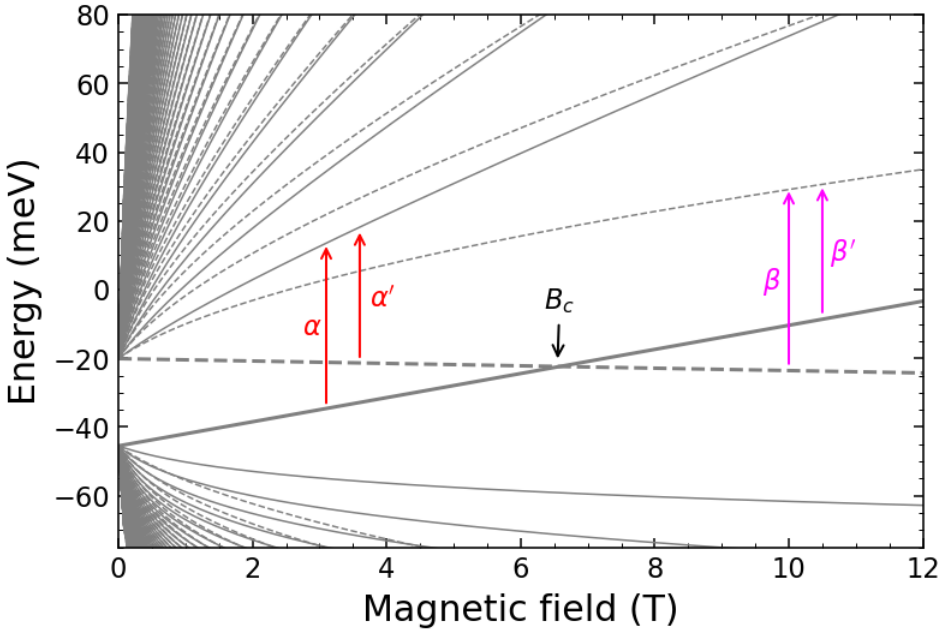

Figure B1: **LLs dispersion for an 8 nm HgTe QW, based on the BHZ model.** The LL0s are plotted in thick lines. Spin up (resp. down) levels are plotted in solid (resp. dashed) line. The α, α', β and β' transitions are indicated by arrows, as well as the critical field B_c.

at a critical magnetic field value B_c. A sketch of the situation is depicted in Fig. B1 where the LL0s are plotted in bold lines. This crossing of the zero-mode LLs has proven to be a very useful way to probe the topological nature of a material as it is only visible when the band structure is inverted. It has been shown that, in the presence crystalline asymmetries, in addition to the classical α and β transitions, "spin-flip" transitions α' and β' are also ac-

tivated in this material [70, 149–151]. Since these transitions involve the LL0s, they should cross when tuning the magnetic field through B_c. However, an avoided crossing is instead experimentally observed in THz magneto-spectroscopy, characterized by an energy gap Δ at the critical field value [70, 149–151]. The origin of this anti-crossing is not fully clear but the latest results tend to assess that, if the Interface Inversion Asymmetry (IIA) plays a small role, many-particles effects should be the dominant driving mechanism [70]. Indeed, it has been shown long time ago that inter-LLs excitations can be described as "magnetic excitons" and are subjected to many-body interactions [70, 152].

To describe the LL0s anti-crossing, a toy-model based on the BHZ model was developed [41, 70]. It can be modeled using the following equation:

$$\Delta E = \sqrt{M^2 \left(1 - \frac{B}{B_c}\right)^2 + \frac{\Delta^2}{4}}, \tag{B.1}$$

where $\Delta E = \frac{|\hbar\omega_{\alpha'} - \hbar\omega_{\alpha}|}{2}$ or $\Delta E = \frac{|\hbar\omega_{\beta'} - \hbar\omega_{\beta}|}{2}$, M is the bandstructure's gap and Δ the

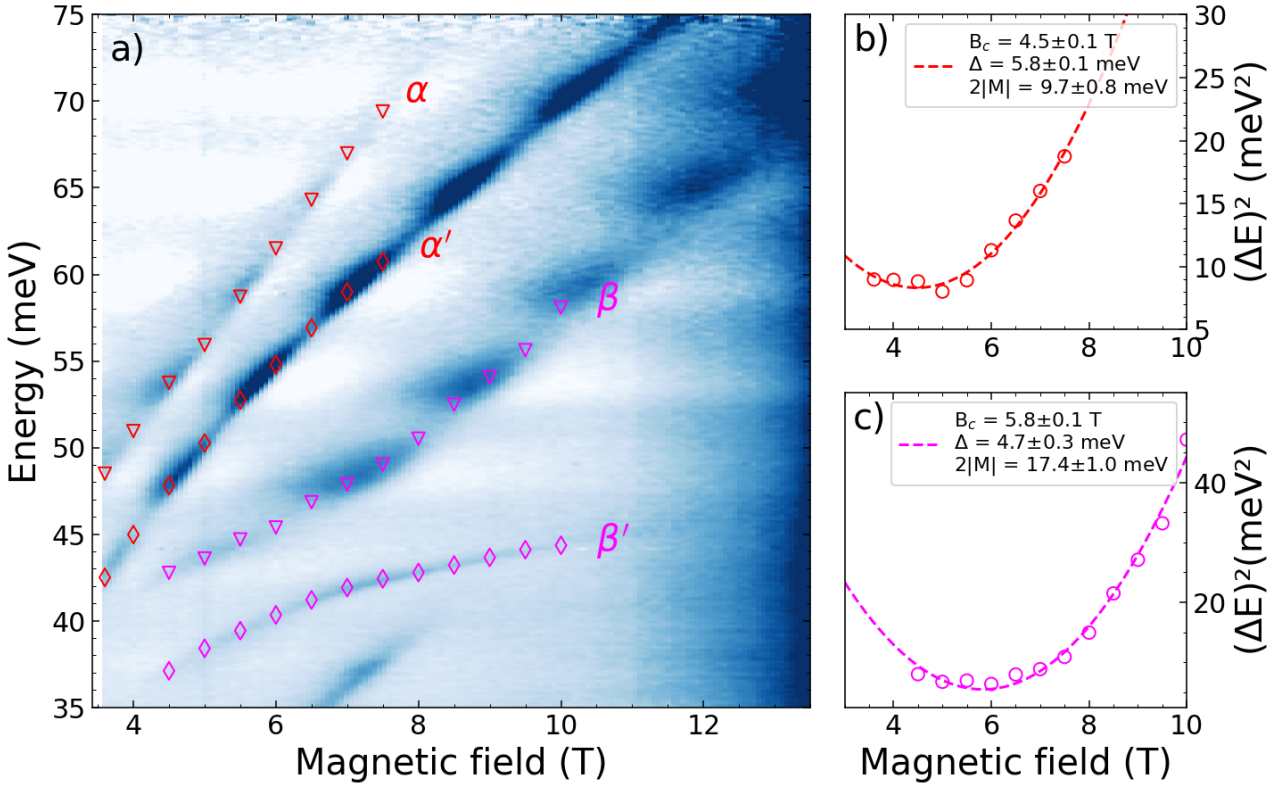

Figure B2: **LL0s anti-crossing in presence of the cavity for 28104-40um.** (a) False-color mapping of the magneto-reflectivity experiments on 28104-40um. The α / α' (resp. β / β') transitions are identified with the red (resp. magenta) markers. (b) (resp. (c)) Fitting, using the toy-model described in the main text, performed to determine the α / α' (resp. β / β') anti-crossing parameters.

anti-crossing gap. In a recent paper, the authors measured the 28104 8-nm HgTe QW's LL0s anti-crossing and they determined the following parameters [153]:

$$\begin{cases} B_c^{\alpha} = 4.9\,T,\ \Delta^{\alpha} = 5.5\,meV,\ 2|M^{\alpha}| = 10.4\,meV \\ B_c^{\beta} = 5.9\,T,\ \Delta^{\beta} = 4.6\,meV,\ 2|M^{\beta}| = 19\,meV \end{cases} \tag{B.2}$$

During my PhD work, we also had the occasion to probe the LL0s anti-crossing of sample 28104-40um. The results are shown in Fig. B2a, as a false-color mapping of the magneto-reflectivity spectra and where the α / α' and β / β' transitions are highlighted with empty markers. The transitions are patterned with interferences, witnessing the presence of the cavity. Using the toy-model of equation B.1, I could extract the anti-crossing parameters and the results are shown in Fig. B2b and c. If no clear deviation in the β parameters can be observed, the α parameters are significantly modified. In particular, the critical field is decreased by almost 0.5 T. One might be tempted to attribute this shift to a change in the electron density within the QW. Indeed, it was shown that the anti-crossing parameters are sensitive to the carrier density inside the well, as it was a signature of the many-body driving mechanism [70]. However, the study showed that for a density modulation of 33 %, the critical field shifted by only 0.2 T, thus barely overcoming the fitting error. We could estimate the difference in carrier concentration between the sample measured in [153] and ours to be around 40 %. Therefore, for a similar change of electron density, we observe a critical field shift almost two times bigger.

The origin of this shift is still unclear but this could be due to a strong coupling effect induced by the cavity created in the thinned sample's substrate. It was shown long time ago that the vacuum field, i.e. the quantum fluctuations of the electromagnetic field's ground-state, can manifest itself through its interaction with matter. In particular, it explains the Lamb shift of the hydrogen's fine structure and the modification of the electron magnetic moment in atoms [154, 155]. More recently, it was demonstrated that the electronic magneto-transport properties of a GaAs-based 2DEG are highly modified when strongly coupled to a cavity [156–158]. In particular, the authors showed that the topological protection of the integer quantum Hall effect as well as the correlations in the fractional quantum Hall effect were affected by the strong light-matter coupling. Even more recently, a group claimed that the LL fan diagram in graphene was modified when embedded in a strong coupling cavity [159]. All these studies highlight the fact that, when strongly coupled to the vacuum field, the matter properties are highly modified. Since we demonstrated that our device operates in the strong light-matter coupling, it could explain the critical field shift experimentally observed. More systematic measurements and theoretical support are of course needed to fully test this hypothesis.

Bibliography

[1] A. Y. Pawar, D. D. Sonawane, K. B. Erande, and D. V. Derle, "Terahertz technology and its applications", Drug Invention Today **5**, 157–163 (2013).

[2] J. Ward, E. Schlecht, G. Chattopadhyay, A. Maestrini, J. Gill, F. Maiwald, H. Javadi, and I. Mehdi, "Capability of THz sources based on Schottky diode frequency multiplier chains", in 2004 ieee mtt-s international microwave symposium digest (ieee cat. no.04ch37535), Vol. 3 (2004), 1587–1590 Vol.3.

[3] H. Eisele and R. Kamoua, "Submillimeter-wave InP Gunn devices", IEEE Transactions on Microwave Theory and Techniques **52**, 2371–2378 (2004).

[4] M. Asada, S. Suzuki, and N. Kishimoto, "Resonant tunneling diodes for sub-terahertz and terahertz oscillators", Japanese Journal of Applied Physics **47**, 4375 (2008).

[5] M. Mukherjee, N. Mazumder, S. K. Roy, and K. Goswami, "GaN IMPATT diode: a photosensitive high power terahertz source", Semiconductor Science and Technology **22**, 1258 (2007).

[6] J. V. Moloney, J. M. Yarborough, M. Fallahi, M. Scheller, S. W. Koch, and M. Koch, *Compact, high-power, room-temperature, narrow-line terahertz source*, (2011) `https://spie.org/news/3523-compact-high-power-room-temperature-narrow-line-terahertz-source`.

[7] C. Sirtori, "Bridge for the terahertz gap", Nature **417**, 132–133 (2002).

[8] J. Faist, F. Capasso, D. L. Sivco, C. Sirtori, A. L. Hutchinson, and A. Y. Cho, "Quantum cascade laser", Science **264**, 553–556 (1994).

[9] M. S. Vitiello and A. Tredicucci, "Physics and technology of terahertz quantum cascade lasers", Advances in Physics: X **6**, `10.1080/23746149.2021.1893809` (2021).

[10] M. Koch, D. M. Mittleman, J. Ornik, and E. Castro-Camus, "Terahertz time-domain spectroscopy", Nature Reviews Methods Primers **3** (2023).

[11] *Handbook of laser wavelengths*, Oct. 2018.

[12] A. V. Gaponov, V. A. Flyagin, A. L. Gol'denberg, G. S. Nusinovich, S. E. Tsimring, V. G. Usov, and S. N. Vlasov, "Invited paper. powerful millimetre-wave gyrotrons", International Journal of Electronics **51**, 277–302 (1981).

[13] V. Flyagin, A. Gaponov, I. Petelin, and V. Yulpatov, "The gyrotron", IEEE Transactions on Microwave Theory and Techniques **25**, 514–521 (1977).

[14] D. B. But, M. Mittendorff, C. Consejo, F. Teppe, N. N. Mikhailov, S. A. Dvoretskii, C. Faugeras, S. Winnerl, M. Helm, W. Knap, M. Potemski, and M. Orlita, "Suppressed Auger scattering and tunable light emission of Landau-quantized massless Kane electrons", Nature Photonics **13**, 783–787 (2019).

[15]A. Andronov, I. Zverev, V. Kozlov, Y. N. Nozdrin, S. Pavlov, and V. Shastin, "Stimulated emission in the long-wavelength IR region from hot holes in Ge in crossed electric and magnetic fields", JETP Lett **40**, 804–807 (1984).

[16]S. Komiyama, N. Iizuka, and Y. Akasaka, "Evidence for induced far-infrared emission from p-Ge in crossed electric and magnetic fields", Applied Physics Letters **47**, 958–960 (1985).

[17]K. Unterrainer, C. Kremser, E. Gornik, C. R. Pidgeon, Y. L. Ivanov, and E. E. Haller, "Tunable cyclotron-resonance laser in germanium", Phys. Rev. Lett. **64**, 2277–2280 (1990).

[18]Y. L. Ivanov, Y. B. Vasilyev, and V. A. Reingold, "Population inversion in the set of light hole Landau levels in germanium", Semiconductor Science and Technology **7**, B636 (1992).

[19]O. A. Klimenko, Y. A. Mityagin, S. A. Savinov, V. N. Murzin, N. V. Dyakonova, P Solignac, and W Knap, "Terahertz wide range tunable cyclotron resonance p-Ge laser", Journal of Physics: Conference Series **193**, 012064 (2009).

[20]A. Andronov, A. Belyantsev, V. Gavrilenko, E. Dodin, E. Krasil'nik, V. Nikonorov, S. Pavlov, and M. Shvarts, "Germanium hot-hole cyclotron-resonance maser with negative effective hole masses", Zh. Eksp. Teor. Fiz **90**, 367–384 (1986).

[21]A. Andronov, A. Beiyantsev, I Gavrilenko, and E. Dodin, "Induced hot-hole millimeter emission in germanium in fields E|| H (cyclotron-resonance negative-effective-mass", JETP Lett **40** (1984).

[22]E. Gornik, K. Unterrainer, and C. Kremser, "Tunable far-infrared solid-state lasers based on hot holes in germanium", Optical and Quantum Electronics **23**, S267–S286 (1991).

[23]E. Gornik, G. Strasser, and K. Unterrainer, "Landau level laser", Nature Photonics **15**, 875–883 (2021).

[24]G. Takacs, "Spectroscopy of the effects of strains and magnetic fields on shallow acceptor levels in germanium", Theses (University of Wollongong, 1999).

[25]J. M. Luttinger, "Quantum theory of cyclotron resonance in semiconductors: general theory", Physical Review **102**, 1030–1041 (1956).

[26]C. Chaubet, "Emission Landau dans les heterojonctions GaAlAs/GaAs et GaInP/GaAs", Theses (Université de Montpellier, 1993).

[27]T. Kurosawa, "On a possibility of negative cyclotron resonance in semiconductors", Solid State Communications **24**, 357–359 (1977).

[28]S. Reich, J. Maultzsch, C. Thomsen, and P. Ordejón, "Tight-binding description of graphene", Physical Review B **66** (2002).

[29]K. S. Novoselov, A. K. Geim, S. V. Morozov, D. Jiang, M. I. Katsnelson, I. V. Grigorieva, S. V. Dubonos, and A. A. Firsov, "Two-dimensional gas of massless Dirac fermions in graphene", Nature **438**, 197–200 (2005).

[30]M. L. Sadowski, G. Martinez, M. Potemski, C. Berger, and W. A. de Heer, "Landau level spectroscopy of ultrathin graphite layers", Physical Review Letters **97** (2006).

[31]K. S. Novoselov, A. K. Geim, S. V. Morozov, D. Jiang, Y. Zhang, S. V. Dubonos, I. V. Grigorieva, and A. A. Firsov, "Electric field effect in atomically thin carbon films", Science **306**, 666–669 (2004).

[32]M. O. Goerbig, "Electronic properties of graphene in a strong magnetic field", Reviews of Modern Physics **83**, 1193–1243 (2011).

[33]S. Gebert, C. Consejo, S. S. Krishtopenko, S. Ruffenach, M. Szola, J. Torres, C. Bray, B. Jouault, M. Orlita, X. Baudry, P. Ballet, S. V. Morozov, V. I. Gavrilenko, N. N. Mikhailov, S. A. Dvoretskii, and F. Teppe, "Terahertz cyclotron emission from two-dimensional Dirac fermions", Nature Photonics **17**, 244–249 (2023).

[34]F. Inamura, G. Ueda, S. Kim, M. Patrashin, I. Hosako, S. Komiyama, and K. Ikushima, "Landau-level terahertz emission from electrically biased graphene", APL Photonics **9** (2024).

[35]M. Orlita, D. M. Basko, M. S. Zholudev, F. Teppe, W. Knap, V. I. Gavrilenko, N. N. Mikhailov, S. A. Dvoretskii, P. Neugebauer, C. Faugeras, A.-L. Barra, G. Martinez, and M. Potemski, "Observation of three-dimensional massless Kane fermions in a zinc-blende crystal", Nature Physics **10**, 233–238 (2014).

[36]F. Teppe, M. Marcinkiewicz, S. S. Krishtopenko, S. Ruffenach, C. Consejo, A. M. Kadykov, W. Desrat, D. But, W. Knap, J. Ludwig, S. Moon, D. Smirnov, M. Orlita, Z. Jiang, S. V. Morozov, V. Gavrilenko, N. N. Mikhailov, and S. A. Dvoretskii, "Temperature-driven massless Kane fermions in HgCdTe crystals", Nature Communications **7** (2016).

[37]T. Morimoto, Y. Hatsugai, and H. Aoki, "Cyclotron radiation and emission in graphene", Phys. Rev. B **78**, 073406 (2008).

[38]P. Plochocka, P. Kossacki, A. Golnik, T. Kazimierczuk, C. Berger, W. A. de Heer, and M. Potemski, "Slowing hot-carrier relaxation in graphene using a magnetic field", Physical Review B **80** (2009).

[39]E. Malic, T. Winzer, F. Wendler, S. Brem, R. Jago, A. Knorr, M. Mittendorff, J. C. König-Otto, T. Plötzing, D. Neumaier, H. Schneider, M. Helm, and S. Winnerl, "Carrier dynamics in graphene: ultrafast many-particle phenomena", Annalen der Physik **529** (2017).

[40]F. Wendler, A. Knorr, and E. Malic, "Ultrafast carrier dynamics in Landau-quantized graphene", Nanophotonics **4**, 224–249 (2015).

[41]B. A. Bernevig, T. L. Hughes, and S.-C. Zhang, "Quantum spin Hall effect and topological phase transition in HgTe quantum wells", Science **314**, 1757–1761 (2006).

[42]M. Konig, S. Wiedmann, C. Brune, A. Roth, H. Buhmann, L. W. Molenkamp, X.-L. Qi, and S.-C. Zhang, "Quantum spin Hall insulator state in HgTe quantum wells", Science **318**, 766–770 (2007).

[43]*Physique des solides* (Saunders College Publishing, 2002).

[44]S. Komiyama, "Streaming motion and population inversion of hot carriers in crossed electric and magnetic fields", Advances in Physics **31**, 255–297 (1982).

[45]C. Liu, T. L. Hughes, X.-L. Qi, K. Wang, and S.-C. Zhang, "Quantum spin Hall effect in inverted type-II semiconductors", Physical Review Letters **100** (2008).

[46]I. Knez, R.-R. Du, and G. Sullivan, "Evidence for helical edge modes in inverted InAs/GaSb quantum wells", Phys. Rev. Lett. **107**, 136603 (2011).

[47]S. S. Krishtopenko and F. Teppe, "Quantum spin Hall insulator with a large bandgap, Dirac fermions, and bilayer graphene analog", Science Advances **4** (2018).

[48]S. S. Krishtopenko, A. V. Ikonnikov, K. V. Maremyanin, L. S. Bovkun, K. E. Spirin, A. M. Kadykov, M. Marcinkiewicz, S. Ruffenach, C. Consejo, F. Teppe, W. Knap, B. R. Semyagin, M. A. Putyato, E. A. Emelyanov, V. V. Preobrazhenskii, and V. I. Gavrilenko, "Cyclotron resonance of Dirac fermions in InAs/GaSb/InAs quantum wells", Semiconductors **51**, 38–42 (2017).

[49]S. S. Krishtopenko, W. Desrat, K. E. Spirin, C. Consejo, S. Ruffenach, F. Gonzalez-Posada, B. Jouault, W. Knap, K. V. Maremyanin, V. I. Gavrilenko, G. Boissier, J. Torres, M. Zaknoune, E. Tournié, and F. Teppe, "Massless Dirac fermions in III-V semiconductor quantum wells", Physical Review B **99** (2019).

[50]S. S. Krishtopenko, S. Ruffenach, F. Gonzalez-Posada, G. Boissier, M. Marcinkiewicz, M. A. Fadeev, A. M. Kadykov, V. V. Rumyantsev, S. V. Morozov, V. I. Gavrilenko, C. Consejo, W. Desrat, B. Jouault, W. Knap, E. Tournié, and F. Teppe, "Temperature-dependent terahertz spectroscopy of inverted-band three-layer InAs/GaSb/InAs quantum well", Physical Review B **97** (2018).

[51]D. Bajoni, "Polariton lasers. hybrid light–matter lasers without inversion", Journal of Physics D: Applied Physics **45**, 313001 (2012).

[52]C. Weisbuch, M. Nishioka, A. Ishikawa, and Y. Arakawa, "Observation of the coupled exciton-photon mode splitting in a semiconductor quantum microcavity", Physical Review Letters **69**, 3314–3317 (1992).

[53]A. Frisk Kockum, A. Miranowicz, S. De Liberato, S. Savasta, and F. Nori, "Ultrastrong coupling between light and matter", Nature Reviews Physics **1**, 19–40 (2019).

[54]A. Imamog¯lu, R. J. Ram, S. Pau, and Y. Yamamoto, "Nonequilibrium condensates and lasers without inversion: exciton-polariton lasers", Physical Review A **53**, 4250–4253 (1996).

[55]J. Kasprzak, M. Richard, S. Kundermann, A. Baas, P. Jeambrun, J. M. J. Keeling, F. M. Marchetti, M. H. Szymańska, R. André, J. L. Staehli, V. Savona, P. B. Littlewood, B. Deveaud, and L. S. Dang, "Bose–Einstein condensation of exciton polaritons", Nature **443**, 409–414 (2006).

[56]H. Deng, G. Weihs, D. Snoke, J. Bloch, and Y. Yamamoto, "Polariton lasing vs. photon lasing in a semiconductor microcavity", Proceedings of the National Academy of Sciences **100**, 15318–15323 (2003).

[57]D. Hagenmüller, S. De Liberato, and C. Ciuti, "Ultrastrong coupling between a cavity resonator and the cyclotron transition of a two-dimensional electron gas in the case of an integer filling factor", Physical Review B **81** (2010).

[58]G. Scalari, C. Maissen, D. Turčinková, D. Hagenmüller, S. De Liberato, C. Ciuti, C. Reichl, D. Schuh, W. Wegscheider, M. Beck, and J. Faist, "Ultrastrong coupling of the cyclotron transition of a 2D electron gas to a THz metamaterial", Science **335**, 1323–1326 (2012).

[59]Q. Zhang, M. Lou, X. Li, J. L. Reno, W. Pan, J. D. Watson, M. J. Manfra, and J. Kono, "Collective non-perturbative coupling of 2D electrons with high-quality-factor terahertz cavity photons", Nature Physics **12**, 1005–1011 (2016).

[60]A. Bayer, M. Pozimski, S. Schambeck, D. Schuh, R. Huber, D. Bougeard, and C. Lange, "Terahertz light–matter interaction beyond unity coupling strength", Nano Letters **17**, 6340–6344 (2017).

[61]H.-T. Chen, W. J. Padilla, J. M. O. Zide, A. C. Gossard, A. J. Taylor, and R. D. Averitt, "Active terahertz metamaterial devices", Nature **444**, 597–600 (2006).

[62]J. F. O'Hara, E. Smirnova, A. K. Azad, H.-T. Chen, and A. J. Taylor, "Effects of microstructure variations on macroscopic terahertz metafilm properties", Active and Passive Electronic Components **2007**, 1–10 (2007).

[63]W. J. Padilla, A. J. Taylor, C. Highstrete, M. Lee, and R. D. Averitt, "Dynamical electric and magnetic metamaterial response at terahertz frequencies", Physical Review Letters **96** (2006).

[64]Y. Toyozawa, "On the dynamical behavior of an exciton", Progress of Theoretical Physics Supplement **12**, 111–140 (1959).

[65]F. Tassone, C. Piermarocchi, V. Savona, A. Quattropani, and P. Schwendimann, "Bottleneck effects in the relaxation and photoluminescence of microcavity polaritons", Physical Review B **56**, 7554–7563 (1997).

[66]F. Tassone and Y. Yamamoto, "Exciton-exciton scattering dynamics in a semiconductor microcavity and stimulated scattering into polaritons", Physical Review B **59**, 10830–10842 (1999).

[67]G. Malpuech, A. Kavokin, A. Di Carlo, and J. J. Baumberg, "Polariton lasing by exciton-electron scattering in semiconductor microcavities", Physical Review B **65** (2002).

[68]G. Christmann, G. Tosi, N. G. Berloff, P. Tsotsis, P. S. Eldridge, Z. Hatzopoulos, P. G. Savvidis, and J. J. Baumberg, "Polariton ring condensates and sunflower ripples in an expanding quantum liquid", Physical Review B **85** (2012).

[69]J. Bloch, I. Carusotto, and M. Wouters, "Non-equilibrium Bose-Einstein condensation in photonic systems", Nature Reviews Physics **4**, 470–488 (2022).

[70]S. S. Krishtopenko, A. M. Kadykov, S. Gebert, S. Ruffenach, C. Consejo, J. Torres, C. Avogadri, B. Jouault, W. Knap, N. N. Mikhailov, S. A. Dvoretskii, and F. Teppe, "Many-particle effects in optical transitions from zero-mode landau levels in HgTe quantum wells", Physical Review B **102** (2020).

[71]S. Messelot, "Terahertz Tamm cavities for light-matter coupling with graphene based materials", Theses (Université Paris sciences et lettres, Dec. 2021).

[72]L. J. Van der Pauw, "A method of measuring specific resistivity and Hall effect of discs of arbitrary shape", Philips Res. Rep **13**, 1–9 (1958).

[73]*Convergence of Terahertz sciences in biomedical systems* (Springer Netherlands, 2012).

[74]W. Zawadzki, "Electron transport phenomena in small-gap semiconductors", Advances in Physics **23**, 435–522 (1974).

[75]E. H. Putley, "Far infra-red photoconductivity", physica status solidi (b) **6**, 571–614 (1964).

[76]*Landau level spectroscopy.* (Elsevier Science Pub, 1991).

[77]L. Dmowski, M. Cheremisin, C. Skierbiszewski, and W. Knap, "Far-infrared narrow-band photodetector based on magnetically tunable cyclotron resonance-assisted transitions in pure n-type InSb", Acta Physica Polonica A **92**, 733–736 (1997).

[78]K. Feng, W. Streyer, Y. Zhong, A. Hoffman, and D. Wasserman, "Photonic materials, structures and devices for Reststrahlen optics", Optics Express **23**, A1418 (2015).

[79]Y. J. Chung, A. Gupta, K. W. Baldwin, K. W. West, M. Shayegan, and L. N. Pfeiffer, "Understanding limits to mobility in ultrahigh-mobility GaAs two-dimensional electron systems: 100 million cm^{-2}/Vs and beyond", Physical Review B **106** (2022).

[80]G. Stillman, C. Wolfe, and J. Dimmock, "Magnetospectroscopy of shallow donors in GaAs", Solid State Communications **7**, 921–925 (1969).

[81]G. Stillman, C. Wolfe, and J. Dimmock, "Chapter 4 far-infrared photoconductivity in high purity GaAs", in *Semiconductors and semimetals* (Elsevier, 1977), 169–290.

[82]Z. Instruments, *Principles of lock-in detection*, https://www.zhinst.com/europe/en/resources/principles-of-lock-in-detection.

[83]Z. Instruments, *Principles of boxcar averaging*, https://www.zhinst.com/europe/en/resources/principles-of-boxcar-averaging.

[84]M. Baenninger, M. König, A. G. F. Garcia, M. Mühlbauer, C. Ames, P. Leubner, C. Brüne, H. Buhmann, L. W. Molenkamp, and D. Goldhaber-Gordon, "Fabrication of samples for scanning probe experiments on quantum spin Hall effect in HgTe quantum wells", Journal of Applied Physics **112** (2012).

[85]K. E. Spirin, D. M. Gaponova, K. V. Marem'yanin, V. V. Rumyantsev, V. I. Gavrilenko, N. N. Mikhailov, and S. A. Dvoretsky, "Bipolar persistent photoconductivity in HgTe/CdHgTe (013) double quantum-well heterostructures", Semiconductors **52**, 1586–1589 (2018).

[86]M. Städele and K. Hess, "Effective-mass enhancement and nonparabolicity in thin GaAs quantum wells", Journal of Applied Physics **88**, 6945–6947 (2000).

[87]D. Some and A. V. Nurmikko, "Real-time electron cyclotron oscillations observed by terahertz techniques in semiconductor heterostructures", Applied Physics Letters **65**, 3377–3379 (1994).

[88]K. Muro, S. Narita, S. Hiyamizu, K. Nanbu, and H. Hashimoto, "Far-infrared cyclotron resonance of two-dimensional electrons in an AlxGa1−xAs/GaAs heterojunction", Surface Science **113**, 321–325 (1982).

[89]C. Chaubet and F. Geniet, "Nonequilibrium occupation of Landau levels and universal critical field in the quantum-Hall-effect breakdown", Physical Review B **58**, 13015–13027 (1998).

[90]C. Chaubet, A. Raymond, and D. Dur, "Heating of two-dimensional electrons by a high electric field in a quantizing magnetic field: consequences in Landau emission and in the quantum Hall effect", Physical Review B **52**, 11178–11192 (1995).

[91]M. Srećković, N. Ivanović, O. Žižić, and S. Bojanić, "Electrical, optical, and thermodynamical aspects of sound propagation in HgTe, HgSe, Hg1−xMnxSe, and MnZn spinel ferrites", Journal of Electronic Materials **32**, 208–214 (2003).

[92]V. Latussek, C. R. Becker, G. Landwehr, R. Bini, and L. Ulivi, "Deformation potentials of the semimetal HgTe", Physical Review B **71** (2005).

[93]M. Grynberg, R. Le Toullec, and M. Balkanski, "Dielectric function in HgTe between 8 and 300K", Physical Review B **9**, 517–526 (1974).

[94]S. Komiyama, H. Sakuma, K. Ikushima, and K. Hirakawa, "Electron temperature of hot spots in quantum Hall conductors", Physical Review B **73** (2006).

[95]W. Zawadzki, S. Klahn, and U. Merkt, "Semirelativistic behavior of electrons in InSb in crossed magnetic and electric fields", Physical Review Letters **55**, 983–986 (1985).

[96]W. Zawadzki and B. Lax, "Two-band model for Bloch electrons in crossed electric and magnetic fields", Physical Review Letters **16**, 1001–1003 (1966).

[97]A. Aronov and G. Pikus, "Indirect optical transitions in crossed electric and magnetic fields", SOVIET PHYSICS JETP **22** (1966).

[98]E. O. Kane, "Band structure of indium antimonide", Journal of Physics and Chemistry of Solids **1**, 249–261 (1957).

[99]L. D. Landau, *Course of theoretical physics vol 5* (Pergamon Press, 1958).

[100]M. Planck, "On the law of distribution of energy in the normal spectrum", Annalen der physik **4**, 1 (1901).

[101]A. Kadykov, S. Krishtopenko, B. Jouault, W. Desrat, W. Knap, S. Ruffenach, C. Consejo, J. Torres, S. Morozov, N. Mikhailov, S. Dvoretskii, and F. Teppe, "Temperature-induced topological phase transition in HgTe quantum wells", Physical Review Letters **120** (2018).

[102]S. Messelot, C. Symonds, J. Bellessa, J. Tignon, S. Dhillon, J.-B. Brubach, P. Roy, and J. Mangeney, "Tamm cavity in the Terahertz spectral range", ACS Photonics **7**, 2906–2914 (2020).

[103]J. C. Cuevas, "Thermal radiation from subwavelength objects and the violation of Planck's law", Nature Communications **10** (2019).

[104]R. Fenollosa, F. Ramiro-Manzano, M. Garín, and R. Alcubilla, "Thermal emission of Silicon at near-infrared frequencies mediated by Mie resonances", ACS Photonics **6**, 3174–3179 (2019).

[105]C. Schneider, M. M. Glazov, T. Korn, S. Höfling, and B. Urbaszek, "Two-dimensional semiconductors in the regime of strong light-matter coupling", Nature Communications **9** (2018).

[106]D. Porras and C. Tejedor, "Linewidth of a polariton laser: theoretical analysis of self-interaction effects", Physical Review B **67** (2003).

[107]M. Pollnau and M. Eichhorn, "Spectral coherence, part i: passive-resonator linewidth, fundamental laser linewidth, and Schawlow-Townes approximation", Progress in Quantum Electronics **72**, 100255 (2020).

[108]D Yavorskiy, Y Ivonyak, D But, K Karpierz, A Krajewska, M Haras, P Sai, M Dub, A Kazakov, G Cywiński, W Knap, and J Łusakowski, "Pressure tuning of HgCdTe epitaxial layers—the role of the highly disordered buffer layer", Journal of Physics D: Applied Physics **58**, 025304 (2024).

[109]Y. Uenishi, H. Tanaka, and H. Ukita, "Characterization of AlGaAs microstructure fabricated by AlGaAs/GaAs micromachining", IEEE Transactions on Electron Devices **41**, 1778–1783 (1994).

[110]F Ramos-Mendieta and P Halevi, "Propagation constant — limited surface modes in dielectric superlattices", Optics Communications **129**, 1–5 (1996).

[111]M. E. Sasin, R. P. Seisyan, M. A. Kalitteevski, S. Brand, R. A. Abram, J. M. Chamberlain, A. Y. Egorov, A. P. Vasil'ev, V. S. Mikhrin, and A. V. Kavokin, "Tamm plasmon polaritons: slow and spatially compact light", Applied Physics Letters **92** (2008).

[112]M. Lopez-Garcia, Y.-L. D. Ho, M. P. C. Taverne, L.-F. Chen, M. M. Murshidy, A. P. Edwards, M. Y. Serry, A. M. Adawi, J. G. Rarity, and R. Oulton, "Efficient out-coupling and beaming of Tamm optical states via surface plasmon polariton excitation", Applied Physics Letters **104** (2014).

[113]T. W. Du Bosq, A. V. Muravjov, and R. E. Peale, "High-reflectivity intracavity Bragg mirrors for the far-infrared p-Ge laser", in Terahertz for military and security applications ii, Vol. 5411, edited by R. J. Hwu and D. L. Woolard (Sept. 2004), p. 167.

[114]E. Gornik, "Far infrared cyclotron emission in semiconductors", Journal of Magnetism and Magnetic Materials **11**, 39–46 (1979).

[115]G. Bauer, M. Overhamm, P. Grosse, W. Mütller, E. Gornik, and H. W. Pötzl, "Landau emission in n-InSb", physica status solidi (b) **75**, 543–551 (1976).

[116]E. Gornik, "Recombination radiation from impact-ionized shallow donors in n-type InSb", Physical Review Letters **29**, 595–597 (1972).

[117]E. Gornik, "Tunable far infra-red sources based on Landau-level transitions", Optics and Laser Technology **7**, 121–126 (1975).

[118]G. S. J. V. Smith, "The characterisation of InSb quantum well heterostructures by electrical measurement", PhD thesis (Cardiff School of Physics and Astronomy, 2019).

[119]N. Goel, J. Graham, J. Keay, K. Suzuki, S. Miyashita, M. Santos, and Y. Hirayama, "Ballistic transport in InSb mesoscopic structures", Physica E: Low-dimensional Systems and Nanostructures **26**, 455–459 (2005).

[120]K.-M. Chang, J.-J. Luo, C.-D. Chiang, and K.-C. Liu, "Wet etching characterization of InSb for thermal imaging applications", Japanese Journal of Applied Physics **45**, 1477 (2006).

[121]Z. Lei, C. A. Lehner, E. Cheah, M. Karalic, C. Mittag, L. Alt, J. Scharnetzky, W. Wegscheider, T. Ihn, and K. Ensslin, "Quantum transport in high-quality shallow InSb quantum wells", Applied Physics Letters **115** (2019).

[122]Z. Lei, E. Cheah, K. Rubi, M. E. Bal, C. Adam, R. Schott, U. Zeitler, W. Wegscheider, T. Ihn, and K. Ensslin, "High-quality two-dimensional electron gas in undoped InSb quantum wells", Physical Review Research **4** (2022).

[123]M. Schwarz, T. D. Vethaak, V. Derycke, A. Francheteau, B. Iniguez, S. Kataria, A. Kloes, F. Lefloch, M. Lemme, J. P. Snyder, W. M. Weber, and L. E. Calvet, "The Schottky barrier transistor in emerging electronic devices", Nanotechnology **34**, 352002 (2023).

[124]J. Keller, G. Scalari, F. Appugliese, S. Rajabali, M. Beck, J. Haase, C. A. Lehner, W. Wegscheider, M. Failla, M. Myronov, D. R. Leadley, J. Lloyd-Hughes, P. Nataf, and J. Faist, "Landau polaritons in highly nonparabolic two-dimensional gases in the ultrastrong coupling regime", Physical Review B **101** (2020).

[125]H.-T. Chen, J. F. O'Hara, A. J. Taylor, R. D. Averitt, C. Highstrete, M. Lee, and W. J. Padilla, "Complementary planar terahertz metamaterials", Optics Express **15**, 1084 (2007).

[126]T. J. Yen, W. J. Padilla, N. Fang, D. C. Vier, D. R. Smith, J. B. Pendry, D. N. Basov, and X. Zhang, "Terahertz magnetic response from artificial materials", Science **303**, 1494–1496 (2004).

[127]C. Jansen, I. A. I. Al-Naib, N. Born, and M. Koch, "Terahertz metasurfaces with high Q-factors", Applied Physics Letters **98** (2011).

[128]B. A. Piot, D. K. Maude, M. Henini, Z. R. Wasilewski, K. J. Friedland, R. Hey, K. H. Ploog, A. I. Toropov, R. Airey, and G. Hill, "Quantum Hall ferromagnet at high filling factors: a magnetic-field-induced Stoner transition", Physical Review B **72** (2005).

[129]R. J. Nicholas, R. J. Haug, K. v. Klitzing, and G. Weimann, "Exchange enhancement of the spin splitting in a GaAs-GaxAl1-xAs heterojunction", Physical Review B **37**, 1294–1302 (1988).

[130]T. Ando, A. B. Fowler, and F. Stern, "Electronic properties of two-dimensional systems", Reviews of Modern Physics **54**, 437–672 (1982).

[131]W. Kohn, "Cyclotron resonance and de Haas-van Alphen oscillations of an interacting electron gas", Physical Review **123**, 1242–1244 (1961).

[132]T. Maag, A. Bayer, S. Baierl, M. Hohenleutner, T. Korn, C. Schüller, D. Schuh, D. Bougeard, C. Lange, R. Huber, M. Mootz, J. E. Sipe, S. W. Koch, and M. Kira, "Coherent cyclotron motion beyond Kohn's theorem", Nature Physics **12**, 119–123 (2015).

[133]E. Gornik, W. Seidenbusch, R. Christanell, R. Lassnig, and C. Pidgeon, "Evidence for impurity states close to the 2D gas in GaAs/GaAlAs heterostructures", Surface Science **196**, 339–345 (1988).

[134]M. Witzany, E. Gornik, W. Ettmiiller, G. Böhm, G. Weimann, W. Knap, and J. L. Robert, "Impurity emission from GaAs/GaAlAs Heterostructures in the FIR", in *High magnetic fields in semiconductor physics iii* (Springer Berlin Heidelberg, 1992), 576–580.

[135]J. G. Michels, R. J. Warburton, R. J. Nicholas, and C. R. Stanley, "An optically detected cyclotron resonance study of bulk GaAs", Semiconductor Science and Technology **9**, 198–206 (1994).

[136]D. M. Mahler, J.-B. Mayer, P. Leubner, L. Lunczer, D. Di Sante, G. Sangiovanni, R. Thomale, E. M. Hankiewicz, H. Buhmann, C. Gould, and L. W. Molenkamp, "Interplay of Dirac nodes and Volkov-Pankratov surface states in compressively strained HgTe", Physical Review X **9** (2019).

[137]D. M. Mahler, V. L. Müller, C. Thienel, J. Wiedenmann, W. Beugeling, H. Buhmann, and L. W. Molenkamp, "Massive and topological surface states in tensile-strained HgTe", Nano Letters **21**, 9869–9874 (2021).

[138]*Fundamentals of semiconductors: physics and materials properties* (Springer, 2005).

[139]P. Pfeffer and W. Zawadzki, "Spin splitting of conduction subbands in III-V heterostructures due to inversion asymmetry", Physical Review B **59**, R5312–R5315 (1999).

[140]W. Zawadzki and P. Pfeffer, "Spin splitting of subband energies due to inversion asymmetry in semiconductor heterostructures", Semiconductor Science and Technology **19**, R1–R17 (2003).

[141]I. Vurgaftman, J. R. Meyer, and L. R. Ram-Mohan, "Band parameters for III–V compound semiconductors and their alloys", Journal of Applied Physics **89**, 5815–5875 (2001).

[142]Y.-S. Kim, K. Hummer, and G. Kresse, "Accurate band structures and effective masses for InP, InAs, and InSb using hybrid functionals", Physical Review B **80** (2009).

[143]R. S. Popovic, *Hall effect devices* (Institute of Physics publishing ltd, 1989).

[144]R. Niu and W. K. Zhu, "Materials and possible mechanisms of extremely large magnetoresistance: a review", Journal of Physics: Condensed Matter **34**, 113001 (2021).

[145]C. Thomas, "Strained HgTe/CdTe topological insulators, toward spintronic applications", PhD thesis (Université Grenoble Alpes, 2018).

[146]H. Ohno, E. E. Mendez, J. A. Brum, J. M. Hong, F. Agulló-Rueda, L. L. Chang, and L. Esaki, "Observation of Tamm states in superlattices", Physical Review Letters **64**, 2555–2558 (1990).

[147]A. B. Henriques, L. K. Hanamoto, P. L. Souza, and B. Yavich, "Observation of densely populated Tamm states in modulation-doped superlattices", Physical Review B **61**, R13369–R13372 (2000).

[148]F. Y. Huang and H. Morkoç, "Electronic surface state (Tamm state) under electric field in semiconductor superlattices", Journal of Applied Physics **71**, 524–526 (1992).

[149]M. Orlita, K. Masztalerz, C. Faugeras, M. Potemski, E. G. Novik, C. Brüne, H. Buhmann, and L. W. Molenkamp, "Fine structure of zero-mode landau levels in HgTe/HgxCd1-xTe quantum wells", Physical Review B **83** (2011).

[150]M. Zholudev, F. Teppe, M. Orlita, C. Consejo, J. Torres, N. Dyakonova, M. Czapkiewicz, J. Wróbel, G. Grabecki, N. Mikhailov, S. Dvoretskii, A. Ikonnikov, K. Spirin, V. Aleshkin, V. Gavrilenko, and W. Knap, "Magnetospectroscopy of two-dimensional HgTe-based topological insulators around the critical thickness", Physical Review B **86** (2012).

[151]M. S. Zholudev, F. Teppe, S. V. Morozov, M. Orlita, C. Consejo, S. Ruffenach, W. Knap, V. I. Gavrilenko, S. A. Dvoretskii, and N. N. Mikhailov, "Anticrossing of landau levels in HgTe/CdHgTe (013) quantum wells with an inverted band structure", JETP Letters **100**, 790–794 (2015).

[152]C. Kallin and B. I. Halperin, "Excitations from a filled Landau level in the two-dimensional electron gas", Physical Review B **30**, 5655–5668 (1984).

[153]S. Ruffenach, S. S. Krishtopenko, A. V. Ikonnikov, C. Consejo, J. Torres, X. Baudry, P. Ballet, B. Jouault, and F. Teppe, *Many-particle hybridization of optical transitions from zero-mode landau levels in hgte quantum wells*, 2025.

[154]W. E. Lamb and R. C. Retherford, "Fine structure of the hydrogen atom by a microwave method", Physical Review **72**, 241–243 (1947).

[155]P. Kusch and H. M. Foley, "The magnetic moment of the electron", Physical Review **74**, 250–263 (1948).

[156]F. Appugliese, J. Enkner, G. L. Paravicini-Bagliani, M. Beck, C. Reichl, W. Wegscheider, G. Scalari, C. Ciuti, and J. Faist, "Breakdown of topological protection by cavity vacuum fields in the integer quantum Hall effect", Science **375**, 1030–1034 (2022).

[157]J. Enkner, L. Graziotto, F. Appugliese, V. Rokaj, J. Wang, M. Ruggenthaler, C. Reichl, W. Wegscheider, A. Rubio, and J. Faist, "Testing the renormalization of the von Klitzing constant by cavity vacuum fields", Physical Review X **14** (2024).

[158]J. Enkner, L. Graziotto, D. Boriçi, F. Appugliese, C. Reichl, G. Scalari, N. Regnault, W. Wegscheider, C. Ciuti, and J. Faist, "Tunable vacuum-field control of fractional and integer quantum Hall phases", Nature **641**, 884–889 (2025).

[159]H. Xue, H.-C. Chan, Z. Lin, D. Boriçi, S. Zhou, Y. Wang, K. Watanabe, T. Taniguchi, C. Ciuti, W. Yao, D.-K. Ki, and S. Zhang, *Observation of cavity-mediated nonlinear Landau fan and modified Landau level degeneracy in graphene quantum transport*, 2025.